



TECHNISCHE  
UNIVERSITÄT  
WIEN

DISSERTATION

# Coherent control over the motional states of a Bose-Einstein condensate and applications

ausgeführt zum Zwecke der Erlangung des akademischen Grades  
eines Doktors der Naturwissenschaften

unter der Leitung von  
**o. Univ.-Prof. Dipl.-Ing. Dr. techn. Hannes-Jörg Schmiedmayer**  
Atominstitut (E141)

eingereicht an der  
Technischen Universität Wien  
Fakultät für Physik

von  
**Ing.-Dipl. Sandrine van Frank**  
Matrikelnummer 1126955  
Mollardgasse 70A/4  
1060 Wien, Österreich

Wien, October 2015

---

S. van Frank

Diese Dissertation haben begutachtet :

---

J. Schmiedmayer

---

S. Jochim



## Abstract

The coherent control of quantum states has been a subject of research for as long as quantum systems have been artificially created in laboratories. The prospect of one day realizing a quantum computer, relying on the coherence properties of quantum systems to multiply the available computational power, is of course one important motivation in that direction. It is not the only one. A precise control allows to initialize systems in specific quantum states and manipulate them in order e.g. to realize precision measurements. Ultracold atoms are an ideal test bed for advanced control schemes. Their isolation from the environment gives them long coherence times, while their response to external excitations is relatively simple to probe compared to other systems. Moreover, they offer a wide tuning range for a variety of parameters, such as density or interaction strength, and thus the possibility to experimentally investigate a whole spectrum of quantum theories. Coherent control of quantum states in ultracold atomic systems is therefore a rich area of research, holding promises both for fundamental tests of quantum mechanics and practical applications.

In this thesis, we developed a scheme to coherently manipulate the motional states of a Bose-Einstein condensate, in a way that is not only preserving the coherence of the system, but is also fast compared to the typical timescales of the system. The experimental system is an elongated condensate on an atomchip, initially in its transverse ground state. The condensate is displaced transversely to excite higher motional states. Using optimal control theory, the displacement is optimized to target specific motional states or a superposition of them. The optimizations rely on a mean-field approximation of the condensate. Both theoretically and experimentally, specific motional state superpositions could be reached in 1.1 ms with efficiencies higher than 98 %.

This control method was applied to the demonstration of a motional state interferometer. In this interferometer, the two paths are the ground and first transverse excited states, while a phase is naturally accumulated in the time between two optimized displacement pulses acting as beam splitters. In this scheme, the challenge lies in the optimization of a pulse that is effective for all phases. The interferometer was optimized numerically and successfully implemented experimentally, yielding an initial contrast of 92 %.

The created motional state superpositions are not stable and a damping is observed on a timescale of about 10 ms. To gain insight into the physics of the system, several damping mechanisms are envisaged and models developed. In particular, the dephasing and decoherence phenomena taking place in the longitudinal direction of the condensate are investigated. A transverse many-body model including three motional state is also designed. Timescales of the damping and dependencies on parameters such as atom number and temperature are extracted and compared to experimental data. From this study, interesting elements on the physics of the motional state superpositions came to light.

The results presented in this thesis demonstrate fast and efficient control over motional states and pave the way toward practical applications, such as a motional state interferometer. They also open a new direction for fundamental questions on out-of-equilibrium

physics in closed systems.

## Zusammenfassung

Die kohärente Kontrolle von Quantenzuständen ist Gegenstand von Untersuchungen seitdem Quantensysteme in Laboren erzeugt werden. Die Aussicht, eines Tages einen Quantencomputer realisieren zu können, der Kohärenzeigenschaften von Quantensystemen nutzt um die verfügbare Rechenleistung zu vervielfachen, ist dafür selbstverständlich eine wichtige Motivation, jedoch nicht die einzige. Präzise Kontrolle ermöglicht es, Systeme in bestimmten Quantenzuständen zu präparieren und zu manipulieren, etwa um Präzessionsmessungen zu realisieren. Ultrakalte Atome sind ein ideales Modellsystem für fortgeschrittene Kontrollschemas. Von ihrer Umgebung isoliert, verfügen sie über lange Kohärenzzeiten; gleichzeitig ist ihre Reaktion auf externe Anregungen im Vergleich zu anderen Systemen relativ einfach zu untersuchen. Außerdem können unterschiedliche Parameter über einen weiten Bereich abgestimmt werden, wie etwa die Dichte oder Wechselwirkungsstärke. Daraus ergibt sich die Möglichkeit, ein Spektrum von Quantentheorien experimentell zu untersuchen. Kohärente Kontrolle von Quantenzuständen in Systemen aus ultrakalten Atomen ist deshalb ein reiches Forschungsgebiet, das sowohl für fundamentale Tests der Quantentheorie als auch für praktische Anwendungen vielversprechend ist.

In dieser Dissertation wurde ein Schema entwickelt um Bewegungszustände eines Bose-Einstein Kondensates gezielt zu manipulieren. Dies geschieht auf eine Art die nicht nur die Kohärenzeigenschaften des Systems bewahrt, sondern auch schnell im Vergleich zur typischen Zeitskala des Systems ist. Experimentell umgesetzt wird dies in einem elongierten Kondensat auf einem Atomchip, welches ursprünglich im transversalen Grundzustand des Fallenpotentials ist. Das Kondensat wird entlang der transversalen Richtung verschoben um höhere Bewegungszustände anzuregen. Mithilfe der Theorie der optimalen Kontrolle

wird die Verschiebung des Kondensats optimiert um bestimmte Bewegungszustände oder deren Überlagerung zu erhalten. Die Optimierungen der "Schüttelpulse" basieren auf einer Beschreibung des Kondensates in einer mean-field Näherung. Verschiedene Überlagerungen von Bewegungszuständen konnten sowohl theoretisch als auch experimentell in 1.1 ms mit einer Effizienz von mehr als 98 % erreicht werden.

Diese Art der Kontrolle wurde angewandt um erstmals ein Interferometer mit Bewegungszuständen zu realisieren. Die beiden Pfade des Interferometers sind hier der Grundzustand und erste transversal angeregte Zustand. In der Zeit zwischen den beiden optimierten Bewegungspulsen die als Strahlteiler dienen, wird eine Phase akkumuliert. Die Herausforderung bei diesem Schema besteht darin, einen effizienten Puls für alle Phasen zu finden. Das Interferometer wurde numerisch optimiert und erfolgreich experimentell umgesetzt und lieferte einen Kontrast von 92 %.

Die so erzeugten Überlagerungen von Bewegungszuständen sind nicht stabil und es wurde eine Dämpfung auf einer Zeitskala von 10 ms beobachtet. Um ein besseres Verständnis zu erlangen wurden einige Dämpfungsmechanismen in Betracht gezogen und theoretische Modelle entwickelt. Insbesondere werden Dekohärenz und Dephasierung entlang der axialen Richtung des Kondensates untersucht. Ein transversales Vielteilchen-Modell, das drei Bewegungszustände beinhaltet, wurde entwickelt um daraus die Zeitskalen

der Dämpfung sowie die Abhängigkeit von Parametern wie Atomzahl und Temperatur abzuleiten und mit den experimentellen Ergebnissen zu vergleichen.

Die in dieser Dissertation präsentierten Ergebnisse demonstrieren schnelle und effiziente Kontrolle über Vibrationszustände und ebnen den Weg für praktische Anwendungen, wie etwa ein Interferometer mit Bewegungszuständen. Außerdem eröffnen sie eine neue Richtung für fundamentale Fragestellungen zur Nichtgleichgewichtsphysik in geschlossenen Systemen.

## Résumé

Depuis que des systèmes quantiques sont créés artificiellement en laboratoire, les chercheurs ont essayé de les contrôler de façon cohérente. La principale motivation de cette recherche est de voir un jour l'ordinateur quantique prendre forme. Mais ce n'est pas la seule. Contrôler avec précision les états quantiques d'un système, c'est pouvoir l'initialiser et le manipuler pour réaliser par exemple des mesures de précision. Les atomes froids sont un support idéal pour ce genre de contrôle. Leur isolation du monde extérieur leur confère des temps de cohérence longs, et leur réponse aux sollicitations externes est relativement facile à sonder comparé à d'autres systèmes. De plus, ils offrent la possibilité d'ajuster de nombreux paramètres, tels que la densité ou la force d'interaction entre atomes, et permettent par là d'explorer expérimentalement une variété de régimes pour tester différentes théories quantiques. Le contrôle cohérent d'états quantiques dans les systèmes atomiques ultrafroids est donc un terrain prometteur, aussi bien pour la recherche fondamentale que pour des applications pratiques de la physique quantique.

Dans cette thèse, une méthode pour contrôler les mouvements quantiques externes d'un condensat de Bose-Einstein est développée, méthode qui non seulement préserve la cohérence, mais est aussi rapide par rapport aux échelles de temps typiques du système. L'objet de l'expérience est un condensat allongé piégé sur une puce atomique et initialisé dans l'état fondamental transverse. Il est déplacé dans une des directions transverses pour exciter des états de mouvement externes d'énergie supérieure. En faisant appel à des théories de contrôle optimal, le déplacement du condensat est optimisé pour cibler ou bien des états particuliers, ou bien une superposition d'entre eux. Ces optimisations se basent sur une description du système de type champ moyen. Avec cette technique, différents états cibles et superpositions d'états ont pu être atteints en 1.1 ms avec une précision supérieure à 98 %.

Cette méthode de contrôle a été mise en pratique dans un nouveau concept d'interféromètre construit sur des états quantiques de mouvement. Les deux bras de cet interféromètre correspondent respectivement à l'état fondamental et au premier état excité transverses. Deux séquences de déplacement qui font office de miroirs semi-réfléchissant, et une phase relative entre les deux états s'accumule durant un temps variable entre les deux déplacements. La difficulté principale de ce concept réside dans l'optimisation d'un déplacement qui soit effectif quelque soit la phase relative entre les deux états. Un tel interféromètre a été optimisé numériquement puis mis en oeuvre expérimentalement avec succès, résultant en un contraste initial de 92 %.

Les superpositions d'états de mouvement ne sont pas stables, comme en atteste la perte de contraste observée sur une échelle de 10 ms. Afin de comprendre les processus physiques à l'oeuvre dans le système, plusieurs mécanismes pouvant expliquer la perte de contraste sont envisagés et modélisés. En particulier, plusieurs phénomènes de déphasage et de décohérence, induits par l'élongation du nuage atomique dans la direction longitudinale, sont explorés. Un autre modèle traitant des comportements à N-corps dans le système est également développé. Des échelles de temps pour la perte de contraste et leur dépendance relative à différents paramètres, tels que le nombre d'atomes ou la température, sont extraites des modèles et comparées aux données expérimentales. Cette étude préliminaire

révèle plusieurs aspects intéressants de la physique des états de mouvement dans les condensats de Bose-Einstein.

Les résultats présentés dans cette thèse ont démontré la faisabilité d'un contrôle rapide et précis des états de mouvement quantiques d'un condensat de Bose-Einstein, ce qui est un premier pas vers des applications pratiques de cette méthode, telles que l'interféromètre présenté dans cette même thèse. Ces résultats ouvrent également la voie à de nouvelles recherches théoriques et expérimentales sur la physique hors d'équilibre des systèmes isolés.

## Acknowledgements

After years of research, months of writing and weeks of a final rush through the final corrections and organizational points, writing the Acknowledgements section of the thesis is an important time to take a step back and reflect on the many things, big and small, that have made this work possible. While hard work and a good dose of luck were essential, they would never have sufficed by themselves. I am indebted to many people, who helped and supported me along the way, both scientifically and personally. Most importantly, I had the chance to work with exceptional people, whose extended knowledge, motivation and sense of humor have greatly contributed to making this time at the institute and in the lab stimulating and enjoyable.

In particular, I would like to thank...

... my supervisor Jörg Schmiedmayer for giving me the chance to work in his group and supervising my work. By sharing his scientific insights and creative ideas, and trusting his students on every aspect of their projects, he feeds the group with a never-fading motivation to (re)search further.

... Thorsten Schumm, who first pulled out my CV and invited me to Vienna for an interview. Through his availability and his facetious encouragements, he has been an important source of support. His scientific knowledge and advice have been priceless, and his generous supplies of éclairs au chocolat and other delicious pâtisseries have also been greatly appreciated.

... the former RbII team members, some of whom I have not had time to (properly) know but passed on their legacy: a fully assembled, mostly automatized experiment, a valuable panel of control tools, important research results and a lot of music on the lab computers. People I did have the chance to meet and work with taught me a lot, both on the theory and on practical aspects: Stephanie Manz, who introduced me to the experiment; Robert Bückler, who shared with me his impressive know-how on the experiment and the on-going projects, his sudden inspirations and his skills in the lab; Jean-François Schaff, for advancing my scientific education and inviting me to some cosy parties at his place; Tarik Berrada for the long and fruitful discussions, his enthusiasm for many topics and his peculiar April's fools jokes.

... the current "atomsheep" team members (in order of appearance): Marine Pigneur, who entrusted me with her adorable cat Arpège, RuGway Wu who slowly shifted to his own project but remained a part of the team nonetheless, Marie Bonneau with whom I shared, in addition to stimulating scientific discussions, relaxing after-work Badminton sessions, and Mira Maiwöger, who in addition to being a great office mate also brought back a much-needed knowledge of German in the team.

... Thorsten, Marie and RuGway for thoroughly (and bravely) proof-reading this manuscript chapter after chapter, as well as Marie and Mira for greatly helping in the last data measurement campaign for this thesis.

... other people from this group and elsewhere, whose help with this work has been precious: Wolfgang Rohringer for his continuous interest in my research topics and his powerful numerical simulations, Johannes Majer for his patient answers to my basic

electronic questions, Antonio Negretti, Simone Montangero and Tommaso Calarco for their regular collaboration on the different optimization projects, Isabelle Bouchoule for her precious input on the homogeneous longitudinal dephasing effect, and Miguel-Ángel García-March for his calculations and simulations of the many-body three-mode problem.

... Selim Jochim for accepting to be a referee at my thesis defense and consequently for reading this hefty tome.

... the “Gemmabilla” crew and other group members with whom I have shared countless meals and discussions, some of which I would rather have avoided, or kept for another — foodless — time. A big thanks goes to the whole atomchip group for contributing to the excellent working environment and jolly international atmosphere.

... the people outside of research, who still are not sure what my thesis is about, but supported me through each step of it: the terrific friends I made in Vienna, either still present or already gone towards new horizons; my friends in France and all around the world, whom I wish I could meet and discuss with more often; my family in Belgium and in France, and in particular my parents Jean and Cécile, who provided me with everything I ever needed, and whom I could never thank enough; my second family in Vienna, who welcomed me whole-heartedly and in their home and in their lives; and finally, but immensely, my partner Florian, who, with much love and support, has tirelessly accompanied me through this incredible adventure.

# Contents

<b>1</b>	<b>Introduction</b>	<b>1</b>
<b>2</b>	<b>Theoretical description of the system</b>	<b>5</b>
2.1	Short history of Bose-Einstein condensation . . . . .	5
2.2	Bose-Einstein condensation of an ideal gas . . . . .	6
2.2.1	BEC in a box potential . . . . .	6
2.2.2	BEC in a harmonic potential . . . . .	8
2.2.3	BEC with finite particle number . . . . .	9
2.3	Weakly interacting Bose gas . . . . .	10
2.3.1	Interaction potential . . . . .	10
2.3.2	Many-body Hamiltonian . . . . .	11
2.3.3	Mean-field approximation: Gross-Pitaevskii equation . . . . .	12
2.4	Quasi-particle spectrum: Bogoliubov approximation . . . . .	15
2.5	One-dimensional interacting Bose gas . . . . .	18
2.5.1	Regimes of interaction . . . . .	19
2.5.2	Description of the transverse direction(s) . . . . .	21
<b>3</b>	<b>Technical features of the experiment</b>	<b>23</b>
3.1	Elements of the setup . . . . .	24
3.1.1	Vacuum chamber and Rubidium dispenser . . . . .	25
3.1.2	Laser system . . . . .	26
3.1.3	External coils . . . . .	29
3.1.4	Atom chip . . . . .	29
3.1.5	Imaging systems . . . . .	32
3.1.6	Waveform generators . . . . .	36
3.1.7	Control and acquisition . . . . .	38
3.2	Trapping and manipulation of atoms . . . . .	39
3.2.1	Neutral atoms in a magnetic field . . . . .	39
3.2.2	Harmonic trap with static fields . . . . .	40
3.2.3	Anharmonic trap with radio-frequency dressing . . . . .	41

3.2.4	Trap simulation . . . . .	43
3.2.5	Transverse displacement of the trap . . . . .	46
3.3	Experimental sequence and procedures . . . . .	48
3.3.1	From MOT to molasses . . . . .	48
3.3.2	Loading to the chip . . . . .	49
3.3.3	In the chip trap . . . . .	49
3.3.4	Imaging . . . . .	50
3.4	Atom number calibration using the Light Sheet . . . . .	54
3.4.1	Two-photon correlation functions . . . . .	54
3.4.2	Photon-per-atom and atom number determination . . . . .	57
3.4.3	Comparison to indirect photon-per-atom measurement . . . . .	57
<b>4</b>	<b>Coherent state manipulation using Optimal Control</b>	<b>60</b>
4.1	Interest for the manipulation of complex systems . . . . .	60
4.2	Control over transverse motional states . . . . .	61
4.3	Specific constraints of our system . . . . .	62
4.3.1	Mean-field effects . . . . .	62
4.3.2	Beyond two-level model . . . . .	65
4.3.3	Beyond-mean-field effects . . . . .	65
4.3.4	Technical limitations . . . . .	66
4.4	Solution brought by optimal control theory . . . . .	67
4.4.1	Concepts of optimal control applied to our experiment . . . . .	67
4.4.2	Application of the CRAB algorithm . . . . .	69
4.5	State-to-state transfer pulse optimization . . . . .	70
4.5.1	Optimization problem initialization . . . . .	70
4.5.2	Pulses optimized close to the quantum speed limit . . . . .	70
4.5.3	Insight on pulse complexity . . . . .	72
4.5.4	Robustness of the pulse . . . . .	73
4.6	Experimental realization . . . . .	76
4.6.1	Initial state characterization . . . . .	76
4.6.2	Implementation of a transfer pulse and monitoring . . . . .	79
4.7	Experimental transfer efficiency . . . . .	80
4.7.1	Principle of state analysis . . . . .	80
4.7.2	Choice of model . . . . .	81
4.7.3	Fitting procedure . . . . .	83
4.7.4	Error estimation . . . . .	86
4.8	Experimental results . . . . .	87
<b>5</b>	<b>Application to interferometry: the motional states interferometer</b>	<b>90</b>
5.1	Interferometry with Bose-Einstein condensates . . . . .	90
5.2	Concept of a Ramsey-type interferometer for motional states . . . . .	93
5.2.1	The well-known Ramsey interferometer . . . . .	93
5.2.2	Transposition to motional states of a BEC . . . . .	94
5.3	Optimization with the CRAB algorithm . . . . .	96

---

5.3.1	“Visibility” as figure of merit . . . . .	97
5.3.2	Optimized second pulse . . . . .	98
5.4	Result of the interferometer . . . . .	100
5.5	Prospects . . . . .	102
<b>6</b>	<b>Complex behaviors in motional state superpositions</b>	<b>104</b>
6.1	Limitations of the Gross-Pitaevskii equation . . . . .	104
6.2	Experimental observations on the loss of contrast . . . . .	105
6.2.1	General considerations . . . . .	106
6.2.2	Evolution at long times . . . . .	106
6.2.3	Experimental data for different parameters . . . . .	112
6.3	Longitudinal effects . . . . .	115
6.3.1	Decay into twin-atom beams . . . . .	115
6.3.2	Longitudinal dephasing in a homogeneous condensate . . . . .	116
6.3.3	Longitudinal dephasing induced by the inhomogeneous density . . . . .	122
6.4	Many-body effects . . . . .	123
6.4.1	Two-mode transverse dephasing . . . . .	124
6.4.2	Three-mode many-body model . . . . .	126
6.4.3	Many-body simulations . . . . .	129
6.4.4	Comparison to experimental data . . . . .	132
6.5	Other considerations . . . . .	133
6.6	Conclusions . . . . .	134
<b>7</b>	<b>Summary and perspectives</b>	<b>136</b>
<b>A</b>	<b>Bogoliubov model</b>	<b>140</b>
<b>B</b>	<b>Data sets</b>	<b>144</b>
<b>C</b>	<b>List of publications</b>	<b>145</b>

# 1

## Introduction

The advent of Bose-Einstein condensation has been an important stepping stone in the study of fundamental concepts in quantum physics. Bose-Einstein condensates (BEC) of dilute gases, when first realized experimentally in 1995 [1–3], triggered a huge interest among physicists: a completely new state of matter was becoming accessible. By lowering the temperature of an atomic gas to almost zero Kelvin, the quantum-mechanical wavefunction of this new object behaved as a coherent matter wave, making it the atomic equivalent of coherent laser light in optics. Considering the great advances enabled by the discovery of lasers, it is no wonder physicists jumped at it.

Bose-Einstein condensates, and more generally ultracold atoms, are relatively simple objects. On the one hand, as coherent matter waves, their basics can be understood with a few concepts and equations from the early days of quantum mechanics, as presented by Bose and Einstein [4]. On the other hand, these objects require a good isolation from the environment, which would otherwise affect the coherence of the system. These two characteristics are of great value when it comes to understanding phenomena observed in other fields in physics. Due to its relative simplicity and its isolation, ultracold atoms were used to model different phenomena occurring in other quantum systems with many particles, e.g. phase transitions [5, 6], turbulences in bosonic superfluids [7, 8], many-body spin dynamics [9, 10], quantum magnetism [11, 12] and simulations of condensed matter in lattices [12, 13].

Bringing a gas of atoms close to absolute zero temperature is a feat of physics and engineering. The progress made in the field of ultracold atoms is intrinsically linked to the successful development of techniques to manipulate atoms. First, without the invention of lasers and the brilliant idea to use them as a cooling tool for atoms through the Doppler effect, in 1975 [14, 15], it is doubtful that Bose-Einstein condensates would ever have seen the light of day. Later on, by combining magnetic field trapping to laser light cooling, the magneto-optical trap [16] allowed to reduce temperatures down to only tens of microkelvin. The feat was complete with the introduction of evaporative cooling,

by which the phase transition to a Bose-Einstein condensate was achieved.

After these original achievements, experimental tools were soon developed to probe and manipulate ultracold atomic samples. Laser light is the basic and indispensable tool to image atoms in many cold atom experiments. The utility of laser light was extended to trapping atoms with the introduction of dipole traps and optical lattices [17]. In other experimental setups, various configurations of magnetic fields are explored in carefully designed atomchips [18]. These techniques allow a high degree of precision in the controlled manipulation of atoms and a remarkable tunability of some fundamental parameters, e.g. temperature, density or interaction strength.

In the early days of Bose-Einstein condensation, studies were focused on the equilibrium properties of these systems or their reactions to small perturbations. With the availability of high-precision setups, a new generation of experiments is born, where more complex schemes can be implemented and non-equilibrium dynamics investigated. In parallel to the necessary engineering effort to improve experimental capacities, new theoretical models need to be developed. In addition to perturbation theory, models encountering many-body problems and out-of-equilibrium physics are required [19].

The new experimental and theoretical advances have already begun to bear fruits. One example of these achievements is the application of ultracold atoms to interferometry and precision measurements. Realized both in free space and with trapped systems, matter wave interferometry has the advantage over conventional optical interferometers that it is sensitive to gravitational and magnetic fields, an important feature for inertial sensing and magnetometry. In double-wells or lattices, the presence of atomic interactions can lead to a gain in sensitivity beyond the standard quantum limit [20, 21]. The theoretical description of the trapped atoms relies on the Bose-Hubbard Hamiltonian, a many-body model close to the Hubbard model for superconducting solid-state materials. Another example is the study of non-equilibrium physics in double-wells. Much theoretical effort has been undertaken in order to develop truly non-equilibrium descriptions [22–27]. The current studies on this topic, experimental and theoretical, aim at a better understanding of fundamental properties of nature, e.g. the relaxation to equilibrium of isolated systems [28, 29], or at formulating analogue models to gravity and space-time, e.g. black holes [30] or inflationary scenarios in the early universe [31, 32]. Applications to quantum information and computing are also widely studied, in particular with trapped ions, which are conveniently addressable individually [33, 34]. For each ion, two electronic hyperfine states can be used as a two-level system, making the ion an ideal quantum bit, or *qubit*. These ions can nowadays be prepared in a state and perform operations with incredible accuracy [35, 36] thanks to a precise control of the phase and duration of microwave pulses. The main limitation of trapped ions is its limited scalability. Ultracold atomic ensembles, with orders of magnitude more particles, are potential candidates to solve the scalability problem [37]. Depending on the study or application, internal states (e.g. hyperfine states of ions) or external states (e.g. spatial states in a double-well or a lattice) are exploited. In all cases, efficient techniques to prepare and manipulate quantum states are key.

In this thesis, an efficient way of manipulating the quantum motional states of a

---

Bose-Einstein condensate (BEC) using optimal control methods is presented. The control scheme is extended to demonstrate a new type of interferometer, based on motional states. The out-of-equilibrium physics induced by the manipulations is also investigated.

To this end, we prepared an elongated condensate of rubidium on an atomchip. Micro-fabricated structures on the atomchip allow to strongly confine, accurately manipulate and probe quantum gases. In the present experiment, this technology permits to create elongated trapping potentials, in which the atoms are initially cooled down to the transverse ground state. It also allows to modify the geometry of the trap and lift the degeneracy of the splitting between the levels, such that levels can be addressed individually. Moreover, the transitions between vibrational levels of the trap, or equivalently between motional states of the condensate, are driven by an accurate displacement of the trapping potential, which is also made possible by the high level of control offered by the atomchip.

We could show that the motional states manipulation conserves the coherence of the system. This opens the door to various applications based on coherence properties, such as interferometry or quantum computing. As a proof-of-principle of the former, we engineered two pulses acting as beam splitters for the motional states, and proved that we could retrieve the phase information for the final motional state. The observed loss of contrast for long interrogation times led us to explore the damping mechanisms present in the system. For all investigations, the read-out of the results was done by imaging the condensate in time-of-flight.

## Outline

This thesis is organized as follows:

- Chapter 2 introduces the theoretical foundations of the work carried out in this thesis. After explaining the phenomenon of Bose-Einstein condensation, it focuses on the special case of the interacting BEC and the implications of an elongated geometry, in particular the presence of longitudinal excitations.
- Chapter 3 presents the experimental setup on which the experiments were conducted. The different elements of the apparatus are first briefly described, before expanding on their application to trap and manipulate BECs. A typical experimental sequence is described step-by-step, from the initial cooling to the final imaging. Imaging is given special attention.
- Chapter 4 is devoted to the manipulation technique applied to the BEC's motional states, which is the central element of this thesis. The motivations for this scheme are laid out and the constraints set by our particular setup presented. An optimal control method is introduced, which allowed, based on mean-field approximations, to optimize transfer pulses between quantum states without loss of coherence. Experimental results for two examples of such transfers are given.
- Chapter 5 shows how two transfer pulses were combined to form an interferometer based on motional states. The optimization of the second pulse is more involved than the first one. After demonstrating numerically that the two transfer pulses

were efficient beam splitters for motional states, we present the experimental results of the new motional state interferometer.

- Chapter 6 gives an account of different physical effects liable to lead to a loss of coherence. The limitations of the mean-field approach are underlined. Effects taking place in the longitudinal direction of the trapping potential, as well as many-body phenomena, are modeled and compared to experimental data.
- Chapter 7 finally concludes this thesis with a summary and an outlook onto future applications of schemes based on motional states.

# 2

## Theoretical description of the system

This chapter gives an overview of the theoretical concepts which are relevant to the experiments presented in this thesis. It starts with a short introduction to the topic of Bose-Einstein condensation of an ideal gas, going from the textbook example of condensation in a box potential in the continuum limit to the more realistic, finite system trapped in a harmonic potential. The case of the weakly interacting Bose gas, appropriate to describe the experimental system, is then shortly reviewed in sec. 2.3. The many-body Hamiltonian and its corresponding Heisenberg equation of motion are given, as well as a simplified, mean-field description translated into the well-known Gross-Pitaevskii equation. The Bogoliubov excitation spectrum, particularly apt to describe the dynamics in a shallow trap, is also introduced. It can be used to treat the elongated dimension of the one-dimensional Bose gas, which is introduced in sec.2.4. The last part highlights the different regimes accessible in the 1d geometry and the characteristics of the quasi-condensate used in these experiments. A description of the transverse dimension is added, as it is where most of the dynamics studied in this thesis takes place.

### 2.1 Short history of Bose-Einstein condensation

In 1924, N. Bose studied the statistical properties of a gas of photons in terms of quanta [4], an idea that A. Einstein helped publish and extended to a more general system of non-interacting Bose particles with mass, introducing the idea of Bose-Einstein condensation [38]. The idea that a macroscopic number of particles could condense into the lowest energy state for low enough temperatures was revolutionary at the time, and it took many years before anyone considered it relevant for experimental applications.

In 1938, when superfluidity in liquid  $^4\text{He}$  was discovered by P.L. Kapitza, J.F. Allen and A.D. Misener [39, 40], F. London drew a parallel between superfluidity and Bose-

Einstein condensation [41]. As superfluid  $^4\text{He}$  is strongly interacting, the connection between superfluidity and Bose-Einstein condensation was not obvious. A theory of interacting Bose gases was developed by Bogoliubov in 1947 [42]. Nevertheless, it took almost sixty more years and the first realization of atomic BECs in 1995 to confirm Einstein's predictions.

The main difficulty for experimentally realizing a Bose-Einstein condensate lies in the instability inherent to the BEC phase. Indeed, at the temperature and pressure conditions required for a BEC to form, the true thermal equilibrium is the solid phase: particles undergo three-body recombination and form a crystal. The BEC is therefore a metastable state, which only occurs if particles are cooled down quickly by two-body collisions and that three-body recombinations are rare. These conditions are met for a very dilute, cold (typically  $< 1 \mu\text{K}$ ) atomic gas trapped in a magnetic or optical dipole trap. The first successes were obtained almost simultaneously in the laboratory of E. Cornell and C. Wieman at JILA, Boulder with  $^{87}\text{Rb}$  atoms [2], then W. Ketterle at MIT with  $^{23}\text{Na}$  [1] and R. Hulet at Rice University with  $^7\text{Li}$  [3]. Nowadays, BECs are routinely produced in many laboratories around the world and exploited to address a broad range of questions of fundamental physics and potential technological applications.

## 2.2 Bose-Einstein condensation of an ideal gas

The textbook case of an ideal gas of non-interacting bosons is somewhat fictitious, as realistic Bose gases usually exhibit interactions between particles. It is nevertheless a good starting point, as it constitutes a simple model that provides knowledge about important basic properties of Bose-Einstein condensation, which can then be extended to the interacting case.

### 2.2.1 BEC in a box potential

The first system considered is an ideal homogeneous gas of non-interacting particles. The particle number  $N$  is fixed, the particles are trapped in a box potential of volume  $V$  and the system is at equilibrium with a temperature  $T$ . It is assumed that the system reaches an equilibrium temperature despite the absence of interactions. From the thermodynamic partition function for a canonical ensemble:

$$Z = \sum_s e^{\beta E_s}, \quad (2.1)$$

where  $\beta = 1/k_{\text{B}}T$  is the inverse temperature parameter and  $s$  stands for the macroscopic states of the gas, one can find the average occupation number of the states. This leads to the famous Bose-Einstein distribution function [43]:

$$N = \sum_i N_i = \sum_i \frac{1}{e^{\beta(\varepsilon_i - \mu)} - 1} \quad (2.2)$$

where  $N_i$  are the average occupation numbers of the single-particle states,  $\varepsilon_i$  their eigen-energies and  $\mu$  is the chemical potential. To avoid occupation numbers of the states to be

negative, the important constraint on the chemical potential is fixed that  $\mu < \varepsilon_0$ , where  $\varepsilon_0$  is the lowest energy eigenvalue of the single-particle states.

The system is constrained by the fixed atom number. If  $T$  decreases,  $\mu$  must increase to keep  $N$  constant. When  $\mu$  approaches  $\varepsilon_0$ , the occupation number of the lowest state  $N_0 = (e^{\beta(\varepsilon_0 - \mu)} - 1)^{-1}$  increases dramatically. The other states, on the contrary, reach a limit of their occupation numbers  $N_i \approx (e^{\beta(\varepsilon_i - \varepsilon_0)} - 1)^{-1}$  and cannot verify the constraint of constant  $N$  on their own. The consequence is that the occupation numbers of the excited states decline while the ground state occupation becomes macroscopic. This phenomenon is called Bose-Einstein condensation.

In the continuum limit ( $N \rightarrow \infty$ ,  $N/V$  constant), the summation can be replaced by an integral and be expressed as a function of the density of states:

$$N = N_0 + \sum_{i>0} N_i = \frac{1}{e^{\beta(\varepsilon_0 - \mu)} - 1} + \int_0^\infty d\varepsilon \mathcal{D}(\varepsilon) n(\varepsilon) \quad (2.3)$$

where  $\mathcal{D}(\varepsilon)$  is the density of energy states, which depends on the geometry of the system. In the example of the homogeneous case in three dimensions, the density in  $k$ -space for positive values of  $k$  is  $\mathcal{D}(k)dk \sim \frac{1}{8}(4\pi k^2 dk) \frac{1}{(\pi/L)^3}$ , ( $4\pi k^2 dk$ ) being the volume between spherical shells of radius  $k$  and  $k + dk$ , and  $\pi/L$  the grid spacing between states. With the energy expressed as  $\varepsilon = \frac{\hbar^2 \pi^2 k^2}{2mL^2}$ , the conversion to energy space gives  $\mathcal{D}(\varepsilon) = 2\pi \left(\frac{L}{2\pi}\right)^3 \left(\frac{2m}{\hbar^2}\right)^{3/2} \sqrt{\varepsilon}$ . Generally, for a box potential of dimension  $d$ , the density of states is given by

$$\mathcal{D}(\varepsilon) = \Omega_d \frac{V}{(2\pi)^d} \frac{1}{2} \left(\frac{2m}{\hbar^2}\right)^{d/2} \varepsilon^{d/2-1} \quad (2.4)$$

where

$$\Omega_d = \begin{cases} 4\pi & \text{for } d = 3, \\ 2\pi & \text{for } d = 2 \text{ and} \\ 1 & \text{for } d = 1. \end{cases} \quad (2.5)$$

We can already note that the density of states in the excited states vanishes as  $\varepsilon \rightarrow 0$  in the 3d case only. In the other cases,  $\mathcal{D}(\varepsilon)$  either stays constant (2d case) or diverges (1d case). Consequently, condensation in the continuum limit only happens in 3d. The number of atoms in the excited states becomes:

$$N_{\text{ex}} = \int d\varepsilon \mathcal{D}(\varepsilon) n(\varepsilon) = \Omega_d \frac{V}{(2\pi)^d} \frac{1}{2} \left(\frac{2m}{\hbar^2}\right)^{d/2} \int_0^\infty d\varepsilon \frac{\varepsilon^{d/2-1}}{e^{\beta(\varepsilon_i - \mu)} - 1}. \quad (2.6)$$

The onset of condensation, characterized by a critical temperature or density, is defined as the limit for which, given the maximum value of the chemical potential  $\mu = \varepsilon_0 = 0$ , the number of atoms in the excited states is (still) equal to the total number of atoms. In the homogeneous 3d case, this can be expressed as [44]:

$$N = N_{\text{ex}} = \frac{V}{4\pi^2} \left(\frac{2m}{\hbar^2}\right)^{3/2} \int_0^\infty d\varepsilon \frac{\sqrt{\varepsilon}}{e^{\beta(\varepsilon_i - \mu)} - 1}. \quad (2.7)$$

The integral can be evaluated analytically using the relation  $\frac{1}{e^x-1} = \sum_{n=1}^{\infty} e^{-nx}$ , yielding

$$\begin{aligned} N_{\text{ex}} &= \frac{V}{4\pi^2} \left(\frac{2m}{\hbar^2}\right)^{3/2} \beta^{-3/2} \sum_{n=1}^{\infty} n^{-3/2} \int_0^{\infty} e^{-y} \sqrt{y} dy \\ &= \frac{V}{4\pi^2} \left(\frac{2m}{\hbar^2}\right)^{3/2} \beta^{-3/2} \zeta\left(\frac{3}{2}\right) \Gamma\left(\frac{3}{2}\right) \\ &= \frac{V}{\lambda_{\text{dB}}^3} \zeta\left(\frac{3}{2}\right) \end{aligned} \quad (2.8)$$

where  $\zeta(n) = \sum_{n=1}^{\infty} \frac{1}{n^s}$  is the Riemann zeta function and  $\Gamma(y) = \int_0^{\infty} t^{y-1} e^{-t} dt$  is the usual gamma function for real numbers. The factor  $\lambda_{\text{dB}} = \sqrt{\frac{2\pi\hbar^2}{mk_{\text{B}}T}}$  is the thermal de Broglie wavelength. Finally, the critical temperature for the onset of condensation in a homogeneous 3d gas of non-interacting particles is found to be:

$$k_{\text{B}}T_c = \frac{2\pi\hbar^2}{m(\lambda_{\text{dB}}^c)^2} = \frac{2\pi\hbar^2}{m} \left(\frac{N}{2.612 V}\right)^{2/3} \approx 3.3125 \frac{\hbar^2 N^{2/3}}{m} \quad (2.9)$$

where  $\lambda_{\text{dB}}^c$  is the thermal de Broglie wavelength at the onset of condensation. The critical density of the gas is:

$$n_c \equiv \frac{N_c}{V} \approx 2.612 \lambda_{\text{dB}}^{-3}. \quad (2.10)$$

Below the critical temperature, we can deduce from equation (1.6) and (1.7) that the condensate fraction is given by:

$$N_0 = N - N_{\text{ex}}(T) = N \left[1 - \left(\frac{T}{T_c}\right)^{3/2}\right]. \quad (2.11)$$

### 2.2.2 BEC in a harmonic potential

The previous description of Bose-Einstein of the ideal gas in a 3d case is a simple model that captures the essential properties of a BEC. In an experimental situation though, the trapping potential is not usually a box, but a harmonic trap. In that case, the density of states in the thermodynamics limit ( $\omega = \prod_{l=1}^d \omega_l^{1/d} \rightarrow 0$ ,  $N \rightarrow 0$ ) becomes [45]:

$$\mathcal{D}(\varepsilon) = \frac{\varepsilon^{d-1}}{(d-1)! \prod_{l=1}^d \hbar\omega_l} \quad (2.12)$$

where  $\omega_l$  are the frequencies of the trap in the different directions. In the 3d case, the critical temperature is given by:

$$k_{\text{B}}T_c = \hbar\omega \left(\frac{N}{\zeta(3)}\right)^{1/3} \quad (2.13)$$

with  $\zeta(3) \approx 1.212$ . The condensate fraction is simply

$$N_0 = N \left[ 1 - \left( \frac{T}{T_c} \right)^3 \right]. \quad (2.14)$$

Here again, the density of states depends on the dimensionality. While condensation is possible in 3d and 2d, the integral of the density of states diverges in the 1d case, indicating the absence of condensation. For the 1d quasi-condensate produced in the course of this thesis, this contradiction is removed if we consider that the system has a finite extent and a finite atom number.

### 2.2.3 BEC with finite particle number

Referring to a transition to the BEC state and a critical temperature is only strictly allowed in the continuum limit. However, as shown in [46], the behavior of the condensate for finite and even low atom number ( $\sim 100$ ) in a general harmonic potential is similar to the case of the continuum. One can show that the total number of particles can be expressed as

$$N = \sum_{i=0}^{\infty} \frac{ze^{-\beta\varepsilon_i}}{1 - ze^{-\beta\varepsilon_i}} = \sum_{i=0}^{\infty} \sum_{j=1}^{\infty} z^j \exp(-j\beta\varepsilon_i) = \sum_{j=1}^{\infty} \frac{z^j}{\prod_{l=1}^3 (1 - x_l^j)} \quad (2.15)$$

where  $z = \beta\mu$  is the *fugacity* and  $x_l = \exp(-\beta\hbar\omega_l)$ . This expression is valid for an anisotropic trap. In particular, for a very elongated trap in the  $l = 3$  direction,  $k_B T \ll \hbar\omega_l$  for  $l = 1, 2$  and

$$N \approx \sum_{j=1}^{\infty} \frac{z^j}{(1 - x_3^j)} = \frac{z}{1 - z} + \sum_{j=1}^{\infty} \frac{z^j x_3^j}{1 - x_3^j}. \quad (2.16)$$

The second term vanishes for low temperature and a “condensation” phenomenon qualitatively similar to the 3d case in the continuum limit appears. The critical temperature, which depends on the trapping potential, is shifted downwards as:

$$\begin{aligned} T_c^{1d} &\approx T_c \left( 1 - \frac{\zeta(2)}{2\zeta(3)^{2/3}} \frac{\sum_{l=1}^3 \omega_l/3}{\prod_{l=1}^3 \omega_l^{1/3}} N^{-1/3} \right) \\ &\approx T_c \left( 1 - 0.73 \frac{\bar{\omega}}{\omega} N^{-1/3} \right) \end{aligned} \quad (2.17)$$

where  $\bar{\omega} = \sum_{l=1}^3 \omega_l/3$  can be very different from  $\omega$  in strongly anisotropic traps.

A peculiarity of condensation in 1d is that it takes place in two steps [47]. First, as temperature is reduced, atoms condense in the ground state of the transverse potential, where the confinement is strong. At this stage, many states are still populated along the longitudinal, weakly confining axis, and the result is a sort of “multimode condensate”. Second, as temperature is brought further down, the overall ground state gets macroscopically populated, leading to a “single-mode condensate”. This is relevant in the frame of

this thesis, because it ensures that a mean-field description in the transverse direction, where the dynamics occurs, is a valid approach even for temperatures higher than the critical temperature for condensation in the overall ground state.

The trapping potential is not the only element having an impact on condensation. Interactions between particles, neglected up to now, actually shift  $T_c$  by a few percent [48]. They also modify the shape of the condensate and its dynamics, as we will see in the coming section.

## 2.3 Weakly interacting Bose gas

The theoretical framework for the study of interacting Bose-Einstein condensates was developed in the 1950's by E. P. Gross [49], L. P. Pitaevskii [50], N. N. Bogoliubov [42] and S. T. Beliaev [51]. The system of interest at the time was the strongly-interacting superfluid helium, but these theories proved to work well for Bose gases with weak interactions<sup>1</sup>.

### 2.3.1 Interaction potential

The basic case of an ideal Bose gas gives good notions on how condensation works and typical values for important parameters, such as the critical temperature  $T_c$  or the critical density  $n_c$ . Some of them are affected by interactions (e.g. the condensation threshold or the shape of the BEC), and additional properties emerge (e.g. collective excitations, the quasiparticle spectrum). This is true in 3d, but becomes even more interesting in 1d, where interactions give access to exotic regimes of quantum degeneracy, as introduced in sec. 2.5.

For a classical gas of identical atoms, in the same internal state and with two-body interactions, which is trapped in an external potential  $V(\mathbf{r})$ , the Hamiltonian can be written as:

$$H = \sum_i \left( \frac{p_i^2}{2m} + V(\mathbf{r}_i) \right) + \frac{1}{2} \sum_{i \neq j} U(\mathbf{r}_i - \mathbf{r}_j). \quad (2.18)$$

Here  $p_i = |\mathbf{p}_i|$  is the momentum of an atom  $i$ ,  $p_i^2/2m$  its kinetic energy,  $V(\mathbf{r}_i)$  its potential energy at position  $\mathbf{r}_i$  in the presence of an external field, and  $U(\mathbf{r}_i - \mathbf{r}_j)$  the short-range potential due to mutual interactions between two atoms  $i$  and  $j$ . The ideal gas corresponds to the limit where the interaction energy is much smaller than the kinetic energy, such that interactions can be neglected. As demonstrated in [53], the interaction energy can be approximated to first order by:

$$U(r_{ij}) \approx \frac{4\pi a_s \hbar^2}{m} \delta(\mathbf{r}_i - \mathbf{r}_j), \quad (2.19)$$

$a_s$  being the  $s$ -wave scattering length, which determines the collisional cross-section of the atoms (in the limit  $k \rightarrow 0$ ). It allows to describe all scattering events by a single

---

1. For a short historical overview of the main contributors to the theory of BECs, see [52].

quantity, independently of the details of the actual interaction potential. This result holds for  $a_s$  much smaller than the average distance between particles:

$$n|a_s|^3 \ll 1, \quad (2.20)$$

that is, for a dilute gas. If this condition is fulfilled, one enters the *weakly interacting* regime.

### 2.3.2 Many-body Hamiltonian

In the second quantization formalism — a representation in terms of occupation number, well-suited for high atom numbers (few hundreds in the present experiments) —, the many-body Hamiltonian of an interacting Bose gas can generally be written as:

$$\begin{aligned} \hat{H} = & \int d\mathbf{r} \hat{\Psi}^\dagger(\mathbf{r}, t) \left( -\frac{\hbar^2 \nabla^2}{2m} + V(\mathbf{r}, t) \right) \hat{\Psi}(\mathbf{r}, t) \\ & + \frac{1}{2} \iint d\mathbf{r} d\mathbf{r}' \hat{\Psi}^\dagger(\mathbf{r}, t) \hat{\Psi}^\dagger(\mathbf{r}', t) U(\mathbf{r} - \mathbf{r}') \hat{\Psi}(\mathbf{r}, t) \hat{\Psi}(\mathbf{r}', t). \end{aligned} \quad (2.21)$$

where  $\hat{\Psi}(\mathbf{r}, t)$  (respectively  $\hat{\Psi}^\dagger(\mathbf{r}, t)$ ) is the field operator that annihilates (respectively creates) a particle at position  $\mathbf{r}$  and time  $t$ . These operators can be decomposed in the basis of the position operator:

$$\begin{aligned} \hat{\Psi}(\mathbf{r}) &= \sum_i \langle r|i \rangle \hat{a}_i = \sum_i \varphi_i(r) \hat{a}_i \\ \hat{\Psi}^\dagger(\mathbf{r}) &= \sum_i \langle i|r \rangle \hat{a}_i = \sum_i \varphi_i^*(r) \hat{a}_i^\dagger \end{aligned} \quad (2.22)$$

where  $|r\rangle$  is an eigenvector of the position operator and the  $\hat{a}_i$ 's (respectively  $\hat{a}_i^\dagger$ ) are the annihilation (respectively creation) operators for a particle in the single-particle state  $\varphi_i(r)$ . The latter obey the bosonic commutation relations:

$$[\hat{a}_i, \hat{a}_j^\dagger] = \delta_{ij}, \quad [\hat{a}_i, \hat{a}_j] = [\hat{a}_i^\dagger, \hat{a}_j^\dagger] = 0. \quad (2.23)$$

The wavefunctions  $\varphi_i(r)$  are  $c$ -numbers that verify the orthonormality condition  $\int \varphi_i^*(r) \varphi_j(r) = \delta_{ij}$ , leading for the field operator to the bosonic commutation relation:

$$[\hat{\Psi}(\mathbf{r}), \hat{\Psi}^\dagger(\mathbf{r}')] = \sum_i \varphi_i(r) \varphi_i^*(r') = \delta(r - r'). \quad (2.24)$$

The first term of eq. (2.21) represents the single-particle Hamiltonian, while the second term expresses binary atomic interactions. In the weakly interacting regime, as previously explained,  $U(\mathbf{r} - \mathbf{r}')$  can be replaced in this equation by a “pseudo-potential”  $g\delta(\mathbf{r} - \mathbf{r}')$ , where  $g = 4\pi a_s \hbar^2/m$ .

It follows from eq. (2.21) and eq. (2.24) that the time evolution for the field operator  $\hat{\Psi}$  can be obtained from the Heisenberg equation:

$$\begin{aligned} i\hbar \frac{\partial}{\partial t} \hat{\Psi}(\mathbf{r}, t) &= [\hat{\Psi}(\mathbf{r}, t), \hat{H}] \\ &= \left( -\frac{\hbar^2}{2m} \nabla^2 + V(\mathbf{r}, t) \right) \hat{\Psi}(\mathbf{r}, t) + g \hat{\Psi}^\dagger(\mathbf{r}, t) \hat{\Psi}(\mathbf{r}, t) \hat{\Psi}(\mathbf{r}, t). \end{aligned} \quad (2.25)$$

This equation can in principle be used to compute the dynamics of the many-body system. However, to do so in practice is computationally heavy and often unreasonably time-consuming with current computing powers. One often resorts to some approximation.

### 2.3.3 Mean-field approximation: Gross-Pitaevskii equation

In the regime of an (almost) pure condensate, in the limit  $T \ll T_c$ , the system consists mainly of a single wavefunction. This condensate wavefunction is well described by a single equation, called the Gross-Pitaevskii equation (GPE) [49, 50]. In this approximation, the corrections brought on by the small non-condensed part are neglected. We will come back to this notion in sec. 2.4. The case considered in this section is one where number of atoms  $N$  is large and the field operator  $\hat{\Psi}$  can be replaced by a complex wavefunction  $\psi$ :

$$\hat{\Psi}(\mathbf{r}, t) \rightarrow \sqrt{N} \psi(\mathbf{r}, t). \quad (2.26)$$

#### Time-independent GPE

The GPE can be derived in different ways. One of them consists in starting from the general Hamiltonian and using a variational formulation. We follow this strategy here.

In the time-independent case, the atoms are considered to be all in the lowest energy level, the ground state. The minimum of the energy functional  $E[\psi] = \frac{\langle \psi | H | \psi \rangle}{\langle \psi | \psi \rangle}$  corresponds to the ground state. As a small variation  $\psi \rightarrow \psi + \delta\psi$  may change the normalization of  $|\psi\rangle$ , a Lagrange multiplier is introduced and the functional to minimize becomes  $E'[\psi] = \langle \psi | H | \psi \rangle - \lambda_E \langle \psi | \psi \rangle$ . Under the normalization constraint  $\int |\psi|^2 dr = 1$ , we find the following expression for the energy functional to minimize:

$$\begin{aligned} E'[\psi, \psi^*] &= N \int dr \left( -\frac{\hbar^2}{2m} \psi^*(r) \nabla^2 \psi(r) + \psi^*(r) V(r) \psi(r) \right) \\ &\quad + \frac{N(N-1)}{2} \int dr \int dr' \psi^*(r) \psi^*(r') U(r-r') \psi(r') \psi(r) \\ &\quad - \lambda_E \left( \int dr \psi^*(r) \psi(r) \right)^N. \end{aligned} \quad (2.27)$$

The functional derivative  $\frac{\delta}{\delta \psi^*}$  yields the variation:

$$\begin{aligned} \frac{\delta E'[\psi, \psi^*]}{\delta \psi^*} &= N \left\{ -\frac{\hbar^2}{2m} \Delta \psi(r) + V(r) \psi(r) + (N-1) \left( \int dr' |\psi(r')|^2 U(r-r') \right) \psi(r) - \lambda_E \psi(r) \right\} \\ &= 0. \end{aligned} \quad (2.28)$$

The part in brackets must vanish and, replacing the general interaction potential by the simplified form of eq. (2.19), estimating that  $N - 1 \approx N$  and replacing  $\lambda_E$  by the chemical potential  $\mu$ , we obtain the well-known Gross-Pitaevskii equation:

$$-\frac{\hbar^2}{2m}\Delta\psi(r) + V(r)\psi(r) + Ng|\psi(r)|^2\psi(r) = \mu\psi(r). \quad (2.29)$$

It can easily be checked that indeed  $\lambda_E = \mu$  by deriving  $\mu = \partial E/\partial N$  [54]. This equation is similar to the time-independent Schrödinger equation  $H\psi = E\psi$  with an additional non-linear term, and the chemical potential instead of the energy per particle  $E/N$ .

### Time-dependent GPE

The time-dependent GPE can also be obtained by variational methods, this time from minimizing the action on a time interval  $[t_1, t_2]$ , following the least action principle. The action  $\mathcal{A}$  can be written in a general form as:

$$\mathcal{A}[\Psi] = \int_{t_1}^{t_2} dt \int dr \mathcal{L}(\Psi, \Psi^*, \dot{\Psi}, \dot{\Psi}^*, \nabla\Psi, \nabla\Psi^*), \quad (2.30)$$

where  $\mathcal{L}$  is the Lagrangian verifying the Lagrange equation for  $N$  particles:

$$\frac{\partial\mathcal{L}}{\partial\Psi^*} - \frac{\partial}{\partial t} \frac{\partial\mathcal{L}}{\partial\dot{\Psi}^*} - \sum_{i=1}^N \nabla_{r_i} \cdot \left( \frac{\partial\mathcal{L}}{\partial\nabla_{r_i}\Psi^*} \right) = 0. \quad (2.31)$$

A valid choice of Lagrangian for the problem is [45]:

$$\mathcal{L} = i\frac{\hbar}{2}[\Psi^*\dot{\Psi} - \dot{\Psi}^*\Psi] - \frac{\hbar^2}{2m} \sum_{i=1}^N \nabla_{r_i}\Psi^* \nabla_{r_i}\Psi - \sum_{i=1}^N \Psi^*V(r_i, t)\Psi - \frac{1}{2} \sum_{\substack{(i,j)=1 \\ i \neq j}}^N \Psi^*U(r_i - r_j)\Psi. \quad (2.32)$$

Assuming again that the system stays in its ground state, this gives for the total action:

$$\begin{aligned} \mathcal{A}[\psi] = N \int_{t_1}^{t_2} dt \int dr \left\{ i\frac{\hbar}{2} \left[ \psi^* \frac{\partial\psi}{\partial t} - \frac{\partial\psi^*}{\partial t} \psi \right] - \frac{\hbar^2}{2m} \nabla\psi(r, t)^* \nabla\psi(r, t) \right. \\ \left. - V(r, t)|\psi(r, t)|^2 - \frac{1}{2}(N-1)g|\psi(r, t)|^4 \right\} \end{aligned} \quad (2.33)$$

and yields the time-dependent GPE:

$$i\hbar \frac{\partial\psi}{\partial t} = -\frac{\hbar^2}{2m} \Delta\psi(r, t) + V(r, t)\psi(r, t) + gN|\psi(r, t)|^2\psi(r, t). \quad (2.34)$$

This equation is again very close to a Schrödinger equation. It will be used in the rest of this work to compute the dynamics of the system driven out of equilibrium. We note from eq. (2.29) and eq. (2.34) that stationary solutions of  $\psi$  must evolve in time as  $\exp(-i\mu t/\hbar)$ .

### Thomas-Fermi limit

For a high number of atoms, the interaction energy increases to the point where the kinetic energy term becomes negligible. This situation is usual in condensed atom experiments. It also corresponds to the chemical potential being higher than the level spacing of the trapping potential  $\hbar\omega_l$  in the direction  $l$  considered. This situation is called the *Thomas-Fermi (TF) limit* and is one of the few analytic solutions to the time-independent GPE (another is the non-interacting case, which we will explicit in section 2.5. In this limit, the GPE simplifies to:

$$V(r)\psi(r) + Ng|\psi(r)|^2\psi(r) = \mu\psi(r), \quad (2.35)$$

which gives for the condensate density:

$$n(r) = |\psi(r)|^2 = \begin{cases} [\mu - V(r)]/g & \text{if } \mu > V(r), \text{ and} \\ 0 & \text{otherwise.} \end{cases} \quad (2.36)$$

This corresponds to an inverted parabola whose boundary is given by the condition  $V(r) = \frac{1}{2}m[\omega_x^2x^2 + \omega_y^2y^2 + \omega_z^2z^2] = \mu$  in 3 dimensions. For a harmonic potential, the density profile in each direction is parabolic:

$$n(r) = n_0 \left( 1 - \frac{x^2}{R_{TF,x}^2} - \frac{y^2}{R_{TF,y}^2} - \frac{z^2}{R_{TF,z}^2} \right). \quad (2.37)$$

The radius of the cloud in each direction  $l$  is then found to be:

$$R_{TF,l} = \sqrt{\frac{2\mu}{m\omega_l^2}}. \quad (2.38)$$

The normalization condition on the wavefunction yields the relation  $N = \frac{8\pi}{15} \frac{\mu}{g} \sqrt{\frac{2\mu}{m\omega^2}}$ , with  $\omega = \prod_{l=1}^d \omega_l^{1/d}$  the geometric mean of the potential frequencies in all directions. In turn, we get the chemical potential:

$$\mu = \frac{1}{2} \hbar\omega \left( 15N \frac{a_s}{l_{ho}} \right)^{2/5} \quad (2.39)$$

where  $l_{ho} = \prod_{l=1}^d l_l^{1/d}$  with  $l_{ho,l} = \sqrt{\hbar/(m\omega_l)}$  the harmonic oscillator length in each direction.

This description is relevant for the experimental system in this thesis, which is an elongated quasi-condensate. The TF approximation gives a good description of the system in its longitudinal direction. This will be further used in sec. 2.5.

## 2.4 Quasi-particle spectrum: Bogoliubov approximation

For a partially condensed system, due to the presence of interactions but also finite temperatures in every experiment, it is relevant for many studies to consider the effects of the non-condensed part of the field operator  $\hat{\Psi}(\mathbf{r}, t)$ .

To describe a partly condensed system, we can separate the field operator  $\hat{\Psi}$  into two parts: the condensate part or ground state (corresponding to  $i = 0$ ) and the non-condensed part or excited states ( $i > 0$ ). This gives the expression for the field operator:

$$\hat{\Psi}(\mathbf{r}) = \varphi_0(r)\hat{a}_0 + \sum_{i>0} \varphi_i(r)\hat{a}_i. \quad (2.40)$$

For the macroscopically populated ground state, we can write the operators  $\hat{a}_0$  and  $\hat{a}_0^\dagger$  as a  $c$ -number  $a_0 = \sqrt{N_0}$ , where  $N_0 = \langle \hat{a}_0^\dagger \hat{a}_0 \rangle$  is the average occupation number of the ground state. The field operator is then replaced by a classical complex field  $\psi_0 = \sqrt{N_0}\varphi_0$ . Writing  $\delta\hat{\psi} = \sum_{i>0} \varphi_i(r)\hat{a}_i$ , we retrieve the Bogoliubov approximation [42]:

$$\hat{\Psi}(\mathbf{r}) = \psi_0 + \delta\hat{\psi} \quad (2.41)$$

where  $\delta\hat{\psi}$  is assumed to be small<sup>2</sup>. This ansatz is used to describe elementary excitations on top of the condensate wavefunction. It can be applied to the computation of the ground state energy when modified by weak interactions, or to the depletion of the condensate wavefunction as in [56].

In the simple case of a uniform condensate in a volume  $V = L^3$ , in the basis of the eigenstates for the non-interacting system, the wavefunction can be expanded onto a plane waves basis:

$$\hat{\Psi}(r) = \frac{1}{\sqrt{L^3}} \sum_k \hat{a}_k e^{ik \cdot r/\hbar} \quad (2.42)$$

which, when plugged into the corresponding many-body Hamiltonian, gives:

$$\hat{H} = \sum_k \varepsilon_k \hat{a}_k^\dagger \hat{a}_k + \frac{g}{2L^3} \sum_{k_1, k_2, q} \hat{a}_{k_1+q}^\dagger \hat{a}_{k_2-q}^\dagger \hat{a}_{k_1} \hat{a}_{k_2} \quad (2.43)$$

with  $\varepsilon_k = \hbar^2 k^2 / 2m$  the energies of the non-interacting states. The operators in the first term can be replaced again by a  $c$ -number corresponding to the occupation number of the ground state,  $N_0$ . The indices of the sum in the second term are chosen such that momentum conservation between annihilated and created particles is enforced. Separating the operators  $\hat{a}_0$  and  $\hat{a}_k$  in the interaction term and ignoring higher order terms, the Hamiltonian can be expanded as:

$$\begin{aligned} \hat{H} &= \sum_{k \neq 0} \varepsilon_k \hat{a}_k^\dagger \hat{a}_k + \frac{g}{2L^3} N_0^2 \\ &+ \frac{g}{2L^3} N_0 \sum_{k \neq 0} (2\hat{a}_k^\dagger \hat{a}_k + \hat{a}_k^\dagger \hat{a}_{-k}^\dagger + \hat{a}_k \hat{a}_{-k}) \end{aligned} \quad (2.44)$$

---

2. These considerations have been extended to the 1d geometry by Mora and Castin [55].

Finally, eq. (2.44) can be linearized using the Bogoliubov transformations:

$$\begin{aligned}\hat{a}_k &= u_k \hat{b}_k + v_{-k} \hat{b}_{-k}^\dagger, \\ \hat{a}_k^\dagger &= u_k \hat{b}_k^\dagger + v_{-k} \hat{b}_{-k}.\end{aligned}\tag{2.45}$$

The quasi-particle operators are assumed to follow the bosonic commutation relations, which imposes the normalization  $u_k^2 - v_{-k}^2 = 1$ . Under these constraints, inserting eq. (2.45) in eq. (2.44), we obtain the expressions for the coefficients:

$$\begin{aligned}u_k &= \left( \frac{\varepsilon_k + gn_0}{2\hbar\omega_k} + \frac{1}{2} \right)^{1/2} \\ v_{-k} &= v_k = \left( \frac{\varepsilon_k + gn_0}{2\hbar\omega_k} - \frac{1}{2} \right)^{1/2}\end{aligned}\tag{2.46}$$

where  $n_0 = N_0/L^3$  is the ground state density and  $\hbar\omega_k$  is the energy corresponding to the elementary excitation in mode  $k$  or dispersion relation of the Bogoliubov spectrum:

$$\hbar\omega_k = \left( \frac{\hbar^2 k^2}{2m} \left( \frac{\hbar^2 k^2}{2m} + 2gn_0 \right) \right)^{1/2}.\tag{2.47}$$

The linearized Hamiltonian for the elementary excitations then becomes:

$$\hat{H}_k = \sum_{k \neq 0} \hbar\omega_k \hat{b}_k^\dagger \hat{b}_k.\tag{2.48}$$

The equations reveal the different properties of the low and high momentum excitations. In the Bogoliubov representation, a particle  $\hat{a}_k$  from the second quantization description is described as a superposition of forward propagating excitations  $u_k \hat{b}_k$  and backward propagating excitations  $v_{-k} \hat{b}_{-k}^\dagger$ . When the momentum is small,  $\hbar^2 k^2 \ll \sqrt{mgn_0}$ , we obtain  $\hat{a}_k \sim u_k (\hat{b}_k - \hat{b}_{-k}^\dagger)$ , which is the expression of a wave. Moreover, the dispersion relation of eq. (2.47) has a linear form:

$$\hbar\omega_k \sim \hbar kc\tag{2.49}$$

where  $c = \sqrt{gn_0/m}$  is the sound velocity in the condensate. Both observations indicate that the low momentum — or long wavelength — excitations are similar to sound waves. They are “phononic” excitations, or “phonons”.

When the momentum is large though,  $\hbar^2 k^2 \gg \sqrt{mgn_0}$ ,  $\hat{a}_k \sim \hat{b}_k$  and the excitation  $\hat{b}_k$  is indistinguishable from the second quantization particle. The dispersion relation is also quadratic, signature of a free-particle behavior. The transition between these two regimes happens around  $\hbar k_h = \sqrt{2mgn_0}$ , which corresponds to a momentum on the inverse healing length  $\hbar\xi^{-1} = \sqrt{mgn_0}$ .<sup>3</sup> This behavior is illustrated in fig. 2.1.

3. The healing length is defined as the scale of variation on which the kinetic energy is equal to the interaction energy:  $\frac{\hbar^2}{2m\xi^2} = nU_0$ .

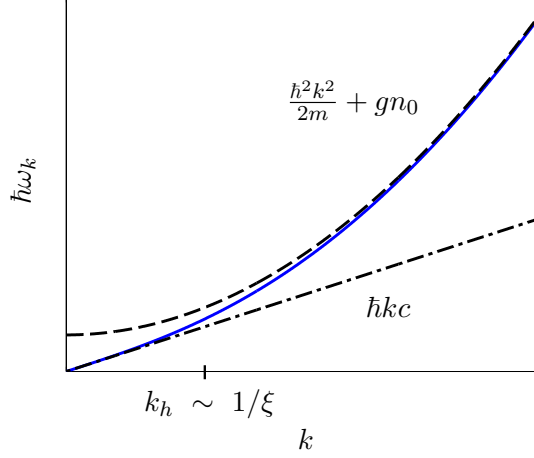


**Figure 2.1: Bogoliubov spectrum of elementary excitations.** The transition between the phonon regime ( $\hbar\omega_k = \hbar kc$ ) and the free-particle regime ( $\hbar\omega_k = \frac{\hbar^2 k^2}{2m} + gn_0$ ) occurs around  $k_h \sim 1/\xi$ .

To relate these results to observed quantities, we consider the field in a “density and phase” representation. For this, we assume there exist two Hermitian operators,  $\hat{n}(r)$  representing the density and  $\hat{\theta}(r)$  the phase, such that

$$\hat{\Psi}(r) = \sqrt{\hat{n}(r)} e^{i\hat{\theta}(r)} \quad (2.50)$$

In the limit of small excitations, this equation becomes:

$$\hat{\Psi}(r) = \sqrt{n_0 + \delta\hat{n}(r)} e^{i\hat{\theta}(r)} \approx \sqrt{n_0} + \frac{\delta\hat{n}(r)}{2n_0} + i\sqrt{n_0}\hat{\theta}. \quad (2.51)$$

Using eq. (2.41) and eq. (2.42), we get the following expression for the density and phase fluctuations for each mode  $k$ :

$$\begin{aligned} \delta\hat{n}_k &\equiv 2n_0 \cdot \text{Re}\{\hat{\Psi}_k\} = \sqrt{\frac{n_0}{L^3}} \left[ (u_k \hat{b}_k + v_{-k} \hat{b}_{-k}^\dagger) e^{ikr} + (u_k \hat{b}_k^\dagger + v_{-k} \hat{b}_{-k}) e^{-ikr} \right] \\ \hat{\theta}_k &= \frac{1}{i\sqrt{n_0}} \text{Im}\{\hat{\Psi}_k\} = \frac{1}{2i\sqrt{n_0}L^3} \left[ (u_k \hat{b}_k + v_{-k} \hat{b}_{-k}^\dagger) e^{ikr} - (u_k \hat{b}_k^\dagger + v_{-k} \hat{b}_{-k}) e^{-ikr} \right]. \end{aligned} \quad (2.52)$$

Assuming the modes have a large enough occupation number that they can be treated classically, we can replace the operators by a complex amplitude  $\beta_k = |\beta_k| e^{i\varphi_k}$  defined by the relation  $\langle \hat{b}_k^\dagger \hat{b}_k \rangle = |\beta_k|^2$ . It then appears clearly that the elementary excitations in density and phase can be represented as waves:

$$\begin{aligned} \frac{\delta\hat{n}_k(r)}{n_0} &= \frac{2}{\sqrt{N_0}} (u_k + v_k) |\beta_k| \cos(kr + \varphi_k) \\ \hat{\theta}_k(r) &= \frac{1}{\sqrt{N_0}} (u_k - v_k) |\beta_k| \sin(kr + \varphi_k) \end{aligned} \quad (2.53)$$

with an amplitude given by:

$$\begin{aligned} \frac{|\delta n_k|}{n_0} &= \frac{2}{\sqrt{N_0}} |\beta_k| \left( \frac{\varepsilon_k}{\varepsilon_k + 2gn_0} \right)^{1/4} \\ |\theta_k| &= \frac{1}{\sqrt{N_0}} |\beta_k| \left( \frac{\varepsilon_k}{\varepsilon_k + 2gn_0} \right)^{-1/4}. \end{aligned} \quad (2.54)$$

These results will be used in sec. 6.3.2, when modeling the evolution of two coupled quasi-condensates.

## 2.5 One-dimensional interacting Bose gas

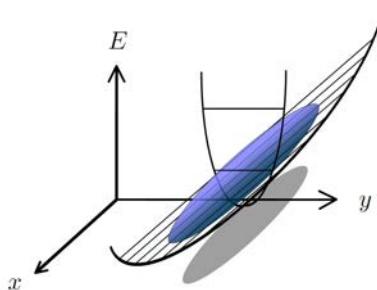


**Figure 2.2: Schematics of the elongated gas in a 1d trapping potential.** The trapping potential is strongly confining in the transverse  $y$  and  $z$  directions, and shallow in the  $x$  direction. The motion is “frozen” in the  $y$  and  $z$  directions.

A 1d condensate corresponds to a configuration where one dimension, referred to as the longitudinal direction, is much longer than the two others, or transverse directions. The conditions to reach this regime are that both thermal and interaction energy are small compared to the level spacing, i.e.  $\mu, k_B T \ll \hbar\omega_\perp$ . Under this condition, the strong confinement “freezes out” any transverse motion. In our experiment, with  $\omega_\perp \approx 2\pi \times 2$  kHz and  $\omega_\parallel \approx 2\pi \times 20$  Hz, the aspect ratio of our traps is typically  $\frac{\omega_\perp}{\omega_\parallel} \approx 200$ . For  $N = 700$ , the chemical potential approximated by eq. (2.39) is  $\mu \approx \hbar \cdot 2\pi \times 600$  Hz. Temperatures are estimated to be below  $T_{\max} \approx 50$  nK  $\approx \hbar/k_B \cdot 2\pi \times 1$  kHz, so the conditions to be in the 1d regime are met.

One should note that the oscillator length in the transverse direction is  $l_\perp = \sqrt{\hbar/(m\omega_\perp)} \approx 250$  nm, which is much larger than the 3d scattering length  $a_s \approx 5$  nm. Therefore the scattering remains a 3d phenomenon [57]. An effective interaction constant in 1d can be derived by integrating over the transverse wavefunctions  $\psi_y$  and  $\psi_z$ :

$$g_x = g \int dy |\psi_y|^4 \int dz |\psi_z|^4 = \frac{g}{2\pi l_\perp^2} \approx 2\hbar\omega_\perp a_s. \quad (2.55)$$

### 2.5.1 Regimes of interaction

For the interacting gas in a 1d geometry, different regimes of degeneracy appear. This only concerns systems with repulsive interactions, as attractive interactions lead to collapse, at least in a homogeneous trap<sup>4</sup>. The physics of 1d systems is interesting from a theoretical point of view because their energy eigenstates are often exactly solvable. They have been studied extensively since the 1960's [60–62], with the purpose to increase the fundamental understanding of quantum theory. Different regimes emerge in these studies, making the 1d configuration richer than the usual 3d model. The different regimes of interaction in 1d can be categorized looking at two dimensionless parameters,  $\gamma$  and  $\tau$ , which depend only on the linear density of the 1d gas  $n_{1d}$  and the temperature  $T$  [63].

The first parameter, called the Lieb-Liniger parameter, quantifies the ratio of interaction energy per particle  $g_{1d}n_{1d}$  to the kinetic energy  $E_K \approx \hbar^2 n_{1d}^2/m$  [64]:

$$\gamma = \frac{g_{1d}n_{1d}}{\hbar^2 n_{1d}^2/m} = \frac{mg_{1d}}{\hbar^2 n_{1d}}. \quad (2.56)$$

This first parameter already reveals some peculiarity of the 1d geometry compared to the 3d configuration, which is that the system becomes more interacting for lower densities. In the limit of  $\gamma \gg 1$ , one enters the strongly correlated Tonks-Girardeau regime. With strong interactions, a “fermionization” phenomenon occurs and bosons exhibit anti-bunching. This happens at low densities where the (repulsive) interaction energy overcomes the kinetic energy  $\hbar^2 n_{1d}^2/m$  and makes the overlap between atoms less favorable energetically. The opposite limit,  $\gamma \ll 1$ , corresponds to the weak interaction limit. The second parameter is the degeneracy parameter:

$$T_d = \frac{\hbar^2 n_{1d}^2}{2mk_B} \quad (2.57)$$

from which two dimensionless reduced temperatures are derived<sup>5</sup>:

$$\tau = \frac{T}{T_d} \quad \text{and} \quad t = \frac{2\hbar^2 k_B T}{mg_{1d}^2} = \frac{T}{\gamma^2 T_d} = \frac{\tau}{\gamma^2}. \quad (2.58)$$

In the limit  $\gamma \ll 1$ , several regimes can be distinguished based on the temperature. For  $\tau \gg 1$ , the system is in the classical, nearly-ideal Bose gas regime. It is for  $\tau \ll 1$  that quantum effects come into play. This domain can be divided into two sub-regions which depend on the interaction parameter  $\gamma$ . At temperatures  $\tau > \sqrt{\gamma}$ , both fluctuations in phase and density are important and one enters a decoherent quantum regime. This regime differs (strongly) from the classical decoherent regime in its first-order coherence properties. At lower temperatures,  $\tau < \sqrt{\gamma}$ , the gas becomes a *quasi-condensate*. This regime is characterized by reduced density fluctuations but strongly fluctuation phase.

4. This is not necessarily the case for a non-homogeneous trap or in excited clouds, as proven by the case of the super Tonks gas [58, 59]

5. These expressions are equivalent, but the second parameter is sometimes preferred to describe an inhomogeneous gas [65].

The nature of the fluctuations is thermal for an important range of parameters. Quantum fluctuations only start to dominate for  $k_B T \leq 0.1\mu$  [66]. A graphical representation of the different regimes of interactions in 1d is presented in fig 2.3. In the experiments realized during this thesis, typical values for the different parameters are  $\gamma \sim 10^{-2}$  and  $\tau \sim 5 \cdot 10^{-2}$ . We are therefore in the weakly interacting quasi-condensate regime.

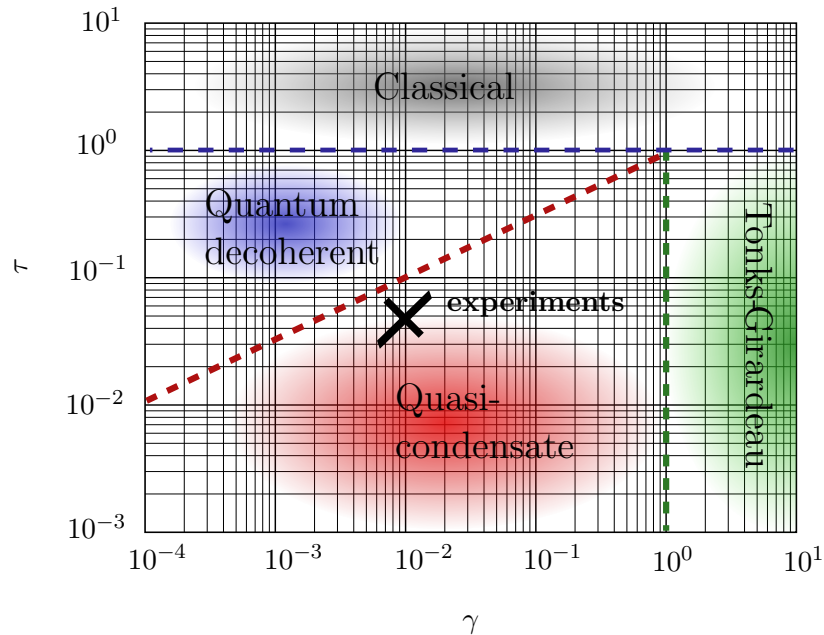


**Figure 2.3: Phase diagram of the homogeneous 1d Bose gas in the presence of interactions and at finite temperature.** Depending on the Lieb-Liniger parameters  $\gamma$  and  $\tau$ , different regimes can be identified. They are separated by smooth crossovers. The quasi-condensate regime, corresponding to  $\gamma \gg 1$  and  $\tau < \sqrt{\gamma}$ , encompasses the parameters of the present experiments.

Due to the phase fluctuations, a quasi-condensate lacks long-range phase coherence and is therefore not a condensate in the strict sense. However, it exhibits the same sort of local correlations as a true condensate and can be thought of as a succession of small condensates with different phases. The “size” of these condensates is determined by the thermal coherence length of the single 1d Bose gas:

$$\lambda_T^{(s)} = \frac{2\hbar^2 n_{1d}}{mk_B T}. \quad (2.59)$$

At equilibrium, this translates into an exponentially decaying the two-point correlation function:

$$C(x, x') = \frac{\langle \hat{\Psi}^\dagger(x) \hat{\Psi}(x') \rangle}{\sqrt{\langle \hat{\Psi}^\dagger(x) \hat{\Psi}(x) \rangle} \sqrt{\langle \hat{\Psi}^\dagger(x') \hat{\Psi}(x') \rangle}} = \exp\left(-\frac{|x - x'|}{\lambda_T^{(s)}}\right). \quad (2.60)$$

In principle, the phase fluctuations can be observed experimentally in different ways. One is to look at the system in expansion after it has been released from the trapping potential [67, 68]. During the expansion, the phase fluctuations transform into differences in density, similarly to speckle patterns in laser light. Another possibility is to make two quasi-condensate interfere, such as to gain access to the relative phase between them and the fluctuations of the relative phase [29]. This type of analysis is adapted in chap. 6 to the analysis of the experimental data presented in this thesis.

The different properties discussed above were in the simple case of a homogeneous Bose gas. However, most experiments are carried out with harmonic trapping potential, which is technically more straightforward to implement. Although the general considerations still hold in the trapped case, some parameters become dependent on the longitudinal position through the position-dependent density. If the density varies slowly compared to the observed quantities, one can apply a *local density approximation* (LDA) [69] to the problem, by considering that the gas is locally homogeneous and integrating over the length of the trapped system. The gas in thermal equilibrium is still described by a global temperature  $T$  and chemical potential  $\mu_0$ , but the local properties depend on a local density, e.g. the chemical potential  $\mu(n(x)) + V(x) = \mu_0$ . This affects the regime parameters  $\gamma$  and  $\tau$ , but the regimes of interactions remain very similar to the homogeneous case.

### 2.5.2 Description of the transverse direction(s)

At the heart of this thesis lies the study the dynamics taking place in the horizontal transverse direction ( $y$  in fig. 2.2). Therefore, most numerical simulations carried out are restricted to that direction. This is partly justified by the fact that the dynamics is only driven in one transverse direction and the motion does not directly couple to the other directions.

With  $\omega_{\perp} \approx 2\pi \times 2$  kHz and  $\mu/\hbar \approx 2\pi \times 0.6$  kHz, the Thomas-Fermi model becomes invalid for the transverse direction. If for both parameters the condition  $(\mu, k_B T) \ll \hbar\omega_{\perp}$  is fulfilled, the wavefunction is the single-particle ground state wavefunction in the transverse trapping potential. In the present case, the kinetic energy dominates, but the interaction energy cannot be totally neglected. For a harmonic trap, the wavefunctions for both transverse directions are:

$$\psi(r) = \frac{1}{\sqrt{2\pi}l_{y,z}} \exp\left(-\frac{r^2}{2l_{y,z}^2}\right) \quad (2.61)$$

with radii

$$l_{y,z} = \sqrt{\hbar/(m\omega_{y,z})(1 + 2a_s n_{1d})^{1/4}}. \quad (2.62)$$

The correction factor  $2a_s n_{1d}$  results in an increase of the transverse wavefunction due to repulsive interactions, in particular at the center of the condensate. The longitudinal density reads [70]:

$$n_{1d}(r) = \frac{\alpha}{16a_s} \left[ \alpha \left(1 - \left(\frac{r}{R}\right)^2\right) + 4 \right] \left[ 1 - \left(\frac{r}{R}\right)^2 \right] \quad (2.63)$$

where  $R = l_x^2 \sqrt{\alpha} / l_{y,z}$  is the radius of the condensate in the longitudinal  $x$ -direction, and the value of  $\alpha$  is found by solving the equation:

$$\alpha^3(\alpha + 5) = (15\chi)^2. \quad (2.64)$$

The parameter  $\chi = Na_s l_{y,z} / l_x^2$  gives an estimate of the ratio between interaction energy and the transverse kinetic energy. For our experimental parameters,  $\chi \approx 0.12$ , which corresponds to the limit  $\chi \ll 5$  for which the condensate is in the 1d mean-field regime.

The effect of interactions is weak, but nonetheless modifies the width of the single-particle Gaussian wavefunction by  $(1 + 2a_s n_{1d}(0))^{1/4} = 1.06$ , or a 6% increase at the center, for a condensate peak density of 25 atoms per  $\mu\text{m}$ .

The wavefunction in the horizontal transverse direction verifies a GPE similar to the longitudinal direction:

$$i\hbar \frac{\partial \psi_y}{\partial t} = -\frac{\hbar^2}{2m} \Delta \psi_y(r, t) + V_y(r, t) \psi(r, t) + g_y N |\psi_y(r, t)|^2 \psi_y(r, t), \quad (2.65)$$

with an effective interaction constant now given by:

$$g_y = g_{1d,y} = g \int dx |\psi_x|^4 \int dz |\psi_z|^4 = g I_x I_z. \quad (2.66)$$

Assuming a Gaussian ground state profile in the transverse  $z$ -direction yields  $I_z = 1/(\sqrt{2\pi} l_z)$ . For the longitudinal  $x$ -direction, we obtain from eq. (2.63) the following expression for  $I_x$  :

$$I_x = \frac{\alpha^2(21 + 9\alpha + \alpha^2)R}{315a_s^2 N^2}. \quad (2.67)$$

This yields, for our experimental parameters,  $g_y \approx h \times 0.4 \text{ Hz}\cdot\mu\text{m}$ . It is an order of magnitude less than the 1d interaction constant,  $g_x \approx h \times 23 \text{ Hz}\cdot\mu\text{m}$ . The effect of interactions in the transverse direction is weak. The effective energy levels of the atoms in the potential stay close to single-particle energy levels with a small upward shift due to the interaction energy. For our experimental densities, this shift is on the order of  $E_{int} = g_{1d} n_{1d}(0) / (\hbar\omega_\perp) / 2 = a_s n_{1d}(0) \approx 13\%$  for the condensate in the ground state of the potential, illustrated in fig. 2.4.

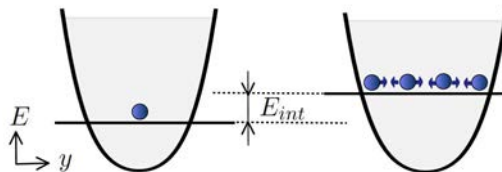


**Figure 2.4: Illustration of the mean-field shift.** Due to repulsive interactions between atoms, the energy of the atoms in the trapping potential is shifted slightly upwards.

# 3

## Technical features of the experiment

In this chapter, the practical implementation of this thesis' work is reviewed. The first section presents the main elements of the hardware, with an emphasis on the atom chip and the *light sheet* imaging system, two special ingredients in this experimental setup. Section 3.2 focuses on the techniques used to produce highly controllable trapping potentials and manipulate the external states of BECs. In the third section, we describe a typical experimental sequence by going through the different stages from BEC preparation to imaging. Finally, in sec. 3.4, we examine the question of calibrating the atom number by using the light sheet imaging.

The goal of this chapter is to introduce the elements that are important for the excitation of motional states. The current setup is the result of years of development, additions and changes, including a complete moving from Heidelberg, Germany to Vienna, Austria in 2006. More detailed information on the setup evolution can be found in the different theses that have been carried out on the same experiment:

- about the original setup in Heidelberg: H. Gimpel [71], Ch. Becker [72], S. Haupt [73], P. Krüger [74], S. Hofferberth [75], S. Wildermuth [76]
- about the upgrades in Vienna: S. Manz [77], T. Betz [78], R. Bücke [79];
- about the atom chip: S. Groth [80], S. Manz [77];
- about the radio-frequency dressing, in particular to realize double-well potentials: T. Schumm [81], S. Hofferberth [82], T. Plisson [83];
- about the two imaging systems in use: B. Engeser [84], R. Bücke [79];
- about the experiment control: M. Brajdic [85], W. Rohringer [86].

### 3.1 Elements of the setup

The experimental setup occupies a volume of about  $10\text{ m}^3$  in a specially air-conditioned and humidity-controlled room, with the necessary optical components organized on a  $3.25\text{ m} \times 1.25\text{ m}$  optical table and the driving electronics placed on top and below the table.

The heart of the experiment, shown on fig. 3.1, is a vacuum chamber equipped with an atomchip and an integrated Rubidium dispenser. The vacuum chamber is surrounded by external coils. The cooling and trapping of the Rubidium atoms is done using laser light, which is prepared and distributed at the back side of the table as seen from the perspective of fig. 3.1 (left), and magnetic fields, produced by the external coils and by the atomchip. At the back side and below the vacuum chamber, this time from the perspective of fig. 3.1 (right), are two cameras used to image the atoms at the end of each experimental cycle. The whole apparatus is controlled remotely from a pre-room using the ADwin system (see sec. 3.1.7).

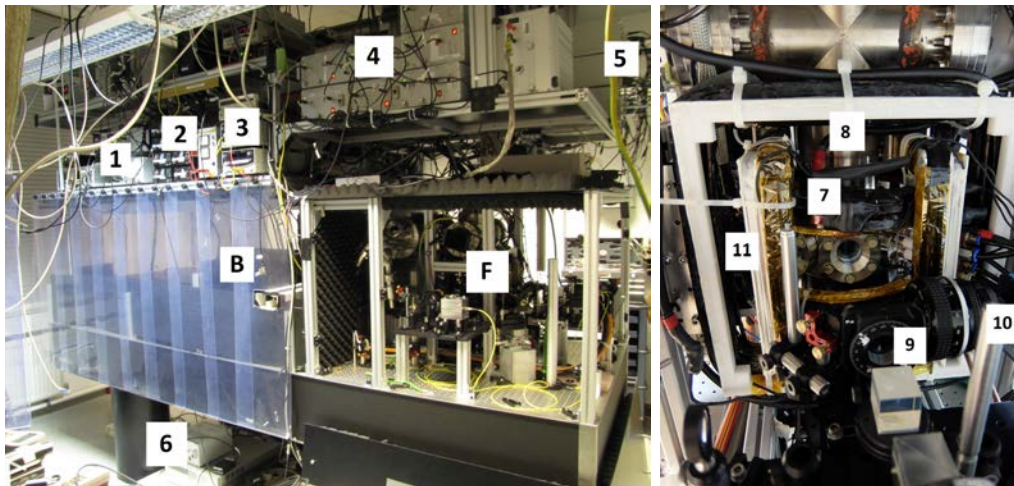


**Figure 3.1: Overview pictures of the experimental setup.** (Left) View of the entire optical table, with most of the optics (lasers, optics) protected by plastic curtains at the back (B), and the vacuum chamber at the front (F). On top is the control electronics for the AOMs (1), the optical shutters (2), the microwave field generator (3), the coils' switches (4) and the chip current control (5). At the bottom is the electronic for the dispenser (6). On the other side of the table, not visible on this picture, are the electronics for the lasers, the ADwin controller and the radio-frequency sources for the cooling and dressing. (Right) View over the vacuum chamber (7), with the chip mounting flange (8), the path for the absorption imaging light and the F=1 optical pumping (9), the MOT camera (10) and an external coil pair (11).

The way the different elements are used during the experimental sequence is detailed in sec. 3.3. In the present section, we start by sharing some technical knowledge regarding the most important elements of the experimental apparatus.

### 3.1.1 Vacuum chamber and Rubidium dispenser

The complete experimental cycle takes place in a single octagonal vacuum chamber made of stainless steel. After establishing pressures in the ultra-high vacuum range by baking-out, the vacuum is maintained by an ion pump<sup>1</sup> and a non-evaporative getter pump<sup>2</sup> (NEG), which passively collects part of the background gas on a large surface. In addition, a titanium sublimation pump (TSP), composed of 3 filaments inside a water-cooled tube, is activated on average once a month.

The optical access to the atoms is provided by eight windows, seven on the different faces of the octagon and one at the bottom, as can be seen on fig. 3.2. The windows are more than 1 inch in diameter and anti-reflection coated for the used wavelength ( $\lambda = 780 \text{ nm}$ ). They allow the cooling and trapping of atoms by letting the laser beams for cooling and optical (re)pumping through (see next subsection for the laser setup and sec. 3.3 for the MOT configuration), and letting photons out for the imaging.

One side of the vacuum chamber is not equipped with a window but with Rubidium dispensers. These are wired-shaped and contain a few mg of Rubidium Chromate mixed with a reducing agent. The Rubidium is set free when heated up by running currents through the dispenser, the quantity released increasing with rising temperature.



**Figure 3.2: Vacuum chamber and windows for optical access.** (Left) Vacuum chamber before assembly, with windows on seven sides and the connection to the Rubidium dispenser coming out to the left. (Right) View from the bottom into the vacuum chamber and onto the atomchip.

The background pressure needs to be kept within a given range for the experiment to work. In the first phase of the sequence, loading efficiently Rubidium atoms from the background vapor into a magneto-optical trap (MOT) requires a pressure of  $1 \times 10^{-9}$  mbar. In the second phase of the sequence, losses and heating of the BEC must be prevented by establishing background pressures on the order of  $1 \times 10^{-11}$  mbar, that is, two orders of magnitude lower. To achieve this, the Rubidium dispenser is switched on and off alternately, desorbing Rubidium at high temperature ( $> 500 \text{ }^\circ\text{C}$ ) and increasing the

---

1. Varian StarCell, 500 L/s  
2. SAES Getters

background pressure during most of the MOT phase, staying inactive as the cooling of the captured atomic cloud takes place. The dispenser is water-cooled to accelerate the temperature drop.

### 3.1.2 Laser system

The experiment counts two laser systems, which take on many functions: cooling, repumping, optical pumping and imaging of the atoms. To realize these functions, two wavelengths of the  $D_2$  line transitions of  $^{87}\text{Rb}$  are used, which are between the electronic ground state  $5^2S_{1/2}$  and the excited state  $5^2P_{3/2}$  at about 780 nm. These transitions are represented in fig. 3.3.

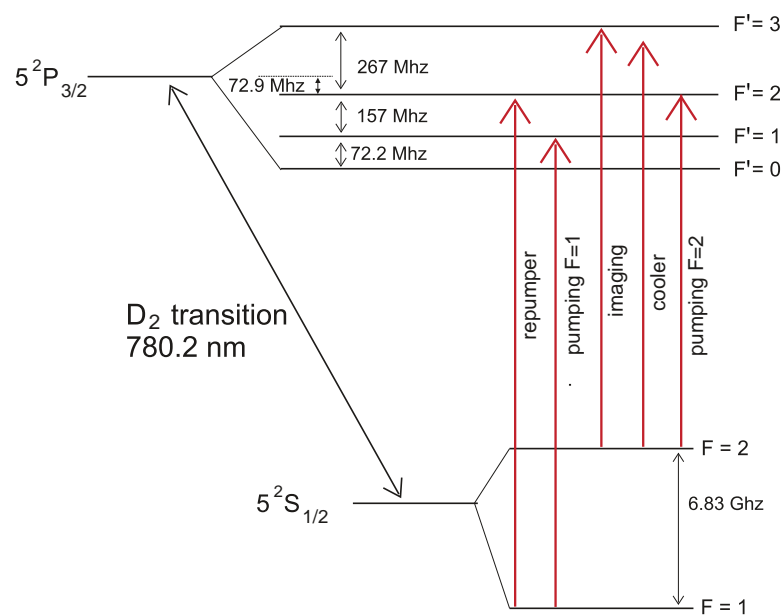


**Figure 3.3: Hyperfine structure of  $^{87}\text{Rb}$  and used laser transitions.** Adapted from [21]. Two different lasers are used for the  $F = 1$  and  $F = 2$  transitions.

The first laser system, called TA100<sup>3</sup> (right lines in fig. 3.3, upper right corner of fig. 3.4), is a combination of an external cavity diode laser (master laser) and an amplifier (TA), mainly used for cooling and imaging the atoms. It realizes the transition between the hyperfine level  $F = 2$  of the ground state to the level  $F' = 3$  of the excited state. The master laser is locked to this transition using a standard Doppler-free spectroscopy with a Rb vapor cell combined to a Pound-Drever-Hall configuration with sideband modulation at 20 MHz) [71].

Laser cooling requires high optical powers. The laser system with its built-in amplifier is able to deliver up to 1 W output power. However, after coupling into an optical fiber, the available power is cut by half. Therefore, an additional external amplifier,

3. Toptica Photonics TA100

the BoosTA<sup>4</sup>, was added. Simply injected with 40 mW taken from the TA output, this complementary amplifier raises the total available power on the transition from  $F = 2$  to more than 1 W. About two-third of the total power, the part produced by the BoosTA, is used for the laser cooling. This is done via a cycling transition, where atoms excited to  $F' = 3$  can only decay to  $F = 2$ , from where they get excited again to  $F' = 3$ . During MOT phase, the light is detuned using AOMs by  $\delta \approx -20$  MHz, and by  $\delta \approx -65$  MHz during the short molasses phase (see sec. 3.3.1). Different optical beams go through a double-pass AOM configuration, which enables the AOM frequency to be changed without affecting the beam alignment. The last third of the power, coming from the built-in amplifier, constitutes a reserve of power for future updates on the experiment. Only a fraction of it is used for imaging and optical pumping in  $F = 2$ .

The part used for imaging is close to resonance with the transition when set to absorption imaging. The frequency is slightly shifted to adapt to a small external magnetic field which enforces a quantization axis, and thus ensures a constant scattering cross-section. When used in fluorescence imaging mode, the light is detuned from the transition by  $\sim -5$  MHz. A very small fraction of the light serves for the optical pumping into  $F' = 2$ . This transition is currently triggered after the molasses phase to “repump” atoms from the  $F = 2$  state into  $F = 1$  before optically pumping them with the second laser.

The second laser system, the DL 100<sup>5</sup> (left lines in fig. 3.3, upper left corner of fig. 3.4), is a single external cavity diode laser that acts on the transition  $F = 1 \leftrightarrow F' = 2$ . It is locked close to this transition by a saturated absorption spectroscopy scheme and a lock-in amplifier. The saturation spectroscopy is obtained using an intense pump beam and a weak probe beam. In addition, the Doppler valleys are subtracted by sending in parallel a (non-overlapping) beam and combining it to the signal on a differential photodiode. The main purpose of this laser is to bring back atoms into the cooling cycle, as there is a small probability (0.01 %) for atoms to be excited to the  $F' = 2$  and fall back to  $F = 1$ . Due to the important level spacing between  $F = 1$  and  $F = 2$  ( $\sim 6.8$  GHz), the atoms cannot come back into the cycling transition. Although the probability is small, the loss over the many necessary cycles is non-negligible, hence repumping is critical. The repumping light excites atoms from  $F = 1$  to  $F' = 2$ , from which they can re-enter the cycling transition. Repumping requires about 30 mW. Finally, the same laser is used for optical pumping into  $F = 1$  to stabilize the atoms into the magnetically trapped Zeeman sub-level  $|F = 1, m_F = -1\rangle$ .

Most fibers on the setup are polarization maintaining, which is important to stabilize the power in the different paths when those are separated by a polarizing beam splitter. These fibers have a core confined between two stress rods that generate birefringence. They thus require to align a linear input polarization with one of the two principal axes of the fiber, such that the output polarization remains stable. As the polarization is defined by the phase between the field components on the two axes, and this phase depends linearly on the frequency, a correct axis can be found by modulating the laser

---

4. Toptica Photonics BoosTA

5. Toptica Photonics DL 100

frequency over some GHz. Then the simplest method is, with a half-waveplate at each extremity of the fiber and a beam splitter or a fast photodiode, to find a configuration of the waveplates insensitive to the frequency. In addition, polarizing beam splitters are placed at strategic positions to guarantee a stable polarization.

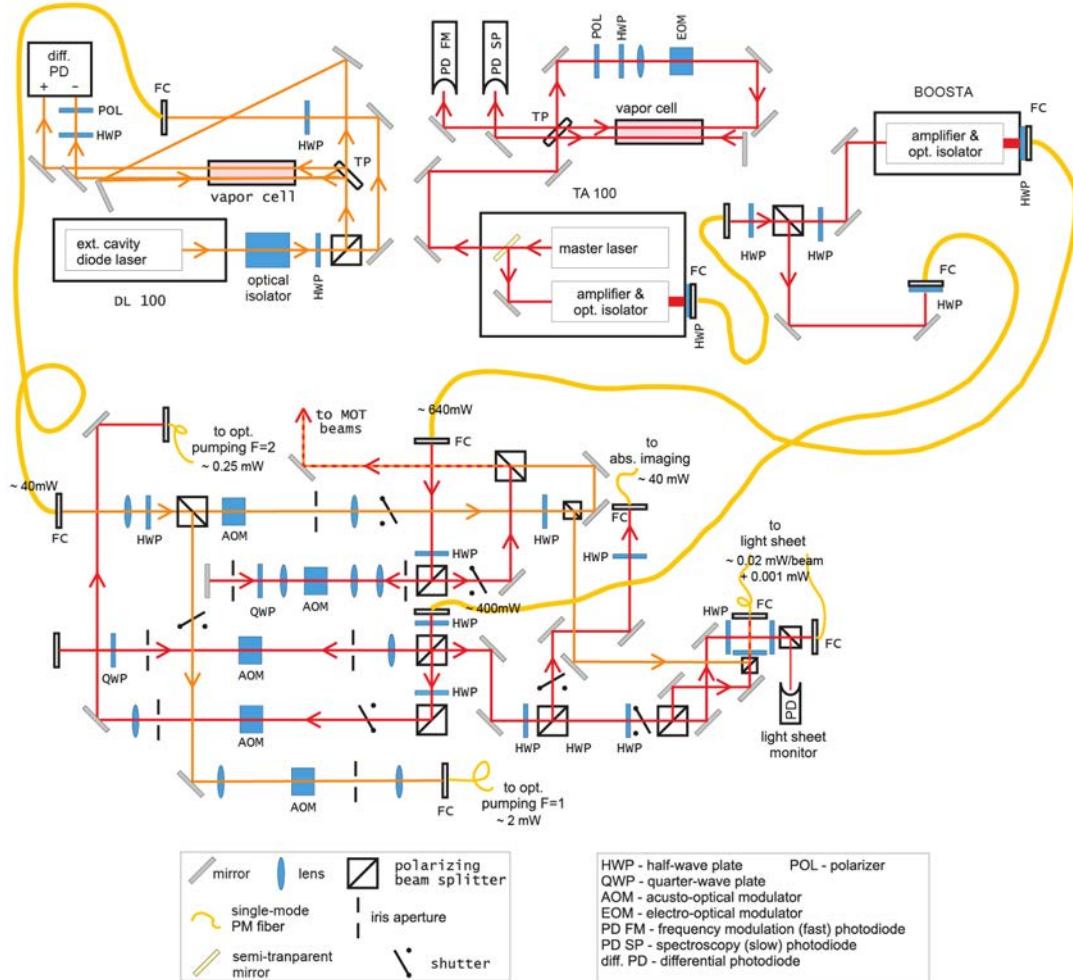


**Figure 3.4: Laser setup.** Adapted from [21]. Red lines indicate the optical path for the  $F = 2$  transition (cooler), while the orange lines indicate the  $F = 1$  (repumper). The upper part represents the two laser spectroscopy arrangements for the  $F = 1$  laser (DL 100) and the  $F = 2$  laser (TA 100). The  $F = 2$  laser uses a dual spectroscopy setup to simultaneously provide a normal Doppler-free spectroscopy and an additional path for Pound-Drever-Hall locking using an electro-optical modulator (EOM) for sideband modulation. Both lasers are coupled into single-mode polarization-maintaining fibers. The TA 100 is amplified by an additional BoosTA. The lower part shows the distribution of the beams to the different destinations.

### 3.1.3 External coils

Throughout the experimental sequence, homogeneous magnetic fields are needed to control the atoms, in particular during the MOT phase, but also in the later stages of the experiment, when those fields are combined to the magnetic fields created by the chip and copper structure wires. The homogeneous magnetic fields are produced by six pairs of coils placed around the vacuum chamber. Each spatial direction has two pairs of coils, one made of thick wire able to produce up to 100 G, plus a pair of thinner wire coils producing a smaller field (up to 10 G) in the opposite direction. These sets are called *big/small bias* and *big/small Ioffe* in the two horizontal directions, and *big/small up-down* in the vertical direction.

There are multiple advantages to this configuration: the big coils provide the large magnetic fields needed, while the smaller coils allow to make more precise adjustments on shorter timescales; moreover, unipolar current sources<sup>6</sup> can be used to supply the coils. A switching of the coils in less than 0.1 ms is obtained with custom-made switches which can withstand 60 A of DC current and the high switch-off induced voltages up to 400 V [87].

Most of the current sources for the coils are operated in current-stabilized mode, in order to output a constant current and ensure a good stability of the fields. Otherwise, these can be affected by thermal drifts and other changing resistance. Only the small Ioffe field, which sets the Larmor frequency or “trap bottom” of the chip trap, is voltage-controlled. For the dressed trap<sup>7</sup> used in the experiments, stability at the sub-milligauss level is required. In current-stabilized mode the circuit is sensitive to low-frequency noises, especially to the 50 Hz of the power network, which compromises the reproducibility of the experiment. The supply is thus used in voltage-control, combined with a high-precision temperature-controlled 1  $\Omega$  resistor<sup>8</sup> and a voltage feedback loop [56]. With this scheme, fluctuations of the fields are constantly monitored, and show a stability better than 100  $\mu$ G in normal working conditions. The details of the implementation can be found in R. Bückler’s PhD thesis [56].

### 3.1.4 Atom chip

While the external coils generate homogeneous fields from the outside of the vacuum chamber, inhomogeneous fields are produced within the vacuum chamber by an atom chip. Although the currents sent through the chip wires to produce those fields are much weaker than in the external coils, the close proximity of the atoms to the atom chip means that the atoms are subjected to strong fields and strong field gradients, and can be trapped in very tight potentials.

6. HP/Agilent 65xx series for all coils except for the small up-down coil, for which a bipolar supply (High-Finesse BCS-5/5) is preferred.

7. See sec. 3.2

8. Isabellenhütte RUG-Z, temperature coefficient < 1 ppm/K

### Chip mounting

The atom chip is fixed on a mount coming into the vacuum chamber from an opening at the top. In this position, time-of-flight measurements can be made when the atoms are released from the chip trap. The mounting consists of ten copper rods and  $\sim 1$  mm copper wires all embedded in a ceramic block that serves as electrical isolator and heat conductor. They are connected to the current supplies via a water-cooled vacuum flange presenting high-current feedthroughs for the copper wires (up to 60A) and a 36-pin connector for the lower current in the chip wires (up to 1A).

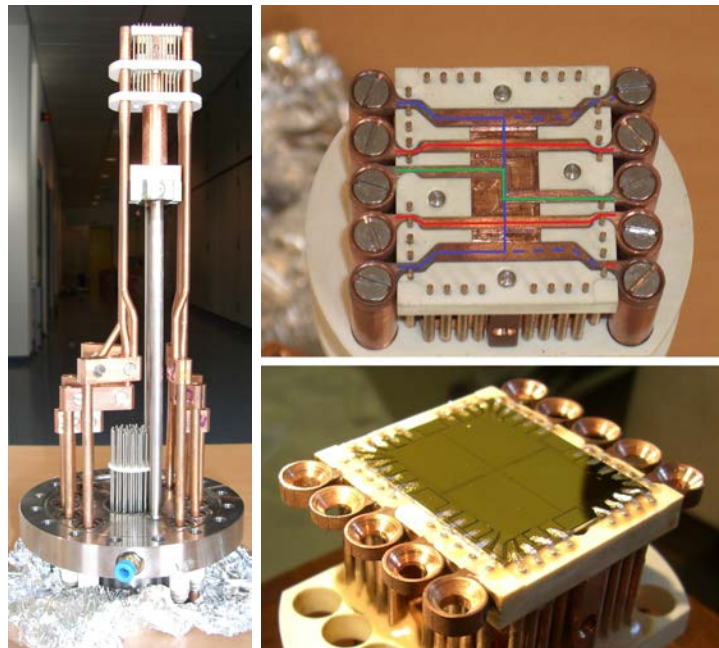


**Figure 3.5: Atom chip and chip mounting.** (Left) Chip mounting, to be placed upside-down in the vacuum chamber. From bottom to top: vacuum flange with feedthroughs for high-current copper wires, steel tube for water-cooling, copper rods and chip connection pins held by a ceramic blocks.

(Top right) Copper structure at the top of the chip mounting, with the U-wire (blue), the Z-wire (green) and the two I-wires (red).

(Bottom right) Atom chip glued to the mounting. The surface is gold-coated, and bond wires to connection pins are visible along the edges.

The copper wires lie about 1 mm below the surface of the chip. They form three main structures, shown in fig. 3.5 (top right panel): a U-shape wire (blue), a Z-shape wire (green) and two I bars (red). The U-shape wire is actually a H-shaped structure connected electrically such as to form a U (see dashed blue line in fig. 3.5 (top right)). It is the largest structure on the chip. In combination with the big bias (and the big up-down) fields, it creates a quadrupole field for the MOT, at a distance of  $\sim 1$  cm below the chip surface. It also serves as an antenna to perform radio-frequency (RF) evaporation on the trapped atoms. The Z-shape wire is a smaller structure that creates

a Ioffe-Pritchard configuration in conjunction with the big bias field. A field is added by the big Ioffe to lower the minimal field (the trap bottom), otherwise very high in this configuration, and which would lead to atom losses. The potential formed, called Z-trap, is used during the first stage of magnetic trapping, when the atoms are transferred closer to the chip (a few millimeters away from the surface) and cooled by RF evaporation. Finally, two I-shaped wires are located on each side of the Z-structure. They can provide additional longitudinal confinement or realize a Stern-Gerlach pulse that separates the atoms of different magnetic states during expansion .

### Chip wires

The atom chip itself was replaced after moving from Heidelberg to Vienna. The new chip consists of two layers of gold wires, insulated from each other to allow wires to cross. It was designed and fabricated by S. Groth [80] in the group of I. Bar-Joseph at the Weizmann institute. It was characterized in the experimental setup by S. Manz during her PhD thesis [77]. The atom chip is based on a silicon wafer with good surface quality, covered by a 100 nm layer of silicon oxide (SiO) for electrical insulation. The smallest structures, at the center of the ground layer of the chip, were fabricated by electron beam lithography. The rest of the wires plus the connectors were fabricated using standard UV-light lithography. The chip is then simply glued to the mounting. Except for the wires, the surface is coated with gold to be used as a mirror during the MOT phase, as explained in sec. 3.3. A photography of the atom chip surface is presented in fig. 3.5 (bottom right panel) and the chip geometry is shown in fig. 3.6.

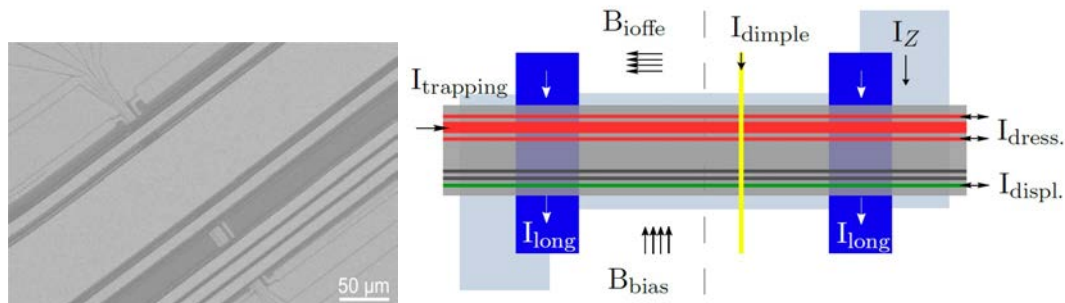


**Figure 3.6: Chip wires.** (Left) SEM image of the center of the chip, with in the center the 80  $\mu\text{m}$  trapping wire, on each side of it the 10  $\mu\text{m}$  dressing wires and, on the bottom right, the second set of three 10  $\mu\text{m}$ -wires.

(Right) Sketch of the same area, showing the 80  $\mu\text{m}$  trapping wire (thick red line) and the two RF dressing wires (thin red lines) as well as the set of 10  $\mu\text{m}$ -wires (thin grey and green line, green indicating the wire used to displace the trap) and the dimple wire (yellow). On this sketch are also represented the I-wires (dark blue), the Z-wire (light blue) and some external fields. The dashed line indicates the location of the chip center. The different wires are not to scale.

The main purpose of this atom chip is to create a trapping potential for elongated quasi-condensates. It was however designed with various other possibilities. The main

trapping function is realized by a straight 80  $\mu\text{m}$ -wire along the  $x$ -direction, combined with two 500  $\mu\text{m}$ -wires perpendicular to the 80  $\mu\text{m}$ -wire. The 80  $\mu\text{m}$ -wire thus defines the longitudinal direction and the two 500  $\mu\text{m}$ -wires impose a weak trapping potential along  $x$ . Two thin wires on both sides of the 80  $\mu\text{m}$  trapping wire are used as antennas to send out near-field radio-frequency magnetic fields to dress the trap (see sec. 3.2.3). Another set of three 10  $\mu\text{m}$ -wire, parallel but further away from the main trapping wire, was initially designed to form a second trapping configuration for dressed potentials, bringing atoms even closer to the chip. This trap is not used in the present work, but the *external* 10  $\mu\text{m}$ -wire, the outside-most wire of this set, is connected to modulate the position of the trap formed with the 80  $\mu\text{m}$  trapping wire.

The center of the atom chip also contains sub-micron structures for creating different potentials. In particular, a 10  $\mu\text{m}$ -wire located 300  $\mu\text{m}$  away from the chip center and perpendicular to the trapping wire can be used to form a *dimple trap*. This was intended to confine atoms in an almost isotropic trap, therefore allowing to study 3d Bose gases with very high densities. Another application for this wire is to measure the longitudinal trap frequency by exciting collective modes, as done in sec. 4.5.

All wires carry DC currents supplied by custom-made current sources. They are powered by car batteries, which has the advantage to avoid noise from the network and grounding the wires. Another aspect to consider is that corrugation of the chip wires modifies the magnetic fields produced by the wires. In the strong confinement directions, this effect is weak, but in the longitudinal direction, it can actually be the main confining effect. Finally, the currents running through the different wires heat up the chip, which modifies slightly the aspect of the chip surface. To get a good reproducibility of the results, the chip should be in a steady state, where the same amount of current goes through the chip at each cycle.

### 3.1.5 Imaging systems

Like many other cold atom experiments, the present setup uses optical imaging to probe the atoms. The setup is currently equipped with three optical imaging systems. One simply records the fluorescence of the atoms and is used during the MOT and molasses phase. The two others are time-of-flight imaging systems, one based on absorption and the other on fluorescence, that image the atoms at the end of each experimental cycle. This type of imaging is destructive, therefore only one image of the atoms can be taken per cycle.

#### MOT camera

The camera<sup>9</sup> used for MOT imaging collects the light re-emitted by the atoms during laser cooling. It can be located on the setup in fig. 3.1 (right panel). It is equipped with a conventional photographic objective of focal  $f = 50$  mm. The sensor is composed of  $640 \times 480$  pixels with a size  $5.6 \times 5.6 \mu\text{m}^2$ . It offers a field of view of about  $2.2 \times 1.6 \text{ cm}^2$ .

---

9. Imaging Source FireWire DMK 21BF04

The access window used for MOT imaging is the same as for optical pumping in  $F = 1$  and absorption imaging. A small mirror positioned slightly off the laser beam path diverts a part of the light emitted by the atoms towards the MOT camera. Two images are taken during the MOT phase at 11 s and 18.5 s from the beginning of the cycle, and one during the molasses phase, at 18.7 s.

### Absorption imaging system

The absorption imaging is a transverse imaging, it probes a plane containing the vertical transverse and the longitudinal axes. It consists of an incoming light beam shining on the atoms through one window, and towards a camera on the other side of the vacuum chamber. The camera used is a cooled, back-illuminated frame transfer CCD camera<sup>10</sup> with a  $1024 \times 1024$  pixels of size  $13 \times 13 \mu\text{m}^2$ . The quantum efficiency is about 70 %. The objective was designed to get high resolution, actually reaching the diffraction limit. It is built from two lenses placed outside the chamber, as described in [84]. The first lens<sup>11</sup> collimates the rays coming from an object point. It has a focal length of  $f = 100$  mm and a diameter of  $d = 30$  mm and is mounted as close as possible to the vacuum chamber. The second lens is a refocusing lens<sup>12</sup> of  $f = 450$  mm and  $d = 40$  mm. The objective has a numerical aperture of 0.12. For focusing, both lenses are mounted on a custom made optical rail, which is attached to a motorized translation stage. The pixel size in object space for this system has been determined to be  $3.44 \mu\text{m}$ , which corresponds to a magnification of 3.78. This camera is used to take two absorption pictures: one image of the atoms in time-of-flight, followed by a background image without atoms.

### Light sheet imaging system

The *light sheet* is the main imaging system used for the experiments in this thesis. It is a fluorescence-based scheme in which atoms fall through a thin *sheet* of light after a long expansion time. The images are taken from below, giving access to the longitudinal and horizontal transverse directions. The system has been developed by R. Bückler during his diploma thesis and is described in detail in [56, 79]. This imaging system consists of three elements: the light sheet, where atoms emit photons in all directions, an objective capturing a small fraction of the photons propagating into the collection solid angle and an EMCCD camera. The main advantages of this time-of-flight fluorescence imaging system compared to absorption imaging are, on the one hand, the absence of blurring from limited depth of field, which would inevitably occur given the size of the expanded cloud; on the other hand, the possibility to image clouds in slices by pulsing the light sheet which enables single slice imaging or, with a high-speed camera, a true 3d tomographic image of the cloud.

The light sheet consists of two counter-propagating beams coming out of fibers at a  $45^\circ$  angle with respect to the absorption imaging axis. The beams are first collimated by

10. Princeton Instrument MicroMAX 1024BFT

11. Melles Griot 06LAI011, monochromatic laser doublet

12. 10Melles Griot 01LAO339, achromat

a fiber outcoupler, then strongly focused in the vertical direction by a single cylindrical lens. The light sheet gets as thin as  $\sim 40\ \mu\text{m}$  vertically, while covering almost 1 cm in the horizontal plane. The vertical thickness is comparable to the depth of field of the objective, allowing to image entire atomic clouds while having full use of the sensitivity and resolution of the system. The adjustable parameters of the light sheet are: its vertical position, its thickness in the vertical direction, its intensity, its detuning, its width in the horizontal direction and its polarization. The vertical position fixes the time-of-flight and is not often modified, as it implies a manual refocusing of the optics. Its thickness and horizontal width also have to be changed manually. The polarization is chosen to be lin- $\perp$ -lin to avoid the formation of an intensity gradient, at the expense of creating a polarization gradient. The two other parameters, intensity and detuning, can be adjusted easily.

To monitor and stabilize the light sheet intensity, some of the imaging light is diverted from one of the light sheet beam paths and sent onto a fast photodiode (see fig. 3.4). The photodiode signal is displayed on an oscilloscope, read out and adjusted every second experimental cycle by modifying accordingly the imaging AOM amplitude. As the signal for stabilization is only monitored on one arm, care has to be taken when changing the overall power, as the balance can be affected.

The objective is placed just below the bottom window of the vacuum chamber, leaving just enough space for the MOT beams. It has been designed to achieve a high photon collection efficiency, which sets constraints on the numerical aperture. It is composed of two sets of lenses. The front part combines four different lenses<sup>13</sup> that offer sufficiently many degrees of freedom to correct for the important spherical aberrations caused by the vacuum window. The rear part consists of two lenses, a doublet<sup>14</sup> and a negative meniscus lens, placed in a tele-photo configuration, giving a final magnification of  $\times 4$  and a pixel size in object space of  $4\ \mu\text{m}$  (this part has been modified since [79]). The complete objective is  $\sim 200\ \text{mm}$  long and has a numerical aperture of  $\text{NA} = 0.34$  in object space, or a 3% solid angle coverage.

The last element of the imaging system is a high-speed electron-multiplying CCD (EMCCD) camera<sup>15</sup>. The EM feature offers the decisive advantage compared to a conventional CCD camera that the relative readout noise is reduced, an important aspect for single-atom detection. The camera also includes a water-cooling circuit that almost cancels the read-out *dark current* (DC) noise by bringing the detector's temperature as low as  $-100\ ^\circ\text{C}$ . Altogether, the back-illuminated EMCCD camera presents a quantum efficiency of  $\eta \approx 80\%$  at 780 nm. The different processes taking place in an EMCCD detector, crucial to determine its noise characteristics, have been studied in depth in [79]. The CCD sensor itself has a surface of  $1024 \times 512$  pixels with pixel size  $16 \times 16\ \mu\text{m}^2$ . The surface is equally divided into two  $512 \times 512$  pixels area, one being an *exposure area*, the other one being used as a *storage area*. Images can be taken every 30 ms in full resolution or every 2 ms in minimum resolution. These are quickly shifted from the exposure area

---

13. Melles Griot

14. Melles Griot 06LAI015

15. Andor iXon+ 897

to the storage area where they are read out. This configuration prevents inhomogeneous illumination of the picture due to a different exposure time, as the read-out takes a finite time. Moreover, no mechanical shutter is needed.

Eventually, about 2% of all emitted photons are detected. With our typical parameters, this corresponds to  $\sim 10 - 15$  photons per atom (ppa). Although this number may seem low, it is sufficient for single-atom sensitivity thanks to the very low background light in the images [88]. On the other hand, photons coming from a single atom are scattered over several pixels due to atomic diffusion in the light sheet, making it difficult to identify single atoms by their position on the images. Attempts to develop algorithms for this purpose have been made but an effective solution has yet to emerge. The resolution of the images is limited due to atomic diffusion, which translates into a fluorescence pattern for each atom of rms size  $r_a \sim 6 \mu\text{m}$ .

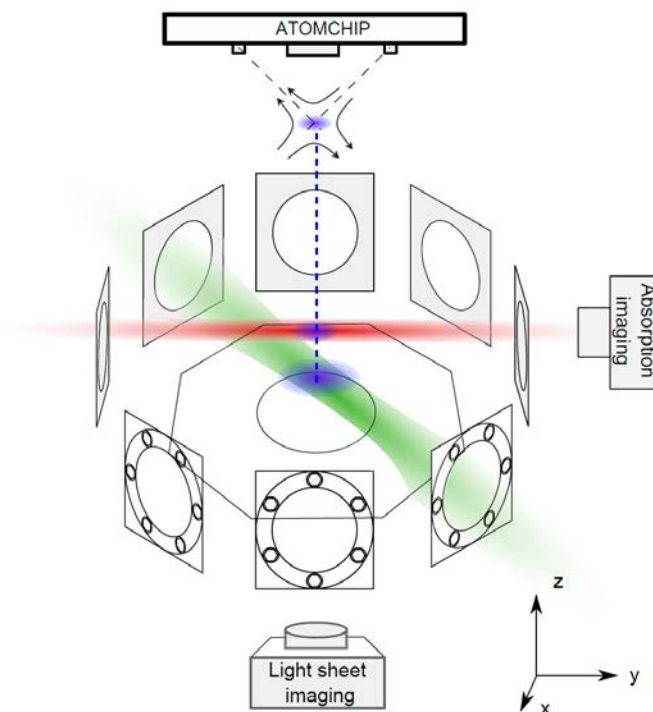


**Figure 3.7: Illustrative exploded view of the vacuum chamber and the imaging systems.** The atoms released from the trap (blue) are imaged in time-of-flight, either by absorption (red beam) after 1.5 to 20 ms propagation or by fluorescence in the light sheet (green beam) after more than 40 ms propagation.

The adjustment of the fluorescence imaging requires to align the light sheet and focus the camera following a special procedure. First, the light sheet is aligned by measuring the optical powers going in and out of the two light sheet fibers. The balance is checked by measuring the optical power coming out of each fiber. Then, the alignment is checked by measuring the recoupling of a beam coming from one fiber into the other. The fiber

ends are attached to a translation stage and alignment is adjusted with micrometer screws. The focusing of the light sheet imaging system is then realized using another translation stage equipped with micrometer screws, on which the camera and objectives are fixed. Once the coarse adjustment is done by a qualitative analysis of the images, fine focusing is done using a small and very dilute thermal cloud and measuring the variance over mean photon number. The idea is that, for a defocused image, the variance is given by the photon shot noise and a value slightly above 2 for the variance-over-mean is expected. For a more focused image, structures appear corresponding to single atoms, which increases the variance-over-mean [88]. The maximum value, typically around 2.4, corresponds to the focus.

### 3.1.6 Waveform generators

At different phases of the experiment, modulated currents are used. Arbitrary waveform generators are programmed directly from the control computers to send out a series of arbitrary waveforms after a TTL signal is received. There are currently three different applications of this on the experimental setup, each functioning differently.

A radio-frequency field is applied to dress the magnetic trap, as explained in sec. 3.2. A digital arbitrary waveform generator<sup>16</sup> produces sinusoidal signals with time-dependent amplitudes. For a constant dressing, we define short waveforms of a one-period cosine and loop over it, which gives a signal of constant amplitude and frequency during a designated period of time. Longer arbitrary waveforms can be defined for amplitude ramps, typically to ramp up and down the signal at the beginning and the end of the dressing phase. The global phase of the signal can also be set, keeping in mind that this affects the distribution in various  $m_F$  states when switching off abruptly the dressed potential. The dressing is applied onto two wires on each side of the trapping wire, in order to realize horizontal (or any other orientation) dressed potentials. For this, two output channels of the generator are set independently such that the amplitude and phase of the signal in each wire are controlled separately. The two channels are locked to a common sample clock. Amplitude ramps must be defined point-by-point and are therefore memory-consuming. For elaborated sequences, such as needed for double-well interferometry experiments [21], the transfer of the sequence to the generator can take longer than one experimental cycle for high sampling rates. To allow a reduction of the sampling rate without distortion of the signal, low-pass filters are added at each output of the generator. The generator is connected to the chip wires through a set of RF switches<sup>17</sup> and 1:1 transformers<sup>18</sup>. The transformers serve as galvanic isolation of the chip wires, ensuring a floating ground on the chip. Inductive current probes<sup>19</sup> are placed on the secondary circuit of the transformer to monitor the AC current.

Another RF field, used for evaporative cooling, is active for most of the intermediate to final stage of the experimental sequence, starting from the Z-trap. It realizes four

---

16. Tabor Electronics 50MS/s Dual-Channel Arbitrary Waveform Generator WW5062

17. MiniCircuits ZX80-DR230-S+

18. MiniCircuits T1-1T

19. Tektronix CT-6

frequency sweeps over a large range that spans from 19 MHz down to the central Larmor frequency of the trap, typically just below 1 MHz. The same model of digital arbitrary waveform generator as for the dressing is used. However, as the frequency is changed continuously over long times, another strategy is applied. A series of one-period cosine waveforms is programmed, which are looped to form units of constant frequency. Several units are concatenated to form a ramp of decreasing frequency. The length of each unit is set so that the decrease in frequency is roughly exponential. The waveforms are initialized at the start of the experiment. Then, for every experimental cycle, a new set of instructions containing the order of the basic waveforms and their lengths is sent to the generator. This scheme creates a less memory-consuming version of the usual frequency sweep using discrete steps and avoids phase jumps. The time constant of the exponential can be set independently for each frequency sweep, as well as amplitude of the signal. The step in frequency is adapted to be rather coarse for the beginning of the evaporation and fine at the end of the evaporation. With a step size smaller than the typical transverse level spacing frequency ( $\sim 2$  kHz), the trap bottom is approached smoothly. The final frequency can be chosen with almost arbitrary accuracy. This generator is connected to the chip via a similar RF switch and 1:1 isolation transformer than the dressing waveform generator and is equipped with the same inductive current probe. The signal is sent on the U-wire structure.

The last element requiring current modulation in the setup is the trap displacement or trap center position modulation, which follows a designed trajectory. As the frequencies contained in the displacing ramp are close to DC, keeping the ground floating on the chip cannot be done through a standard isolation amplifier, as is the case with the evaporation and dressing RF generators. In the past [56], the signal from an arbitrary waveform generator was sent through a custom-made DC isolation amplifier. The amplifier, used for galvanic isolation, was limiting the bandwidth of the signal to  $\lesssim 4$  kHz. This is a major drawback if one wants to realize fast displacements of the trapping potential. Instead, a synthesized function generator<sup>20</sup> with floating output is now used to produce the arbitrary waveforms. The waveforms are defined point-by-point and every new ramp is sent to the generator at the beginning of the experimental cycle. This DC ramp generator is isolated from the ADwin control electronics ground via an optocoupler on its Transistor-Transistor Logic (TTL) input and a USB isolator<sup>21</sup> on its digital command input. It is connected either directly on the external 10  $\mu\text{m}$ -wire, which was also used in [56], or combined with dressing on the two 10  $\mu\text{m}$ -wires connected in series. In the latter case, shown in fig. 3.8, a custom-made bias-T, the DP400, adds up the two signals, as shown in fig. 3.8. In both cases, the bandwidth is  $> 100$  kHz. This is an essential and significant improvement as compared to the previous configuration. The DP400 was specially designed to comply with the particular constraint of the setup: adding a low-frequency modulation (0 – 20 kHz) to the high-frequency RF signal ( $\sim 750$  kHz) and sending the current onto the RF wires without grounding the atom chip. A mechanical

---

20. Stanford Research Systems DS345

21. Cesium

relay<sup>22</sup> is introduced in the loop connecting the DP400 to the chip wire, such as to avoid induced currents during evaporation. This relay, rather designed for higher power applications, takes  $\leq 15$  ms to open and close.

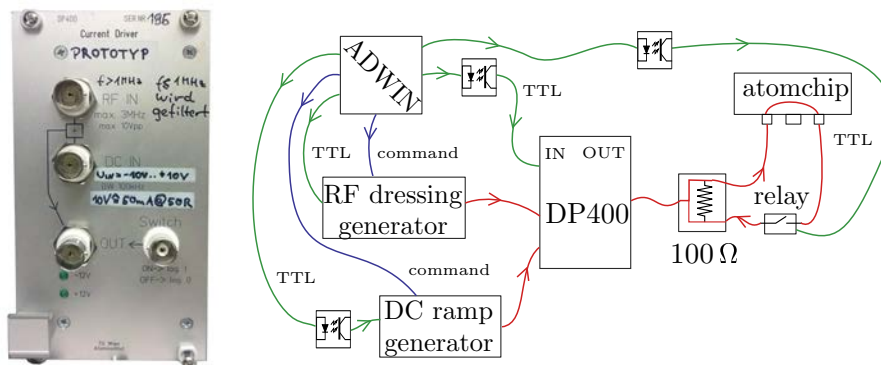


**Figure 3.8: Custom-made bias-T DP400.** (Left) Photograph of the DP400 interface. (Right) Schematics of the connections to and from the DP400. The ADwin sends the waveforms to the two generators (blue lines) at the beginning of the sequence. It also triggers the two generators, the DP400 and the relay during the experimental cycle via TTL signals (green lines). Several TTL signals are passed through optocouplers to avoid grounding issues. The dressing signal and the displacement ramp (red lines) are fed to the DP400 which adds them. The resulting signal is sent onto a loop passing by the two dressing wires of the chip. A mechanical relay keeps the loop open when no dressing is applied. As the DP400 output must be connected to a  $50\ \Omega$  resistance, an additional  $100\ \Omega$  resistor is placed in parallel to the two ( $50\ \Omega$ ) dressing wires.

Another synthesized function generator, not used in this thesis, allows to drive the ground state hyperfine transition by shining a microwave field ( $\sim 6.83$  GHz) into the vacuum chamber from an external antenna. This configuration has been used in the past to address the transition between the *clock states* ( $F = 1, m_F = -1$ ) and  $F = 2, m_F = 1$  [83, 89], and more recently to study partial microwave outcoupling from the trap state ( $F = 1, m_F = -1$ ) [90].

### 3.1.7 Control and acquisition

Most of the experiment is centrally controlled by a sequencer, or stand-alone real-time computer, the so-called the ADwin<sup>23</sup>. The sequencer is equipped with 32 analog voltage channels (16 bits,  $\pm 10$  V) and 64 digital TTL channels (0-5 V) that act as triggers. The time resolution is set by the control program to  $25\ \mu\text{s}$ . Sequences are defined by the user using an extended MATLAB graphical interface, where a number of parameters can be manually set or are calculated. Limits on the parameters can also be set. The values are then transmitted from a dedicated computer through the ADwin to the different elements in the laboratory via an Ethernet connection at the start of every cycle. Once

<sup>22</sup>. Tyco Electronics Connectivity relay T9A

<sup>23</sup>. Jäger ADwin Pro

the instructions are transmitted, the commands are executed autonomously. Only the waveform generators described in the previous section and the cameras do not get their command from the ADwin, but directly from the six other control computers mostly via GPIB connections. At each cycle, currents and magnetic fields are monitored via current probes on oscilloscopes and analog control probes<sup>24</sup> on one of the computers. The input parameters, processed pictures and calculated values (e.g. cloud size or number of atoms) are displayed and stored on two different locations. The computers communicate through a local network. All programming and read-out is done using MATLAB interfaces.

## 3.2 Trapping and manipulation of atoms

Magnetic fields are used all along the experimental cycle during the different phases. We provide here some basics to understand how neutral atoms are influenced by magnetic fields, in the particular case of <sup>87</sup>Rb. We then apply these notions to explain how atoms are trapped below the atom chip and how different trap geometries are obtained. We also explain how we use the atom chip to displace the atoms.

### 3.2.1 Neutral atoms in a magnetic field

In the absence of external magnetic field, the atomic levels are given by the hyperfine splitting caused by the nuclear magnetic moment in the electromagnetic field of the electrons. The coupling is represented by a term:

$$H_{hfs} = A \mathbf{I} \cdot \mathbf{J} \quad (3.1)$$

with A a constant determined by experiment,  $\mathbf{I}$  the operator for the nuclear spin and  $\mathbf{J}$  for the electronic angular momentum, in units of  $\hbar$ . The presence of an external magnetic field introduces a coupling between magnetic moment of the electrons and of the nucleus with the magnetic field. The Hamiltonian becomes

$$H = H_{hfs} + H_M \quad (3.2)$$

with

$$H_M = -\vec{\mu} \cdot \vec{B}. \quad (3.3)$$

The magnetic moment  $\vec{\mu}$  of the atoms has two components, electronic and nuclear. For <sup>87</sup>Rb, the latter is several orders of magnitude smaller and is therefore neglected, and the magnetic moment can be expressed as:

$$\vec{\mu} \approx -\frac{\mu_B g_F \vec{J}}{\hbar} \quad (3.4)$$

with  $\mu_B$  the Bohr magneton and  $g_F$  the Landé g-factor. At field values of typically a few Gauss (weak field), an atom experiences a Zeeman shift of a few MHz. This shift depends

---

24. National Instruments USB-6218

on the strength of the magnetic field. The total electronic angular momentum vector  $\vec{J}$  of an atom precesses around the external magnetic field  $\vec{B}$  with an angular frequency:

$$\nu_L = g_F \mu_B |\vec{B}| / \hbar \quad (3.5)$$

called the Larmor frequency. An atom in a varying external field can follow the field adiabatically if the change is slow compared to the Larmor frequency,  $\dot{\vec{B}}/|\vec{B}| \ll \omega_L$ . In other words, the quantization axis with respect to which the quantum states are defined aligns itself on the local magnetic field, while the atom remains in the same quantum state  $m_F$ . The atom then experiences a spatially varying potential:

$$V_{\text{mag}} = m_F g_F \mu_B |\vec{B}(\vec{r})|. \quad (3.6)$$

The effect of this potential depends on the sign and value of the product  $m_F g_F$ . States with  $m_F g_F > 0$  are *weak-field* seekers and can be trapped at a minimum of magnetic field. On the contrary, states verifying  $m_F g_F < 0$  are attracted to strong field values. As there can be no local maximum in a region devoid of charges and currents [91], only weak-field seekers can be trapped. These states are, for the case of  $^{87}\text{Rb}$ ,  $|F = 1, m_F = -1\rangle$ ,  $|F = 2, m_F = 1\rangle$  and  $|F = 2, m_F = 2\rangle$ . In the present experiment, the choice was made to use the  $|F = 1, m_F = -1\rangle$  trapping state, on the grounds that three-body losses are reduced as compared to  $F = 2$ .

### 3.2.2 Harmonic trap with static fields

Building on the first realizations of atom trapping with free-standing wires [92, 93], the idea quickly came around to fabricate micro-wires on small integrated structures [94–96]. These structures, built on *atom chips*, present the triple advantage to be very robust, versatile and to allow for very strong magnetic gradients thanks to their proximity with the atomic cloud. A comprehensive book on atom chips has been published in 2010 [18].

The central concept of the trapping used in this experiment is the *side guide trap*, combination of a DC current-carrying wire and a homogeneous bias field resulting in a field minimum in the plane perpendicular to the wire (illustrated in fig. 3.9). The field in  $1/r$  produced by the wire cancels the homogeneous field at a distance:

$$d_0 = \left( \frac{\mu_0}{2\pi} \right) \frac{I_t}{B_b} \quad (3.7)$$

from the wire. Typically,  $B_b \approx 30 \text{ G}$  and  $I_t = 1 \text{ A}$  giving  $d_0 \approx 70 \mu\text{m}$ . In the vicinity of the field minimum, a quadrupole trap with axes tilted at  $45^\circ$  and field gradient:

$$\frac{dB}{dr} = \left( \frac{\mu_0}{2\pi} \right) \frac{I_t}{d_0^2}. \quad (3.8)$$

is formed. However, it cannot be used as such. First, in the idealized geometry of an infinitely long wire, the atoms are not trapped in the elongated direction. Second, this field configuration presents a zero of the magnetic field at the minimum of the trap. This

poses the problem of Majorana transitions [97], or spin flips at the zero of the magnetic field due to the cancellation of the quantization axis. At that point, atoms can jump between Zeeman states and escape the trapping potential. To avoid both effects, two longitudinal wires perpendicular to the trapping wire and 3.1 mm away from each other are fabricated on the chip (see in fig. 3.6). Sending a DC current in both wires (with same amplitude  $I_h$  and same orientation) creates a field in the longitudinal direction of the form  $V_{\parallel} = V_{0,\parallel} + \frac{1}{2}m\omega^2 r^2$ . The confinement produced is very shallow but non zero, and the minimum of the potential is lifted. More quantitatively, the longitudinal frequency expected with  $I_h = 0.5$  mA is around  $2\pi \times 10$  Hz and the minimum of the trap becomes  $V_{0,\parallel} \approx h \cdot 350$  Hz. The addition of a longitudinal confinement transforms the trap into a Ioffe-Pritchard type configuration.

To increase the tuning range of the trap bottom, an additional external field, the Ioffe field, is added. Larmor frequencies on the order of  $h \cdot 1$  MHz can be obtained. With transverse trap frequencies on the order of  $2\pi \times 4$  kHz, the expected aspect ratio of the ideal elongated trap would be  $\omega_{\perp}/\omega_{\parallel} \sim 400$ .

### Additional effects

In practice, technical imperfections and other physical effects complicate the situation. This must be taken into account when doing precise simulations.

First, corrugation of the wires is an important limitation of our setup. To realize strongly interacting elongated gases, longitudinal trap frequencies below 5 Hz are necessary. However, inhomogeneities on the chip surface, such as wire edges and grainy structures in the material, result in a fragmentation of the condensate. The condensation takes place at a local trap minimum mostly created by height variations of the chip wires, and the longitudinal confinement is set by the chip corrugation. Control over this parameter is therefore limited, and was never accurately simulated. In practice, traps shallower than 15 Hz have never been obtained. An alternative to setting the longitudinal confinement with magnetic fields would be to create a hybrid trap, using laser light to contain atoms within certain limits. A time-averaged optical dipole potential would allow to create e.g. a box potential [98], or other kinds of exotic geometries.

Second, contrary to the ideal case, the wires have a finite size. With the distance from the chip  $d_0$  on the same of magnitude as the wires sizes, the field distribution seen by the atoms starts to differ from the infinitely thin wire model. Analytic expressions exist to model these imperfect wires, which are used in the simulations of the chip trap (see sec. 3.2.4).

Third, to locate accurately the trap minimum, gravity must also be taken into account. It induces a *gravitational sag* of about  $g/\omega_{\perp}^2 \sim 30$  nm, which is on the order of 10 % of the size of the transverse wavefunction.

### 3.2.3 Anharmonic trap with radio-frequency dressing

The technique of RF dressing was first proposed in 2001 [99]. The intention was to confine ultracold atoms in a 2d trap, an idea that was experimentally realized in 2004

at the LPL<sup>25</sup> [100]. Since then, different geometries have been investigated, including double wells and ring traps [101, 102].

The application of this technique to the creation of double wells on atom chips was pioneered on the setup used in these experiments [103, 104]. It has been used to study the dynamics of a bosonic Josephson junction [105], realize atom interferometry with external states [106–108], entangle internal atomic states with motional states [109] and is an ideal candidate for sub-shot-noise metrology [110]. More recently, on the present setup, the versatility of double-wells was pushed a step further in the direction of precise control over the coupling/decoupling between two 1d quasi-condensates under the influence of tunneling and interactions, and a Mach-Zehnder interferometer for ultracold atoms [108, 111] was realized.

### Concept of RF dressing

The basic idea is the following: a near-field RF magnetic field  $\vec{B}_{RF}(\vec{r})$  is used to couple internal states of the atoms, here the Zeeman states. The effect is similar to the dressing of internal states by a laser field in atom optics. The coupling of the bare atomic states to a spatially-varying RF field introduces a spatial dependence of the  $m_F$  states, effect that can be used to create new trapping configurations. Effectively, the trapped atoms experience a new *dressed* potential, whose geometry can be quite flexible.

Assuming a linearized polarized RF field, the complete magnetic field can be decomposed into static and oscillatory parts [101]:

$$\vec{B} = \vec{B}_s(\vec{r}) + \vec{B}_{RF}(\vec{r}) \cos(\omega_{RF}t). \quad (3.9)$$

Both parts can be associated with the Rabi frequencies:

$$\Omega_s(\vec{r}) = g_F \mu_B |\vec{B}_s(\vec{r})| / \hbar \quad (3.10)$$

$$\Omega_{RF}(\vec{r}) = \frac{1}{2} g_F \mu_B |\vec{B}_{RF,\perp}(\vec{r})| / \hbar \quad (3.11)$$

where only the part of  $\vec{B}_{RF}(\vec{r})$  perpendicular to the quantization axis effects the atoms, at least within the *rotating wave approximation* (RWA). The RWA is a convenient approach to describe a potential modified by an oscillatory field. The Hamiltonian of the system is then written in a rotating frame turning around the local quantization axis at the frequency of the RF field. In this approximation, the dressed potential takes the simple form:

$$V_d = m'_F \sqrt{\left[ \hbar \omega_{RF} - g_F \mu_B |\vec{B}_s(\vec{r})| \right]^2 + \left[ \frac{1}{2} g_F \mu_B |\vec{B}_{RF,\perp}(\vec{r})| \right]^2} \quad (3.12)$$

$$= m'_F \hbar \sqrt{\delta(\vec{r})^2 + \Omega_{RF}(\vec{r})}, \quad (3.13)$$

where  $m'_F \in \{-1, 0, 1\}$  corresponds to the new quantum numbers for  $F = 1$ . The first term in eq. (3.13) is a resonance term, which represents the energy shift introduced by a RF

---

<sup>25</sup>. Laboratoire de Physique des Lasers, Villetaneuse, France

photon of energy  $\hbar\omega_{RF}$ . Minima of the dressed potential correspond to low values of this term. For a negative value of the detuning at the trap center,  $\delta(0) = \hbar\omega_{RF} - g_F\mu_B|\vec{B}_s(0)| < 0$ , the resonance term vanishes along a three-dimensional equipotential surface where  $\hbar\omega_{RF} = g_F\mu_B|\vec{B}_s(\vec{r})|$ . The second term in eq. (3.13) describes the strength of the coupling between the atom and the RF field. It is always positive and acts as an effective Ioffe field. Its presence avoids spin-flips at locations where  $\delta(\vec{r}) = 0$ . The position-dependence of the coupling between bare states arises both from the detuning to the local Larmor frequency and the RF coupling strength. In the case of the coupling strength, the dependence is due to the spatial change of RF polarization with respect to local magnetic field.

The effect of this oscillatory field is to transform the initial static potential, which is harmonic and isotropic in the transverse direction, into an anisotropic potential flattened along a preferred direction. This direction is set by the angle of the RF field in the transverse plane. The transformation can be made adiabatically, such that atoms are loaded smoothly from the static trap into the dressed trap. The RF dressing amplitude has a major impact on the shape of the potential. For small amplitudes, the dressing is weak and leads to single anharmonic traps. Beyond a certain critical value, a heap forms at the center, eventually establishing a barrier that splits the trap into two. This property was used to create controllable double-well potentials in [21]. Once the wells are well-separated, their shape is close to harmonic at their minima.

### Implementation

The implementation is done by two thin wires on each side of the trapping wire, such as to form a 45° angle with the trap center. Each wire carries up to 100 mA peak-to-peak of AC current, producing fields of  $\sim 2.5$  G. The intensities and phases can be set individually in each wire:

$$I_{RF1} = I_1 \cos(\omega_{RF}t + \phi_1), \quad (3.14)$$

$$I_{RF2} = I_2 \cos(\omega_{RF}t + \phi_2). \quad (3.15)$$

The tilt of the potential can be adjusted by changing either the relative amplitude of the currents or their relative phase. To realize a dressing along the horizontal axis, the polarizations of the individual RF fields created by the wires must be linear and orthogonal, with equal amplitudes. Then, the dressing is done mostly in the direction perpendicular to the RF polarization: a polarization along  $z$  gives a deformation mostly along  $y$ .

#### 3.2.4 Trap simulation

In the frame of this project, RF dressing is used to make the trap anharmonic and optionally to slightly tilt it. The reason for this is that the scheme employed to address non-classical motional states relies on the ability to couple the center-of-mass motion and the intrinsic dynamics of the condensate along the direction of the displacement, the  $y$ -direction. The weak anharmonicity of the trapping potential in the transverse direction

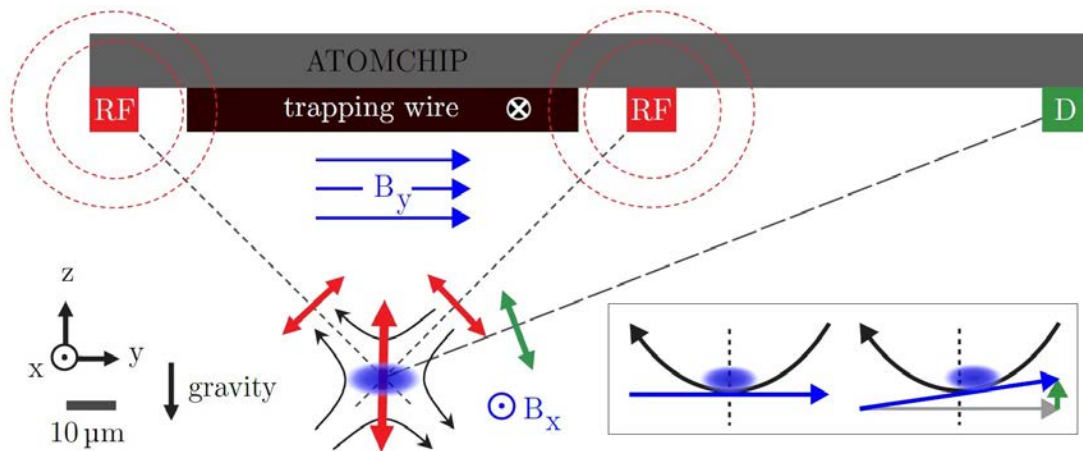


**Figure 3.9: Schematic of the small chip wires and the produced fields.** *Adapted from [56].* (Main area) The transverse potential is a quadrupole trap formed by combining an inhomogeneous field produced by the current  $I_t$  in the trapping wire and a homogeneous field in the  $y$ -direction, the bias field. Another homogeneous field along  $x$ , the Ioffe field, defines the Larmor frequency at the trap center  $\nu_L$ . The RF dressing field is formed by the currents in the two dressing wires,  $I_{RF}$ , set to form an RF field along  $z$  (red arrows). The resulting anisotropic transverse potential is shown as ellipse in the center of the quadrupole. Finally, the displacement of the trap center is accomplished by a current in an auxiliary wire (D), leading to a magnetic field, aligned at  $\sim 19^\circ$  with respect to the  $z$ -axis (green arrow). (Inset) Field configuration for trap displacement. The transverse trap position is defined by cancellation of the chip wire field (black) and the bias field (blue). Adding a weak field along  $z$  (green) tilts the bias field slightly, leading to a horizontal shift of the trap minimum.

is the ingredient that makes it possible. The additional anisotropy of the trap between the transverse directions introduces a detuning of the energy levels along the vertical transverse  $z$ -direction with respect to the energy levels along  $y$ .

We use accurate simulations of the chip trap to find a suitable potential. For the dressing amplitudes used in this project, the RWA generally gives a good approximation of the real potential [104]. However, because of the high sensitivity of the protocol proposed to the exact potential shape, the potential is calculated using Floquet analysis [112], an approach that goes beyond RWA. The field parameters playing an important role for the anharmonic potential are:

- the amplitude of the field produced by the trapping wire, which determines the position of the static trap bottom and quadrupole gradient, together with
- the amplitude of the bias field; these two field parameters are completed by
- the amplitude of the Ioffe field, which determines the Larmor frequency of the static trap, but also influences the shape of the dressed potential;
- the amplitudes of the RF dressing, which are chosen to be equal for a horizontal trap, or unbalanced for a tilted trap;
- the phases of the RF dressing, which must be experimentally adjusted to ensure e.g. a relative phase of  $\pi$  for a horizontally dressed trap.

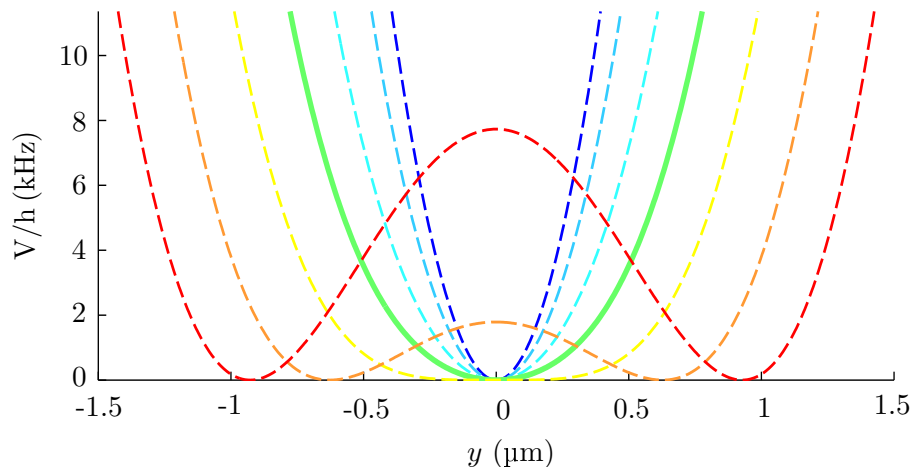


**Figure 3.10: Deformation of the potential along  $y$  under the action of the RF-dressing.** Simulated potential for different values of the RF dressing intensity, going from  $B_{RF} = 0$  (blue dashed line) to  $B_{RF} = 1.74$  G peak-to-peak (red dashed line). The green full line corresponds to the dressed trap configuration in the experiment,  $B_{RF} = 0.87$  G.

The longitudinal frequency is strongly affected by corrugation. Therefore it is not simulated directly from positions of the wires and their (idealized) geometry. However, from the knowledge of the longitudinal frequency in the static trap, it is possible to infer the variation for increasing RF field values.

The final trap chosen is very close to the one used for twin-beam project in [56]. The choice has been guided by various considerations such as geometry, confinement strength, fragmentation and heating rate. The parameters selected for this trap are, in the trapping wire,  $I_t = 1$  A, the bias field  $B_y = 34.1$  G and for longitudinal confinement  $I_H = 0.5$  A. The Ioffe field is set to  $B_x = 1.07$  G. These parameters yield in the static trap a trap bottom  $\nu_L = 824$  kHz and a transverse level spacing or static frequency  $\nu_0^\perp = 4.14$  kHz for an atom in the trapped state  $|F = 1, m_F = -1\rangle$ . The trap center is located at  $d_0 = 49$   $\mu\text{m}$  below the chip surface. The RF dressing amplitude is cranked up to  $24 \text{ mA}_{\text{pp}}$ , giving an RF field  $B_{RF} = 0.87$  G. For an RF frequency of  $770$  kHz, this leads to a detuning  $\delta(0) = -54$  kHz and a coupling  $\omega_{RF}(0) = 147$  kHz at the trap center. The relative phase between the two RF wires is set to  $\pi$ . The simulated potential can be approximated by the sixth-order polynomial:

$$V(y) = \alpha_2 \left( \frac{y}{r_{0,y}} \right)^2 + \alpha_4 \left( \frac{y}{r_{0,y}} \right)^4 + \alpha_6 \left( \frac{y}{r_{0,y}} \right)^6, \quad (3.16)$$

with  $\alpha_2 = h \times 1331$  Hz/2,  $\alpha_4 = h \times 62.7$  Hz and  $\alpha_6 = -h \times 0.63$  Hz.  $r_{0,y} = 252$  nm is the rms radius of the single-particle ground-state wavefunction in the  $y$ -direction. The energy differences between the first three single-particle levels of the potential are  $E_{01} = h \times 1.77$  kHz and  $E_{12} = h \times 1.93$  kHz. In the other directions, the confinement remains essentially harmonic with  $\omega_z = 2\pi \times 2.58$  kHz and  $\omega_x = 2\pi \times 16$  Hz. This potential is used further on to carry out the optimization of the displacement (see chap. 4).

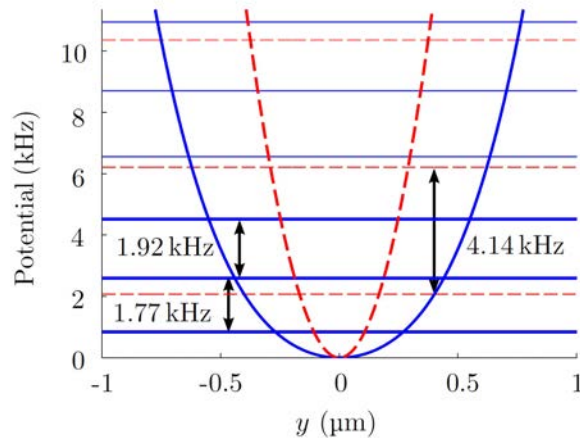


**Figure 3.11: Simulated static and dressed potentials as used in the experiments.** Static potential with its single-particle eigenvalues (red dashed lines), and dressed potential with its single-particle eigenvalues (blue continuous lines).

Once a suitable trap is designed using numerical tools, a series of measurements is done to ensure that the experimental potential corresponds to the simulations. The prominent techniques for trap characterization are RF spectroscopy to determine the trap bottom, and the triggering of collective dipolar excitations (sloshing) to measure the trap frequencies. These measurements are presented in detail in sec. 4.6.1.

### 3.2.5 Transverse displacement of the trap

In order to rapidly displace the potential in the transverse direction, small currents modulated at low frequencies (0 – 20 kHz) are sent on the chip. Regarding the choice of displacement direction, the  $y$ -axis offers a decisive advantage due to the configuration of the imaging system: features in the  $y$ -direction get stretched during time-of-flight and details in that direction are well-resolved with the light sheet. A displacement in the  $z$ -direction is also conceivable, applying for example a modulation to the trapping current. However, the features of interest would not be visible on the light sheet which integrates along that direction. A work-around would be to install a high-speed camera, able to take enough shots as the atomic cloud falls through the light sheet, to get a good resolution ( $\geq 1,000$  frames per second).

#### Displacing using an external wire

Conceptually, the simplest option to displace the potential in the  $y$ -direction is to apply a current to an auxiliary wire running parallel to the main trapping wire. For this scheme, a single waveform generator can be connected to this wire. The wire should be as far as possible from the trapping wire in order to create a magnetic field almost aligned with the  $z$ -axis. We use the external 10  $\mu\text{m}$ -wire (shown in green in fig. 3.6 and

fig. 3.9), located at a distance of  $140\ \mu\text{m}$  from the trapping wire, and  $150\ \mu\text{m}$  from the trap center. The effect of an additional field along  $z$ , as depicted in fig. 3.9, is to add a slight tilt to the external homogeneous field. The trap minimum, which is the point where the trapping and external fields cancel out, is displaced along  $y$ . Depending on the sign of the current and hence the orientation of the magnetic field, the potential is mainly displaced to the left or to the right.

Due to the finite distance to the wire, there is a slight misalignment of the displacement field with the  $z$  axis, leading to a residual displacement along the vertical direction. The anisotropy of the trap and stronger confinement in the  $z$ -direction help reduce this effect. The movement of the trap minimum caused by a current in the  $10\ \mu\text{m}$ -wire can be estimated from simulations to be  $26\ \text{nm mA}^{-1}$  along  $y$  and  $9\ \text{nm mA}^{-1}$  along  $z$ . The axis of the potential can be aligned on the displacement axis, using the flexibility offered by the RF dressing to tilt the trap.

Care must be taken when connecting any device to the chip. Here, forming a loop with the external  $10\ \mu\text{m}$ -wire induces currents during evaporation, which in turn leads to a reduced atom number in the chip trap. With a relay keeping the loop open during all evaporation phases and more generally all the time except when activating the  $10\ \mu\text{m}$ -wire, deleterious effects are limited. In practice, with this precaution, no significant difference of atom number or heating rate appear compared to the case with the  $10\ \mu\text{m}$ -wire disconnected.

### Displacing with dressing wires

A slow current modulation can also be transmitted through the RF dressing wires. This configuration requires additional electronics, but it has several advantages over the previous scheme. Adding a slow current to the RF dressing requires either a waveform generator that can be programmed to output arbitrary ramps ranging from DC to  $\sim 1\ \text{MHz}$ , or an additional device able to add the signals from the already available sources. In the first option, the device must present a floating output, or have special isolation transformers, as the lower frequencies will be filtered by regular transformers (see sec. 3.1.6). The second option has the advantage to integrate the already existing generators, using the specifically developed bias-T presented in sec. 3.1.6 and fig. 3.8. The device has for inputs the RF and DC signals from the two generators. It adds the two signals and sends it out on the two dressing wires, connected in series. This configuration forms a current loop and produces a linear field aligned vertically. There again, depending on the sign of the current and hence the orientation of the magnetic field, the potential is mainly displaced to the left or to the right.

One advantage of using the RF dressing wires to operate the displacement is that a perfect alignment with the horizontal axis is fulfilled, which is the one we optimized the displacement for, and also the best for imaging. Compared to the configuration used previously in [56], where the DC part was produced with a different generator devoid of floating output, this scheme offers the advantage of an extended bandwidth.<sup>26</sup>

<sup>26</sup>. This advantage is mitigated in the present case as we use an arbitrary waveform generator specified

Furthermore, modifying the setup to include a separate supply for each wire, one could imagine displacing the whole transverse plane and create more involved motional states structures such as circular modes.

The main drawback compared to the external wire scheme is the necessity of adding an electronic device, which increases the probability of having noise. As the RF wires are relatively closer to the atoms than the external wire, the same level of noise also produces stronger magnetic fields. Relays have been placed close to the chip in that configuration as well, in order to limit the impact of induced currents and other noises. However the loop must be closed earlier to allow for dressing of the trap. With the last evaporation ramp taking place during that time, losses in atom number are observed. A slight modification of the trapping potential is also observed, with a shift in the trap bottom of +1% and of the frequency of about -5%.

### 3.3 Experimental sequence and procedures

Like in any ultracold atom experiment, several stages are necessary to prepare an ultracold sample and extract valuable information. In this section, we follow step-by-step the formation, manipulation and imaging of a degenerate gas on our atom chip, using the different pieces of equipment described in sec. 3.1. A whole sequence takes 36 s, the different stages are presented in this section.

#### 3.3.1 From MOT to molasses

The first step of the experimental sequence is a magneto-optical trap (MOT) [113]. A combination of laser beams and magnetic fields collect atoms from the background gas and pre-cools them. Simultaneously, the dispenser vaporizes  $^{87}\text{Rb}$  atoms to increase temporarily the background pressure. Here, the usual six beams configuration is adapted to the special technology installed: the chip is used as a mirror for two counter-propagating beams impinging at  $45^\circ$  on its gold-coated surface. This allows to create a MOT by reflection. The MOT beams are composed of cooling light ( $\sim 20$  mW per horizontal beam and  $\sim 40$  mW per  $45^\circ$  beam) and repumper light (a few mW per beam). An additional magnetic quadrupole field is approximated by combining the field produced by the U-shaped wire on the chip to a homogeneous bias field [96, 114] (see sec. 3.1.4), which has the advantage to pre-position the MOT for later transfer to the chip trap. Due to irregularities on the chip surface, the reflected MOT beams have interference patterns and shadow areas, perturbing the MOT formation. Adjusting two external fields — bias and up-down — allows to change the quadrupole's position and axes. Iteratively optimizing of the MOT beams and the external fields, a MOT of reasonable size and regular shape can be obtained.

The MOT is active for 18.5 s, which is the time needed to collect atoms from the moderate background pressure. In the last 2 s, the dispenser is switched off to allow the background pressure to drop to acceptable levels for the rest of the cycle. The MOT is

---

with floating output, i.e. a  $1\text{ M}\Omega$  resistance at the power input.

then moved closer to the chip in 200 ms, ramping the fields and the laser detuning. A short phase of optical molasses or sub-Doppler polarization gradient cooling takes place, cooling the atoms further. For this, the MOT fields are mostly switched off and the detuning brought to  $-70$  MHz with respect to the cooling transition. The small coils are used as compensation fields for ambient magnetic fields. Unfortunately, the proximity to the atom chip causes shadows and induces heavy losses of atoms. This phase is hence limited to a few ms.

### 3.3.2 Loading to the chip

The loading into the chip trap goes through several stages: pumping into a trappable state, transfer into the  $Z$ -trap, first evaporative cooling and finally transfer from the  $Z$ -trap to the final static trap.

At the end of the molasses phase, the atoms are pumped from  $F = 2$ , where they are in a mixture of different Zeeman states, to the state  $|F = 1, m_F = -1\rangle$ , which can be trapped. For this, two short pumping beams ( $< 1$  ms) are used: the optical pumping  $F = 2 \leftrightarrow F' = 2$ , which lets the atoms fall into  $F = 1$  after a few scattering events, and the optical pumping  $F = 1 \leftrightarrow F' = 1$  with  $\sigma^-$  polarization, which rapidly pumps all atoms in  $|F = 1, m_F = -1\rangle$  (see description of the laser setup in sec. 3.1.2).

When all atoms are in  $|F = 1, m_F = -1\rangle$ , the light is turned off and the  $Z$ -shaped wire (see sec. 3.1.4) is switched on, as well as the bias and Ioffe fields. The first values for the fields are set to get a good mode-matching with the molasses. They are then ramped up for 2 s to compress the atoms into a tighter, already elongated trap of transverse frequency  $\sim 2\pi \times 200$  Hz and longitudinal frequency  $\sim 2\pi \times 20$  Hz. A first evaporative cooling is applied, during which spin flips to untrapped state occur for atoms resonant with the evaporation RF frequency. Ramping down the RF frequency effectively modifies the trap depth and lets the “hottest” atoms escape, bringing down the temperature.

At the end of the  $Z$ -trap stage, about  $2.5 \cdot 10^6$  atoms at  $\sim 50$   $\mu$ K are ready to be transferred to the chip trap. This trap has initially parameters loosely matching the  $Z$ -trap, but is then ramped up. The chip trap is formed by the trapping  $80$   $\mu$ m-wire, the small bias and the small Ioffe fields (see sec. 3.2.2). After the transfer, a second evaporation ramp cools the cloud to  $\sim 20$   $\mu$ K. A last compression phase gives the trap its final static shape and position. Thanks to its high confinement, an evaporation ramp at this stage allows to attain high phase-space densities, producing a quasi-condensate with  $10^2 - 10^4$  atoms at low temperature (down to  $< 20$  nK).

### 3.3.3 In the chip trap

Once the atoms are loaded in the static trap, different procedures can be applied in the current setup configuration. These procedures are specific to the different projects carried out on the setup, making use of a small set of tools.

The most used tool is the RF dressing described in sec. 3.2.3. With it, the trap can be deformed further, all the way from the static harmonic trap to a completely decoupled double-well potential. It has been extensively used to split and recombine atomic clouds.

If the last evaporation ramp is applied before splitting, then a 1d quasi-condensate is split into two quasi-condensates with a fixed relative phase. The phase can also be tuned by tilting the double-well. This was used to study the bosonic Josephson junction [105] and realize a Mach-Zehnder interferometer [108].

If the last evaporation ramp is applied after splitting in a decoupled double-well, two 1d quasi-condensates with undefined relative phase are formed. By outcoupling a small fraction of the atoms, one could in principle follow the formation of a defined phase during the measurement process (upcoming project, follow-up of [90]). This kind of weak measurement could also be used to follow the dynamics of a single trapped condensate. Outcoupling atoms can be done by changing their internal state to the untrapped Zeeman state  $|F = 1, m_F = 0\rangle$  with a RF radiation, or to the hyperfine state  $|F = 2, m_F = 0\rangle$  either with a micro-wave radiation or via a two-photon laser Raman transition. The last option is preferable due to its high outcoupling rate. A Raman laser setup has been assembled and is planned to be installed within the year.

Another procedure of importance in the last projects is the displacement of the trapping potential for realizing transfers to different motional states. This procedure is explained in chap. 4. It has been used for twin-beam production [115] and Ramsey-type interferometry with non-classical external (motional) states [116]. This action relies on a weak RF dressing, as this scheme cannot function in a harmonic potential.

A tighter, almost 3d trap can be activated by running a current into the dimple wire. A condensate with a homogeneous phase can be obtained by cooling down further in this trap. It has been used for measuring Hanbury-Brown Twiss correlations [117].

Finally, as the atoms fall from the trap to be imaged, a Stern-Gerlach pulse can be applied during time-of-flight to improve the quality of the images. It has for effect to separate the three Zeeman states freed from the dressed trap at switch-off. Due to spurious ambient fields, these three states are not perfectly overlapped transversely on fluorescence images, which causes a slight blurring e.g. of interference fringes. A longitudinal magnetic field gradient from one of the I-shaped wires helps correcting this effect by separating the states during time-of-flight.

### 3.3.4 Imaging

Finally, the last step of a typical experimental sequence is the extraction of information, which requires to probe the atomic clouds on length scales of micrometers. This is possible using cameras and relatively simple optics (see sec. 3.1.5). Standard optical imaging techniques for cold atoms probing are absorption and phase contrast imaging. Both rely on an incoming light beam being modified by the atoms (absorbed and/or phase shifted), then looking at the change in the imaging light. In other systems other approaches, such as micro-channel plates [118] and electron microscopes [119], have also been implemented.

On our setup, absorption and fluorescence imaging systems have been installed. Phase contrast imaging is not used, although it offers the possibility to do non-destructive imaging, in part because it requires complicated phase shifting optics, and because it is less sensitive than absorption imaging. In this work, absorption imaging has only been

used for calibration and characterization measurements. The main results have been obtained using an unusual system of fluorescence imaging, the light sheet.

### Absorption imaging

Absorption imaging gives direct quantitative information about the atom number with a good signal-to-noise ratio and is relatively easy to implement. The idea is that a short pulse ( $\sim 50 \mu\text{s}$ ) of incoming imaging light  $E_i$ , upon encounter with an atomic cloud, gets partly absorbed by the atoms and becomes, following the Beer-Lambert law:

$$E_{\text{out}} = tE_{\text{in}}, \quad (3.17)$$

with, away from saturation,

$$t = e^{-OD/2} = \exp\left(-\frac{\sigma_s n_{\text{int}}}{2} \frac{1}{1 + (2\delta/\gamma)^2}\right). \quad (3.18)$$

In this equation  $OD$  refers to the optical density of the cloud,  $n_{\text{int}} = \int n(y)dy$  is the integrated column density in the direction of the light beam ( $y$ ),  $\sigma_s$  the scattering cross-section of the atoms,  $\delta$  the light field detuning and  $\gamma$  the atomic linewidth. At resonance with the imaging transition  $F = 2 \leftrightarrow F' = 3$ , that is for  $\delta \rightarrow 0$ , the light beam is attenuated by:

$$\frac{I_{\text{out}}(x, z)}{I_{\text{in}}(x, z)} = e^{-\sigma_s n_{\text{int}}(x, z)}. \quad (3.19)$$

The atom number can be determined by taking two images with the same imaging beam intensity. Assuming a homogeneous distribution of the atomic density over the area of one pixel,  $A$ , the number of atoms in one pixel is:

$$N = \frac{A}{\sigma_s} \ln\left(\frac{I_{\text{out}}}{I_{\text{in}}}\right), \quad (3.20)$$

where  $I_{\text{in}}$  and  $I_{\text{out}}$  are estimated from the intensity (in any unit, e.g. number of counts) detected at this pixel in the absence or in the presence of atoms, respectively. Differences may arise between the incoming beam of the two images, typically if the intensity or the position of the beam fluctuates. Position fluctuations caused by mechanical vibrations are limited by the floating optical table. Intensity fluctuations over the whole beam are corrected by comparing zones without atoms in both absorption images.

The scattering cross-section depends on the light intensity and the magnetic sub-level of the atoms as:

$$\sigma_s = \frac{\sigma_0}{1 + I/I_0^{\text{sat}}}, \quad (3.21)$$

where  $\sigma_0 = 3\lambda^2/2\pi$  and  $I_0^{\text{sat}} = \Gamma\hbar\omega/\sigma_0$ .  $\Gamma$  is the natural linewidth of the optical transition, which in the case of the D2-line of  $^{87}\text{Rb}$  is  $\Gamma = 2\pi \times 6.07 \text{ MHz}$ . A magnetic quantization axis is established using the small bias field, such that the  $\sigma^+$  polarized light pumps to the state of maximal cross-section. In general, using intensities higher than

$I_0^{\text{sat}} = 1.67 \text{ mW cm}^{-2}$  should be avoided, as the response of the atoms becomes non-linear (except for saturated absorption imaging where this feature is actually exploited, see sec. 3.4.3).

In practice, four images are taken. A first image of the atoms is taken with light switched on (giving  $I_{\text{out}}$ ) during the expansion of the cloud, at some time of interest between 1.5 ms and 25 ms. The time limits correspond to times when the densities are low enough and before the atoms fall out of the field of view. A second image with light on is taken once the atoms have left the field of view (giving  $I_{\text{in}}$ ). Another couple of images is taken later on without light, after read-out of the first two, in order to subtract dark counts and stray light contributions. The setup is described in sec. 3.1.5. Although this imaging system is generally used after some in-trap procedure, it can also be activated to image thermal clouds from earlier times in the sequence, e.g. during loading to the chip trap.

Absorption imaging is limited by two processes: the back-action of absorbed photons and the photon shot noise of the imaging light. The first limits the spatial resolution, while the second prevents the detection of single atoms, at least in this simple apparatus (absorption imaging of a single atom has otherwise been realized in [120]). In the limit of a dilute sample, the net signal is given by  $\gamma_{\text{at}} = \gamma_{\Delta t} \sigma_s n_{\text{int}}$ , where  $\gamma_{\Delta t}$  is the mean photon number arriving at the detector area  $A$  during the exposure time  $\Delta t$ . The noise, on the other hand, is in first approximation  $\sqrt{\gamma_{\Delta t}(1 - \sigma_s n_{\text{int}})} \approx \sqrt{\gamma_{\Delta t}}$ . The signal-to-noise ratio of absorption imaging is therefore:

$$\text{SNR}_{\text{abs}} = \frac{\gamma_{\text{at}}}{\sqrt{\gamma_{\Delta t}}} = \sqrt{\gamma_{\Delta t}} \sigma_s n_{\text{int}} = \sqrt{\frac{I_{\text{in}}}{\hbar\omega} \Delta t A} \sigma_s n_{\text{int}}. \quad (3.22)$$

One can increase the beam intensity or the exposure time to enhance the signal-to-noise ratio, but thereby loses in spatial resolution. For very dilute clouds, it is more interesting to switch to fluorescence imaging

### Fluorescence imaging

Fluorescence imaging is in principle simpler to implement than absorption imaging, as it does not even necessitate a special alignment of the optics with respect to the imaging beam, but it yields a weaker signal. Despite this fact, it is much better at detecting few atoms: because the detected signal is (ideally) only composed of fluorescence photons, the shot noise of the incoming beam does not degrade the signal-to-noise. It is enough to gather a few fluorescence photons emitted per atom on a high-sensitivity detector to count atoms [79].

The fluorescence imaging is set up to detect atoms after a long time-of-flight, for far-field imaging. This can give access to the in-trap momentum distribution of the quantum gas, which is an essential ingredient for the experiments of this thesis. The atoms are released from the trapping potential and take  $\sim 46 \text{ ms}$  to reach the counter-propagating light beams of the light sheet. Each atom takes some  $100 \mu\text{s}$  to pass through, depending on the exact position and thickness of the light sheet. An exposure time  $\geq 5 \text{ ms}$  suffices

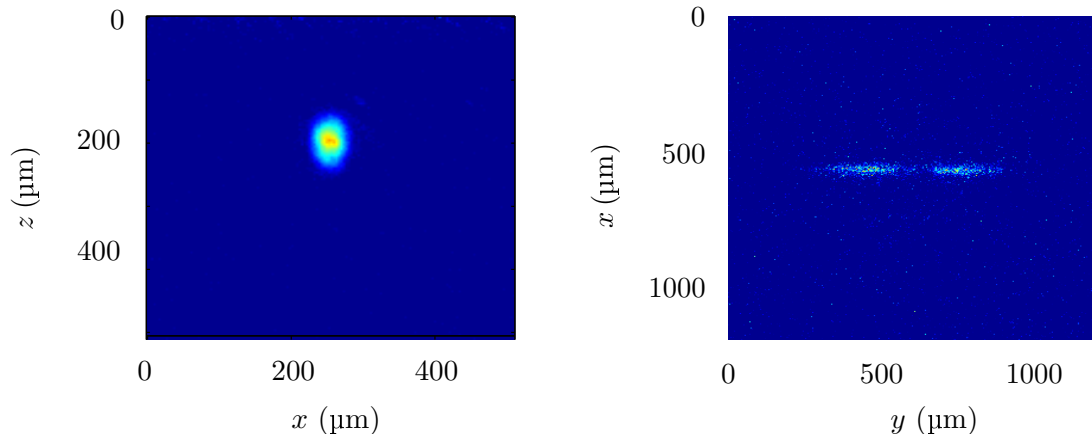


**Figure 3.12: Typical experimental images.** (Left) Absorption image of a BEC in the static trap with about 2500 atoms, after 6 ms time-of-flight. (Right) Light sheet image of a  $\sim 700$  atoms BEC, after excitation to the first excited state by displacement in the dressed trap and a 46 ms time-of-flight.

for the whole cloud to cross. Within the light sheet, each atom scatters up to 1000 photons, of which only a few ( $\sim 12$ ) reach the detector. The exact amount of scattering depends on the parameters of the light sheet, such as intensity and detuning. The light is red-detuned from the atomic transition by about half the atomic linewidth, which reduces the scattering rate of the atoms but increases the absorption probability of atoms moving towards one or the other light beam. This optical molasses effect, also used in the MOT, limits the heating of the atoms in the beams' direction which in turn improves the spatial resolution.

In the case of fluorescence imaging, only a small part of the photons emitted by the atoms is collected. This fraction depends on the solid angle coverage of the optics:  $f_c = \frac{\Omega}{4\pi} = \frac{NA^2}{4}$ ,  $\Omega$  denoting the solid angle covered. The signal-to-noise ratio depends on this factor as:

$$\text{SNR}_{\text{fluo}} = \sqrt{\frac{I_{\text{in}}}{\hbar\omega} \Delta t A} \sqrt{f_c \sigma_s n_{\text{int}}}. \quad (3.23)$$

Assuming similar imaging parameters for both absorption and fluorescence imaging,  $\text{SNR}_{\text{fluo}} = \sqrt{\frac{f_c}{\sigma_s n_{\text{int}}}} \text{SNR}_{\text{abs}}$ , proof that at low optical densities  $OD = \sigma_s n_{\text{int}} < f_c$  such as obtained after a long expansion time, fluorescence imaging becomes advantageous.

One difficulty arising with fluorescence imaging is the absence of a straightforward method to extract atom numbers, as there is for absorption imaging. It relies entirely on the knowledge of the fluorescence light field and characteristics of the imaging optics (see sec. 3.1.5). The noise behavior of the camera and the resolution have been thoroughly investigated by R. Bückler during his master thesis [79] and an optimal configuration has been defined. In the end, this characterization of the whole light sheet imaging system allows to determine the column density at each pixel, using only two pictures taken at each cycle and regular calibration scans. The reader is referred to [56, 79] for

detailed information, while here the basic steps are quickly sketched out. A reference image without imaging light, taken after the signal image, allows to calculate the gain of the camera at each pixel simply from technical noise (mainly clock-induced charges). This is done at each cycle as the gain may drift over time. The background light, homogeneous over the whole image, is estimated from the intensity in regions without atoms. Additionally, stripe structures appear on the images due to the back-illumination of the CCD, result of interferences between back and front surfaces of the sensor. This effect is corrected using a reference flat field image with a uniform coherent illumination. Once these elements are deducted, only the actual photon signal from the atoms is left. Knowing the number of photons emitted on average by each atom, the number of atoms is finally obtained. Extracting the number of photons per atom (ppa) is however not completely trivial and can be done in two ways. A simple but indirect method consists in taking images of the same cloud alternatively in absorption and in light sheet, and calibrate the light sheet signal with the absorption as reference. An alternative, more direct way is to extract the ppa from correlation function. Both methods are discussed in the following section.

### 3.4 Atom number calibration using the Light Sheet

Extracting the number of atoms from either absorption or fluorescence pictures relies on a number of assumptions. Although absorption seems to immediately yield the desired quantity, a number of technical difficulties get in the way of this simple idea, as will be discussed in sec. 3.4.3. Therefore, using the light sheet pictures directly to get an absolute atom number calibration, without resorting to another imaging system with its own set of flaws, is enticing. This direct approach, initially proposed in [88] and presented in sec. 3.4.1, consists in computing the correlation functions of fluorescence pictures to extract information about the photon statistics and identify the contribution from individual atoms. The photon-per-atom number (ppa) is derived from these contribution, as shown in sec. 3.4.2. This is compared to the indirect method for ppa calibration via absorption imaging in sec. 3.4.3.

#### 3.4.1 Two-photon correlation functions

After treatment, the experimental light sheet images yield a corrected signal,  $S$ , representing the number of photons emitted by the atoms and collected by the optics. Signal and number of atoms are related by the simple formula  $S = pN$ , from which the atom number  $N$  can be determined. But for this, the number of photons  $p$  detected per atom (ppa) must be calibrated. For a dilute cloud, one can consider the approach of looking for clusters of photons on the images, as photons emitted from the same atom will land in the same region. Atoms will indeed have an “image” of rms radius  $r_a$ . However, it is difficult to separate these clusters as they overlap and are not regular. By measuring coincidences between photons, or more precisely single-atom autocorrelation functions, one can determine  $p$ , and hence  $N$ , from light sheet pictures only.

Correlation functions are well-known in the field of optics, where they are used to investigate the coherence and the quantum correlations properties of photons. Classical optics experiments are limited to recording light/photon flux intensities, often with a single detector. Slightly more advanced measurements with two detectors give access to (delayed) coincidences between photons, e.g. in HBT experiments [121, 122]. The photon detection rate and coincidence rate was generalized to coincidences between any number of photons by R. J. Glauber [123]. This new definition surpasses the definition of coherence in the interference sense, the only one used until then, and considers higher order regularities.

This analysis in terms of correlation functions, originally proposed for electromagnetic fields, can be extended to matter waves. In that case, the  $n$ -th order correlation function, expressed as a function of the quantum field  $\hat{\Psi}(x)$ , is:

$$G^{(n)}(x_1, x_2, \dots, x_{2n}) = \langle \hat{\Psi}^\dagger(x_1) \dots \hat{\Psi}^\dagger(x_n) \hat{\Psi}(x_{n+1}) \dots \hat{\Psi}(x_{2n}) \rangle. \quad (3.24)$$

It is an important tool in the study of ultracold atoms. The first order correlation function for example,  $G^{(1)}(x_1, x_2) = \langle \hat{\Psi}^\dagger(x_1) \hat{\Psi}(x_2) \rangle$ , yields information on the spatial coherence of the system. In the special case  $x = x_1 = x_2$ , it becomes the single-particle density matrix  $\rho^{(1)}(x) = \langle \hat{\Psi}^\dagger(x) \hat{\Psi}(x) \rangle$ . When normalizing this function to the density, one obtains the commonly plotted function

$$g^{(1)}(x_1, x_2) = \frac{G^{(1)}(x_1, x_2)}{\sqrt{G^{(1)}(x_1, x_1)} \sqrt{G^{(1)}(x_2, x_2)}} = \frac{G^{(1)}(x_1, x_2)}{\sqrt{n(x_1)n(x_2)}}, \quad (3.25)$$

which takes values between 0 and 1 and informs on the coherence range of the system. The second-order correlation function  $G^{(2)}(x_1, x_2) = \langle \hat{\Psi}^\dagger(x_1) \hat{\Psi}^\dagger(x_2) \hat{\Psi}(x_1) \hat{\Psi}(x_2) \rangle$  gives information about density correlations, and can be used for example to characterize spatial bunching or anti-bunching effects of the atoms.

The quantity of interest here is the two-photon correlation function:

$$G^{(2)}(\delta x, \delta y) = \sum_{x,y} \langle \hat{S}(x + \delta x, y + \delta y) \hat{S}(x, y) \rangle / N_{\text{pix}}, \quad (3.26)$$

where  $\hat{S}(x, y)$  denotes the background-corrected signal at position  $(x, y)$ . This function shows the probability to have two photons distant by  $(\delta x, \delta y)$  on an area made of  $N_{\text{pix}}$  pixels. If correlations exist in the photon distribution, they appear in the two-photon correlation function as structures of size specified by the correlation distance of the photons. For a broad thermal cloud, as shown in fig 3.13, a decomposition of the  $\hat{G}^{(2)}(\delta x, \delta y)$  function into three contributions of different characteristic correlation lengths can be made (see also [79]):

- a Kronecker-like contribution at the center of the correlation image,  $P \cdot \delta(\delta x, \delta y)$ , occupying a single pixel. This corresponds to a signal showing no correlation between pixels, which is white noise (e.g. detection noise, photon shot noise). The amplitude  $P$  of the peak equals the variance of the total detection noise;

- a peak structure a few pixels wide proportional to the atom number,  $N \cdot A(\delta x, \delta y)$ , where  $A$  is some function with the imaged size of an atoms:  $A(\delta x, \delta y) \approx 0$  for  $\sqrt{\delta x^2 + \delta y^2} > r_a$ . This signal is due to pairs of photons impinging on two different pixels but coming from the same atom. They belong to the same cluster of averaged rms size  $r_a$  and correspond the atom's autocorrelation;
- a broad Gaussian base extending over a large range of the image. This contribution arises from correlations between two photons emitted by different atoms, it coincides with the extend of the thermal cloud scaled by a  $\sqrt{2}$  factor.

The thermal cloud needs to be hot enough to avoid a contribution of the Hanbury Brown and Twiss bunching [117].

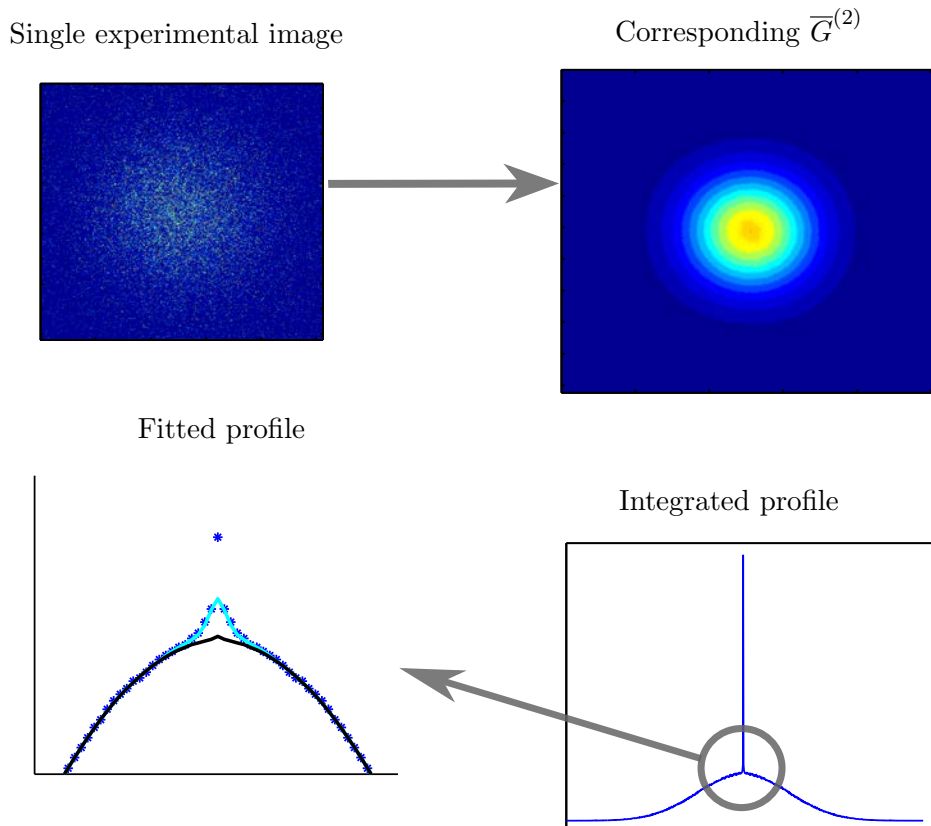


**Figure 3.13: Correlation analysis of a thermal cloud.** For each experimental image a correlation function  $\hat{G}^{(2)}(\delta x, \delta y)$  is computed, which are then averaged to give  $\overline{G}^{(2)}$ . As can be seen on the integrated profile, the dominating features are the Gaussian background and the central Dirac distribution. A zoom on the top of the Gaussian profile shows the atomic shot noise peak. The Gaussian background is fitted by the  $\hat{G}^{(2)}$  function of the averaged image  $C^{(2)}$  (black line), while the atomic shot noise can be approximated by a Voigt function (cyan line).

Assuming a homogeneous illumination, all atoms contribute equally in the second

term, hence the linear dependence on atom number. The number of coincidences per atom is  $\sum_{\delta x, \delta y} A(\delta x, \delta y) = \langle \hat{p}(\hat{p} - 1) \rangle \approx p^2$ , thus yielding directly the averaged photon-per-atom number we are looking for. An averaged number of atoms can be estimated from the same set of images using the relation  $N_{av} = S_{av}/p = S_{av}/\sqrt{\sum_{\delta x, \delta y} A(\delta x, \delta y)} = S_{av}^2/(\sum_{\delta x, \delta y} N \cdot A(\delta x, \delta y))$ . How these numbers are deduced from experimental images is explained next.

### 3.4.2 Photon-per-atom and atom number determination

The useful quantities are the total signal  $S$  and the atom shot noise contribution  $N \cdot A(\delta x, \delta y)$ . From those, one simply gets the photon-per-atom number as  $p = N \cdot A(\delta x, \delta y)/S$ . The natural condition for this contribution to be distinguishable from the white noise is that the pixel size in object space be smaller than the size of the imaged single atom  $r_a$ .  $S$  is computed from a 2d Gaussian fit of the averaged picture, excluding the baseline. The atom shot noise contribution to the correlation function  $N \cdot A(\delta x, \delta y)$  is also estimated by a fit. It requires taking multiple images of a thermal cloud, then treating them in a series of steps:

1. Compute the  $\hat{G}^{(2)}$  functions of all individual experimental images, then average them to obtain  $\overline{G^{(2)}}$ .
2. Compute the  $\hat{G}^{(2)}$  function of the averaged image, to obtain the normalization function  $C^{(2)} = \sum_{x,y} \langle \hat{S}(x + \delta x, y + \delta y) \rangle \langle \hat{S}(x, y) \rangle / N_{\text{pix}}$ . Due to the averaging over many pictures, the photon distribution homogenizes and the clusters disappear. This function is very similar to  $\overline{G^{(2)}}$  but the atomic shot noise is washed out.
3. Subtract from  $\overline{G^{(2)}}$  the function  $C^{(2)}$ , to be left with the central structures only.
4. Fit the atomic shot noise peak with an adequate function, excluding the central pixel with the Dirac. A 2d Voigt profile faithfully reproduces the observed peak. The atomic shot noise is then simply given by the amplitude of the function.

### 3.4.3 Comparison to indirect photon-per-atom measurement

As previously mentioned, the number of photons per atom can be measured indirectly by taking the ratio of the signal measured on the light sheet,  $S$ , to the number of atoms measured in absorption,  $N_{abs}$ . The method is simple but depends greatly on how well the atom number is measured in absorption.

For a number of reasons, an absolute calibration with absorption imaging is more complicated in practice than it is in theory. The main hurdle is that the experimental cross-section is reduced compared to the ideal cross-section. This comes from a combination of different effects: imperfect polarization of the imaging beam, imperfect alignment with the quantization axis and transient populations of different states during optical pumping. These effects can be accounted for by introducing a scaling factor that replaces the ideal

scattering cross-section and saturation intensity by effective values:

$$I_0^{\text{sat}} \rightarrow I_1^{\text{sat}} = \alpha I_0^{\text{sat}} \quad (3.27)$$

$$\sigma_0 \rightarrow \sigma_1 = \sigma_0/\alpha. \quad (3.28)$$

To determine the factor  $\alpha$ , one approach developed in [124] is saturation absorption imaging. The method consist in comparing the measured optical densities of the same atomic sample for a broad range of imaging light intensities, typically more than one order of magnitude below and above saturation. It considers the optical depth:

$$\text{od}(x, z) = \sigma_0 \int n(x, y, z) dy = -\alpha \ln \left( \frac{I_{\text{out}}(x, z)}{I_{\text{in}}(x, z)} \right) + \frac{I_{\text{in}}(x, z) - I_{\text{out}}(x, z)}{I_0^{\text{sat}}}, \quad (3.29)$$

which reduces to the expression of the optical density  $OD$  for low intensities, when the first term is dominant. For high intensities the second term, usually not included, dominates. In that limit, the optical depth depends both on the incident imaging field  $I_{\text{in}}$  and on the parameter  $\alpha$ , which allows to calibrate them experimentally.

The difficulty resides in the calibration of the camera necessary to this scheme. The details of this procedure will be later explained in [125]. Here, we will only note that a calibration of the intensity received by each pixel as a function of the detected counts is complicated by the inhomogeneity of light profile on the camera. However, a good agreement has been found between values of  $\alpha$  estimated by approximating the intensity at every pixel by its average value, or by making 2d Gaussian fits of the clouds.

Some preliminary results of this calibration have already been presented in [21]. The latest results show that the factor  $\alpha$  lies around 1.2 for our experimental implementation. Once this correction factor is introduced on  $N_{\text{abs}}$ , the results of the analysis on the light sheet pictures corroborates rather well the value of the atom number found by indirect measurement, as shown in fig 3.14.

In conclusion, we have presented in this chapter the important technical features relevant to the experiments carried out in this thesis. In a nutshell, the specificity of the experimental apparatus are:

- an atom chip, which allows for the creation of tight magnetic traps with transverse frequencies in the kHz range,
- the use of rf-dressing to vary the geometry of the transverse confinement from a harmonic single well to an anharmonic or a double well,
- a time-of-flight fluorescence imaging system, the light sheet, which allows to probe features of the BEC with single-atom sensitivity, with a particular emphasis on the horizontal transverse direction, which extends considerably in time-of-flight.

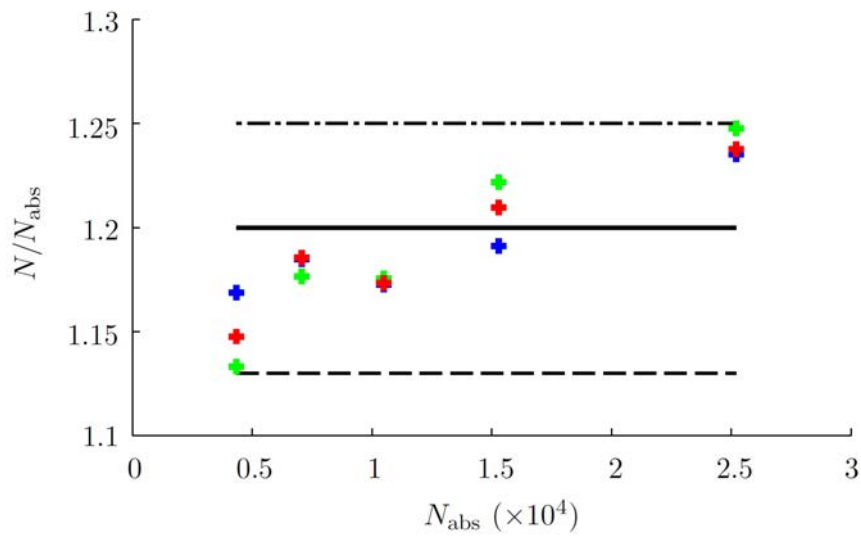


**Figure 3.14: Comparison between the atom number found from light sheet pictures and from absorption pictures.** The number of atoms is estimated for different atom numbers and different intensities of the light sheet (blue, green and red crosses).  $N_{\text{abs}}$  corresponds to the number of atoms measured with normal non-saturated absorption imaging. The atom number corrected by a factor  $\alpha = 1.2$  (black continuous line) is in reasonable agreement with the light sheet data. Limits on these data correspond to  $\alpha = 1.13$  (black dashed line) and  $\alpha = 1.25$  (black dash-dotted line)

# 4

## Coherent state manipulation using Optimal Control

In this chapter, we present the central elements of this thesis:

- the conception and implementation of pulses for the manipulation of non-classical motional states, which modify the transverse wavefunction of the condensate and create new motional states and superpositions thereof;
- the key role of optimal control in the optimization of such transfer pulses, such that target superposition states are reached with very high speed and accuracy.

The specificities of our system relevant for these manipulations, the role of interactions in particular, are highlighted in sec. 4.3. The optimization of transfer pulses is explained in sec. 4.4 and the result of this optimization for a state-to-state transfer in sec. 4.5. The different steps for the experimental implementation of an optimized pulse are presented in sec. 4.6. Finally, the analysis of the experimental results is detailed in sec. 4.7. The results of this chapter are partly published in ref. [116] and in ref. [126].

### 4.1 Interest for the manipulation of complex systems

Exploring the physics of complex systems is fundamental to the quest of understanding the “real” world. In the last decades, in order to observe the counter-intuitive phenomena predicted by quantum mechanics, physicists have been artificially isolating particles and observing their individual properties (e.g. single-particle interference, transitions between quantized energy levels), or at most the properties of a small number of them (e.g. entanglement). However, most realistic systems consist of many particles that - exception made for the photon - can interact among themselves and with their environment. This property makes their behavior more complex, but also allows physicists to manipulate and store them with promising perspectives, e.g. for building quantum memories. Therefore, going beyond the simple single-particle representations is an important step forward in

our understanding of the world and for technological applications. The complexification can be multiform, with many new effects coming in such as interactions, dephasing or decoherence.

On the other hand, gaining scientific knowledge about nature means observing and interpreting it in terms of theoretical models. As the situation complexifies, so do the models. It is therefore crucial to be able to test models in well-understood, engineered situations. In this sense, creating and controlling semi-complex physical systems is a good way to test the validity of the models. Furthermore, good control schemes can create new configurations and enable the study of various, sometimes novel, phenomena. Thus they are unique tools to understand them, and in turn to take advantage of these new effects for useful applications (e.g. for measurements) or to limit their impact.

In this chapter, we present to control quantum states of an interacting Bose-Einstein condensate consisting of hundreds of atoms. Instead of the more common transitions between internal states, we demonstrate here coherent manipulations of motional states, which are external degrees of freedom. Moreover, the system is complex due to the presence of atomic interactions, whose effects invalidates the simple single-particle description. In that view, we present an approach based on optimal control theory and mean-field description, that allows precise control despite the presence of beyond-mean-field effects.

## 4.2 Control over transverse motional states

Our goal is to manipulate the transverse wavefunction of a quasi-BEC with high accuracy, splitting and recombining it, creating in this way coherent superpositions of different motional states - or equivalently, of vibrational levels of the trapping potential. The system is, as described in chap. 2, an effective 1d quasi-condensate in a dressed trap. In this potential, the quasi-BEC is initially in its transverse ground state. To realize a transfer, the approach adopted here consists in displacing the minimum of the trap along the horizontal transverse direction ( $y$ -direction). By definition, the ground state and the first excited state are orthogonal in a harmonic potential. A displacement in these conditions would only trigger a center-of-mass oscillation, that is a classical motion. For the transfer to be effective, the trapping potential is made slightly anharmonic. This way, during the displacement, the wavefunction experiences a force that effectively establishes a coupling between its (classical) center-of-mass movement and its (non-classical) intrinsic motion. The effect is that not only the wavefunction is displaced but also that higher intrinsic or motional states become accessible. Moreover, the anharmonicity lifts the degeneracy between the level splitting energies. The displacement can then induce transitions to specific energy levels, on condition that an appropriate displacement is executed. Contrary to the harmonic situation where only a classical oscillation is triggered, the final state reached with this controlled displacement scheme is a non-classical one. Furthermore, the wavefunction conserves its coherence during the displacement. This manipulation is illustrated in fig. 4.1.

In principle, a sinusoidal displacement at the frequency corresponding to the first level splitting of the trap would drive transitions between the ground and first excited

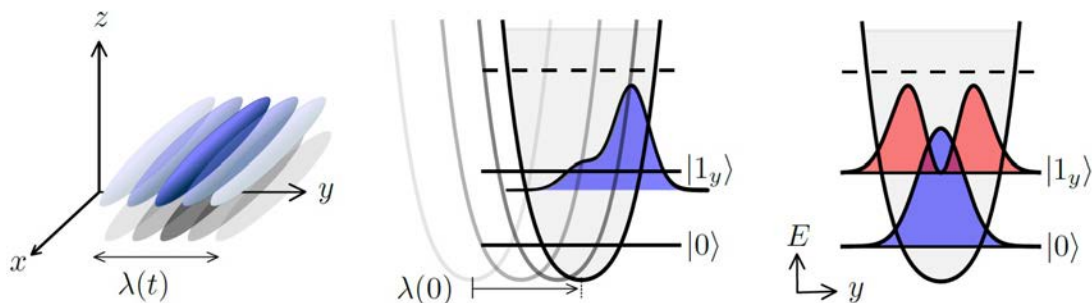


**Figure 4.1: Schematic of the coherent manipulation sequence.** (Left) Representation of the BEC subjected to a fast displacement  $\lambda(t)$  in the  $y$ -direction. (Middle) Displacement of the trapping potential under the influence of a control pulse. The anharmonicity in the  $y$ -direction leads to changes in the intrinsic motion of the wavefunction. The solid lines represent the transverse ground state  $|0\rangle$  and the lowest-lying excited state  $|1_y\rangle$ . The other states (dashed line) have higher energies. (Right) Final and target state of the controlled displacement: a coherent superposition of the transverse ground state wavefunction (blue) and lowest-lying excited state wavefunction (red).

motional states of the condensate. We will see in sec. 4.3 that this simple approach is insufficient in our case, but that more advanced techniques like optimal control can be easily and profitably implemented.

### 4.3 Specific constraints of our system

In the control of quantum states, a key factor is the precision with which the desired state is reached. In order to reach a good precision, a number of effects present in our physical system, which are generally overlooked or not relevant in other applications, must be considered.

#### 4.3.1 Mean-field effects

The physical system at hand, described in detail in chap. 2, is a 1d quasi-condensate of  $^{87}\text{Rb}$ , an isolated system of many bosons exhibiting repulsive interactions between atoms. Although it is in essence a many-body system, it is well described by a Gross-Pitaevskii equation given in chap. 2 in first approximation. This representation is already a level of complexity above the Schrödinger equation, with an additional interaction term. This non-linearity must be considered for accurately controlling the system.

In the transverse directions, the trap confinement is strong enough that the energy of interactions ( $\mu \sim 0.5\text{kHz}$ ) is small compared to the kinetic energy ( $\mu \sim 2\text{kHz}$ ). Nevertheless, the effect of interactions cannot be overlooked, because they modify the effective level splitting experienced by the atoms. If atoms are added to one state, the global interaction energy naturally changes, but also the transfer of atoms between

states lead to a change in the interaction energy. The interaction energy depends on the distribution of atoms in different motional states, as wavefunctions corresponding to different motional states have different spatial extensions. In the case of a dynamics, continuous transfer between the ground state and the first excited state, the effective energy gap between both states is slowly shifted.

This can be understood in a mean-field picture by considering the energy felt by a particle in the first excited state. The energy difference experienced by the system when a particle is transferred from the ground state to the first excited state can be simply derived from the total energy of an atom in the first excited state, and written as:

$$\Delta E(N_1) = E_1 - E_0 + \left[ N_1 g_1^y - (N - N_1 - 1) g_0^y + 2(N - 2N_1 - 1) g_{01}^y \right] \quad (4.1)$$

where  $N$  is the total number of atoms,  $N_1$  the number of atoms in the first excited state,  $E_0$  and  $E_1$  the single-particle energies of ground and first excited states.  $g_0^y$  ( $\sim 0.4 \text{ Hz } \mu\text{m}$ ) is the effective 1d interaction constant in the  $y$ -direction for the condensate in the ground state,  $g_1^y \simeq \frac{3}{4} g_0^y$  is the effective 1d interaction constant in the  $y$ -direction for the condensate in the first excited state and  $g_{01}^y \simeq \frac{1}{2} g_0^y$  the cross-interaction constant between the two. The factor 2 in front of the term  $g_{01}^y$  comes from exchange symmetry [127, 128].

From this equation, it appears that the energy needed to transfer the first atom from ground state to first excited state corresponds to the single-particle level splitting:  $\Delta E(1) = E_1 - E_0$ . For this first atom, the repulsion from the ground state wavefunction is the same before and after transfer, which due to the particular ratio between different effective 1d interaction constants in the harmonic potential. As our potential is close to harmonic, the system exhibits an effective level splitting corresponding to the trap level splitting or the single-particle energy difference  $E_{01}^{\text{s.P.}} \simeq E_1 - E_0$ . As atoms get transferred from the ground state to the first excited state, the global energy increases, but the effect of repulsion and thus the interaction energy decreases due to the increased spatial extension of the wavefunction. Transferring the last atom to the first excited state requires less energy:  $\Delta E(N - 1) = E_1 - E_0 - \frac{1}{4}(N - 1)g_0^y$ . The effect of interactions between particles is illustrated in fig. 4.2(a). Next to these schematics, fig. 4.2(b) gives a quantitative account of how much the effective level splitting between the ground state  $|0\rangle$  and the lowest-lying excited state  $|1_y\rangle$ ,  $E_{01}^{\text{eff}}$ , changes as 700 atoms are transferred from ground to first excited state. The system then starts in the ground state with an effective level splitting  $E_{\text{start}} \simeq E_{01}^{\text{s.P.}} = \hbar \cdot 1.76 \text{ kHz}$  and gets transferred to the first excited state where it experiences a final effective level splitting  $E_{\text{end}} \approx \hbar \cdot 1.66 \text{ kHz}$ . This change in frequency can also be observed in GPE simulations and in experimental data, as will be shown in sec. 4.5.

As a consequence, it can already be foreseen that, for driving transitions, the changes in interaction energy will have to be considered for high precision transfers.

### Shortcomings of the sinusoidal drive

In the case of a non-interacting system, the level splitting is given solely by the potential. Driving the system at or close to the level splitting frequency allows to transfer

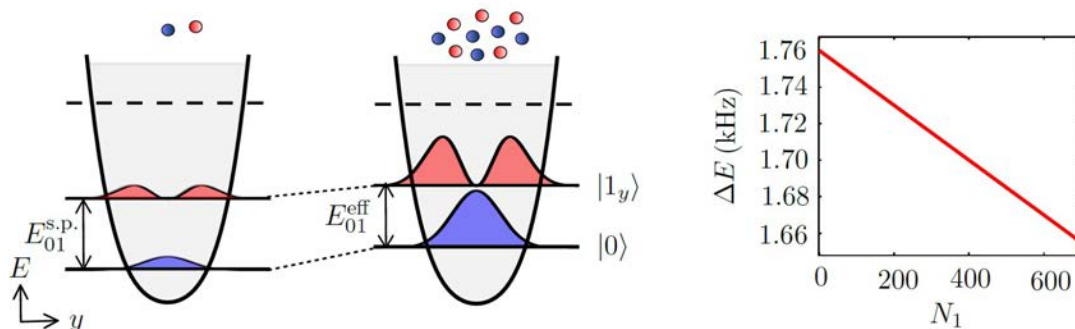


**Figure 4.2: Effect of the mean-field on the level splitting.** (Left) Schematics of the effective energy difference between the levels for single particles and for interacting wavefunctions of many atoms.

(Right) Shift of effective energy difference as atoms get transferred from ground state to first excited state, for the characteristic trap and atom number ( $N = 700$ ) in this thesis.

atoms between levels. This is often referred to as a Rabi driving [129]. Here, this would correspond to driving the system between ground and first excited state using a sinusoidal displacement of the potential, i.e. a single-frequency transfer pulse. However, due to interactions, the level splitting is not fixed, therefore a single-frequency pulse cannot be in resonance with the two-level transition during the entire transfer time. This effect gets more dramatic as the number of atoms increases. For our typical atom number  $N = 700$ , as seen in fig. 4.2(b), the effective level splitting changes by 100 Hz when transferring all atoms from the ground state  $|0\rangle$  to the first excited state  $|1_y\rangle$ .

Driving this transition with a sinusoidal displacement is complicated not only by the presence of interactions, but also by the presence of higher levels, whose energy splitting is higher than, but not very far from,  $E_{01}^{\text{s.p.}}$ . Simulations carried out with a one-dimensional GP solver show that, for a non-interacting system driven at resonance, the amplitude of the sinusoidal drive must be kept under  $\sim 0.01 \mu\text{m}$  to avoid populating higher states. In this condition, a complete transfer ( $> 99\%$ ) can be reached in  $\sim 20$  ms. For 700 interacting  $^{87}\text{Rb}$  atoms, the minimum driving duration required to obtain a complete transfer is  $T_{\text{pulse}} \simeq 9 \text{ ms}^1$ . We attribute this faster transfer, as compared to the non-interacting case, to the interplay between the transfer process and the interaction-induced exchanges between states (see sec. 4.3.2). A chirped sinusoidal pulse, a sine with a frequency optimized to adapt to the time-dependent effective level splitting, can reach 92% in 1.1 ms, which is better than the simple sine drive but not as good as a fully optimized pulse, as presented in sec. 4.2.

As already pointed out, a full population transfer is the case where the largest variation of mean-field energy is experienced. Superpositions for which less atoms are transferred to the first excited state can actually be realized with a sinusoidal drive on shorter times. In that case, good transfer efficiencies are obtained. For example, an equal superposition

1. Single-frequency drive of frequency  $\nu_{\text{drive}} = 1.70 \text{ kHz}$  and amplitude  $d_{\text{drive}} = 0.034 \mu\text{m}$ .

of  $|0\rangle$  to  $|1_y\rangle$  can be reached in a time  $T_{\text{pulse}} \sim 2.5$  ms in the GP simulations.

Experimentally, attempts to reach a complete transfer or a half transfer with a sinusoidal drive were fruitless. A short driving pulse lead to a state close to an equal superposition of ground and first excited states, but unstable. The complete transfer could not be achieved at all. Our general aim is to have a generic method to create any superposition in a short time, and therefore we turn to a more sophisticated approach. The reason for this constraint of time limit is clarified in the sec. 4.3.3.

### 4.3.2 Beyond two-level model

The problem considered is essentially a transfer between two motional states, or vibrational levels of a potential, the ground and the first excited state. However, a first naive representation in terms of transitions within a two-level system rapidly shows limitations.

On the one hand, interactions can lead to transitions to higher levels. Although the level spacing of the transverse potential is non-degenerate, the difference in level splitting  $E_{12} - E_{01}$  is only  $\sim 0.6$  kHz, which is already on the order of the interaction energy for  $N = 700$  atoms. Therefore, two atoms in the first excited state can exchange energy to become one atom in the ground state plus one atom in the second excited state. We will come back to this aspect in sec. 4.6.

On the other hand, the system does not necessarily remains in a superposition of ground and first excited state during the transfer process. In fact, a complex transfer pulse such as shown in sec. 4.5, is composed of many frequencies which drive transitions to a number of higher levels. The initial and final states can be described in terms of a two-level system, but the transient states definitely leave this space.

In the remaining part of this thesis, a description in terms of a two-level system will be sometimes used, for example in chap. 5. Although it is helpful to grasp some of the concepts, one must remain aware of the restrictions imposed on these descriptions.

### 4.3.3 Beyond-mean-field effects

In a previous work [130], we already performed a complete transfer of a BEC from the transverse ground state to the first excited state of the trap in 5 ms and studied both theoretically and experimentally the behavior of the atomic cloud in the excited state. We clearly observed loss processes in the form of twin-atom beams production, which start forming after 2 to 3 ms after the start of the transfer process [115]. These atoms originate from collisions in the first excited state and are emitted in pairs as they are transferred back into the transverse ground state with a gained momentum in the longitudinal direction (see fig. 4.3).

This effect goes beyond the scope of the Gross-Pitaevskii equation, showing that the mean-field approximation, although powerful, is unable to fully describe the behavior of the system in this case. In the scope of this work, these processes are unwanted effects. Therefore, the goal is to design a transfer pulse that can reach any superposition state in a time  $< 2$  ms with high fidelity. This requirement is all the more stringent

if one wishes to concatenate different transfer pulses, as will be the case in chap. 5. Another motivation to look for shorter transfer pulses, partly considered in chap. 6, is to separate the timescales of excitation dynamics and decay processes, thereby simplifying the analysis of the decoherence mechanisms.

Other effects that arise at different timescales are dephasing effects coming from the extension of the condensate in the longitudinal direction, two-body diffusion coming from shot-to-shot fluctuations or many-body effects. These mechanisms are investigated in chap. 6.

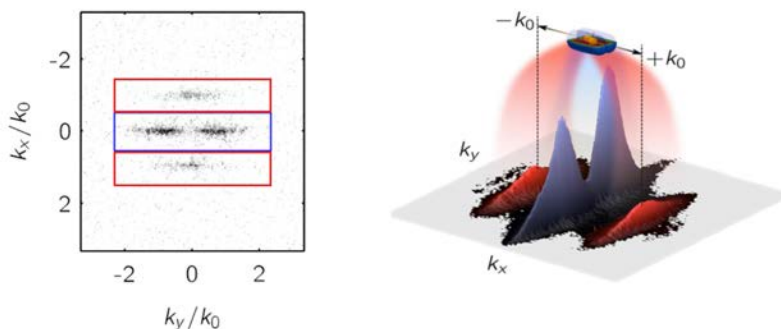


**Figure 4.3: Decay of the first excited state into pairs of opposite momentum.**

(Left) Experimental fluorescence picture showing the atomic density in the horizontal plane after time-of-flight. In the center (blue box) is the double-peak profile characteristic for the first excited state. On the sides (red boxes) are the two beams of opposite momentum atom pairs.  $k_0$  is the absolute value of the momentum of each atom pair.

(Right) Schematic of the collision processes giving rise to opposite momentum pairs in the longitudinal direction. *Adapted from* [115].

#### 4.3.4 Technical limitations

For every realistic experiment, some technical constraints have to be considered. The first constraint concerns the amplitude of the transfer pulse. During the transfer pulse, the wavefunction explores the potential and experiences the effect of the anharmonicity. From measurements of the trap frequencies, we can get a good approximation of the trapping potential around its center (for details of the method, see sec. 4.6). We allow for a displacement of the potential up to about  $1 \mu\text{m}$  away from its initial position. In the region explored by the wavefunction, the potential is then well approximated by a sixth-order polynomial. Outside of this region, the approximation fails.

The second experimental constraint is the limited bandwidth of electronics. The new DP400 setup installed to implement displacement pulses offers a bandwidth of 100 kHz, which is much higher than the level splitting of the potential. Nevertheless, any attempt at a pulse design should take into account this limit on the maximum allowed frequency, e.g. to avoid “kinks” in the displacement pulse.

## 4.4 Solution brought by optimal control theory

To achieve high performance in the coherent transfer process, we can employ numerical optimization methods. One of the most powerful approaches, particularly versatile and therefore applied in many fields of engineering and science, is optimal control theory (OCT). Optimal control has a long history, which can be traced back to the beginnings of the classical calculus of variations [131]. A common application of OCT is the calculation of trajectories for satellites and space rockets. In the field of quantum mechanics, OCT was first applied in the 1980's, where it was used to design laser pulses for the control of chemical reactions [132, 133]. Since then, optimal control has raised interest in many fields of quantum mechanics, including cavity quantum electro-dynamics [134], atomic spins [135], trapped ions [136, 137] and Bose-Einstein condensates [138, 139]. In general, optimal control techniques have been successfully applied to steer the dynamics of (effective) few-body systems and of non-linear systems [130, 140]. Moreover, they are also well on the way to control generic many-body systems [141]. This makes optimal control an ideal candidate to design fast transfer pulses with high efficiency for our complex system.

### 4.4.1 Concepts of optimal control applied to our experiment

The task of control theory is to identify the best trajectory to bring a system from an initial state to a final state with minimal expenditure of resources. For this, one has to find a control law for which the corresponding trajectory, under some constraints, reaches a certain optimality criterion. The optimality criterion is written as a cost functional, which is a function of the states and the control parameter.

In our case, the optimality criterion expresses how close we get to a specified target state. We have a well-defined initial state which is the transverse ground state of a 1d quasi-condensate. We choose as target some specific superposition of ground and first excited transverse states. The control parameter is the position of the trap in the horizontal transverse direction ( $y$ -direction). With all this, the task of the optimization is to bring the system from its initial state to its target state by varying the trap position. Constraints on the control pulse are its duration, its initial and final values, its maximum amplitude and frequency component.

For the optimization of transfer pulses, we describe the system as a condensate wavefunction using an effective one-dimensional GPE along the  $y$ -axis, with the Hamiltonian:

$$\hat{H}_{\text{GP}}[\psi, t] = -\frac{\hbar^2}{2m} \frac{\partial^2}{\partial y^2} + V(y - \lambda(t)) + g_y N |\psi(y, t)|^2 \quad (4.2)$$

where  $g_y(N)$  the effective one-dimensional interaction constant in the  $y$ -direction [142]. The minimum of the potential  $V$  can be spatially displaced along  $y$  by a distance  $\lambda(t)$  (as represented in fig. 4.1(b)). Under this action, the wavefunction undergoes a transformation computed by split-step analysis methods [143]. The wavefunctions of the different motional states are the stationary solutions of the GPE in the potential at rest and are obtained numerically by imaginary time propagation [144].

As already mentioned in sec. 4.3.3, beyond-mean-field effects are not taken into account in those simulations. The system can exhibit many-body behavior such as collisional decay processes and it has a finite temperature, phenomena that are not included in the GPE [115, 145]. For this reason, we expect the dynamics to deviate from the model's predictions at long times. Nevertheless, at very low temperatures and for short times, we expect the GPE to be valid and indeed observe a very good agreement (see experimental results in sec. 4.7).

To quantify the transfer efficiency, depending on which quantity is the more convenient, we use either the overlap fidelity  $\mathcal{F}$  or the infidelity  $\mathcal{J}$ , which are defined as:

$$\mathcal{J} = 1 - \mathcal{F} = 1 - |\langle \psi_{\text{target}} | \psi_y(T_{\text{pulse}}) \rangle|^2, \quad (4.3)$$

where  $\psi_{\text{target}}$  is the goal state of the optimization, constructed from the stationary GPE solutions of the final potential, and  $\psi_y(T_{\text{pulse}})$  is the actual wavefunction obtained at the final time of the pulse,  $T_{\text{pulse}}$ . The optimization process must therefore maximize the overlap fidelity, that is, look for  $\lambda(t)$  such that  $\mathcal{J}$  reaches a satisfactorily small value for the shortest possible time  $T$  within experimental constraints.

Another interesting concept in the context of optimal control is the notion of a quantum speed limit (QSL). It has been suggested that the limit on the speed for any evolution to an orthogonal state is set by a universal scaling law of the form [146, 147]:

$$T_{\text{QSL}} \equiv \max \left( \frac{\pi \hbar}{2E}, \frac{\pi \hbar}{2\Delta E} \right), \quad (4.4)$$

where  $E = \langle \Psi | H | \Psi \rangle$  is the initial energy ( $\Psi$  the initial state) and  $\Delta E = \sqrt{\langle \Psi | (H - E)^2 | \Psi \rangle}$  is the energy variance. Such a limit can be estimated analytically only for time-independent Hamiltonians and only in a few simple cases (e.g the Landau-Zener model [148]). The problem is indeed complicated for time-dependent Hamiltonians, as the energy or its fluctuations need to be computed over all possible paths in the space of control pulses that realize the transformation. However, for cases where the target state is the ground state of the final Hamiltonian, there is strong numerical evidence that the QSL is given by the formula:

$$T_{\text{QSL}} \simeq \frac{\hbar}{\Delta E_0} \arccos |\langle \Psi_{\text{final}} | \Psi_{\text{initial}} \rangle|, \quad (4.5)$$

$\Delta E_0$  being the energy gap between the two quantum states. For more general target states, it is not clear whether such a limit is correct. In addition, the above formula is only valid for linear Hamiltonian. Nevertheless, we can consider it as a first rough guess of the shortest times we can reach. In that case, the quantum speed limit in our system would be given by the level spacing between  $|0\rangle$  and  $|1_y\rangle$ :  $T_{\text{QSL}} \approx \nu_y^{-1} \simeq 0.5$  ms, that is, a period of the classical dipole oscillation in the potential. This is considerably faster than the transfer duration obtained by a single-frequency sinusoidal drive considered in sec. 4.3.1.

### 4.4.2 Application of the CRAB algorithm

We use the recently developed Chopped RANdom Basis algorithm (CRAB) [149] to find a fast and efficient coherent transfer pulse. The optimization has been carried out in collaboration with Antonio Negretti.

The main idea of the algorithm is to expand the control pulse onto a (non necessarily orthogonal) basis, in the present case as a sum of Fourier components. This allows to truncate, and therefore to reduce, the available space for the control pulses. Importantly, the expansion coefficients are time-independent and are treated in the algorithm as independent variables. This recasts the optimization problem, that is, the search of an extremum of some cost functional, into a minimization of a function depending only on a limited number of time-independent variables (i.e. the frequency components in our case, with both phase and amplitudes). The latter can then be performed with a direct search method (e.g. the Neelder-Mead minimization [150]). An important aspect of the CRAB approach is the breaking of the orthogonality condition of the chosen basis functions, which enlarges the subspace of functions explored by the algorithm. The CRAB strategy enhances the convergence of the algorithm and reduces the operation time compared to harmonic driving while keeping high fidelity. Thus, it provides great flexibility and requires less computational time, because at each iteration of the algorithm only a single forward propagation of the equation of motion of the quantum system is performed. Key factors of this algorithm are that it is easy and quick to implement and that it allows to take into account the experimental limitations (detailed in sec. 4.3). Moreover, the minimization can be done on different figure of merits without the need to adapt the code to a specific one, which is required for some applications (see chap. 5 and chap. 6).

Here, our goal is to find an optimal shape of the control pulse  $\lambda(t)$  introduced in eq. (4.2). To this end, we express the control pulse on a frequency basis:

$$\lambda(t) = a_0 + \sum_{k=1}^{k_{\max}} a_k \cos(2\pi\nu_k t) + b_k \sin(2\pi\nu_k t), \quad (4.6)$$

where  $k_{\max}$  is the largest admissible wave vector frequency due to the limited bandwidth,  $\nu_k = k/(qT)$  with  $k, q \in \mathbb{N}$ . The standard Fourier components correspond to  $q = 1$ ,  $q > 1$  correspond to frequencies between Fourier harmonics. The CRAB algorithm then looks for the optimal sets of time-independent coefficients  $\mathcal{A} = \{a_k : k = 2, \dots, qk_{\max}\}$  and  $\mathcal{B} = \{b_k : k = 1, \dots, qk_{\max}\}$ , as well as the optimal set of time-independent frequencies  $\mathcal{W} = \{\nu_k : k = 1, \dots, qk_{\max}\}$ , that minimizes the cost function.

The constraint  $\lambda(0) = \lambda(T) = 0$  is implemented by imposing appropriate conditions on the amplitude of the coefficient, such as for example:

$$a_0 = - \sum_{k=1}^{k_{\max}} a_k \quad (4.7)$$

to impose that  $\lambda(0) = 0$ . (The condition for  $\lambda(T) = 0$  is of similar nature but must be defined for each value of  $q$ .) The constraint on the maximal amplitude of the pulse

is realized by defining the coefficients as  $a_k = \eta \cos(A_k)$  and  $b_k = \eta \cos(B_k)$  with the amplitude  $\eta \in [0, 1 \mu\text{m}]$ . The range of admissible values of the control pulse is then limited and we rather seek the optimal set of coefficients  $A_k$  and  $B_k$ .

The optimization is carried on 80 values of each parameter  $a_k$ ,  $b_k$  and  $\nu_k$ . The control pulse  $\lambda(t)$  is then fed at each optimization loop to a GP solver, which allows to compute the time-dependent dynamics numerically. The modulus square of the scalar product of the final state with the goal state is what is used as the minimization criterion for the optimization.

## 4.5 State-to-state transfer pulse optimization

### 4.5.1 Optimization problem initialization

The initial state is the horizontal transverse wavefunction  $|0\rangle$ , described in a good approximation by a GPE of the ground state of the trap in that direction. We optimize transfer pulses for two different target states. In a first example, we optimize for a balanced superposition of the ground state  $|0\rangle$  and first excited state  $|1_y\rangle$ , with a relative phase arbitrarily chosen to be zero. For this “half transfer” pulse, a good candidate for the cost function is:

$$\mathcal{J}_{half} = 1 - \mathcal{F}_{half} = 1 - |\langle \psi_{\text{target}} | \psi_y(T_{half}) \rangle|^2 \quad (4.8)$$

with the target state defined as

$$|\psi_{\text{target}}\rangle = \frac{|0\rangle + |1_y\rangle}{\sqrt{2}} \quad (4.9)$$

and where  $|\psi_y(T_{half})\rangle$  represents the state of the system at the end of the half transfer pulse.  $\mathcal{F}_{half}$  will be further called the “fidelity” of the pulse, whereas  $\mathcal{J}_{half}$  will be referred to as the “infidelity”.

In a second example, we take the full transfer to the first excited state. For this “full transfer” pulse, the appropriate cost function is:

$$\mathcal{J}_{full} = 1 - \mathcal{F}_{full} = 1 - |\langle 1_y | \psi_y(T_{full}) \rangle|^2. \quad (4.10)$$

### 4.5.2 Pulses optimized close to the quantum speed limit

The optimization was first carried out for different durations of the transfer pulse, with the aim to find a good compromise between fast control and high fidelity. The shorter the pulse, the more difficult it gets to reach high fidelities. The results of these optimizations are summarized in fig. 4.4(left).

For the experimental implementation of the half transfer pulse, we selected the pulse giving a theoretical fidelity  $\mathcal{F}_{half} \simeq 99\%$  for a duration  $T_{half} = 1.19$  ms. This value of the fidelity corresponds to 50.23% of ground state, 48.78% in the first excited state, and 0.98% in higher excited states. The reason for this choice is practical: from an experimental

point of view, it is not relevant to target higher fidelities, because the read-out method employed only allows a precision on the order of a few percent for the determination of the populations in different states (read about the state analysis method in sec. 4.7). For the full transfer pulse, the choice went to a  $T_{full} = 1.09$  ms pulse yielding a theoretical fidelity  $\mathcal{F}_{full} \simeq 99.5\%$ . Both pulses are represented in fig. 4.4(right).

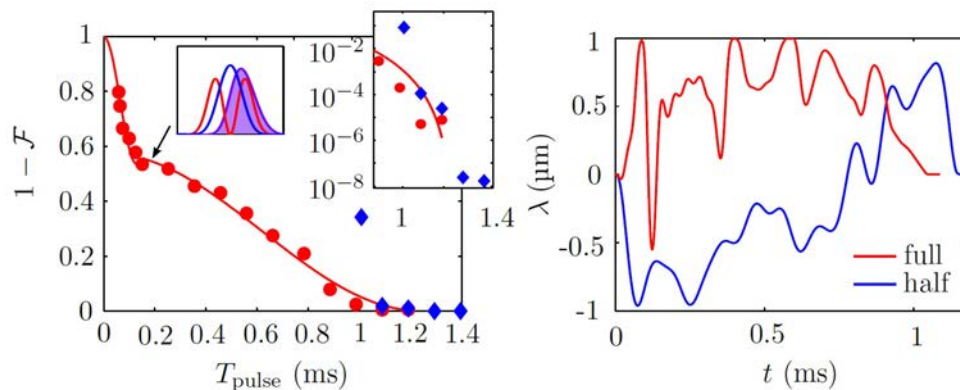


**Figure 4.4: Optimized pulses.** (Left) Infidelity reached after optimization for different transfer times  $T_{pulse}$ , for the full transfer (red circles) and the half transfer (blue diamonds). The red lines are fits of the data for the full transfer optimizations, according to a  $\propto \cos^2 \beta T$ . The inset represents the modulus square of the final wavefunction for  $T = 0.15$  ms (purple area), with the ground and first excited states shown as references. (Inset) Same as main figure on  $0.9 - 1.4$  ms, plotted in log scale. (Right) Selected half transfer pulse (blue line) and full transfer pulse (red line), corresponding to a good compromise between speed and efficiency for the experimental implementation.

It should be noted that this pulse is extremely fast with regard to the relevant times of the problem. A duration of 1.19 ms corresponds to only about twice the timescale set by the level spacing  $\nu_{s.p.}^{-1} = h/E_{s.p.} = 0.57$  ms, which is the typical timescale of the problem and a good approximation for its quantum speed limit. The constraint on the maximum displacement is expected to also play a role in this final time obtained for the optimized pulse.

A CRAB optimization was performed for a full transfer at different transfer times  $T$ . The results, reported as red points in fig. 4.4(left), show that the infidelity  $1 - \mathcal{F}$  decays monotonically one inflection point, which can be interpreted as a signature of two typical timescales. First, within the fastest timescale (lasting about 0.15 ms) the optimal solution performs an almost rigid translation of the initial wave packet, which maximizes the overlap with one of the two lobes of the first excited state of the trap (see inset in fig. 4.4, left). This stems from the fact that simply displacing the initial ground state already yields a figure of merit of about 60%. Second, the longer timescale plays a role if one aims to solve the full problem, which obviously requires to modify the wavefunction shape by means of more complex and longer system parameters manipulations. This optimal dynamics has also a geometric interpretation: it is composed of two optimal transitions,

the first between the initial state and the intermediate state depicted in fig. 4.4 (left, inset), and the second between the latter and the goal state. Each transformation displays a monotonic decay of the final figure of merit as a function of the total transformation time  $T$ , which can be fitted via a  $\cos^2(T)$  decay (blue lines), that is, they are compatible with two concatenated optimal transformations at the quantum speed limit. The blue diamonds in fig. 4.4(left) shows the results for the half transfer pulse. We rely on these results to choose pulses presenting a good compromise between high speed and high fidelity, at  $\sim 1.1 - 1.2$  ms.

As can be inferred from the shape of the pulse in fig. 4.4(right), the wavefunction gets brutally - but in a controlled way - displaced along the  $y$ -axis. A look at the vertical axis shows that the constraint on the maximum displacement of the trap minimum is verified. This displacement corresponds to about 4 times the initial wavefunction size ( $r_{0,y} = 252$  nm). A Fourier decomposition of the pulse, as detailed in the next section, proves that the constraint on the bandwidth is also satisfied.

### 4.5.3 Insight on pulse complexity

The number of frequencies retained for the optimization was  $N_f = 80$ . Gaining an insight on the specific role of each frequency is an impossible task, but some information can be obtained from the decomposing the pulse into its Fourier elements:

$$\lambda(t) = \frac{a_0}{2} + \sum_{k=1}^{N_f} a_k \cos\left(\frac{2\pi kt}{T}\right) + b_k \sin\left(\frac{2\pi kt}{T}\right) \quad (4.11)$$

with

$$a_k = \frac{2}{T} \int_0^T dt \lambda(t) \cos\left(\frac{2\pi kt}{T}\right),$$

$$b_k = \frac{2}{T} \int_0^T dt \lambda(t) \sin\left(\frac{2\pi kt}{T}\right).$$

where  $\nu_k = k/T$ .

The Fourier spectrum of the full transfer pulse, shown in fig. 4.5, reveals the high number of frequencies that compose it. By comparison, the pulse used in ref. [115] and ref. [130] had a relatively simple structure, with a main frequency around the single-particle level splitting. Qualitatively, the spectrum exhibits a rather continuous behavior with a number of prominent peaks. It appears that after  $\nu_k \geq 20$  kHz, all frequencies have close to zero amplitude, which means that a large band of high frequencies does not play a role in the optimization. Therefore, the cut-off frequency imposed by the electronics does not compromise the pulse optimization.

Furthermore, a number of the peaks can be matched with single-particle transitions from the ground state to higher states. These transitions are indicated as blue lines in fig. 4.5. However, not all peaks could be matched with meaningful transitions, even when accounting for the shifts caused by interactions by solving the Bogoliubov-de Gennes equations for the ground and the first excited states. This analysis shows just how optimal control can bring about effective though highly non-intuitive solutions.

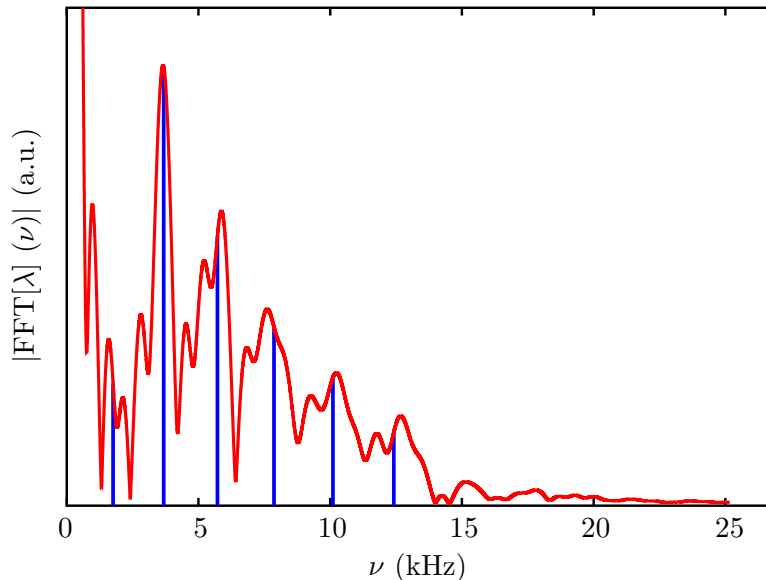


**Figure 4.5: Fourier spectrum of the full transfer pulse.** The vertical lines correspond to single-particle transitions from the ground state.

#### 4.5.4 Robustness of the pulse

The optimal control scheme is sensitive to deviations of experimental parameters from the parameters used for the optimization. As fluctuations and drifts cannot be altogether prevented, it is important to identify and characterize the potential culprits. In particular, fluctuations in atom number are in the best case on the order of 10% and sometimes more. The optimization is carried out for a given potential shape and a given number of atoms. For a realistic implementation, the pulses must be robust to small deviations of the potential shape and fluctuations of the atom number.

The main contributors to the transverse potential shape close to its minimum are the RF dressing parameters and the external Ioffe field. If we consider small changes around their optimal value, we can estimate the dependence of the harmonic and quartic terms of the potential by linearizing eq. (3.16):

$$\alpha_2^y = 665.5 + 7.6 \times \delta B_{\text{Ioffe}} - 42.6 \times \delta I_{RF} \quad (4.12)$$

$$\alpha_4^y = 62.7 - 1.8 \times \delta B_{\text{Ioffe}} + 6.9 \times \delta I_{RF} \quad (4.13)$$

with  $[\alpha_2^y, \alpha_4^y, \delta B_{\text{Ioffe}}, \delta I_{RF}]$  expressed respectively in [Hz, Hz, mG, mA]. Therefore, a change in the potential shape is directly related to changes in  $B_{\text{Ioffe}}$  or  $I_{RF}$ . This will effect the pulse efficiency. To estimate by how much, we simulate GPE evolutions in potentials with small variations from the initial shape. The results are plotted in fig. 4.6,

for a half transfer pulse (left) and a half transfer pulse (right). We observe on this plot that the full transfer is more sensitive to changes in the potential shape. For this pulse, a change of 1% in the  $\alpha_2^y$  or in the  $\alpha_4^y$  parameters leads to a 5% decrease in the pulse's efficiency. This situation would arise for example if we have fluctuations on  $\delta B_{\text{Ioffe}} > 0.8$  mG or fluctuations on  $\delta I_{RF} > 0.16$  mA. The active stabilization of the Ioffe field ensures that  $\delta B_{\text{Ioffe}}$  remains below  $10^{-5}$  at 0.5 G. The precision on the amplitude for the RF dressing given by the Tabor is indicated to be  $\pm 1\%$  at 1 kHz, which is close to the limit in fluctuations estimated from eq. (4.13). However, as these fluctuations are fast compared to the response time of the atoms, their effect averages out and the output of the full transfer pulse is stable to about 1%. If long time drifts occur, they can be corrected with our ADwin control.

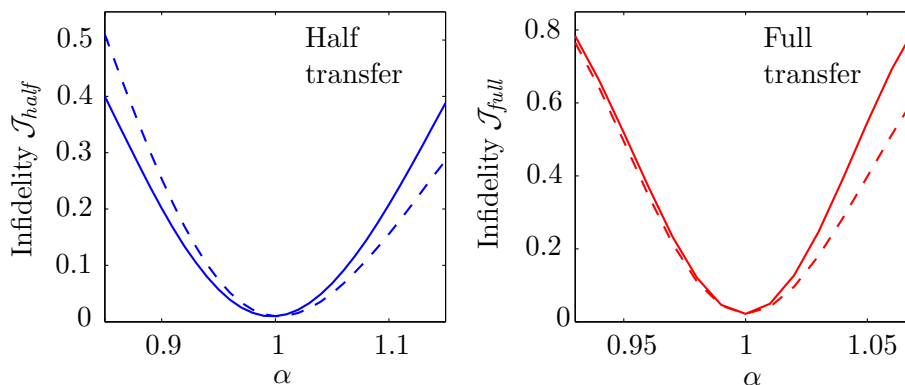


**Figure 4.6: Robustness of transfer pulses against changes in the potential shape.**  
 (Left) Infidelity obtained from simulations with half transfer pulse for a scaling  $\alpha$  of  $\alpha_2$  (continuous line) or  $\alpha_4$  (dashed line).  
 (Right) Same for full transfer pulse.

Changes in atom number introduce shifts in the effective level splitting. Numerically, it modifies the non-linearity parameter of the GP simulations. Therefore, it affects the efficiency of the control pulse. Nevertheless, the speed of the transfer is here turning into another advantage. As can be seen in fig. 4.7(left), an optimization for a “fast” transfer ( $\sim 1$  ms) yields very similar pulses for very different atom numbers. We specify here that the pulses shown for  $N = 1$  atom and  $N = 7000$  atoms have been optimized starting from, as initial guess, the pulse optimized for  $N = 700$  atoms. Conversely, with the same optimization procedure, the shape of the optimal “slow” pulses ( $\sim 5$  ms) will look qualitatively different for different atom numbers, as appears in fig. 4.7(right). This non-intuitive result of the fast pulse being less sensitive can be understood as an effect of phase accumulation over the duration of the pulse. This phase accumulation is directly dependent on the effective energy difference between the states, therefore on the population of each state. The accumulated phase difference will be greater for a longer pulse than a short one, resulting in an improved robustness to atom number changes for the “fast” control pulse.

Finally, fig. 4.8(left) presents a numerical simulation of the variation of the pulse's

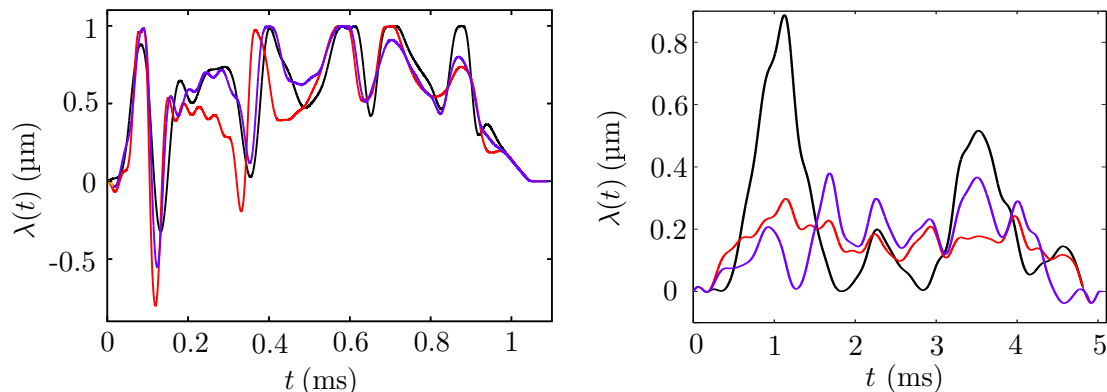


**Figure 4.7: Optimal full transfer ramps for different pulse lengths and atom numbers.** (Left) Pulse optimized to realize a full transfer in  $T_{\text{full}} = 1.09$  ms for  $N = 1$  (non-interacting gas, black line), for  $N = 700$  (red line) and for  $N = 7000$  (purple line). (Right) Same for  $T_{\text{full}} = 5.1$  ms.

outputs and infidelity as a function of the atom number variation, for different pulses realizing a full transfer. This numerical investigation confirms that, although a slow pulse can approach the target state with better precision at  $N = 700$  atoms, the fast pulse is more robust against a change of atom number. In addition, pulses optimized without taking into account interactions ( $N = 1$ ), perform much worse in both cases, and even really poorly for the slow pulse. This highlights again the importance of taking into account the interactions in the formulation of the optimization problem. For a change of 10 % to 20 % in atom number, which is typically on the order of the fluctuations observed in the experiment, the output populations change by 0.05 % to 0.1 %. The pulse is therefore very robust against fluctuations in atom number.

On the other hand, the fidelity can drop quickly if errors arise on the transfer pulse, in particular on the amplitude as shown in fig. 4.8(right). It is thus necessary to control the displacement with a good accuracy. For this, the knowledge of the filter function of the electronics, as presented in chap. 3, and its integration into the optimization algorithm play an important role. The on-line control during the experiment is done in two ways: by measuring the current into the wires and comparing it to the reference for a good general agreement, and by ensuring that the transfer fidelity is high for absolute verification.

In the end, the application of optimal control, and more precisely of the CRAB algorithm, allowed us to develop successful and fast state-to-state transfer pulses. Trajectories were optimized to obtain full and half transfer pulses. Transfers to other superpositions are conceivable as well — e.g. 25 % and 75 % pulses were also developed — or to higher excited states. The efficiency of the optimized pulses reached more than 99 %, and this in a record time of 1.09 ms. The speed-up of the transformation ultimately hits the quantum speed limit, the characteristic timescale of the system set by the level splitting, but also by the constraints imposed to the system. The optimization results in pulses whose shape is non-trivial. They displace the wavefunction rapidly on more than 4 times its size, making it explore a large range of the trapping potential. The transformation

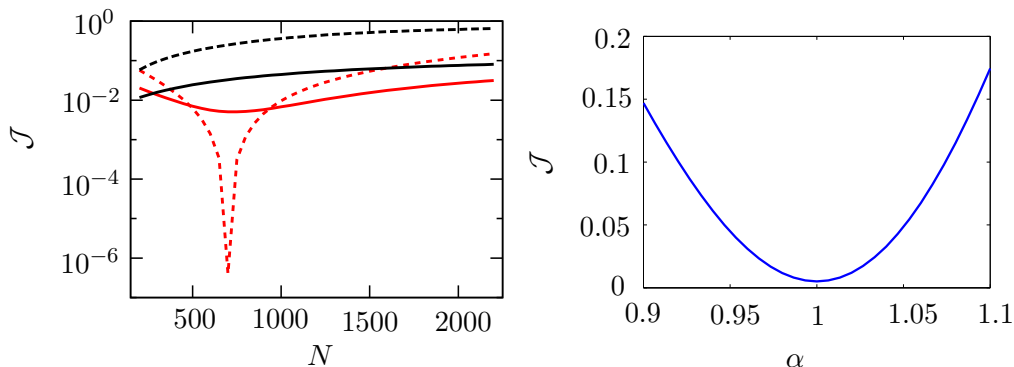


**Figure 4.8: Robustness of full transfer pulses.** (Left) Infidelity vs. atom number for different pulses: the desired fast pulse optimized for  $N = 700$  (red line), a slow pulse optimized for  $N = 700$  (dashed red line), and a comparison to pulses optimized for  $N = 1$  (fast: black line, slow: dashed black line).

(Right) Infidelity as a function of the amplitude of the fast pulse optimized for  $N = 700$ ,  $\alpha$  representing here the scaling factor.

process cannot therefore be thought of as a Rabi drive, but as a really complex and non-perturbative process. This process turns out to be robust against perturbations in different quantities: changes in atom number, uncertainties in the trapping potential. This study is important for an experimental realization. Fluctuations in atom number will be the most relevant perturbative effect in our experiment, as it is unavoidable.

## 4.6 Experimental realization

### 4.6.1 Initial state characterization

Initially, the condensate is prepared in the transverse ground state of the potential by cooling the  $^{87}\text{Rb}$  atoms in the dressed trap (see chap. 2 for BEC and chap. 3 for trapping). The atom number in the trap after cooling is  $N \simeq 700$  atoms, with non-avoidable fluctuations on the order of 10%. The longitudinal profile is Thomas-Fermi and the condensate is transversely in its ground state, with a 1d peak density of  $n_{1d}(0) \simeq 25 \mu\text{m}^{-1}$ , a chemical potential  $\mu_0 \simeq h \cdot 600 \text{ Hz}$  and a radius  $R \simeq 20 \mu\text{m}$  (see details in chap. 2).

The assumption that the atomic cloud is indeed in the transverse ground state of the trap depends in part on its temperature. Temperatures on the order of 60 nK or higher, for a 1d quasi-condensate, can be estimated from longitudinal profiles by a fit to the thermal fraction. In this series of experiments, there is very little to no thermal fraction visible. This indicates very low temperatures, difficult to estimate but low enough to be in the ground state universally. We estimate an upper limit for the temperature at about 50 nK. Other methods exist [68, 88, 151], but they also fail in the present case due to the very low temperature, chemical potential and densities. More detailed considerations can be found in ref. [56].

The trapping potential can be simulated from the magnetic fields (see chap. 3). The

agreement with the experimental potential can be checked by a series of measurements explained in the next two paragraphs. We first characterize the trap in the absence of dressing field (i.e. the static, harmonic trap), then the trap which is made anharmonic by the RF-dressing.

For the static trap, the transverse frequency  $\nu_0^\perp$  and the longitudinal frequency  $\nu_0^\parallel$  can be measured by triggering a collective dipole mode. A small ( $\sim 1\%$  of its nominal value) but sudden change of current in an appropriate wire — e.g. trapping wire for the transverse frequency, dimple wire for the longitudinal frequency — triggers an oscillation of the whole cloud in the trap. The frequency of this oscillation, for a harmonic potential, corresponds to the frequency of the trap. These oscillations can be followed by imaging the cloud in time-of-flight and the frequency extracted by fit.

The trap frequency in the  $y$ -direction, which is the most relevant frequency for the problem, can be measured to a precision  $< 1\%$ . This part of the characterization is shown in fig. 4.9(a) and fig. 4.9(b) and yields  $\nu_0^\perp = (4.170 \pm 0.013)$  kHz and  $\nu_0^\parallel = (14.4 \pm 0.6)$  Hz.

We also measure the Larmor frequency at the trap center  $\nu_L$  (“trap bottom”) by RF spectroscopy, using a weak RF pulse with a narrow bandwidth ( $< 1$  kHz). When  $\nu_{RFpulse} = \nu_L$ , the atoms in the trap are transferred to the untrapped state  $m_F = 0$ . We compare the measurements of  $\nu_0^\perp$  and  $\nu_L$  to the values of the trap simulations to ensure that the external bias and Ioffe fields, as well as the chip currents in the trapping wire and the H-wires are correctly set (see Table 4.1 for values). The longitudinal frequency  $\nu^\parallel$  is mainly set by the corrugation of the potential.

When activating the RF dressing, the trap frequencies and the trap bottom are modified depending on the frequency and the amplitude of the RF field, as well as the relative phase between the two RF wires (see chap. 3 for details on the geometry). Using AC current probes, we can measure its frequency and have an estimate of its amplitude. Because of the lack of precision on the measurement of the amplitude, we cannot rely on this measurement alone to get an accurate description of the dressed potential, thus it is necessary to characterize the dressed potential as well as the static one. The description gets complicated in the dressed trap case due to the multiplicity of the transitions, as explained in chap. 3. Nevertheless, a trap bottom can again be probed using a weak RF pulse to transfer trapped atoms to untrapped states [104] at the effective trap bottom frequency  $\nu_{TB,dressed}$ . The procedure to adjust the trap bottom consists of two steps. First, the trap bottom obtained from each RF wire addressed separately is measured, which guaranteed that the amplitudes of both RF fields at the center of the trap are equal. Second, the relative phase between the two wires is set by scanning its value and comparing the evolution of the trap bottom to simulations, in order to obtain a linearly polarized field in the vertical direction (see also ref. [21]). The final result on the trap bottom matches to a good extent the simulations.

With the RF dressing linearly polarized in the vertical direction, the trapping potential is mostly deformed in the  $y$ -direction, also modifying slightly the potential in the other directions. It is possible to use the same collective oscillation method to probe the frequency close to the center of the potential  $\nu_y$ , but not to get a full description of the trap shape in the  $y$ -direction, which is the one of interest. The anharmonicity is visible

through a damping of the dipole oscillation as shown in fig. 4.9(e), but the fitted frequency and damping cannot be directly related to the potential shape. We therefore combine the knowledge of this frequency to another approach, based on the control pulse itself. Its sensitivity makes it a good tool to investigate the shape of the potential, in particular its anharmonicity. We finely tune the parameters of the experiment by comparing the response of the condensate to the control pulse with the numerically simulated response. This approach leads to very good agreement between experimental and numerical results, and the experimental characterization of the trap parameters coincide in turn with the potential simulations. The measured trap parameters and the corresponding values for the different fields are summarized in Table 4.1.

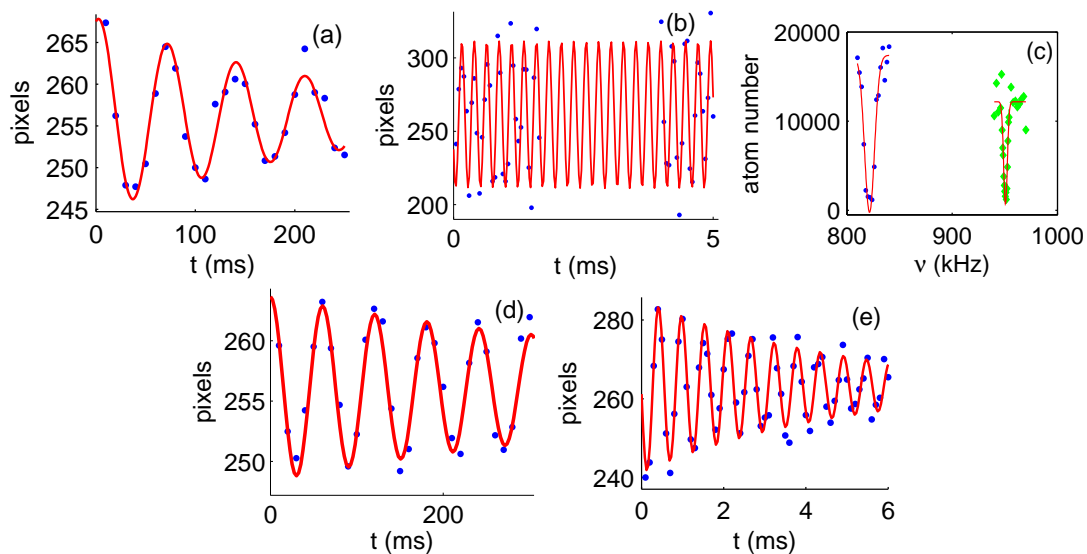


**Figure 4.9: Traps characterization.** (a) Static trap longitudinal frequency measurement, estimated by a fit (red line) to the oscillation of the atomic cloud in the trap as seen after 46 ms time-of-flight (blue points). (b) Static trap transverse frequency measurement. (c) RF spectroscopies of the static trap (blue points) and the dressed trap (green diamonds) with Gaussian fits (red lines). (d) Dressed trap longitudinal frequency measurement. (e) Dressed trap horizontal transverse frequency measurement.

A good knowledge of the trapping potential's characteristics is essential, because the transfer scheme is sensitive to its shape, as shown in sec. 4.5. The potential is initially measured to be used in the simulations for the pulses optimizations. The description offered by the measurements is only partial, as the non-harmonic terms cannot be characterized experimentally. However, together with the accurate trap simulations, they are sufficient for the pulses to work efficiently.

The last element to be corroborated is the atom number. For the imaging of the condensate with the light sheet, this requires to calibrate the number of photons per atom imaged by the EMCCD camera. The best method so far is to use the LS analysis method described in chap. 3. This is nevertheless time-consuming and cannot be done on

**Table 4.1: Trap calibration parameters.**

Trap calibration measurements				
$\nu_0^\perp$	$\nu_L$	$\nu_y$ (dressed)	$\nu^\parallel$ (dressed)	$\nu_{TB}$ (dressed)
4.18 kHz	822 kHz	1.77 kHz	25 Hz	951 kHz
Corresponding field settings				
$I_t$	$I_h$	$B_{\text{bias}}$	$B_{\text{Ioffe}}$	$RF_{\text{dressing}}$
1 A	0.5 A	34.1 G	1.07 G	24 mA

a regular basis. But as the atom number and the number of emitted photons per atom can sometimes drift (due e.g. to changes in the imaging intensity or a slight misalignment of the light-sheet beams), it is necessary to have a quicker method to make regular checks. For this, the atom number can be evaluated from absorption with an approximate correction factor of 1.2 coming from the absorption efficiency (see explanation in chap. 3). The photon-per-atom number can then be measured by comparing the corrected atom number in absorption and number of photons counted with the fluorescence imaging system.

#### 4.6.2 Implementation of a transfer pulse and monitoring

Once the system is initialized as a 1d quasi-condensate with 700 atoms in the dressed trap corresponding to the simulation, the state manipulation begins. The effective potential is displaced along or close to its horizontal transverse direction, as depicted in fig. 4.1(a), following one of two possible experimental approaches described in chap. 3. In a time window of  $\simeq 1$  ms, the minimum of the effective potential describes one of the trajectories depicted in fig. 4.4(right) before stabilizing at its original position again.

Following in real time the evolution of one condensate in particular is not possible on our experiment, as we only have destructive methods to image the atoms. What we can do is monitoring the current in the dressing-and-shaking wires via an AC current probe. The signal obtained shows that the experimental realization of the transfer pulse follows the optimized trajectory, indicating that the bandwidth of the electronics described in chap. 3 was properly taken into account and that no other detrimental effect comes into play.

A more convincing way to ensure that the transfer pulse completes its task is to follow the evolution of the condensate wavefunction under the action in the trap. As the imaging system used is a fluorescence imaging of the cloud after long time-of-flight, what can actually be measured is a momentum density distribution at one point in time during or after the pulse. To trace the evolution of the wavefunction, we repeat several times the entire experiment and interrupt the state manipulation at different time points. The dynamics is then nicely visualized by integrating the experimental images along the longitudinal  $x$ -axis and concatenating them following the interruption time. This

operation is illustrated in fig. 4.10.

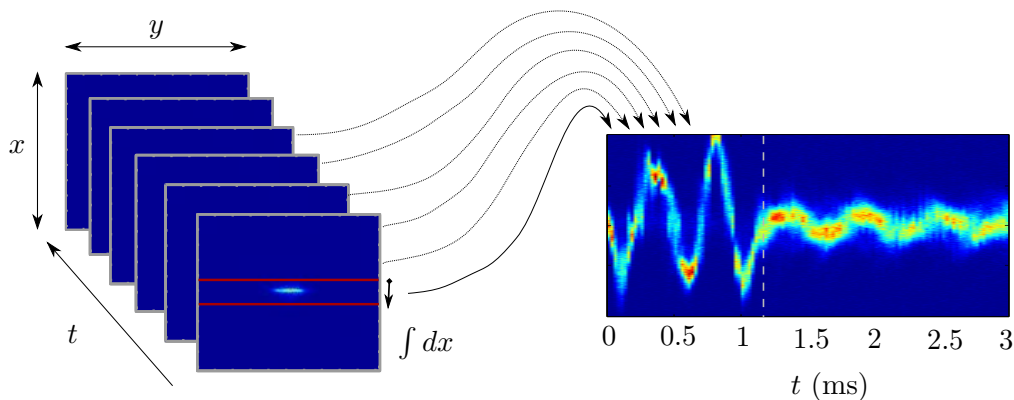


**Figure 4.10: Illustration of experimental momentum distribution concatenation for follow-up of the dynamics.** The transfer pulse is interrupted at different time points and the condensate imaged. The images are then integrated along the  $x$ -axis and concatenated, such as to follow the momentum dynamics in the transverse  $y$ -direction.

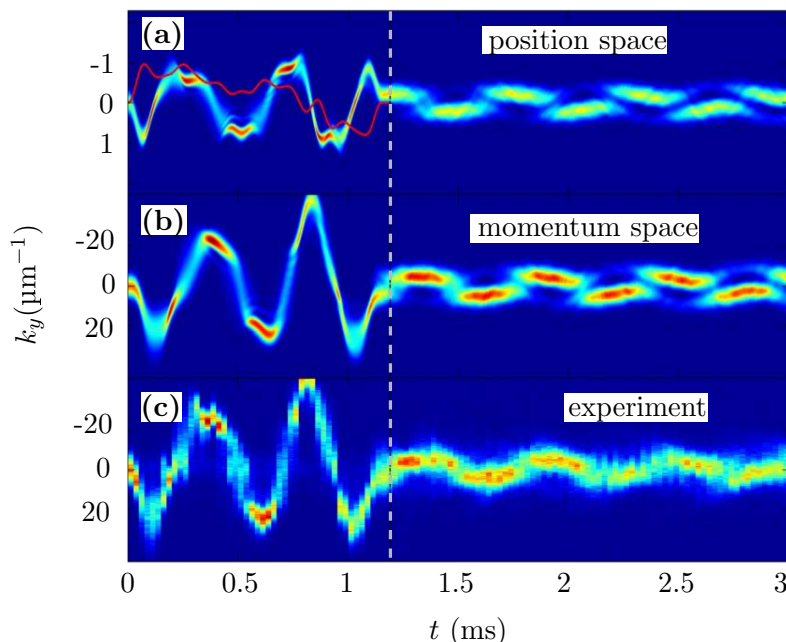
Once concatenated, the experimental data are compared to GPE simulations of the evolution represented in the same way. In the limit of infinite expansion time, the density distribution imaged after time-of-flight is homotetic to the in-trap momentum distribution, which can be easily computed by Fourier transform from the simulated wavefunction in position space. Here, the time of flight is sufficiently long to make this assumption (time-of-flight  $t_{TOF} \gg \hbar/E_{s.p.}$ ). Moreover, the fast transverse expansion of the cloud due to high confinement causes the atomic interactions to become rapidly negligible, hence the expansion can be considered ballistic.

Figure 4.11(a) shows as an example the GPE evolution of the atomic density distribution in the trap under the influence of the half transfer pulse. The corresponding momentum distribution, shown in fig. 4.11(b), is also computed and can be compared to the experimental data represented on fig. 4.11(c). The qualitative agreement between the numerical simulation and the experimental data is very satisfactory, both during and after the pulse, especially considering that the numerical simulations were conducted without free parameter. A quantitative comparison, explained in sec. 4.7, of the momentum distributions after the pulse can be carried out to extract the fidelity of the transfers.

## 4.7 Experimental transfer efficiency

### 4.7.1 Principle of state analysis

We want to check experimentally the wavefunction at the end of the control pulse. We would like to know the composition of the final state in terms of motional states, but we do not have access directly to the wavefunction in the trap. What we do have access to, thanks to our imaging system in time-of-flight, is the transverse momentum distribution during and after the pulse. From such distributions, we would like to infer



**Figure 4.11: Dynamics of the excitation and interference patterns observed during and after the half transfer pulse.** (a) Optimized trap displacement  $\lambda(t)$  along the  $y$ -direction (red solid line) and simulation of the in-situ density. (b) Simulated momentum distribution. (c) Measured momentum distribution. The time-of-flight images were integrated along the longitudinal  $x$ -direction and concatenated to show the time evolution.

in which superposition state the wavefunction in the trap before release is, and how close we are to the target.

Single images are not enough to determine the final state. The main idea of the analysis is to use the evolution of the transverse momentum distribution to acquire knowledge about the in-trap wavefunction. We know from comparison to GPE simulations that a mean-field approach is a very good tool to describe the dynamics of the wavefunction in the trap and reproduce the experimental data. Together with our accurate description of the potential shape, it gives an almost perfect comparison between simulated and experimental momentum distributions - within the limitations of the GPE - without free parameters. To extract populations in different states however, we do not seek to reproduce the dynamics during the transfer pulses, whereby unnecessary complications and mistakes can arise, but we attempt to reproduce the patterns observed after the transfer.

#### 4.7.2 Choice of model

As can be visualized with 1d GP simulations, different superpositions of motional states evolving in time display different features. From such simulations (see fig. 4.12), we get an intuitive idea of how a superposition of the two first energy levels will come out in the experimental data. Specific “beating” patterns arise from interferences between

the different occupied motional states. These patterns also appear in the momentum distributions. An analysis method consists in fitting the experimental data with such simulated evolutions. For this, a model must be chosen.

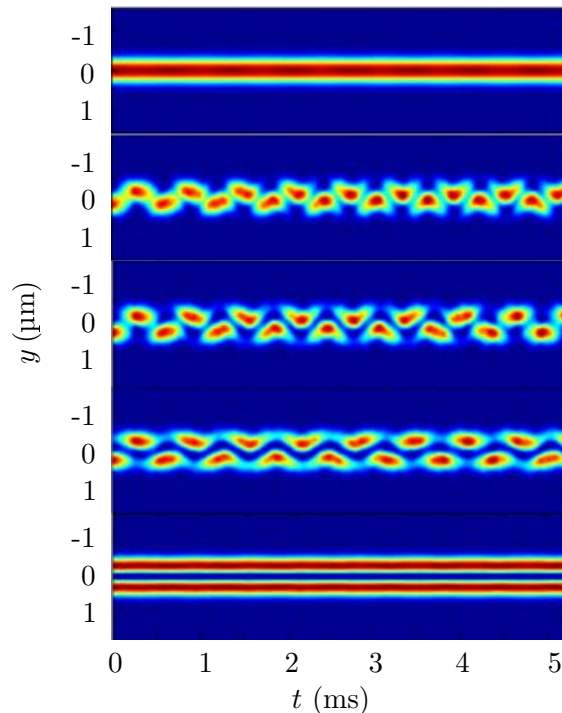


**Figure 4.12: Time evolution of in-trap densities for different superpositions of ground state and first excited state, simulated by GPE for  $N=700$  atoms.** Top to bottom: All atoms in the ground state; 25 % in the first excited state; 50 % in the first excited state; 75 % in the first excited state; all atoms in the first excited state.

The simplest description of our experimental system is a coherent sum of two wavefunctions corresponding to the ground state  $\psi_0$  and the first excited state  $\psi_1$ . The propagation is then carried by a relative phase  $\theta_{01}$  between the two states, which evolves at the rate given by the level splitting  $E_{01}$ :

$$\psi = \psi_0 + e^{i\theta_{01}}\psi_1 = \psi_0 + e^{i\frac{E_{01}}{\hbar}t}\psi_1. \quad (4.14)$$

We observe with this simple description the main feature of the interferences pattern, the “beating”, and from this it is already possible to get an estimation for the populations in the two lower-lying states. This only works approximately though, as additional effects are not reproduced, like the slow modification of the interference pattern that takes place on the timescale of a few “beating” periods (see e.g. the third panel in fig. 4.12). The reason for this discrepancy is that we disregard the higher excited states, in particular the second excited state. This is obviously a shortcoming of the method if more than two states are initially populated by the transfer pulse. The presence of a second excited state, even weakly populated, leads to periodic modulation of the interference pattern. Actually,

the problem appears even in the case where only two states are initially populated, because couplings between the different states are induced by the interatomic interactions, and even for an initial state consisting only of  $|0\rangle$  and  $|1_y\rangle$ , a small fraction of atoms from  $|1_y\rangle$  may be periodically transferred to the second excited state. Therefore, a model that includes the second excited state is recommended to get a more faithful representation of the dynamics.

A 1d GP modeling of the experimental patterns can be used to infer the populations in two or more vibrational levels:  $p_0$ ,  $p_1$ , etc. For this, we start from a given initial superposition of  $k$  states:

$$|\psi_{\text{initial}}\rangle = \sum_k \sqrt{p_k} e^{i\theta_k} |k_y\rangle, \quad (4.15)$$

where  $k \in \{0, 1, 2\}$ , corresponding to the three lowest-lying states. We then propagate this superposition in time, using the GP solver, in the potential at rest  $V(y)$ . We compute the corresponding momentum distribution and compare its evolution to the experimental densities after time-of-flight. By a fitting procedure, explained in the next section, we infer the superposition of motional states which is most likely to have generated the experimentally observed beating patterns. The reason we chose to restrict the model to a three-states superposition is twofold. First, multi-mode simulations show that the main features of the experimental data can be reproduced by a 3-mode description similar to ref. [152]. Second, fitting procedures only work well for a limited number of parameters.

For a ballistic expansion, the width after time-of-flight is mainly given by the in-trap momentum. If we express the momenta as wave numbers  $k_y$ , a distance  $\delta y$  in the experimental image then corresponds to  $\delta k_y = \alpha \delta y$  with  $\alpha = m/\hbar t_{\text{TOF}} \simeq 0.03 \mu\text{m}^{-2}$ . To account for experimental imperfections such as finite imaging resolution in the light sheet, the GPE result is convoluted with a Gaussian filtering function of  $m/(\hbar t_{\text{TOF}}) \cdot 40 \mu\text{m} \simeq 1.20 \mu\text{m}^{-1}$  rms width, as was previously done in ref. [130]<sup>2</sup>. The simulated momentum distribution is sampled in time to match the experimental timestep. It is then ready to be fitted to the experimental data.

### 4.7.3 Fitting procedure

The fitting procedure consists in finding the combination of parameters  $p_k$  and  $\theta_k$  most likely to have generated the observed momentum distribution density, using a regression method. As explained in the previous section, we can reproduce the dynamics observed in the momentum distribution, using a GPE model. As the interference patterns in the dull time dynamics depend on the populations and phases of the states coherently occupied, we can fit the full time dynamics to analyze the final state superposition obtained with any transfer pulse.

Using eq. (4.15), the natural input parameters of the simulation are the populations of the three states  $p_0$ ,  $p_1$ ,  $p_2$  and their respective phases  $\theta_0$ ,  $\theta_1$ ,  $\theta_2$ . To limit the number

<sup>2</sup> In some of the data presented in this thesis, the broadening was a bit more important than in previous experiments, likely due to a slight misalignment of the light sheet at the time the measurements were taken. We adapted the filter function to reproduce the broadening of the data.

of input parameters and therefore the size of the search space, we can neglect the global phase which does not play any role here and consider only the two relative phases  $\theta_{01}$  and  $\theta_{02}$ . We have in addition a small offset parameter  $k_{\text{shift}}$  that accounts for a small global offset of the momentum distribution from the center of the image.

Altogether, six parameters of a non-linear function need to be fitted, requiring an adapted non-linear regression algorithm. Generally speaking, a non-linear regression attempts to solve a minimization problem, e.g. minimize the distance between some data and the proposed model by adjusting the model's parameters. A common example of minimization objective is the sum of squared residuals of the least square approach. The minimization procedure is an iterative approach following the next steps:

1. it starts with an estimated initial value of each parameter in the equation;
2. it generates the curve (in the case of a 2-dimensional problem) or surface (3-dimensional problem) from the model using the initial values;
3. it calculates the residual;
4. it then adjusts the parameters to bring the curve closer to the data points. Several algorithms exist that use different approaches to adjust the variables;
5. it repeats step 4 until the conditions of step 6 are met;
6. it stops the process when the adjustments only make a difference on the residual smaller than a set inferior limit;
7. it reports the best-fit results on the parameters.

There exist several types of non-linear regression methods, the most common ones being based on the evaluation (or the approximation) of gradients or second-order derivatives. Two well-known examples of this approach are the steepest-descent method and the Gauss-Newton algorithm. They have been adapted to work with more than one parameter. For the problem at hand, one direct search method proved to work better: the Nelder-Mead simplex method [150]. This type of algorithm does not rely on gradients and is often used for numerical optimizations where derivatives are not necessarily known. This has the advantage that it can sometimes solve problems where gradient-based methods fail, typically in the presence of small noise. The inconvenient is that, because it does not evaluate derivatives, it also does not give any standard error nor confidence interval to estimate the quality of the fit. We will see in the next section how we get around this difficulty.

The simplex method works on the following principle: given  $N$  initial parameters, it starts from  $N+1$  vectors of initial values and calculates the residual for each vector. It discards the vector yielding the largest residual, then chooses a new one depending on a determined set of rules. For example, it could be to replace the worst vector with another vector which is its reflection through the centroid of the remaining  $N$  sets. For the new vector, it calculates again the residuals, compares it to the values obtained for the other vectors, discard the worst, etc. The set of vectors is called a *simplex*, the vectors are its *vertices*. For a two-dimensional space, a simplex is a triangle, in a three-dimensional space, it would be a pyramid. The procedure is repeated until the size of the simplex gets below a specified tolerance value.

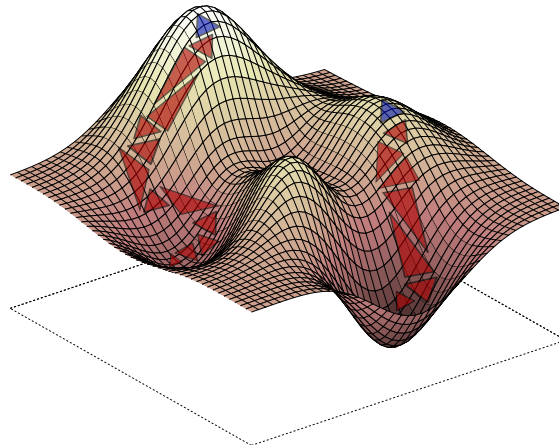


**Figure 4.13: Illustration of a search with the Nelder-Mead algorithm.** The simplex (blue) starts from an initial given set of parameters and searches its way downhill via reflections, expansions, contractions and shrinking.

In the specific case of the Nelder-Mead algorithm, the assortment of rules consist in four possible operations: a *reflection*, an *expansion*, a *contraction* and a *shrink* [153]. The choice of operation depends on the result of the set reached in a first reflection and how it compares to the sets already evaluated. With this ensemble of operation, the Nelder-Mead algorithm adapts the step size to the local landscape. A minimum can thus be located with arbitrary accuracy without the need to set a defined small step size. This method does not retain information about past steps as it proceeds, and does not rely on any assumption other than the surface is continuous and presents a unique minimum in the search area.

We used in this thesis the MATLAB algorithm `fminsearch`, in its modified version `fminsearchbnd` developed by John D'Errico<sup>3</sup>. The original version of the algorithm does not accept bound constraints, which are necessary to limit our parameter space (both for the populations that cannot assume negative values and for the phases that are  $2\pi$ -periodic). However, simple transformations can be applied to convert an initial bound constrained problem into an unconstrained one.

Applied to our problem, the algorithm converges quickly, but not always to the same value of the parameters and objective function. It is a general downside of the Nelder-Mead algorithm that it does not always converge for more than one parameter. This may be caused by a complex structure of the optimization landscape, or by the presence of local minima. To increase the probability to reach the global minimum, we run the non-linear regression several times starting from different initial values.

The minimization problem for the search algorithm is defined in terms of the distance between the experimentally observed momentum distribution and a GPE numerical simulation. This distance is conveniently estimated as a sum-of-squares of the distance

3. This function can be downloaded for free on the MATLAB File-exchange website.

between data points and numerical points:

$$\chi^2 = \sum_i \frac{(y_i - y(x_i))^2}{w_i^2} \quad (4.16)$$

where the  $y_i$ 's are the experimental points, the  $y(x_i)$ 's are the simulated points, the  $w_i$ 's are the error bars on the experimental points and  $\chi^2$  is a dimensionless quantity called the "goodness-of-fit". This is a weighted least-square regression with the weight given by the error bars on the data. The error bars are set by the shot noise on the individual light sheet images, as introduced in Chap.2. A good estimator for the weights are thus  $\alpha_i \simeq \sqrt{2y_i}/\sqrt{N_s}$ ,  $N_s$  being the number of repetitions for each averaged image, for experimental points above background noise. We do not consider regions where background noise is dominant in the minimization problem.

A test of the fit quality can be conducted on  $\chi^2$ . There exist statistical tests to calculate the probability that the data is well described by a given model. A quick indicator that the model reproduces the data can be obtained considering the *reduced*  $\chi^2$  parameter :

$$\chi_r^2 = \frac{\chi_{min}^2}{r},$$

where  $r = N - p = (\text{number of data points}) - (\text{number of fit parameters})$  is the number of degrees of freedom. A good match between the data and the model occurs when  $\chi_r^2 \simeq 1$  as, for a good agreement, each data point differs from its expected value by about the standard error. Therefore, each term in the sum of the  $\chi^2$  statistics should be of order one, with the result  $\chi_{min}^2 \simeq N$ . As the number of degrees of freedom is almost equal to the number of data points in our fits,  $\chi_r^2$  is expected to be close to unity. If  $\chi_r^2 \gg 1$ , the model should be rejected. If  $\chi_r^2 \ll 1$ , the error bars have probably been overestimated. In our case,  $0.8 < \chi_r^2 < 3$  depending on the dataset.

Practically, one fit as takes on the order of several minutes. We repeat the fit procedure typically 5 times, starting from different initial guesses for the parameters randomly distributed between appropriate values. Finding the best-fit parameters requires about 10-20 minutes with this fit method.

#### 4.7.4 Error estimation

Once the best-fit parameters are obtained, we look for the uncertainty of the fit by estimating the variances and co-variances of the different parameters and deduce from them the confidence intervals of the fit. The simplex algorithm, as explained above, does not rely on any gradient or second derivative to find a minimum, and therefore does not automatically yield information about certainty of the result as would derivative-based methods. Nevertheless, it is possible to estimate a confidence interval around the best-fit value. One option is, in the case the function is well-behaved around the best-fit parameters, to estimate the Hessian matrix at this point. This is the (square) matrix of second-order partial derivatives for the (scalar-valued) function of interest. From this

matrix, information about the best-fit point can be retrieved (e.g. if it really is the minimum in that region) and the confidence intervals calculated.

The Hessian matrix  $H$  is the same as the information matrix in statistical problems. The covariance matrix, or error matrix,  $C$  is given by  $C = 2H^{-1}$ . The elements of the covariant matrix then quantify the statistical errors on the best-fit parameters and the square-root of its diagonal elements give information on the uncertainty of the fits,  $\alpha_i = \sqrt{C_{ii}}$ . In order to calculate a valid Hessian, the function must be convex around the best-fit parameters. In general, a continuous and twice differentiable function is convex if and only if its Hessian matrix is positive semidefinite. More visually, a twice differentiable convex function will only “curve up” and not present inflection points. Getting a visual representation of the six-dimensional function being impossible, we can only check the convexity in a few directions. We make sure that the numerical approximation of the Hessian matrix gives only positive values (proof that we found a minimum) and small uncertainty in the evaluation<sup>4</sup>.

Finally, the deviation from the best-fit values are given by the confidence intervals on each parameter:

$$CI_i = [x_i - t^* \sqrt{C_{ii}}; x_i + t^* \sqrt{C_{ii}}] \quad (4.17)$$

where  $x_i$  are the best-fit parameters. The factor  $t^*$  is given by Student’s  $t$ -distribution and depends on the confidence limits one wants to calculate (deviation of  $1\sigma$ ,  $2\sigma$ ...) as well as on the degrees of freedom. Note that calculating the covariance matrix brings more than simply evaluating the change in residual for each parameter individually. This second method only gives the true confidence intervals if the parameters are uncorrelated. In the presence of correlations between uncertainties, each individual interval calculated individually tends to underestimate the span of the true confidence interval. It would correspond to a case where the Hessian matrix is diagonal. For a non-diagonal Hessian, performing the matrix inversion is necessary.

The combination of a simplex algorithm and a Hessian estimation is not a standard approach, but it yields sensible and reproducible results for the analyses we carried out. Other, more standard approaches exist, like the Monte-Carlo or the bootstrapping methods. Unfortunately, they require to generate and fit many datasets. “Many” is typically several thousands and in our case, this requires very long computational times. Moreover, they rely on assumptions such as the statistical distributions of the parameters or the absence of correlations between the parameters, which we cannot assume here.

## 4.8 Experimental results

To gather detailed experimental data, we measure the momentum density distributions with a sampling time of  $t = 0.025$  ms, averaging over 5 repetitions for each time. This is enough to get a good readability of the interference patterns on the integrated momentum distribution plots. The fitting procedure is then carried out on the first millisecond after

---

4. Can be computed using the package DERIVEST developed by John D’Errico, also available for free on the MATLAB File-exchange website.

the transfer. This time limit for the fit is set to avoid including the detrimental effects leading to a decay of the contrast in the interference patterns (see chap. 6).

For the transfer to a balanced superposition  $\frac{1}{\sqrt{2}}(|0\rangle + |1_y\rangle)$ , the fit for the experimental dataset used in the next chapter yields  $p_0 = 50\%$  and  $p_1 = 46\%$ . This corresponds to a fidelity of  $\mathcal{F}^{half} = 96\%$ . As can be seen in fig. 4.14, the qualitative agreement is also very satisfactory. The confidence interval at  $1\sigma$  (68% confidence range) is estimated to 3% on  $p_0$  and  $p_1$ , while the  $2\sigma$  confidence interval (95% confidence range) is estimated to 6%. The relative phase between ground and first excited state is  $\phi_{01} = -0.03\pi$ . Even better result have been obtained recently, with a fidelity of  $\mathcal{F}^{half} = 99\%$  for a transfer time of 1.09 ms.

For a full transfer to the first excited state, the fidelity of the transfer reached is  $\mathcal{F}^{full} = (99.3 \pm 0.6)\%$ . This number is the population in  $p_1$ . The other states' populations are  $p_0 = (0.3 \pm 0.2)\%$  and  $p_2 = (0.4 \pm 0.3)\%$ . With this pulse, we verified experimentally the robustness to changes in atom number for  $N \in [300, 2000]$  and retrieved a behavior very similar to fig. 4.8 (left, full red line).

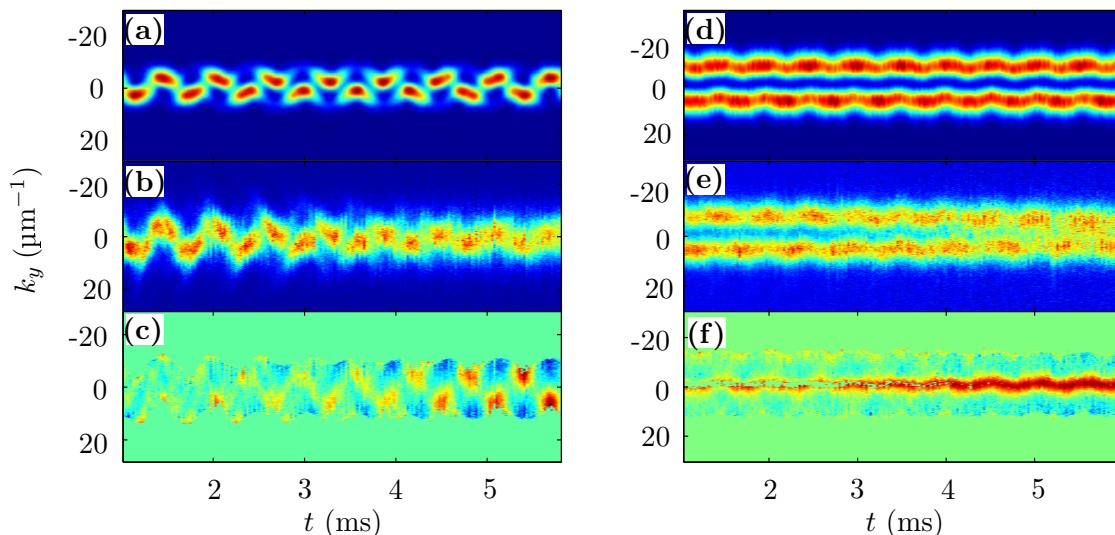


**Figure 4.14: Comparison between simulated and experimental density distributions after transfer.** (Left) Half transfer. (a) Best fit GP momentum distribution during the first 1 ms. (b) Experimental momentum distribution. (c) Residual (i.e. sum-of-square of the distance between fitted and experimental momentum distributions). (Right) Full transfer. (d), (e) and (f) similar to (a), (b) and (c).

In both cases, the reduced  $\chi^2$  is  $< 3$ , showing that the model is good but could be improved. It is possible that a small fraction of the atoms were excited to higher levels during the transfer process. However, to stay within an acceptable range of parameters for the algorithm, we are limited to a 3-mode model. A significant proportion of atoms coherently excited to a higher state would nevertheless appear in the density patterns as an additional interfering wavefunction, which is not observed. We also note that these fits are based on Gross-Pitaevskii simulations, which represent a unitary evolution for

a mean-field description of a system at zero temperature. Some discrepancy between the model and the experiment (e.g. many-body or finite temperature effects) may have systematic effects on the estimation of the parameters. As the model describes well the main features of our data, it is nevertheless unlikely that these discrepancies have a qualitative effect on the results.

In conclusion, the application of optimal control strategies to the manipulation of quantum motional states proved to be very successful in this work. Following a trajectory optimized by the CRAB algorithm, the sudden displacement of the trapping potential could lead to transfers between two motional states of the condensate, reaching a target state with high efficiency and on very short times. In two examples, one of a full transfer from ground state to first excited state, one of a half transfer from ground state to an equal superposition of ground and first excited state, transfer pulses with theoretical fidelities  $\geq 99\%$  for pulse lengths  $< 1.1$  ms were optimized. Experimentally, fidelities  $\geq 96\%$  were measured on the resulting time-of-flight momentum distributions. These methods are now available for developments and studies. In chap. 5, we pushed the pulse optimization concept further and implemented a whole interferometer sequence with two pulses. In chap. 6, we show how this pulses give access to the complex dynamics of out-of-equilibrium state superpositions.

# 5

## Application to interferometry: the motional states interferometer

In this chapter, we present a concept of interferometer based on the motional states of a Bose-Einstein condensate. This interferometer relies on the optimized pulses described in the previous chapter. First, the general ideas behind interferometers and their applications to cold atoms are introduced. In a second section, we then give more details about the motional state interferometer and how it relates to the concepts developed by Ramsey for molecules. In sec. 5.3, the optimization of the pulses for the specific purpose of the interferometer is detailed. Finally, the results of the experimental implementation are given in sec. 5.4. The results of this chapter are published in ref. [116].

### 5.1 Interferometry with Bose-Einstein condensates

When they meet, waves can combine constructively or destructively, forming a crest and trough pattern. They are said to interfere. Interference phenomena are common and can take place in many circumstances. They are for example observed on the water surface or with light. The important notion with interferences is that although intensities are measured, what is summed is the amplitudes of the waves. The interference patterns represent the squared sum of the amplitudes. This property lead to the surprising result that two overlapping waves, if they are locally out-of-phase, can simply result in no intensity at all at that point. Therefore, the phase of each wave, or rather the phase difference between the waves plays a dominant role.

This property is of great interest, and interferometers are continuously developed to study or make use of it. Generally speaking, an interferometer is a device capable of measuring minute changes in phase difference, using the evolution of interference patterns. When combining two waves with a fixed relative phase on such a device, the constructive or destructive interference is measured as an increase or a decrease of the intensity signal.

A retardation or shift in the phase of one of the waves, due for example to changing environmental conditions, leads to a change in the measured output intensity, which can be quantified. If the cause of the phase shift is known, it can be measured this way with high precision.

Quantum-mechanical wavefunctions can also overlap and interfere. Given the right experimental conditions, matter exhibits wave-like behavior, and so atomic wavefunctions have the potential to be used for interferometry, similarly to light. Whether matter-wave interference is observed or not depends in part on the de Broglie wavelength of the particle. It was hypothesized by Louis de Broglie in his PhD thesis in 1924 [154] that the de Broglie wavelength of an electron is associated to its momentum  $p$  through the Planck constant  $h$  by the formula:  $\lambda_{\text{dB}} = \frac{h}{p}$ . As it is now well known, all types of matter obey this rule. To realize an interferometer with matter instead of light is therefore possible. For this, an incoming beam must be coherently split, then recombined. If each path is exposed to different influences, a relative phase is gained which is read out after recombination. The advantage of using atoms as opposed to light is that they are sensitive to external forces, such as electromagnetic fields or gravity, which is not the case — or very weakly — for photons. They are potentially better sensors for precision measurements in situations where such forces are involved. For example, a caesium atom interferometer can potentially measure rotations with a sensitivity  $10^5$  better than a laser ring gyroscope [155], and a gain of  $10^4$  on measuring accelerations [156]. The second condition for interferometry to be effective is that the recombined waves have as much as possible a stable phase relation between them. The quality of the interference pattern and thus the measurement accuracy depend on the degree of coherence of the input waves. Both spatial coherence and temporal coherence are important.

In a historical perspective, the development of matter-wave interferometers has faced two major challenges. First, typical de Broglie wavelengths of most particles at common temperatures, given by  $\lambda_{\text{dB}} = \frac{h}{p} = h/\sqrt{2\pi m k_{\text{B}} T}$ , are much less than a nanometer. This means equivalently a very short coherence length, which makes it difficult to observe wave-like behavior. The first experiments were realized with low-mass particles such as neutrons and electrons, which have a relatively large de Broglie wavelength [157, 158]. Second, atoms are absorbed or scattered by solid materials, so there are no such things as solid mirrors or beam-splitters for atoms. Although diffraction from surfaces or gratings were initially used — and still are — in atomic interferometry experiments [159, 160], the development of lasers in the 1960's was a significant step forward in the advancement of the field and the resolution of both major issues. Laser-light interaction with atoms led to the development of laser cooling [161, 162], by which the de Broglie is notably increased, and atom trapping [16, 163–165], while analogs of mirrors and gratings appeared in the form of “light gratings” [166, 167].

In parallel, Rabi demonstrated the coherent manipulation of internal states of atoms using resonant radio frequency [168]. His work was followed by Ramsey's creation of long-lived coherent superposition of quantum states [169]. Put together, these various techniques led to the development of matter-wave interferometers, with applications in precision measurement of inertial effects (gravimeters, gyroscopes or gradiometers),

frequency and time (atomic clocks [170]) or fundamental constants (Newton's constant  $G$ , fine structure constant).

Altschuler and Franz first patented the concept of a matter-wave interferometer in 1973 [171], followed by several proposals of possible experimental realizations [172–175]. The first experimental cold-atom interferometer, set up by Chu and co-worker [176, 177], used stimulated Raman transitions. Although this kind of interferometers remains prevalent, many other types have been explored and developed. Many use cold atoms and light gratings, either continuous or pulsed; some consist in splitting and generating interferences between different internal states (e.g. the Ramsey interferometer), between momenta (e.g. the Bragg interferometer) or both (e.g. the stimulated Raman or the Ramsey-Bordé interferometer); some classify as near-field (e.g. the Talbot-Lau interferometer) or far-field interferometers (e.g. the Mach-Zehnder interferometer). A systematic categorization of all interferometers is a substantial task with so many different types around, but a good review on the subject was written by Cronin and Pritchard in 2009 [178].

A subfraction of atom interferometers use trapped atoms or BECs. A big advantage of having trapped atoms instead of atoms flying in free space is that there is no effect of gravitational fields on the trajectories, and no expansion. The time that can be allocated to the measurement is significantly increased, which improves the quality of the measurement. As for free space interferometers, trapped atoms and BEC interferometers consist in splitting and recombining internal or external states, with the purpose of reading-out a phase difference. The external states in the trapped case are actually obtained by transforming the initial trapping potential into a double-well structure, so the splitting occurs in position space and not in momentum space like other external state interferometers. Such interferometers, called “double-well interferometers” can be achieved with high accuracy on atom chips. This has been demonstrated using static magnetic fields in combination with radio-frequency [103, 108], optical [179], or microwave fields [109]. As the location of the atoms is well defined, these interferometers can be used to probe atom-surface interactions like the Casimir effect or to study fields varying on short distances.

With their low temperatures, Bose-Einstein condensates are well-suited to observe interferences. Moreover, they present a homogeneous phase. As predicted theoretically in [180, 181], at zero temperature, an atomic gas is a coherent state that can be described by a classical field  $|\Psi_0|e^{i\phi}$  with a well-defined amplitude  $|\Psi_0|$  and a phase  $\phi$  associated with this coherent state. The phase of a condensate, being the argument of a complex number and not an observable, cannot be probed directly, but a relative phase can be measured. Andrews and coworkers demonstrated experimentally the spatial coherence of a BEC in 1997 [182]. As for the temporal coherence of BECs, it is experimentally limited by phase diffusion at non-zero temperatures and fluctuations of atom number. However, measurements have shown the robustness of the relative phase [183–185].

A particularity of BECs in the interferometer world is that they exhibit non-negligible atom-atom interactions. These interactions lead to mean-field shifts and dephasing effects, which tend to limit the interrogation time of trapped interferometers. However,

interactions can also generate non-classical correlations between atoms [184, 186, 187], and lead to an improvement of the phase sensitivity beyond the standard quantum limit. It can also reduce the effect of interaction-induced dephasing [108]. Altogether, BECs are still under investigation to determine whether or not they make good candidates for high-precision measurements [188, 189]. This field of research is active and novel types of interferometers are regularly proposed, like the one we present in this chapter.

## 5.2 Concept of a Ramsey-type interferometer for motional states

### 5.2.1 The well-known Ramsey interferometer

In the 1930's, Isidor I. Rabi discovered nuclear magnetic resonance and demonstrated an apparatus for magnetic resonance [129, 168, 190, 191]. Norman F. Ramsey, a graduate student of Rabi at the time, wanted to improve the measurement accuracy and in 1949 invented the separated oscillatory fields method [169, 192, 193]. The setup, represented in fig. 5.1 (top left), differs from the original setting by the presence of two oscillatory fields in the central region, where in Rabi's apparatus there was only one oscillatory field.

A molecular or atomic beam initially propagating through the central region experiences, in addition to a static magnetic field, two phase-stable microwave pulses that coherently split, then mix two nuclear spin angular momentum states of the particles. The length and intensity of each pulse are adapted to correspond to two " $\pi/2$  pulses", i.e. pulses that rotate the angle between the angular momentum and the oscillatory field by  $\pi/2$  radians. The two zones where interaction with the magnetic field occurs are short and separated by a long zone without interaction.

Upon entering the first interaction zone, the particles are all in the same angular momentum state. After passing this first zone, the ensemble is in an equal superposition of both momentum state. In the intermediate region, the magnetic moment simply precesses at the Larmor frequency imposed by the static field. In the second interaction zone, if the frequency of the oscillatory field is exactly the Larmor frequency, there is no delay or phase shift between the oscillatory field and the angular momentum. In this case, an oscillatory field of the same length and intensity as the first one — another  $\pi/2$  pulse — completely reverses the direction of the angular momentum compared to the initial one. If the frequencies differ slightly, the fields gets out of phase with the Larmor precession and the result will be a coherent mixture of both angular momenta. The ratio of particles in one or the other momentum state depends on the phase shift accumulated before entering the second zone, thus on the frequency difference between the oscillatory field and the Larmor frequency. In the end, one observes a sinusoidal variation of the probabilities to find the particles in one or the other state when the frequency (or the phase) of the microwave pulses is scanned across resonance. These sinusoidal pattern is often called "fringes", as illustrated in fig. 5.1 (top right).

Similar setups are still being developed and applied to different problems with great success. A famous example is the atomic clock, which was relying on a microwave

transition between two atomic hyperfine levels, and is now applied similarly using electronic transitions in so-called optical clocks. The time is set by locking the microwave or optical frequency to an atomic transition. Another famous example is the work of Serge Haroche, who received Nobel Prize in 2012 (together with David Wineland) for his experiments on photon counting in a cavity, which also rely on a Ramsey setup [194, 195]. There, photons are counted by measuring the perturbation they produce on the Ramsey fringes.

In many versions of the Ramsey interferometer, the central idea is that the internal state is affected by external fields and undergoes transitions, as pictured in fig. 5.1 (bottom left). The external degree of freedoms are not considered. However, the absorption and the emission of a photon is accompanied by a recoil, and thus the particles gain or lose momentum. The wave packet can be split or recombined in space, as shown in fig. 5.1 (right), making the Ramsey pulses a close analog to the beam splitters used in optics. Christian J. Bordé was the first one to propose a spatial version of the Ramsey interferometer, where different external paths are labeled by different internal states [174]. This kind of interferometers requires at least one additional pulse to form a closed area — Bordé’s proposal was with four pulses —, but has the advantage that it can probe inertial effects.

We propose here a scheme following the spirit of the temporal Ramsey interferometer, with a kind of state that was not studied before: the non-classical motional states of a BEC. The specific “beam splitters” for this type of states are developed and tested. More than a demonstration of precision measurement, what we show here is a proof-of-principle.

### 5.2.2 Transposition to motional states of a BEC

As described in the previous chapter, we developed a scheme to split the BEC wavefunction into two wavefunctions with different intrinsic motion, that we call motional states. The scheme, depicted in fig. 5.2 (top), consists in displacing the trapping potential and thereby modifying the wavefunction, following an optimized trajectory. The idea is to combine two of these displacement pulses to build an interferometer. They would be equivalent to optical beam splitters, but for motional states of ultracold atoms. There are however some differences to take into consideration compared to other atom interferometers.

The first “beam splitter” was described in chap. 4 in the form of a half transfer pulse. This pulse splits an initial wavefunction - the transverse ground state of the trapping potential - into two parts corresponding to the ground state and to the first excited state of the transverse potential with a controlled and reproducible relative phase. They represent the two “paths” of the interferometer after the first beam splitter. In a simplified two-level picture, this can be represented on the Bloch sphere<sup>1</sup> of the two states as a  $\pi/2$  pulse or  $90^\circ$  rotation from the ground state  $|0\rangle$  to an equal superposition of ground state  $|0\rangle$  and first excited state  $|1_y\rangle$  with a fixed relative phase. This is represented in

1. The Bloch sphere is a geometrical representation of the pure state space of the two-level quantum system.

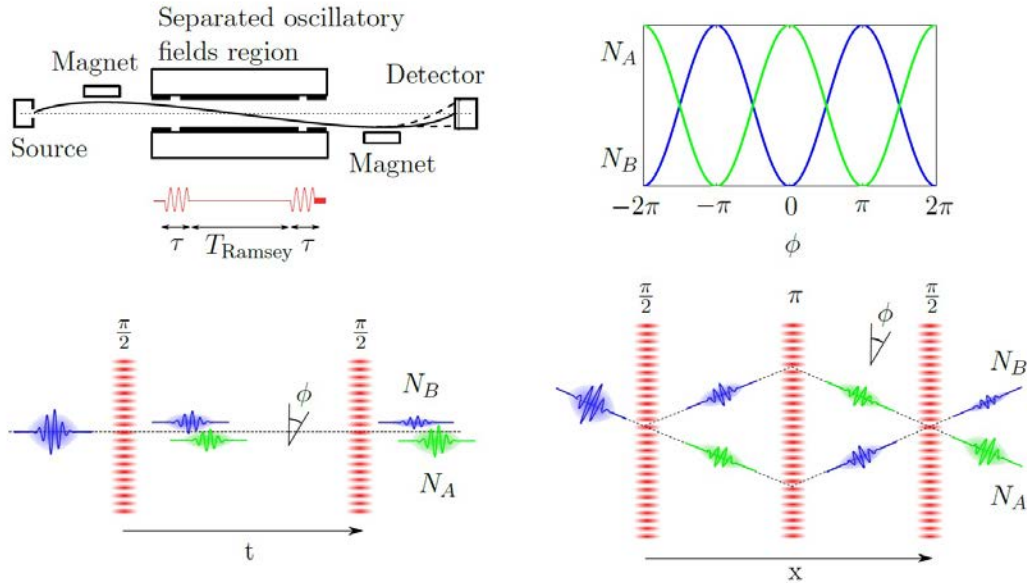


**Figure 5.1: Different versions of the Ramsey interferometer.** (Top left) Original Ramsey setup of separated oscillatory fields. Molecules emerge from the source, are deflected by an inhomogeneous field produced by the first magnet, pass through the separated oscillatory field region and are finally deflected towards the detector by the second magnet. In the separated oscillatory fields region, microwave pulses act for a time  $\tau$  and are separated by a time  $T_{\text{Ramsey}}$ . The strength of the deflection at the second magnet changes with the molecular state after the two pulses, which in turn depends on the amplitude and length of the pulses.

(Bottom left) Temporal Ramsey interferometer. The wave packet is coherently split by a first  $\pi/2$ -pulse into two components with different internal states. This interferometer is sensitive to state-dependent phase shifts. Depending on the different phase accumulated between the two components, the recombination at the second  $\pi/2$ -pulse yields a different final superposition of the two components.

(Bottom right) Spatial Ramsey interferometer, also referred to as Ramsey-Bordé interferometer. The incoming wave packet is coherently split by a first  $\pi/2$ -pulse into two components with different momenta, so they get spatially separated. The intermediate  $\pi$ -pulse acts as a mirror to allow recombination at the second  $\pi/2$ -pulse. This interferometer is sensitive to inertial effects.

(Top right) Illustration of the variation in populations in each state or “fringes” seen at the output of an interferometer as the  $\phi$  varies.

fig. 5.2 (bottom) as action (1). It should be reminded that this step relies heavily on the successful optimization of the half transfer pulse for this specific purpose. Because higher levels of the potential are accessible, a non-optimal displacement can lead to more states populated than the two desired ones at the end of the pulse. The analysis (see chap. 4) showed that the beam splitter has the desired behavior, with an almost perfect splitting between ground and first excited state and only 4% losses. The fact that these

two states interfere after splitting shows that the splitting is done coherently.

After the splitting, the two parts of the wavefunction are held in the trap at rest, where they spatially overlap. The phase difference between the two paths of the interferometer evolves during this time. It accumulates due to the different energies of the different vibrational levels of the potential:  $\Delta\phi = \phi_1 - \phi_0 = E_{01}^{\text{eff}}t/\hbar$ . Again in a simplified picture, this would correspond to step (2) in fig. 5.2 (bottom), a rotation around the vertical axis of the Bloch sphere.

In principle, a second beam splitter then converts the accumulated relative phase a relative population for read-out. In the present interferometer, this role is assumed by a second displacement pulse that acts as a mixing beam splitter between the two wavefunctions. This action can be visualized as step (3) in fig. 5.2 (bottom), a point on the equator being transformed by a  $\pi/2$  pulse into a different superposition, still lying on the surface of the Bloch sphere. This second beam splitter is more demanding than the first one: as in optics, to be able to make sense of the output of the interferometer in terms of accumulated phase, the ratio of populations of the wavefunctions must depend in some way, typically sinusoidally, on the relative phase. In other terms, we would expect to see some oscillation for each state's population, or "fringes", as we increase the interrogation time.

However, the system at hand is more complex than a coherent photon beam going through a physical beam splitter, in which only two states are coupled. The first reason for this is the transfer process used as a beam splitter. As already mentioned, during the displacement, transfers can occur between several accessible energy levels, therefore the real process is not a simple exchange of particles by interference between two paths. It is not a priori obvious that a transfer pulse optimized for a given relative phase would work for any relative phase so that the output would always be a superposition of the two first trapped states. The second reason is that the particles have inter-atomic interactions, which impact both states individually, but also introduces cross-talks between the two states due to the spatial overlap. As shown in chap. 4, these interactions imply an additional dynamics of the wavefunction and transfers between motional states. This could affect the amplitude and/or the shape of the fringes.

The question is then whether or not it is possible to optimize a second beam splitter that would work for every relative phase. A strict analytical proof is hardly conceivable. A reasonable guess would be that the effect of interactions will lead to a degradation of the fringes, but as interactions are small in our system, there is a high chance that some fringes will appear. To answer the question more quantitatively, we turn again to the CRAB algorithm.

### 5.3 Optimization with the CRAB algorithm

The optimization of the first beam splitter of the interferometer was already explained in chap. 4. The second beam splitter can be designed using the same optimal control algorithm as before, only the target is not anymore a given motional state. Instead, we need to optimize a sort of operator for states within the two-level space formed by

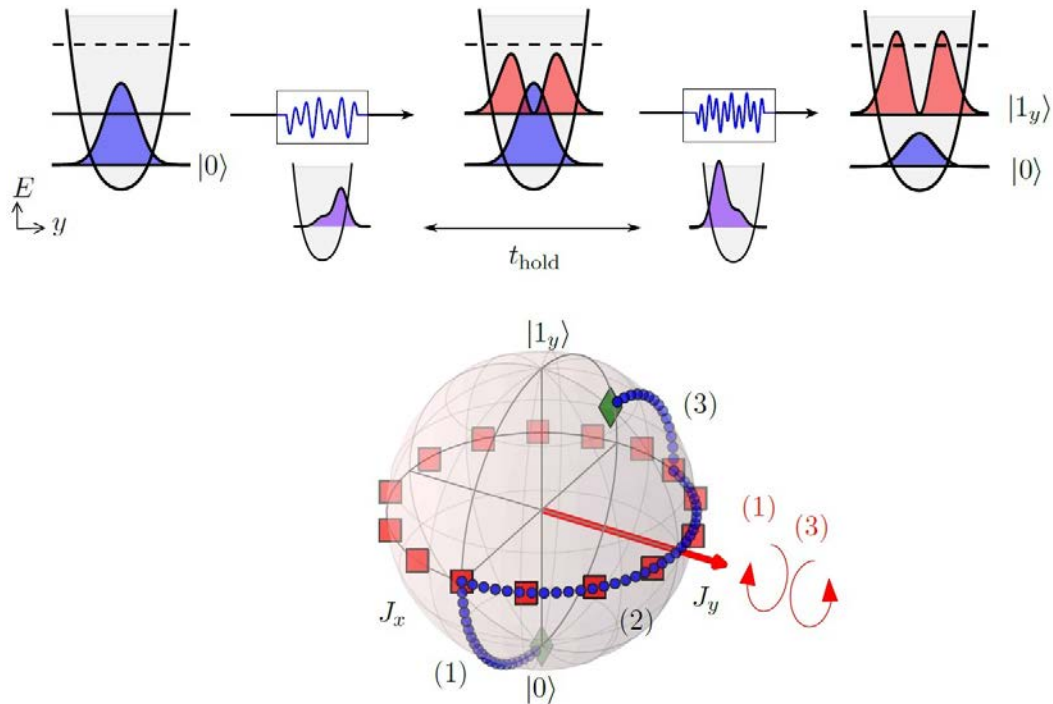


**Figure 5.2: Motional state interferometer.** (Top): Steps of the interferometric sequence. The condensate is initially in the ground state  $|0\rangle$  of the transverse potential at rest. A first pulse displaces the potential and generates a splitting of the initial wavefunction into a coherent, equal superposition of  $|0\rangle$  and  $|1_y\rangle$ . The potential remains at rest for a duration  $t_{\text{hold}}$ , during which a relative phase accumulates between the two states. A second pulse displaces the potential, recombining the system into a new coherent superposition of  $|0\rangle$  and  $|1_y\rangle$  depending on the accumulated relative phase.

(Bottom) Bloch sphere representation of a trajectory (blue dots) within the two-level subspace of motional states during the interferometric sequence. (1) is the first pulse that prepares a balanced coherent superposition. (2) is the phase accumulation time corresponding to a rotation around the vertical axis. (3) is the second pulse and corresponds to a  $90^\circ$  counter-clockwise rotation around  $J_y$ . The red squares show the points on which the second pulse was optimized.

the ground and first excited states. Therefore, the figure of merit has to be rethought. Moreover, the optimization relying on a state comparison, it has to be carried out for many initial states.

### 5.3.1 “Visibility” as figure of merit

For the second beam splitter, we do not consider a state-to-state transfer anymore. The figure of merit has to translate a new goal, which is to see interference fringes. To optimize the second pulse of the interferometer, two options present themselves:

1. to optimize a general  $\pi/2$  pulse;

2. to target the highest amplitude of the fringes.

The first option resembles the concept of the usual Ramsey interferometer. It is also more demanding in terms of constraints and computational time, as it aims for a one-to-one mapping of the whole Bloch sphere with sufficient density. However, for the interferometer scheme proposed here, the pulse needs only be efficient for equal superposition states with any relative phase. With this end in view, it is enough to optimize a pulse for the states lying on the equator of the Bloch sphere. For a non-interacting system, the result of both optimization methods would be similar, as an operator optimized for two orthogonal states would work for any superposition of them. For an interacting system this is not the case. Interactions introduces a non-linear coupling between motional states, and it is unclear whether a single pulse can be found that realizes transfers with high efficiency for all superpositions<sup>2</sup>. Opting for the second approach puts the emphasis on the amplitude of the fringes, leaving the exact shape of the fringes unconstrained. In the perspective of a precision measurement, this approach would also be more interesting. For these various reasons, we carried out the optimization based on a visibility criterion.

A good visibility requires an important variation of the populations in ground state and first excited state, with the constraint that the system remains within the two-level space. Therefore, we define here the figure of merit as:

$$\begin{aligned} \mathcal{J}^{(2)} = & |1 - \max_{t_{\text{hold}}} (p_0) + \min_{t_{\text{hold}}} (p_0)| \\ & + |1 - \max_{t_{\text{hold}}} (p_1) + \min_{t_{\text{hold}}} (p_1)| \\ & + \max_{t_{\text{hold}}} (1 - p_0 - p_1) \end{aligned} \quad (5.1)$$

where  $p_0$  (resp.  $p_1$ ) is the ground state (resp. first excited state) population at the end of the second pulse, and the maximum is taken over several different values of the phase accumulation time  $t_{\text{hold}}$  for which the numerical optimization was performed. Varying  $t_{\text{hold}}$  instead of the phase is a natural way to introduce the effect of interactions into the optimization. The first and second terms maximize the amplitude of the oscillation of  $p_0$  and  $p_1$  respectively. The third term of eq. (5.1) minimizes the transfer of population to higher energy levels. This is necessary as the system is not strictly closed and many motional states can be populated during the transfer process.

### 5.3.2 Optimized second pulse

Once an appropriate figure of merit was defined, the optimization itself was carried out in a fashion similar as for simple state-to-state transfer, but starting from several states on the equator of the Bloch sphere. The choice was made to optimize the second pulse of the interferometer for 15 points describing the first oscillation period. The obtained pulse has a duration of 1.6 ms and yields a value for the figure of merit of  $\mathcal{J}^{(2)} = 0.3695$ , in which all three terms in eq. (5.1) contributes roughly by the same amount.

---

<sup>2</sup> For the same reason, simply applying a time-reversed version of the first pulse does not lead to good results.

The optimized pulse and the expected output fringes for the whole interferometric sequence are shown in fig. 5.3 and in fig. 5.4(b). As for the shape, we observe an oscillation of  $p_0$  and  $p_1$  as a function of  $t_{\text{hold}}$ . It has a periodicity of 0.58 ms, in agreement with the effective level splitting evaluated in sec. 4.3.1. The shape of the fringes at the end of the optimization is, as would be expected in the usual Ramsey interferometer, close to a sine wave. This is true for long holding times although the optimization was only carried out on the first fringe. A small deformation is visible on all fringes, which is due to interactions. As shown in Fig 5.4(c), a small fraction of the atoms, on the order of  $p_{\text{res}} \sim 10\%$ , is transferred to higher excited states. This indicates that the optimization of the second pulse, which consists in finding a good compromise for all points on the equator of the Bloch sphere, fails to completely bring back the wavefunction within the lowest-two-level subspace.

When applying this pulse to the wavefunction, the displacement observed is again important, as for the first pulse, but still well described by a GPE. Simulated evolutions of the momentum distributions during the two pulses of the interferometer are compared in fig. 5.3 to the experimentally observed densities in time-of-flight. We observe similar behaviors in both cases.

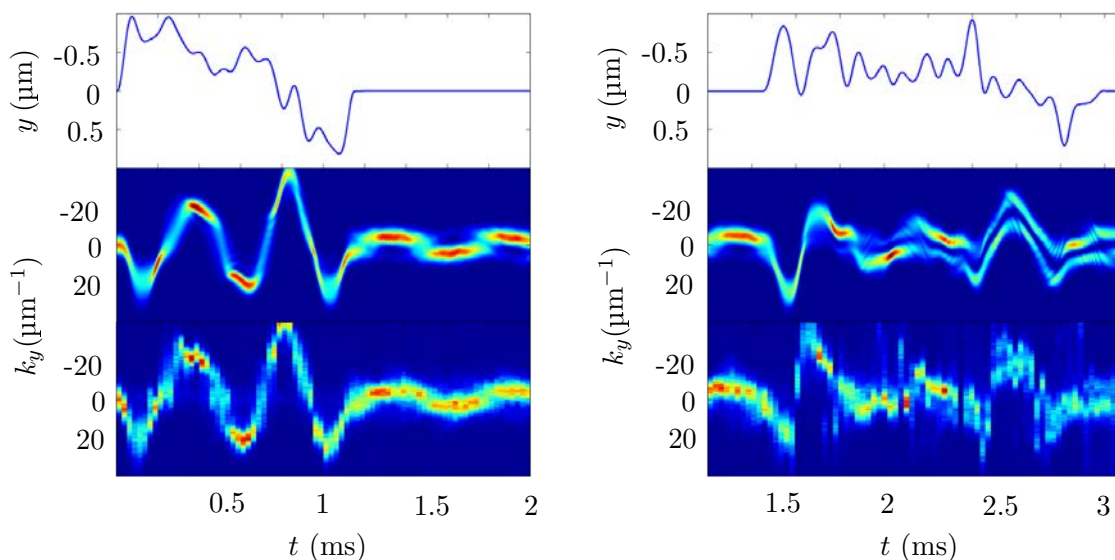


**Figure 5.3: Two optimized pulses and corresponding momentum distributions.** (Left) First pulse of the interferometer, showing the optimized displacement pulse (top), the evolution of the momentum distribution under the action of the pulse as simulated with GPE (middle) and the evolution of the experimental profiles measured in time-of-flight (bottom). (Right) Second pulse of the interferometer, with evolutions measured after a phase accumulation time  $t_{\text{hold}} = 0.25$  ms. The  $x$ -axis shows the absolute time  $t$  starting at the beginning of the interferometric sequence.

## 5.4 Result of the interferometer

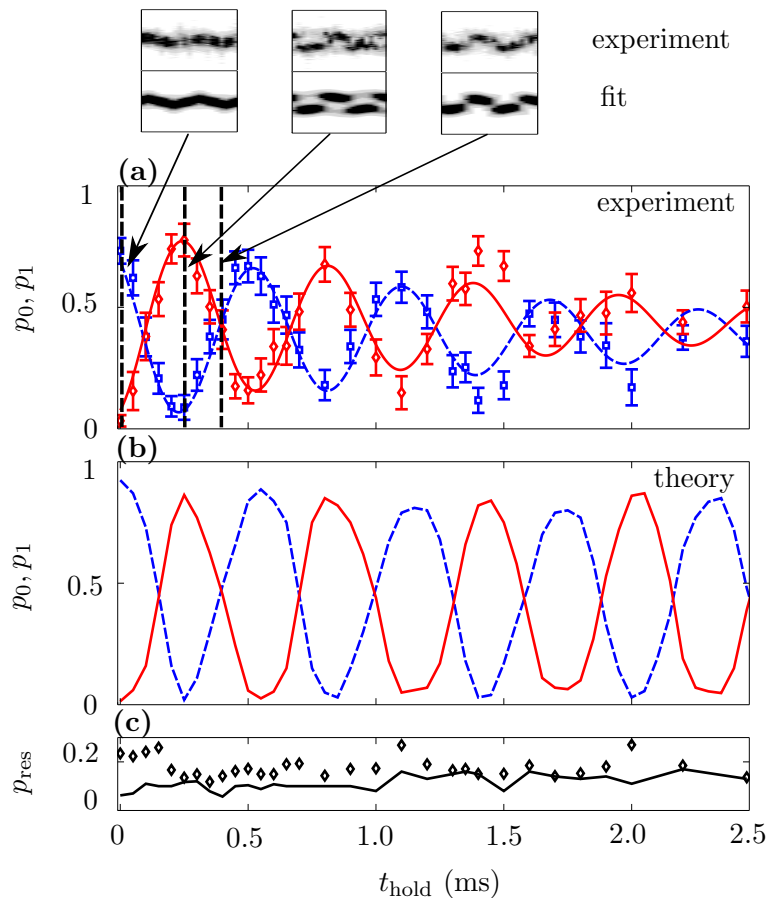
At the end of the CRAB optimization procedure, as already indicated, the figure of merit of the interferometer reached  $\mathcal{J}^{(2)} = 0.3695$ . To be able to compare the simulation results with the experimental results, we define a new “experimental” figure of merit which is the contrast. Common in the interferometry community, the contrast is defined as  $\mathcal{C}(p_i) = \frac{\max(p_i) - \min(p_i)}{\max(p_i) + \min(p_i)}$  ( $i \in 0, 1$ ). The theoretical contrast of the optimized motional state interferometer is  $C(p_0) \approx C(p_1) \approx 97\%$ .

Figure 5.4(a) shows the experimental interferometric signal, where  $p_0$  and  $p_1$  are obtained by the same state analysis method as described in chap. 4. Each point on this graph represents one fit to a momentum distribution evolution, as the ones shown in the insets. The populations are extracted by the same method presented in sec. 4.7. With 5 repetitions, each point therefore consists of 200 data point or 2 hours of measurement. In this dataset, the displacement was driven using the DP400 (see chap 3).

Fringes with a shape close to a sine wave appear, as the solid lines emphasize. Qualitatively, the experimental results are in good agreement with the numerical simulations on the first interferometric fringe: the shape is similar, the period and the initial phase of the oscillation match. Quantitatively, the contrast reaches  $C = (92 \pm 5)\%$ , and the Ramsey period measured is  $(0.57 \pm 0.02)$  ms. The fit residuals, interpreted as a population in higher excited states and possibly an incoherent fraction, amount to 15%–25% depending on  $t_{\text{hold}}$ .

It is worth mentioning that the holding times  $t_{\text{hold}}$  chosen for the experiment — corresponding to 12 points within one period — differ from the ones used for the numerical optimization of the second pulse. The results match nevertheless. This indicates that the pulse is valid for all points on the equator of the Bloch sphere, not only for the 15 points it was optimized on. In that sense, we believe to have a “real  $\pi/2$  pulse” for the points on the equator of the Bloch sphere.

A basic estimation of the phase sensitivity of this interferometer can be carried out from the slope of the fringes compared to the uncertainty of the measured populations. As illustrated in fig. 5.5, the projection of the error bar on the fringe gives an estimation for the phase uncertainty. Both the steepness of the slope and the population uncertainty play an important role. The sensitivity is best measured at the point of steepest slope, which corresponds here to the average value of the fringes, or the offset of the fitted sine. The first crossing of the fringes with this level occurs at  $t_{\text{hold}} \approx 0.1$  ms. At that point, the uncertainty on the population projected on the time is  $\sim 0.016$  ms (dark grey zone in fig. 5.5). This is equivalent to an error on the phase estimation of  $\phi = 2\pi\nu_{01}t_{\text{hold}} \approx 0.1$  rad. As  $t_{\text{hold}}$  increases, this error amplifies due to the reduction of the fringes’ amplitude. After 3 fringes, the error becomes  $\phi \approx 0.3$  rad (light grey zone in fig. 5.5). The phase can also be evaluated directly on the superposition after the first pulse of the interferometer, by a fit to the momentum distribution as explained in sec. 4.7. The uncertainty on the phase determination is estimated to  $\phi \approx 0.25$  rad for fits on 2 periods, and  $\phi \approx 0.15$  rad for more than 4 periods. The interferometer performs therefore better than the direct fit



**Figure 5.4: Interference fringes of the motional-states interferometer.** (a) Experimental data. Populations of the ground state  $p_0$  (blue circles) and first excited state  $p_1$  (red diamonds), extracted from a fit to the experimental density images, as a function of the phase accumulation time  $t_{\text{hold}}$ . The error bars indicate the  $1\sigma$  confidence interval of the fit. The blue and red dashed lines are exponentially damped sines. (b) OCT optimization data. Populations of the ground state  $p_0$  (blue dashed line) and first excited state  $p_1$  (red line) as a function of the phase accumulation time  $t_{\text{hold}}$ . (c) Populations in higher excited states in the optimization (black solid line) compared to residual part in the fits to experimental data (black diamonds). The top insets are examples of experimental momentum distributions (upper row) and their corresponding fitted GPE momentum distribution (lower row) for the 3 different hold times indicated by the vertical dashed lines in panel (a).

to estimate the phase in the limit of short holding times  $t_{\text{hold}}$ .

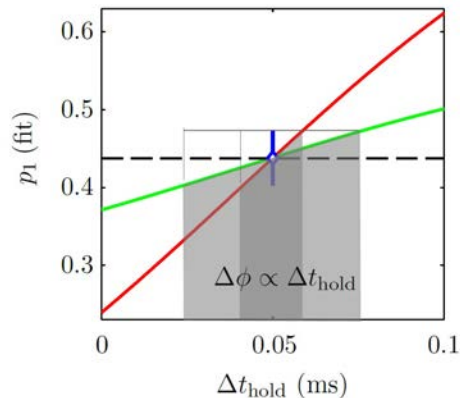


**Figure 5.5: Phase sensitivity of the interferometer.** The phase sensitivity, proportional to the sensitivity on  $t_{\text{hold}}$  (grey zones), depends both on the slope of the fringes (lines) and the uncertainty on the population, e.g. the population of the first excited state  $p_1$  (blue error bar). In this interferometer, the slope of the fringes is better for the first fringe (red line) than for example the third fringe (green line). The reference value taken to evaluate the sensitivity is the mean value of the fringes (dashed line).

## 5.5 Prospects

We demonstrated a new kind of interferometer, which exploits the motional states of a quantum mechanical object. To the best of our knowledge, it is the first interferometer based on external states where the two arms of the interferometer do not separate spatially in time. This interferometer is sensitive to changes of the trapping potential and could in principle be used to measure perturbations in the effective level splitting during the holding time.

The aim of this project was to show that this interferometer works in principle. In addition, a comparison of the interferometer's phase sensitivity with a direct read-out from momentum distributions showed one advantage of the interferometer. However, this advantage is lost for holding times longer than a couple of milliseconds. This is directly linked to the reduction of contrast after a few fringes, which can be seen on the experimental data (see fig. 5.4(a)). This indicates a loss of coherence in the created superposition over time. Fitting an exponentially damped sine to the experimental fringes reveals a damping time constant of  $(1.6 \pm 0.7)$  ms. A closer look at the density patterns after the first pulse reveals that this loss of contrast is already present in the equal superposition between the two pulses, and that the damping timescales correspond. It is therefore not an effect of the second pulse.

This decay is not present in 1d GPE simulation, which is why it does not appear on the simulated results of fig. 5.4(b)). This divergence is to a certain extent expected, as the 1d GPE model does not account for various effects such as finite temperature, influence of the longitudinal direction, many-body dephasing or decoherence. The question is therefore: which effect is responsible for the rapid loss of contrast? The next chapter will

be dedicated to looking at this question from different perspectives and shedding light on the properties of out-of-equilibrium motional state superpositions.

# 6

## Complex behaviors in motional state superpositions

In this chapter, we investigate different mechanisms reaching beyond the 1d GPE model described in chap. 2 and chap. 4, that could explain the loss of contrast observed experimentally both on the interferometric contrast and on the momentum distributions. We start by reflecting on the different limitations of the 1d GPE approximation. In a second section, we analyze the behavior of the damping in our data. In the rest of this chapter, we then review several mechanisms that could explain this damping: sec. 6.3 focuses on effects involving the longitudinal dimension of the system, which is not modeled in the 1d GPE, and sec. 6.4 proposes a many-body description of the system in the transverse  $y$ -direction. The last section gathers some shorter investigations.

### 6.1 Limitations of the Gross-Pitaevskii equation

Up to now, the quasi-condensate has been described using a 1d Gross-Pitaevskii equation, which is a convenient mean-field representation for a system with many interacting particles. This kind of representations provides a practical framework to understand some aspects of Bose-Einstein condensation and the role of interactions between atoms. It is very powerful to describe the dynamical evolution of a wavefunction in a trap, as we showed in the previous chapters. However, it has limitations. In the present case, as revealed at the end of chap. 5, the 1d GPE does not reproduce the decay of the created motional state superpositions observed experimentally. The question is then: what is the source of this discrepancy?

There are several assumptions behind the GPE formalism. The main one is that all atoms are in the same condensate wavefunction or single-particle state, at zero temperature. The system must also be dilute, such that it remains weakly interacting. Moreover, only low energy collisions are considered in the model, such that interactions

can be understood as a  $s$ -wave scattering and written in the form of a delta function  $g\delta(x_i - x_j)$ .

In several aspects, our quasi-condensate satisfies these criteria. It is a dilute, weakly interacting system, and initially mostly in the ground state  $|0\rangle$ . But there are some potential complications. First, the system is initially at a low but finite temperature, and this temperature increases after the transfer to higher motional states. In the GPE model, these thermal excitations are ignored. Second, as a result of the displacement, the system occupies mainly the two lowest energy levels, but some atoms remain in higher excited states. These atoms can lead to high energy collisions. Third, the description of the condensate is limited to one transverse direction, ignoring in particular the elongated dimension of the system and the exact shape of the profile in this direction. This one-dimensional model neglects possible couplings and energy transfers into other directions. Fourth, the mean-field approach, by construction, does not take into account the quantization of the field, as a many-body description would. These different limitations will be addressed when investigating different models in sec. 6.3.2 to 6.5. In the following, we carry out an experimental investigation of the loss of contrast.

## 6.2 Experimental observations on the loss of contrast

The data experimentally available are exclusively momentum distributions of the in-trap atomic cloud. As presented earlier, the trapping and the manipulation of the BEC are realized on an atom chip using small current-carrying wires. In this chapter, we consider data taken both with the external 10  $\mu\text{m}$ -wire and the DP400 (see sec. 3.2.5). As explained in detail in chap. 4, the experimental data are 2d pictures taken after a long time-of-flight, integrated along the vertical direction as the expanded atom cloud falls through the light sheet, and as fluorescence photons are recorded on an EMCCD camera. We have access to two directions of the atomic cloud with our imaging: the horizontal transverse direction, which expands considerably during the time-of-flight due to the original tight confinement, and covers hundreds of pixels on the detector, and the longitudinal direction, which is weakly confined and is only about one-tenth of the transverse length after time-of-flight. For a dilute, fast expanding cloud, the obtained density profiles in time-of-flight are equivalent to the momentum distribution in the trap. We consequently obtain a good read-out of the momentum distributions in the horizontal transverse direction, which is the one where the displacement and the subsequent dynamics take place. We have a poorer read-out in the longitudinal direction, and none in the vertical transverse direction. These conditions have their advantages and drawbacks. They are ideal to follow the displacement dynamics, but limit the access to other features potentially explaining the damping or other interesting physical phenomena.

### 6.2.1 General considerations

After the displacement pulse, the BEC is transformed into a superposition of two motional states. Experimentally, an interference pattern is observed, similar to what is shown in 1d GPE simulations. This pattern then damps out and disappears, as can be seen on fig. 4.14. For the dataset used to study the interferometer in chap. 5, this loss of contrast occurred quickly, with an exponential decay constant of 1.5-2 ms. This timescale was the same in two methods of investigations: a fit of the center-of-mass oscillation, or a state analysis of the momentum distributions over time. After 5-6 ms, no interference pattern was visible anymore, and no further revival of oscillations was found on the next milliseconds.

On a different dataset, which will be exploited in this chapter, a similar decay was observed, but on a longer timescale. This dataset was taken two years later than the interferometer data, therefore the experimental conditions might have changed. One difference is the technique used to drive the displacement: in the interferometer case, the DP400 was used (see chap. 3), while in the later dataset, the 10  $\mu\text{m}$ -wire was adopted. The data taken with the DP400 showed a faster decay, as discussed in sec. 6.5. For the present study of the decay mechanisms, we chose to connect the distant 10  $\mu\text{m}$ -wire to limit noise sources. The data presented below are taken in this configuration.

### 6.2.2 Evolution at long times

In order to get some insight on the cause(s) of the loss of contrast, we apply again a half transfer pulse and observe the produced superposition at different times. The momentum distributions show a slow “wash out” of the beating patterns (fig. 4.14 (left)).

Focusing on momentum distributions at long times ( $> 10 - 15$  ms), we observe that the profiles are qualitatively similar to a ground state profile. There is no visible beating pattern anymore, which was the signature of a coherent interference of  $|0\rangle$  and  $|1_y\rangle$ . Three possible explanations come to mind:

1. The system decays to  $|0\rangle$ , hence the disappearance of any interference pattern.
2. There is a randomization of the phase or *dephasing* phenomenon. In this case, the populations in  $|0\rangle$  and  $|1_y\rangle$  do not change and the system stays coherent, but averaging over all phases leads to a reduced contrast of the interference.
3. The populations in  $|0\rangle$  and  $|1_y\rangle$  do not change but coherence is lost, due to some *decoherence* phenomenon. In this case, there is no well-defined phase anymore even, even on single realizations.

In the first case, the final profile after full decay matches the ground state profile of the trapping potential. In the second case, due to averaging, the final profile is similar to the third case. The profile can be represented as a statistical mixture of  $|0\rangle$  and  $|1_y\rangle$  in the

form:

$$n_{\text{dephasing}}(t) = \sum_i n_{\text{dephasing},i}(t) \quad (6.1)$$

$$= |\psi_0|^2/2 + |\psi_1|^2/2 + \sum_i (\cos(\omega_{01}t + \theta_i)\psi_0\psi_1) \quad (6.2)$$

$$= \frac{|\psi_0|^2 + |\psi_1|^2}{2} = n_0 + n_1 = n_{\text{decoherence}}, \quad (6.3)$$

where  $\theta_i$  represent a phase offset for different realizations  $i$ .

We observe the experimental profiles at long times. For the latest data sets (see app. B), the longest times of observation available are  $t \sim 12 - 14$  ms. We integrate the momentum distributions for  $N \approx 700$  over one period of the beating (0.58 ms) and compare it to a statistical mixture of  $|0\rangle$  and  $|1_y\rangle$  in equal proportions, and to  $|0\rangle$ , as shown in fig. 6.1. The qualitative comparison indicates that the transverse size of the final state is neither completely compatible with a statistical mixture of  $|0\rangle$  and  $|1_y\rangle$ , nor with a pure ground state  $|0_y\rangle$ . However, when accounting for the emission of a small fraction of  $|1_y\rangle$  into twin-beams (see sec. 6.3.1), the profiles at later times agree with a statistical mixture.

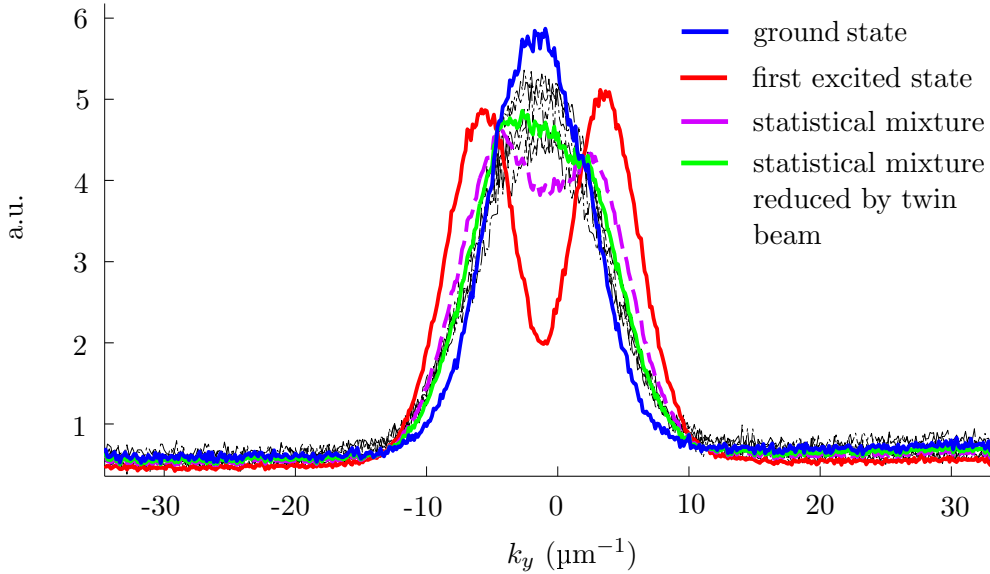


**Figure 6.1: Profiles at long times.** Many profiles at long times after a half transfer pulse (black dotted lines) are plotted together with the profiles obtained experimentally for the ground state  $|0\rangle$  (blue) and the first excited state  $|1_y\rangle$  (red). They are compared to a statistical mixture of  $|0\rangle$  and  $|1_y\rangle$  (purple dashed line) and the same mixture taking into account a 15% fraction emitted into twin-beams (green line).

To gain more insight, we turn to the correlation functions of the transverse profiles. The second-order correlation function  $G^{(2)}$ , presented in sec 3.4.1, can reinforce features

that are already present in experimental images but hardly visible. In particular, it highlights effects that occur in the individual images but that disappear when averaging.

The difference between a decohered and a dephased state can emerge in the  $G^{(2)}$  functions at long times. Indeed, a loss of coherence on single realizations yields a second-order correlation of the form:

$$\begin{aligned} G_{\text{decoherence}}^{(2)}(k, k') &= \langle n_{\text{decoherence}}(k) \cdot n_{\text{decoherence}}(k') \rangle \\ &= \frac{1}{4} (|\psi_0(k)|^2 + |\psi_1(k)|^2) (|\psi_0(k')|^2 + |\psi_1(k')|^2) \\ &= n_{\text{incoh}}(k) \times n_{\text{incoh}}(k'), \end{aligned} \quad (6.4)$$

whereas a dephasing yields a different second-order correlation function:

$$\begin{aligned} G_{\text{dephasing}}^{(2)}(k, k') &= \langle n_{\text{dephasing},i}(k) \cdot n_{\text{dephasing},i}(k') \rangle \\ &= \frac{1}{4} (|\psi_0(k)|^2 + |\psi_1(k)|^2) (|\psi_0(k')|^2 + |\psi_1(k')|^2) \\ &\quad + \langle \cos^2(\omega_{01}t + \theta_i) \rangle \cdot \psi_0(k)\psi_1(k)\psi_0(k')\psi_1(k') \\ &= G_{\text{decoherence}}^{(2)}(k, k') + \frac{1}{2} \psi_0(k)\psi_1(k)\psi_0(k')\psi_1(k'). \end{aligned} \quad (6.5)$$

The difference between a completely “decohered” state and a “dephased” state is shown in fig. 6.2. This type of representation must be understood as two-dimensional map of the coincidences between two elements of a vector, e.g.  $x_i$  and  $x_j$ . The elements on the diagonal of the map give information about the local correlations for  $x_i = x_j$ , while the anti-diagonal elements represent points located at the same distance from the center of the vector,  $N_{\text{vector}}/2 - x_i = N_{\text{vector}}/2 - x_j$  ( $N_{\text{vector}}$  the total number of elements in the vector). Peaks on the anti-diagonal therefore indicate the probability of correlated features in two different regions of the profiles on single images. In the case of a dephasing in an equal superposition of  $|0\rangle$  and  $|1_y\rangle$ , the probability is high to have a single feature either left or right from the center, as illustrated in fig. 6.2 (top left), hence the two strong peaks on the diagonal in the  $G^{(2)}$  representation. On the other hand, a decohered superposition presents constantly two peaks (see fig. 6.2 (top right)), and therefore exhibits four peaks in the  $G^{(2)}$ .

Experimentally, the second-order correlation function of the transverse patterns is extracted from individual transverse profiles, which are integrated long the two other dimensions. From experimental data with  $N \approx 700$  atoms, we extract the  $G^{(2)}$  function at short times (right after the half transfer pulse) and at long times (13 ms after the end of the pulse). Their evolution over one period is presented in fig. 6.3 and fig. 6.4.

At short times, the beating in the momentum distribution translates into an evolution of the pattern of the  $G^{(2)}$ , which also resembles a beating on the diagonal, with the interesting apparition of two “blobs” on the anti-diagonal every half-period. This can be interpreted as follows: for the equal superposition state  $|\psi\rangle = \frac{1}{\sqrt{2}}(|\psi_0\rangle + e^{i\phi}|\psi_1\rangle)$ , a phase of  $\phi = 0$  or  $\pi$  corresponds to the density having only one peak on one side or on the other, respectively. A phase of  $\pi/2$  or  $3\pi/2$  yields a density with two symmetrical

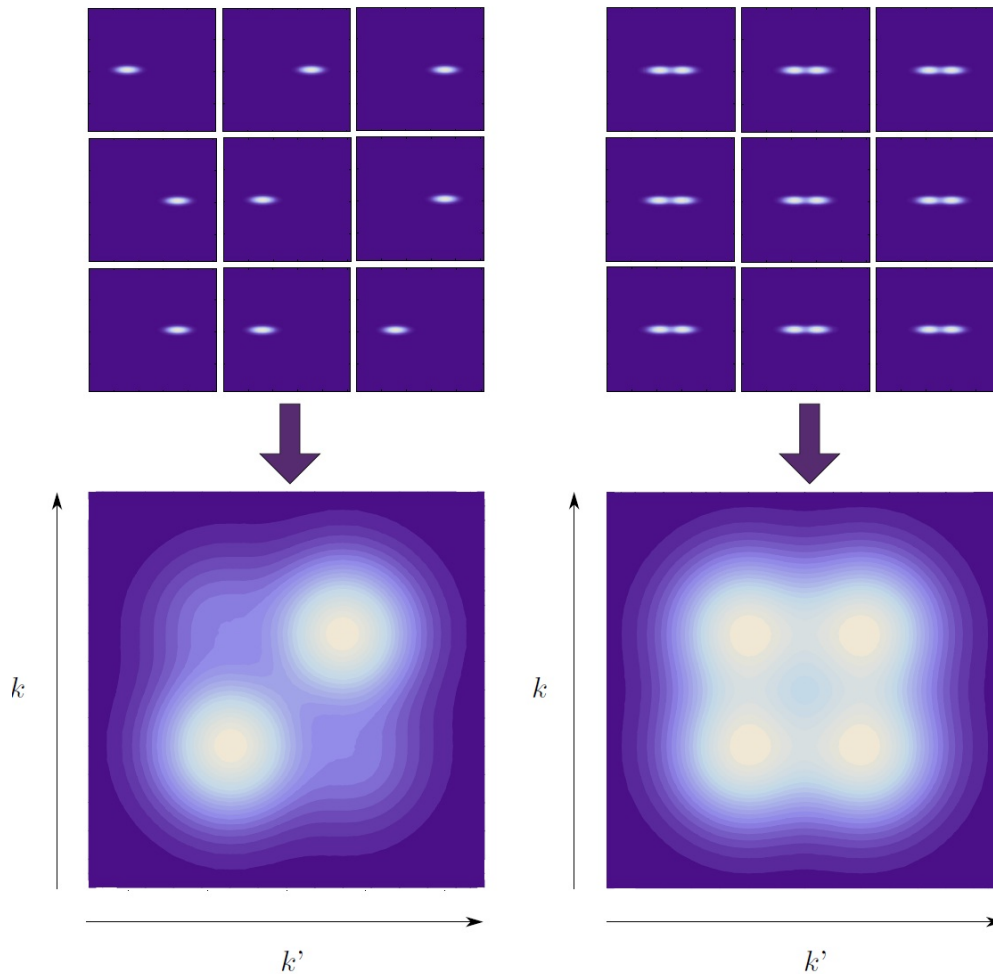


**Figure 6.2: Simulated second-order correlation functions.** (Left) For a superposition of ground and first excited states with a random phase, where individual shots exhibit perfect coherence — dephasing. (Right) For a statistical mixture of ground and first excited state with no phase relation, where the coherence on individual shots is lost — decoherence.

peaks. A  $G^{(2)}$  with a single blob on the diagonal corresponds to a phase of  $\phi = 0$  or  $\pi$ , whereas the  $G^{(2)}$  with more features detect two peaks in the momentum distribution and thus shows correlations on the anti-diagonal. For the phase having exactly a value of  $\pi/2$  or  $3\pi/2$ , four blobs of equal size appear. This is visible for  $t = 1.45$  ms in fig. 6.3. These patterns evolve at the same speed as the relative phase between  $|0\rangle$  and  $|1_y\rangle$ .

At long times, the beating in the  $G^{(2)}$  disappears, as shown by fig. 6.4. The general shape is a square. Compared to fig. 6.2, it appears that the final pattern is closer to a decohered state, which exhibits four blobs, than a dephased state. The square feature is due at least in part to the lower population in the first excited state due to twin-beam

emission.

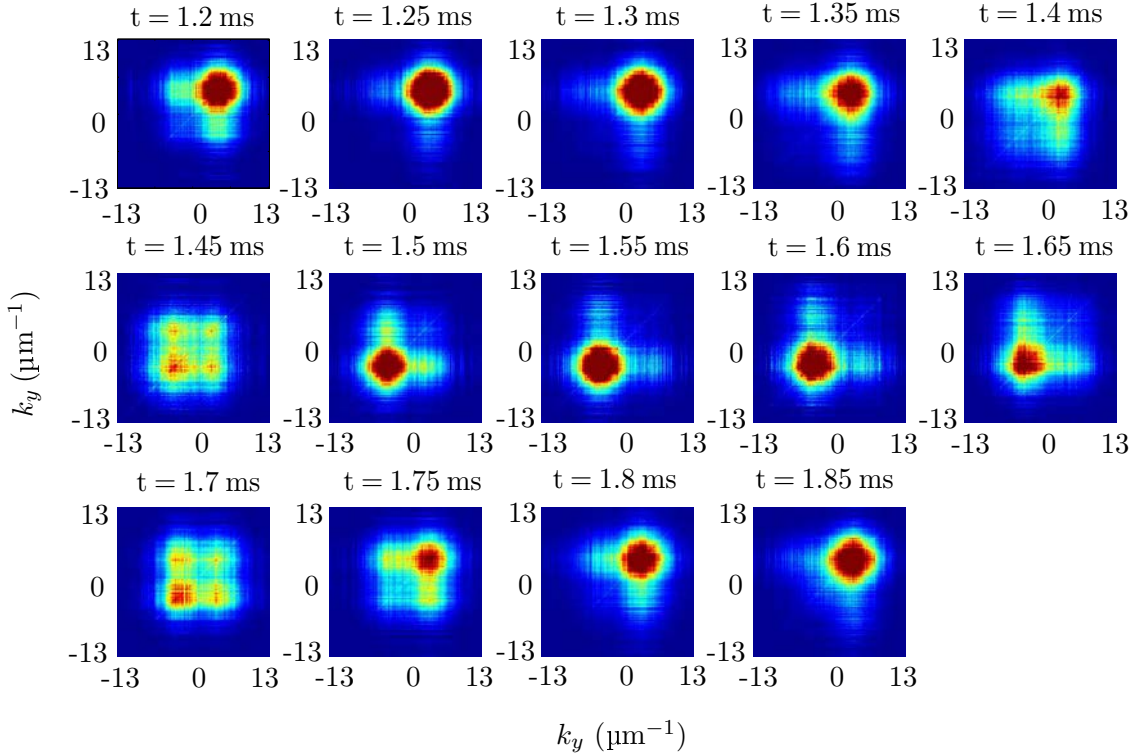


**Figure 6.3: Experimental correlation functions  $G^{(2)}$  at short times (right after half transfer).** The correlation functions for  $t = 1.2$  ms to  $t = 1.85$  ms, where  $t$  indicates the time starting from the beginning of half transfer pulse, which lasts 1.09 ms. The data cover more than one period of the beating.

All the observations showed so far are based on images that have been integrated along the longitudinal direction and, in the case of momentum distributions observations, averaged over a few shots (typically 5). However, looking at single, non-integrated pictures yields similar results. There is no immediate sign on the experimental images that the signal deteriorates upon averaging. The clouds after time-of-flight were also examined in slices longitudinally, in case structures were to be seen in the longitudinal direction, and that the integration would be hiding. We did not observe significant differences as compared to the integrated images.

In addition to observations at long times, the evolution towards the final state can be studied. In order to extract a timescale for the damping, we test an exponential decay model on different observables. A first method is to fit the center of mass motion of the momentum distribution. The oscillation can be approximated by a function of the form:

$$f(t) = a \sin(2\pi\nu_1 t + \phi_1) \sin(2\pi\nu_2 t + \phi_2) \exp(-t/\tau) + c \quad (6.6)$$

which corresponds to a modulated sine with an exponential decay. The modulation accounts for the effect of the second excited state on the shape of the distribution, as seen

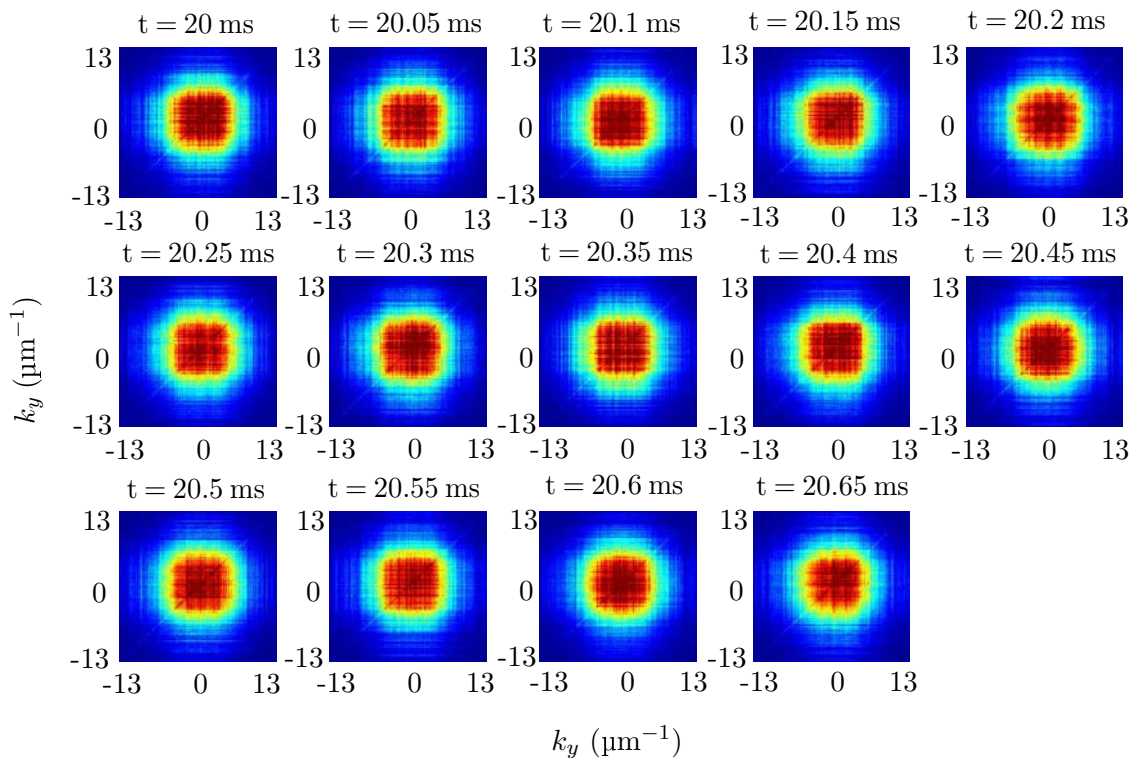


**Figure 6.4: Experimental correlation functions  $G^{(2)}$  at long times.** The correlation functions for  $t = 20$  ms to  $t = 20.65$  ms, where  $t$  indicates the time starting from the beginning of the half transfer pulse, which lasts 1.09 ms.

in chap. 4. This method has the triple advantage to be fast and simple and not to rely on any modeling of the mechanism behind the loss of contrast, except for the exponential evolution. A second method is to fit the evolution of the momentum distributions, as was performed in chap. 4 and chap. 5, but on a long timescale, and including in the fit model the loss of contrast. However, this requires to make assumptions on the mechanism behind the loss of contrast. As discussed before, there are three reasonable hypotheses: some dephasing or decoherence effect, or a decay to  $|0\rangle$ . In the first two cases, the final state can be approximated by a statistical mixture of  $|0\rangle$  and  $|1_y\rangle$ , in the third by  $|0\rangle$ . We thus conduct fits to the momentum distribution including either a growing fraction of a statistical mixture of  $|0\rangle$  and  $|1_y\rangle$ , or a growing fraction placed incoherently in  $|0\rangle$ . In the rest of the chapter, we will refer to these two fit models as the *dephasing fit* (which is valid for both first and second cases) or the *decay fit*, respectively. In both, we assume an exponential decaying coherent fraction with a decay constant  $\tau$ . The twin-beam emission is not accounted for in those fits.

### 6.2.3 Experimental data for different parameters

To study the impact of different quantities on the loss of contrast, two different parameters are varied: the number of atoms and the temperature of the initial BEC. The variations with respect to these parameters can then be used to compare to the theoretical models of sec. 6.3 to 6.5.

#### Atom number

The atom number can be varied experimentally by changing the final frequency value of the last evaporation ramp. With this technique, the atom number was varied from  $\sim 450$  to  $\sim 2800$  atoms. Fig. 6.5 shows the evolution of the momentum distribution for  $N = 450$ ,  $N = 900$  and  $N = 1500$  atoms, where the atom number shot-to-shot fluctuates around these averaged values by about 15%. A small qualitative difference appears, with a faster loss of contrast at higher atom numbers, as shown in fig. 6.5. All the data presented here are produced with a half transfer pulse. As a result of the robustness of the pulse, underlined in chap. 4, the variation in atom number does not significantly affect the ratio of ground state and first excited state in the superposition at the end of the pulse. We therefore can use the same pulse for all atom numbers.

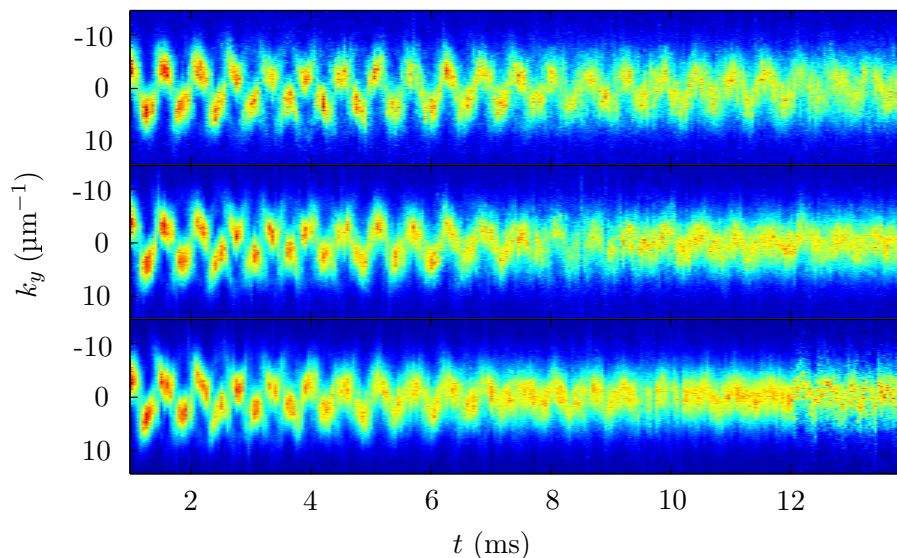


**Figure 6.5: Experimental momentum distribution for different atom numbers.** (Top)  $N = 450$ . (Middle)  $N = 900$ . (Bottom)  $N = 1500$ .

The evolution of the momentum distributions are fitted as explained above to extract the exponential decay time of this evolution. The results are plotted in fig. 6.6 (left). They reveal a clear dependency of the damping time on the atom number, for the two different fits of the momentum distributions proposed in sec. 6.2.2. This tendency also appears in the fit of the center-of-mass but important error bars do not allow to draw conclusions from that method. We attribute this outcome to the fact that the center-

of-mass oscillation exhibits a behavior that does not agree so well with an exponential decay. Other types of decay behavior (i.e. linear and polynomial) did not perform better.

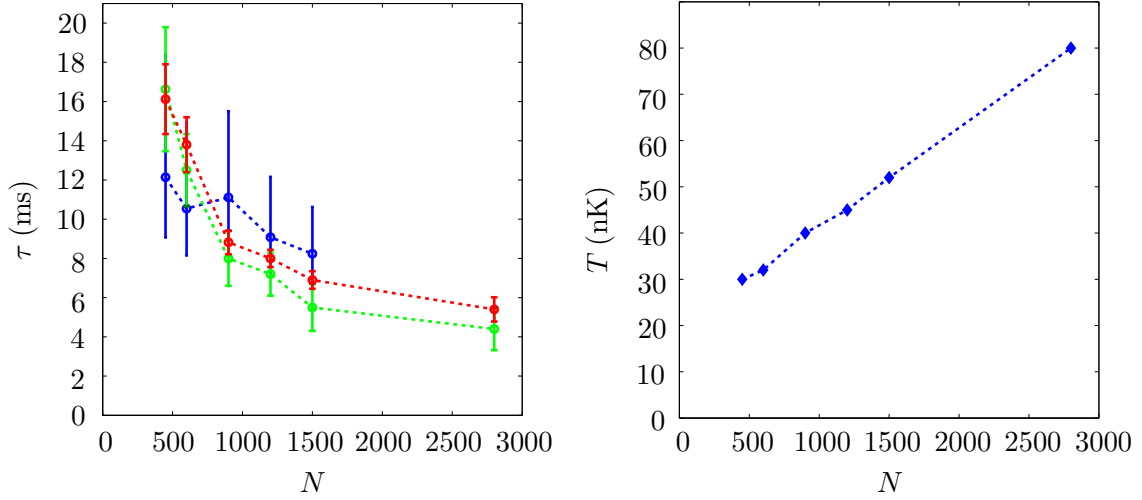


**Figure 6.6: Results of the fits on experimental data for different atom numbers.**

(Left) Decay time obtained by fitting the center-of-mass motion with different methods: a fit with eq. (6.6) to the center-of-mass (blue), a fit of the entire momentum distribution with a growing incoherent fraction with a ground state distribution (red) and a growing fraction of a statistical mixture of ground state and first excited state (green).

(Right) Temperature of the initial BEC as a function of  $N$  obtained by changing the evaporation ramp.

Changing the evaporation ramp does not only affect the atom number, but also the temperature. The temperature for each atom number is indicated in fig. 6.6 (right). In this low temperature range, where no measurable thermal fraction is present, temperatures are estimated from the quasi-condensate model based on the Yang-Yang integral equations [196], a method which was presented in ref. [56].

In an ideal situation, we would like to keep the temperature constant while changing the atom number. This is however challenging, and a reliable method to do so is still missing. Recent attempts to outcouple a fraction of the atoms from the trap with a microwave pulse instead of the radio-frequency evaporation led to increased atom number fluctuations and excited additional motions. Acting on the evaporation ramp remains the only way to change the atom number without inducing instabilities in the system, such as increased number fluctuations or excitation of breathing modes in the longitudinal direction.

## Temperature

Changing the temperature of the initial condensate is done by including a preparation time before executing the displacement,  $t_{\text{prep}}$ . During that time, the atomic cloud naturally heats up due to small perturbations of the trapping potential. The evolution of

the temperature as a function of  $t_{\text{prep}}$  is plotted in fig. 6.7 (right). The atoms remain however trapped and the atom number is stable. The data are again taken with a half transfer pulse. We note that the temperature varies linearly with the atom number, as was also observed in another atomchip experiment. [197].

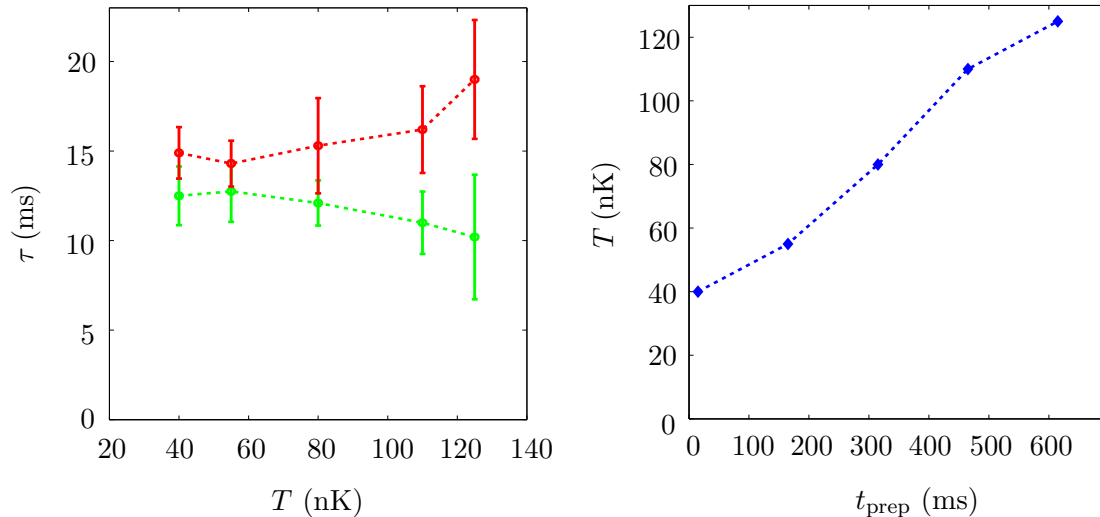


**Figure 6.7: Results of the fits on experimental data for different atom temperatures.** (Left) Decay time obtained by fitting the entire momentum distribution with a growing fraction of a statistical mixture of ground state and first excited state (green). (Right) Temperature of the initial BEC as a function of  $t_{\text{prep}}$ .

The momentum distributions for different temperatures are all qualitatively similar, and a fit to the experimental data reveals that the decay time  $\tau$  is comparable within error bars for temperatures ranging from  $T = 40$  nK to  $T = 80$  nK. For higher temperatures, a significant thermal fraction appears and the assumption that  $T \ll \hbar\omega_{\perp}$  breaks down. The models for the fits do not take into account a thermal fraction, therefore the decay constant found with these fits for high temperatures is not valid. However, the variation can be interpreted: at long times, the transverse profiles are larger due to the thermal fraction, and the decay fit attempts to accommodate for these broader profiles by increasing the decay constant. The dephasing fit is less sensitive to this effect, as the dephased state (statistical mixture of  $|0\rangle$  and  $|1_y\rangle$ ) is broader than the ground state.

From the results for  $T \leq 80$  nK, we can conclude that temperature has no effect on the damping mechanism, at least for temperatures where the quasi-condensate model is valid. Moreover, we can infer that, in the previous data for different atom number, the increased temperatures did not impact significantly the results, and the main contributor to the change in damping time was the variation in atom number.

From the different observations of experimental data at long times and for different parameters, it can be concluded that the final profiles resemble a decohered state with a reduced fraction of first excited state. The option of a dephased state is still possible due to the averaging over the longitudinal direction, which can reduce the contrast from

individual “slices” of the quasi-condensate. In the next section, we investigate theoretically and numerically some physical phenomena taking place in this dimension.

## 6.3 Longitudinal effects

The experimental system in the transverse direction occupies only two or three modes. In the longitudinal direction, due to the weak confinement, many modes are populated. The system can be described as a quasi-condensate, as defined in chap. 2. Damping mechanisms of different natures may take place, which we now investigate using different models.

### 6.3.1 Decay into twin-atom beams

One of the first ideas, stemming from some previous work done on the first excited motional state, is to look for the apparition of “atom pairs” in the longitudinal direction. These pairs, already mentioned in sec. 4.3.3, propagate in opposite directions with the same momentum. They were discovered in the same laboratory and understood as a decay mechanism from two-body collisions in  $|1_y\rangle$  [198]. For the experimental parameters of these past experiments, it was observed that a BEC transferred with 97 % efficiency to the first excited state sees almost 40 % of its atoms leave the source cloud in the form of atom pairs.

Theoretically, this phenomenon also takes place for other motional state configurations. Twin-beam were observed, although with a weaker production efficiency, in the present set of experiments. The lower efficiency is expected from the lower population in  $|1_y\rangle$ . Starting from the same atom number, only half the population gets transferred to  $|1_y\rangle$ , which results in a lower efficiency and speed of atom pairs production. Simulations with a density matrix expansion, the detail of which can be found in ref. [56], give an estimate of atom pair production of 6.3 % of the total atom number after 6 ms and 11 % after 12 ms for  $N = 700$  atoms.

At higher atom numbers, the percentage of atoms decaying into twin-beams increases experimentally only by a few percent, as shown by the symbols in fig. 6.8. Theoretically, at a constant temperature of 25 nK, the efficiency would be  $> 25\%$ . This discrepancy can be explained by the higher temperatures of the high atom number datasets. Indeed, temperatures have also shown to lower the production efficiency, both numerically and experimentally [56]. For the data presented here, temperatures were ranging from  $T \simeq 25$  nK for the lowest atom number to  $T \simeq 60$  nK. By adapting the temperature in the simulations, we see that the production of twin-beams does not exceed 18 %. The population in twin-beams estimated from the same experimental data as in sec. 6.2.3 match the simulations to a couple of percent, as can be seen in fig. 6.8. For higher atom numbers, and hence higher temperatures, the simulations overestimate the efficiency of the process.

These twin-beams propagate along the longitudinal direction with a momentum  $\pm k_0$  equivalent to the energy of their source state [115, 198], here  $|1_y\rangle$ . The impact of this

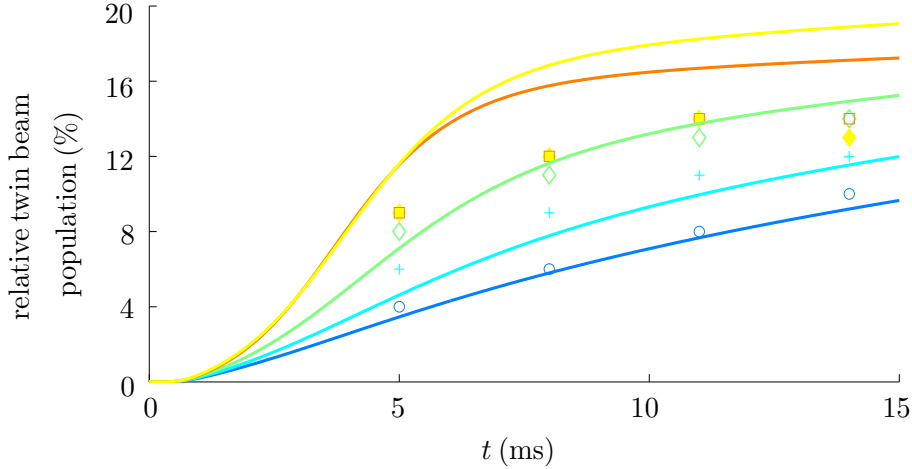


**Figure 6.8: Population of twin-beams relative to the total number of atoms.** Relative twin-beam population in simulations (lines) and experimental data (symbols), for  $N=450$  (blue),  $N=600$  (cyan),  $N=900$  (green),  $N=1200$  (yellow) and  $N=1500$  atoms (red).

production on the source cloud is not completely known. The minimal effect is a depletion of the first excited state, which increases the proportion of atoms in the transverse ground state as compared to other levels. Atoms in the twin-beams could also collide with atoms of the source cloud and lead to decoherence. However, the cloud is very dilute and the number of such collisions should be low, even for the highest atom numbers. Moreover, collisions would equally affect the twin-beams. On the experimental pictures, they present sharp profiles for relatively long times, at least for the low atom numbers. There is also no clear sign that the density profiles in the longitudinal direction are affected, which would be the case if secondary collisions with momentum transfer were occurring. Therefore, it seems unlikely that collisions explain the important loss of contrast. We expect additional effects to contribute.

### 6.3.2 Longitudinal dephasing in a homogeneous condensate

An effect that is well studied and understood in elongated condensates and double-well physics is the 1d dephasing caused by phase fluctuations [107, 199, 200]. It is here a consequence of having an elongated trapping potential, as many modes in the longitudinal direction are accessible even for configurations with low temperature and chemical potential. Small thermal or quantum fluctuations modify the condensate wavefunction, as described in chap. 2, which leads to a loss of long-range coherence [201, 202]. In an atom interferometer, phase fluctuations are not immediately destructive for the signal. That is because, right after splitting, they are almost the same for both condensates. They do not influence the relative phase between them, which is the value read out at the end. However, if these fluctuations evolve differently in each condensate after splitting, they lead to a decrease of the interference signal's contrast over time when this signal is integrated along the longitudinal direction [107].

The motional states superpositions can be viewed as two quasi-condensates in the longitudinal direction, which are spatially overlapping. They have a similar profile longitudinally but, due to the different extents of their transverse wavefunctions, the effective interaction constant of one (corresponding to  $|1_y\rangle$ ) is only 3/4 of the other (corresponding to  $|0\rangle$ ). Therefore, the evolution of the fluctuations in the longitudinal direction differs for both states, potentially leading to a fast blurring of the relative phase between them. Moreover, the splitting leads to a change of geometry for the transverse wavefunction of one of the condensate. This could potentially lead to additional excitations, which we omit here.

Despite the limited resolution in the longitudinal direction, we attempted to analyze a few slices of the atomic cloud in that direction, but did not find a clearly slower contrast decay in the slices than in the integrated pictures. From phase fluctuations, we would expect that, if one manages to isolate a zone of homogeneous phase, the contrast in that zone should remain high. Slices of the quasi-condensate, containing fewer phase zones, should also perform better than the whole quasi-condensate. On the experimental images, although there is a hint that the contrast in a short slice (a few pixels wide after time-of-flight) decays slower than the global contrast, the effect is hardly noticeable, if there at all. This is mainly due to the low resolution of the images in the longitudinal direction, as the cloud in that direction only expands over 25 pixels. The coherence length for the system of condensates,  $\lambda_T = \frac{\hbar^2 n_0}{mk_B T}$ , which gives an estimate of the “size” of the homogeneous phase zones, is  $\lambda_T \simeq 2.3 \mu\text{m}$  in the trap and expands over  $25.3 \mu\text{m} \equiv 3.2$  pixels at the point of imaging. This short correlation length, in conjunction with small shot-to-shot fluctuations of the center-of-mass position and possible mixing of the different zones during free fall, makes it difficult to reach a conclusion from observations of slices alone.

A description of the phenomenon and the estimation of timescales of longitudinal dephasing for the present problem is an important step in understanding the physics happening in the system. It is a valuable indicator of the presence or absence of longitudinal dephasing for a homogeneous condensate, as well as its relevance in the observed contrast loss. In the following sections, we will present a Bogoliubov model developed in collaboration with Isabelle Bouchoule<sup>1</sup>. We first investigate a simplified version of the problem where the two condensates are fully decoupled, for which numerical simulation can be compared to an analytic solution. We will then consider the role of interactions, which introduce an effective coupling between the two condensates. We will finally reflect on the response of the system to initial fluctuations coming from the splitting process.

### Bogoliubov model for a pair of condensates

To study the longitudinal dephasing in a motional state superposition, a Bogoliubov model of excitations in 2 coupled homogeneous quasi-condensates was developed. The two quasi-condensates are considered to be confined in a box potential of size  $L$ , to have

1. Laboratoire Charles-Fabry, Palaiseau, France

equal densities but different interaction constants due to the difference in their transverse extensions. The problem is treated as a system of coupled GPE. By adopting a field density representation for the quasi-condensates,  $\Psi_i = \sqrt{n_{i,0} + \delta n_i} e^{i\theta_i}$ , and linearizing the system, we obtain a set of four coupled equations for the density fluctuations  $\delta n_i$  and the phase  $\theta_i$ . Details about these calculations and simulations are given in app. A.

The spectrum of excitations presents 4 branches, of which 2 with positive frequencies, similar to ref. [203]. The observable of interest in our case is the contrast of the interference patterns integrated along the longitudinal direction. This contrast depends on the relative phase difference at each time, and is defined as:

$$C(t) = \left( \left\langle \left| \frac{1}{L} \int dz e^{i(\theta_0(z,t) - \theta_1(z,t))} \right|^2 \right\rangle \right)^{1/2} \quad (6.7)$$

$$= \left( \frac{1}{L^2} \iint dz dz' e^{-\frac{1}{2} \langle (\theta_0(z,t) - \theta_1(z,t) - (\theta_0(z',t) - \theta_1(z',t)))^2 \rangle} \right)^{1/2}. \quad (6.8)$$

### Uncoupled quasi-condensates

As a preliminary comment, it must be noted that this case is only a way to get an analytic expression of the dephasing and contrast loss, and to estimate the dephasing in the absence of interaction between the condensates. This case is not physical, as the wavefunctions have a big overlap and thus the system has a non-negligible cross-interaction constant  $g_{01}$ .

For the case of a pair of uncoupled quasi-condensates, the contrast of the interference patterns can be expressed analytically, following eq. (6.8) and the calculations of app. A, by:

$$C = \left( \frac{1}{L^2} \iint dz dz' e^{-\frac{1}{2} \frac{mk_B T}{n_i \hbar^2} [4|z' - z| + 4|c_0 - c_1|t - 2|z' - z - (c_0 - c_1)t| - 2|z' - z + (c_0 - c_1)t|]} \right)^{1/2} \quad (6.9)$$

where  $c = \sqrt{gn/m}$ . As can be seen from this equation, the contrast diminishes in time depending on the relative speed of sound  $c_0 - c_1$ . This is a first particularity of the Bogoliubov model with different motional states, as compared to a more traditional problem of quasi-condensates in a double-well. In the case where the ‘‘individual’’ interaction constants  $g_0$  and  $g_1$  are not equal, the excitations in each sub-system, which are phonons with a different speed of sound, tend to propagate at different speeds, leading to a variability of the relative phase along the quasi-condensates. A similar situation is described in ref. [204] for the case where the number of atoms in each well is different, which is analogous, in the fully separated case, to having different interaction constants. In the present system, this speed difference is non-negligible: in a harmonic oscillator model,  $g_1 = \frac{3}{4}g_0$ . This approximation holds as the wavefunction is only slightly deformed due to anharmonicity and interactions, and is confirmed by numerical calculations. This leads to a relative speed of sound  $c_0 - c_1 = (1 - \sqrt{\frac{g_1}{g_0}}) c_0 \simeq 0.13 c_0$ .

We use this model for a first set of simulations taking simple assumptions. We start from a homogeneous quasi-condensate with  $N_i = 700$  atoms of homogeneous length

$L = 40 \mu\text{m}$ . Density fluctuations in a quasi-condensate are small, so we neglect them. As presented in chap. 2, the initial phase fluctuations follow the Bogoliubov spectrum at thermal equilibrium [205]:

$$\theta(z) = \sum_{k \neq 0} \sqrt{\frac{1}{n_i L}} (u_k - v_k) |\beta_k| \sin(kz + \arg(\beta_k)) \quad (6.10)$$

with

$$u_k - v_k = \left( \frac{\hbar^2 k^2 / 2m}{\hbar^2 k^2 / 2m + 2g_0 n_i} \right)^{-1/4}. \quad (6.11)$$

Then, the splitting into two motional states is modeled as an instantaneous process that creates two exact copies, so that the system after splitting consists in two uncoupled quasi-condensates of  $N = 350$  atoms with the same phase fluctuations. The initial relative phase is zero.

The concept of the simulations can be summarized as follows: the problem is expressed in the basis of the “+” and “-” modes (see app. A), corresponding to the two branches of the spectrum, where the evolution of the modes is simulated. At each timestep of the simulation, the phase variance is computed in the ground/first excited state basis to evaluate the contrast. The evolution of the contrast in time is plotted. The result of the simulation is compared to the analytic solution found in eq. (6.9).

The different results are presented in fig. 6.9. Several simulation runs, with initial fluctuations randomly drawn from the Bogoliubov distribution, are averaged. We see that the averaged evolution presents a drop in contrast identical to the one predicted by the analytic solution. The first part of the evolution is an exponential decay with a decay time  $\tau = \frac{\lambda_T}{2(c_0 - c_1)} = 13.2 \text{ ms}$ . This exponential decay shape is typical for a system where the thermal coherence length is shorter than the length of the quasi-condensate [206], in which phase correlations are lost on long length scales. The contrast reaches a plateau at  $C = 0.21$  after about 25 ms, which corresponds to  $\sqrt{\lambda_T / L}$ . This plateau depends on the length of the condensates, as for short condensates, only high momentum modes contribute. As they are sparsely populated, the contrast remains high. For long condensates, many low-momentum modes associate and scramble the phase. We also observe in these simulations peaks at long times. They appear due to the rephasing of the different phononic modes in the homogeneous condensate. Their position is given by the frequency difference between the propagation modes  $2\pi/(\omega^+ - \omega^-)$ . In the real trapping potential, these frequencies are incommensurate and the revivals would not appear.

From eq. (6.9), we notice the dependence of the contrast on two parameters: the density and the temperature of the uncoupled condensates. The decay time increases with density and decreases with temperature. This is in contradiction with our experimental results, where temperature does not play a significant role, and the decay time decreases with atom number and hence with density. On the other hand, the decay time given by the uncoupled condensate model,  $\tau = 13.2 \text{ ms}$ , is compatible with the experimental one. However, as it is, the model is not complete, as the cross-interactions have been left aside.

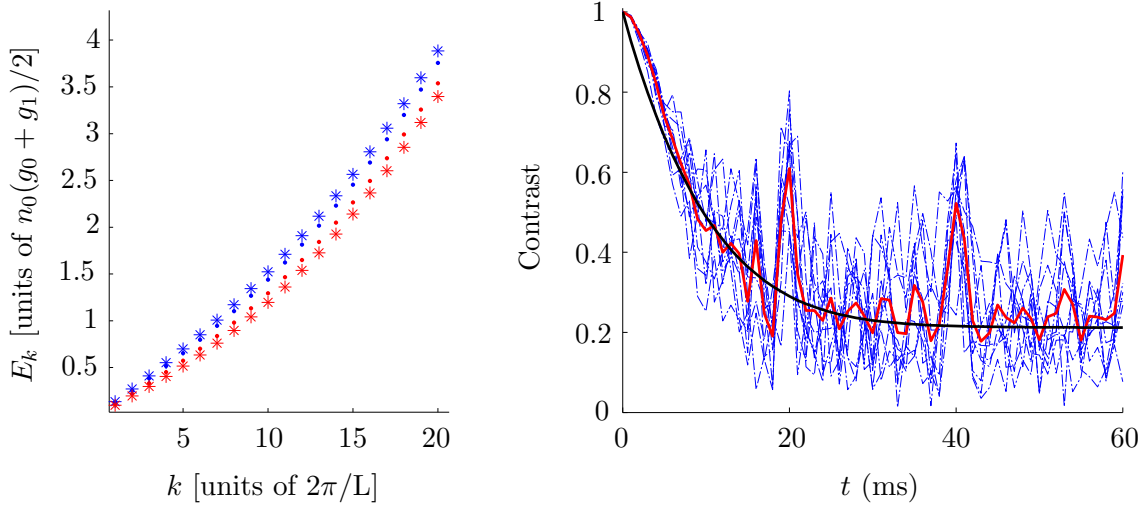


**Figure 6.9: Uncoupled condensates.** (Left) Bogoliubov spectrum of the first 20  $k$ -modes, for the uncoupled case (dots) and the coupled case  $g_{01} = \frac{1}{2}g_0$  (asterisks). (Right) Contrast evolution in time for the uncoupled case; ten individual evolutions (blue dashed lines) are run to produce an averaged evolution (thick red line) and compared to the theoretical contrast (black line).

### Coupled quasi-condensates

In addition to their respective interaction constants, the quasi-condensates are coupled by a “cross-interaction” constant  $g_{01}$ . This cross-interaction constant stems from the overlap of the two wavefunctions and, although it resembles the usual tunneling term in double-well potentials, it is not totally equivalent. It is proportional to the wavefunction squared. It is non-negligible compared to the other interaction terms: given the wavefunctions’ overlap, we can estimate from a harmonic oscillator model that  $g_{01} \simeq \frac{1}{2}g_0$ .

We included this term in the simulations following the linearized Bogoliubov model. As the term  $g_{01}$  is non-zero in the transfer matrices (eq. (A.14) and eq. (A.15)), the basis of the Bogoliubov modes is not the ground/first excited state basis, but the  $+/-$ -modes. The principle of the simulation is the same as before. The results are shown in fig. 6.10 (left).

For the case of coupled quasi-condensates, the contrast remains high much longer than in the uncoupled case. It seems there is a rephasing or relocking mechanism associated with the cross-interaction constant. This is reminiscent of the 1d Bosonic Josephson problem, where a coupling due to tunneling is established and competes against phase fluctuations to “lock” the relative phase [105].

This evolution is far from reproducing the experimental result, which shows a much faster decay of contrast towards low values. Either the effect causing the fast decay is not this type of longitudinal dephasing, or some element is missing. One aspect we did not consider so far is the impact of the “splitting”, or how additional fluctuations may be

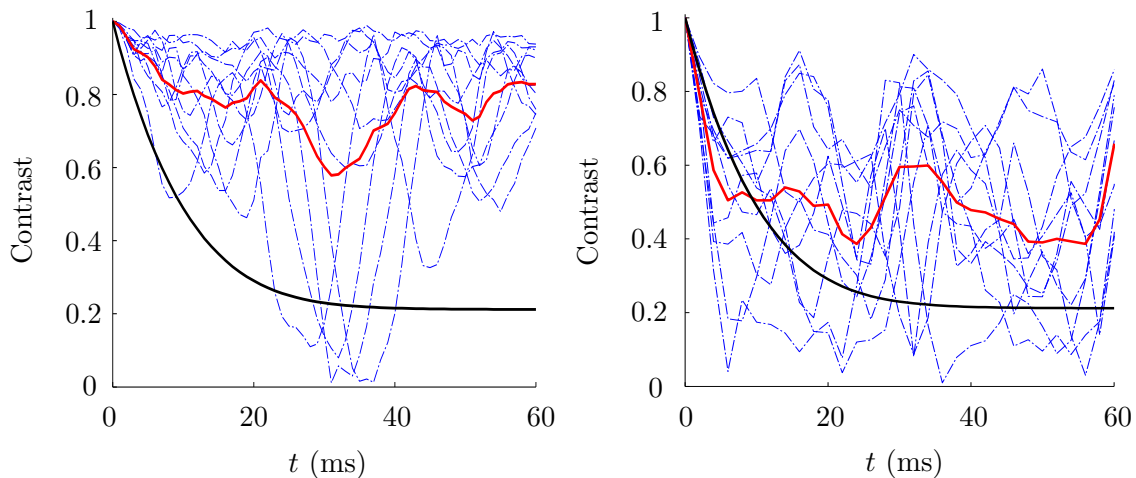


**Figure 6.10: Contrast reduction for coupled condensates.** (Left) Without splitting fluctuations. (Right) With splitting fluctuations. The black line represents again the theoretical contrast for the uncoupled case.

added to the system by the fast transfer displacement.

### Splitting fluctuations

So far, we have assumed that the splitting process was creating two perfectly identical copies containing each half the atom number of the initial condensate. However, fluctuations can appear during the process. In optics, a photon beam going through a beam splitter comes out as two beams with binomial fluctuations, due to the fact that each photon randomly “decides” which path to take. In the case of atoms in a double-well, the particles also randomly go into one of the two wells with equal probability if they do not have time to correlate. As the splitting process in our system is fast compared to other energy scales, we take as first assumption that the condensates in each state gets additional binomial fluctuations from the transfer. The binomial density fluctuations  $\delta\hat{n}(z)$  created during the process are:

$$\langle \delta\hat{n}(z)\delta\hat{n}(z') \rangle = \frac{n_0}{2}\delta(z-z'). \quad (6.12)$$

In a Luttinger liquid description [207], which provides a collective description of the excitations, these fluctuations can be associated to the phonon modes with no correlations between different momenta, which gives [204]:

$$\langle \delta n_k \delta n_{k'} \rangle = \frac{n_0}{2}\delta_{k,-k'}. \quad (6.13)$$

Similarly, we get the associated phase fluctuations:

$$\langle \theta_k \theta_{k'} \rangle = \frac{1}{2n_0}\delta_{k,-k'}. \quad (6.14)$$

These additional density and phase fluctuations can be integrated in the calculation of the relative phase evolution. We ran simulations of the coupled system including them, this time using all four equations for the density and phase fluctuations. The results of these simulations are displayed in fig. 6.10 (right). It appears that adding splitting-induced binomial fluctuations impacts the contrast, especially at short times. The contrast drops rapidly, in  $\sim 6$  ms, but stabilizes at a higher contrast,  $C \sim 0.5$ . The slope of the initial contrast drop is compatible with the observed loss of contrast on the experimental data. However, it stabilizes around an intermediate contrast value of 0.5. At this value, interference fringes would still be visible. It seems that this type of longitudinal dephasing does not entirely explain the data, which show a (close to) complete loss of contrast.

Additional simulations indicate a sensitivity of the contrast evolution to the density and temperature: a lower temperature and/or increased densities improve the contrast. Accounting for both density and temperature change as in the data of sec. 6.2.3, the initial slope in contrast decay increases slightly with atom number, similarly to the experimental results in fig. 6.6, as is shown in fig. 6.11. The dependency on temperature of this model is however not observed experimentally. This could be in part due to the limited sensitivity of our fit methods.

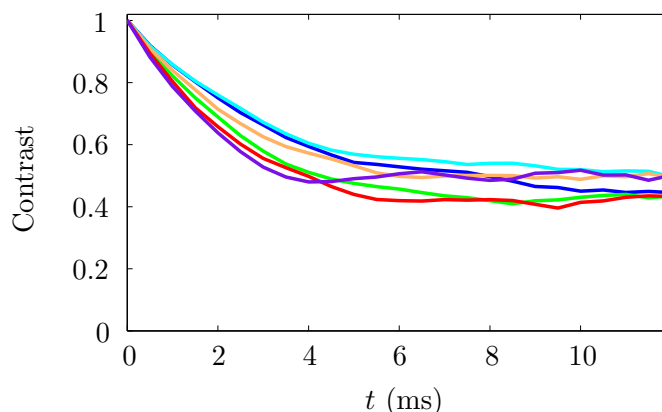


**Figure 6.11: Contrast evolution for different atom numbers and temperatures.** Both atom number and temperature are varied to match the experimental data of sec. 6.2.3, with  $N = 450$  (blue),  $N = 600$  (cyan),  $N = 900$  (orange),  $N = 1200$  (green),  $N = 1500$  (red) and  $N = 2800$  atoms (purple).

One assumption of this model is that the condensate is homogeneous, omitting the fact that the trapping potential is not box-like, but close to harmonic. In the next section, this aspect is investigated.

### 6.3.3 Longitudinal dephasing induced by the inhomogeneous density

Quasi-condensates are not homogeneous, but rather present a 1d Thomas-Fermi profile longitudinally (see chap. 2 for details). Therefore, the density changes along the length of the condensate. Due to mean-field effects, as described in sec. 4.3.1, this

leads to different relative phase rotation speeds and a broadening of the relative phase distribution. To simulate the effect of a varying density, the longitudinal profiles of the two quasi-condensates are divided into  $\sim 400$  small regions of homogeneous density  $n(z) = \frac{\mu}{g_{1d}} [1 - (\frac{z}{R})^2]$  with  $R$  the TF radius of the quasi-condensates. The system can be seen as two strings of small condensates, with a local coupling constant between them. This simplified model assumes no coupling between adjacent slices in each individual condensate. The evolution is simulated by solving the system of coupled equations:

$$\begin{cases} i\hbar\partial_t\Psi_0 &= -\frac{\hbar^2}{2m}\partial_z^2\Psi_0 + \frac{1}{2}m\omega_z^2z^2\Psi_0 + g_0|\Psi_0|^2\Psi_0 + g_{01}|\Psi_1|^2\Psi_0 - \mu\Psi_0 \\ i\hbar\partial_t\Psi_1 &= -\frac{\hbar^2}{2m}\partial_z^2\Psi_1 + \frac{1}{2}m\omega_z^2z^2\Psi_1 + g_1|\Psi_1|^2\Psi_1 + g_{01}|\Psi_0|^2\Psi_1 - \mu\Psi_1 \end{cases} \quad (6.15)$$

for each pair of slices along the condensates, using a split-step method.

The central part of the cloud is denser, therefore the effective level splitting is reduced (see chap. 4) and relative phase is evolving slower than at the edges of the cloud. When integrating the contrast over all slices, it is expected to first drop, but then go through revivals as the different slices rephase. We indeed observe an effect of the relative phase distribution broadening caused by the inhomogeneous density in the simulations, but it is weak, as shown in fig. 6.12. The contrast remains higher than 90 %, and exhibits revivals. On the density distribution, this drop in contrast is almost invisible. Therefore, this type of dephasing does not explain the experimental observations for our typical parameters. Combined with a coupling between slices, we expect the effect to be even weaker.

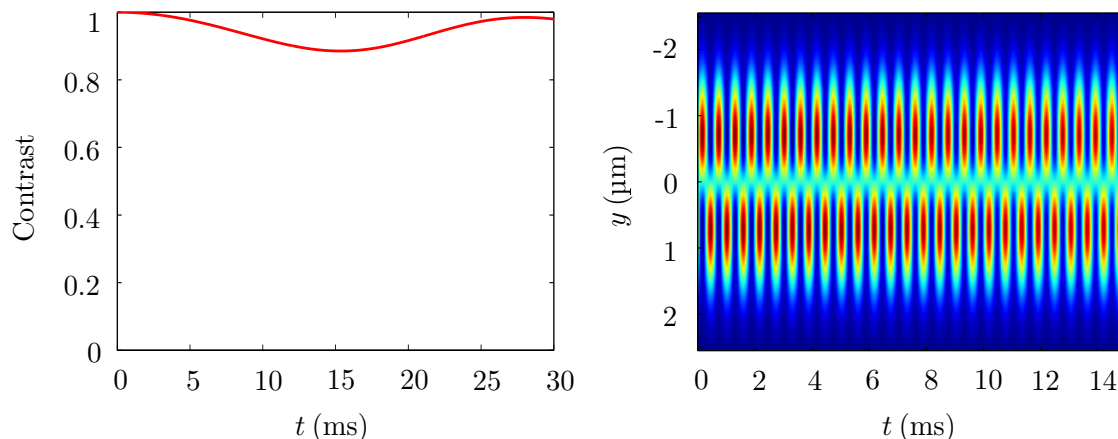


**Figure 6.12: Effect of longitudinal inhomogeneous dephasing.** (Left) On the contrast of the in-trap density distribution. (Right) On the in-trap density distributions.

## 6.4 Many-body effects

In the description used so far, many-body effects are mainly neglected. The system being composed of several hundreds to several thousands of atoms, it is expected to

obey mean-field equations for most cases. As we saw, when it comes to modeling the transfer process, a GPE formulation shows a very good agreement with experimentally observed densities. The mean-field approximation is powerful to describe phenomena in Bose-Einstein condensates and is in many cases preferred to many-body approaches. The reason is that many-body simulations are often more complete, but also computationally more involved and often untraceable.

However, a simple GPE cannot describe all phenomena occurring in our system. The previous section already presented some effects arising from the elongated character of the system. In addition, the mean-field approximation, by construction, is blind to the microscopic properties of individual atoms and does not account for collisions or quantum fluctuations. In this section, we present a many-body model of the motional state problem. This model has been developed in collaboration with Miguel-Ángel García-March and co-workers<sup>2</sup>. All considerations relate to the horizontal transverse direction and neglect the two other dimensions. The model does not account for finite temperatures.

### 6.4.1 Two-mode transverse dephasing

We start with the minimal configuration to describe our system, a 1d model comprising only the ground and first excited state in the  $y$ -direction. To develop the many-body model, we begin with the usual Hamiltonian in second quantization:

$$\begin{aligned} \hat{H} = & \int dy \Psi^\dagger(z) \left( -\frac{\hbar^2}{2m} \partial_{yy} + V(y) \right) \Psi(y) \\ & + \frac{g_y}{2} \int dy \Psi^\dagger(y) \Psi^\dagger(y) \Psi(y) \Psi(y). \end{aligned} \quad (6.16)$$

We estimate the rate of two-mode dephasing or phase diffusion that could arise from number fluctuations in the ground and excited states. This effect is recurrent in double-well physics and has been studied many times [108, 208–210]. The uncertainty on the atom number in each well after splitting brings an uncertainty on the difference of chemical potential. This leads to a different relative phase evolution and, in turn, to a broadening of the relative phase distribution. Here, we follow the approach of ref. [152], and, assuming weak interactions between atoms, approximate the field operator  $\hat{\Psi}$  describing the condensate by:

$$\hat{\Psi} \simeq \hat{a}_0 \psi_0 + \hat{a}_1 \psi_1, \quad (6.17)$$

where the  $\psi_i$  are the two lower-lying eigenstates of the non-interacting part of the Hamiltonian (taken to be real and normalized to  $\int |\psi_i|^2 dy = 1$ ) and the  $\hat{a}_i$  are annihilation operators associated with the modes, fulfilling the commutation relation  $[\hat{a}_i, \hat{a}_j^\dagger] = \delta_{ij}$ . From the full many-body Hamiltonian describing the condensate and eq. (6.17), we obtain the following effective two-mode Hamiltonian:

$$\hat{H}_{2m} = \Delta E \hat{J}_z + U \hat{J}_z^2 + 4U_{01} \hat{J}_x^2, \quad (6.18)$$

---

2. ICFO Institute of Photonic Sciences, Barcelona, Spain

with

$$\Delta E = E_{01} - (N - 1)(U_{00} - U_{11}), \quad (6.19)$$

$$U = U_{00} + U_{11} - 2U_{01}, \quad (6.20)$$

$$\text{and } U_{ij} = \frac{1}{2}g_{1D} \int |\psi_i|^2 |\psi_j|^2 dy, \quad (6.21)$$

where we use the usual spin representation for the many-body two-level system by introducing the operators  $\hat{J}_x = (\hat{a}_0\hat{a}_1^\dagger + \hat{a}_0^\dagger\hat{a}_1)/2$ ,  $\hat{J}_y = (\hat{a}_0\hat{a}_1^\dagger - \hat{a}_0^\dagger\hat{a}_1)/2i$  and  $\hat{J}_z = (\hat{a}_1^\dagger\hat{a}_1 - \hat{a}_0^\dagger\hat{a}_0)/2$ , which satisfy angular momentum commutation relations.

This Hamiltonian resembles the bosonic Josephson Hamiltonian, with an additional energy offset between the two modes. This energy offset is given here by the difference of chemical potential between the ground and first excited states (first term,  $\propto \hat{J}_z$ ). The second term ( $\propto \hat{J}_z^2$ ), which comes from interactions, is responsible for a “phase diffusion” mechanism, which is again a type of dephasing, as in sec. 6.3.2. The difference is that this dephasing does not come from the elongated character of the condensate, but from fluctuations during the splitting process. It is therefore a shot-to-shot phenomenon that averages over many realizations. We call it “two-mode dephasing”. Two-mode dephasing can lead to squeezing at short times [211], generation of strongly non-classical states [212] and a loss of coherence at longer times [181, 209]. The third term is generally neglected in bosonic Josephson junctions due to the weak overlap between the modes.

In the second term of eq. (6.18), it is apparent that phase diffusion is reduced compared to e.g. the case of a double-well system [108], as the modes have a significant spatial overlap. This is similar to the case of a spinor condensate in which two spin states share the same external wavefunction and have similar scattering lengths [20, 213]. It is also reminiscent of the phase locking experienced by the coupled quasi-condensates presented in the previous section.

We can evaluate the phase diffusion rate if we assume e.g. a binomial distribution of the atoms in each mode (i.e.  $\Delta\hat{J}_z = \sqrt{N}/2$ ), which is a fair assumption if the first  $\pi/2$  pulse is performed quickly compared to the other energy scales (in particular compared to interactions that may induce squeezing). It is then given by [181, 209]:

$$R = \frac{2\Delta\hat{J}_z U}{\hbar}. \quad (6.22)$$

We compute the two wavefunctions  $\psi_0$  and  $\psi_1$  in the trapping potential  $V_y$  to obtain the energies  $U_{00}/h = 0.34$  Hz,  $U_{11}/h = 0.26$  Hz, and  $U_{01}/h = 0.15$  Hz. This yields  $U/h = 0.31$  Hz, and a phase diffusion rate  $R = 52$  mrad ms<sup>-1</sup> = 8.3 mHz ms<sup>-1</sup>. The corresponding timescale at which two-mode dephasing becomes visible is therefore  $\tau_{2m} \sim 20$  ms. This rate increases with atom number fluctuations and can become significant if the fluctuations are much stronger than in the binomial case ( $\Delta p \gtrsim 20\sqrt{N}$ ,  $p$  being the population difference between the two modes). This could be the case, e.g. due to technical fluctuations in the transfer efficiency, although we do not have to date decisive arguments going along this line.

The timescale of two-mode dephasing is therefore longer than observed on the experimental system. Another element to consider is the single realization behavior as compared to the averaged distributions: for two-mode dephasing, in a simple 1d transverse, zero temperature picture, single shots are expected to have a full contrast, which is only washed out by averaging. On the experimental data, there is no qualitative difference of contrast between individual and averaged images, as confirmed by the  $G^{(2)}$  functions. This argument dismisses at first glance the two-mode dephasing as an explanation for the observed loss of contrast. Nevertheless, there is a possibility that this dephasing takes place but remains unnoticed. This can happen if, considering again that the condensate is not 3d but is elongated in the longitudinal direction, this phenomenon actually occurs in many “slices” of the quasi-condensates, and is therefore averaged out on every single realization due to the longitudinal integration. Here again, a better resolution in the longitudinal direction could help extricating the signatures for longitudinal or two-mode dephasing.

### 6.4.2 Three-mode many-body model

In the previous model, only two states were taken into account. Nevertheless, due to interactions, a small fraction of atoms unavoidably gets transferred to the second excited state. This small fraction consists only of a few atoms, which, more stringently than in the two-mode approximation, leads to a situation which would be better described in a many-body approach, where the behavior of atoms can be modeled. Other phenomena such as fragmentation could also take place in our system. These concerns motivated our choice to extend the many-body model to include the second excited state and pushing further the analysis.

#### Three-mode Hamiltonian

The field operator is this time expanded in a fixed basis of three modes:

$$\hat{\Psi} = \hat{a}_0\psi_0 + \hat{a}_1\psi_1 + \hat{a}_2\psi_2, \quad (6.23)$$

which correspond to the first three motional states. In this basis, the Hamiltonian can be re-written as:

$$\begin{aligned} \hat{H}_{3m} = & \sum_i n_i E_i \\ & + \sum_{i \neq j} U_{ij} [(a_i^\dagger)^2 a_j^2 + (a_j^\dagger)^2 a_i^2] + 4 \sum_{i \neq j} U_{ij} n_i n_j + \sum_i U_i n_i (n_i - 1) \\ & + 2U_{11}^{20} [(a_1^\dagger)^2 a_0 a_2 + a_1^2 a_0^\dagger a_2^\dagger] \\ & + 4U_{11}^{20} [n_1 a_0^\dagger a_2 + n_1 a_2^\dagger a_0] \\ & + 2U_{22}^{02} [a_0^\dagger n_2 a_2 + a_2^\dagger a_0 n_2] + 2U_{00}^{02} [a_2^\dagger n_0 a_0 + a_2 a_0^\dagger n_0] \end{aligned} \quad (6.24)$$

where  $n_i = a_i^\dagger a_i$  and  $U_{ij}^{kl} = \frac{g_{ij}}{2} \int dx \phi_i \phi_j \phi_k \phi_l$  (all wavefunctions are defined as real). The hats are omitted from now on for simplicity of notation.

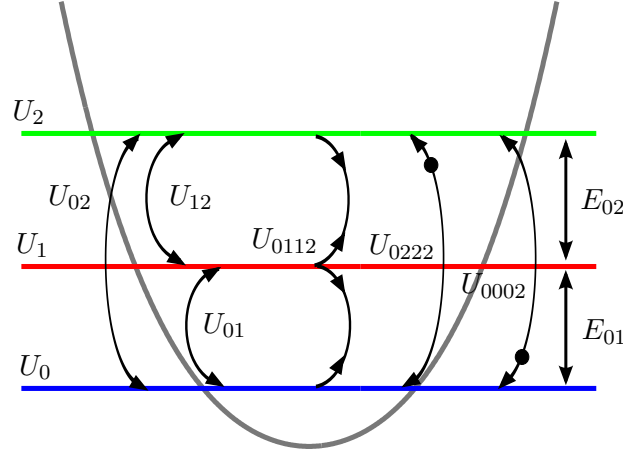


**Figure 6.13: Illustration of the trapping potential and the Hamiltonian interaction parameters.**

From the Hamiltonian in eq. (6.24), we can derive the equations of motion. In the Heisenberg picture, they correspond to:

$$i\frac{da_i}{dt} = [a_i, H_{3m}]. \quad (6.25)$$

We obtain the following equations of motion for the three modes:

$$\begin{aligned} i\frac{da_0}{dt} = & 2U_{01}a_0^\dagger a_1^2 + 2U_{02}a_0^\dagger a_2^2 + 4U_{01}n_1 a_0 + 4U_{02}n_2 a_0 \\ & + 2U_0 n_0 a_0 + E_0 a_0 + 2U_{0112}(a_2^\dagger a_1^2 + 2n_1 a_2) + 2U_{0222}n_2 a_2 \\ & + 2U_{0002}(a_0^2 a_2^\dagger + 2n_0 a_2), \end{aligned} \quad (6.26)$$

an equation similar to eq. (6.26) for  $a_2$ , and

$$\begin{aligned} i\frac{da_1}{dt} = & 2U_{01}a_1^\dagger a_0^2 + 2U_{12}a_1^\dagger a_2^2 + 4U_{01}n_0 a_1 + 4U_{12}n_2 a_1 \\ & + 2U_1 n_1 a_1 + E_1 a_1 + 4U_{0112}(a_0 a_2 a_1^\dagger + a_0^\dagger a_2 a_1 + a_2^\dagger a_0 a_1). \end{aligned} \quad (6.27)$$

These equations can be used to simulate the many-body dynamics after splitting, the results of which are presented in sec. 6.4.3.

### Comparison to mean-field evolution

In order to get a physical insight into the role of the different parameters and to compare this model to the GPE used earlier, we consider a classical version of the equations of motion. For this, we assume that we can treat the operators as  $c$ -numbers,  $\alpha_i = \sqrt{N_i} \exp(i\phi_i)$ . We obtain equations of motion for the amplitudes and phases of the

fields:

$$\begin{aligned}
\frac{dN_0}{dt} = & -4U_{01}N_0N_1 \sin 2(\phi_0 - \phi_1) - 4U_{02}N_0N_2 \sin 2(\phi_0 - \phi_2) \\
& + 4U_{0112}N_1\sqrt{N_0N_2}[\sin(2\phi_1 - \phi_2 - \phi_0) + 2\sin(\phi_2 - \phi_0)] \\
& + 4U_{0222}N_2\sqrt{N_0N_2} \sin(\phi_2 - \phi_0) \\
& + 4U_{0002}N_0\sqrt{N_0N_2} \sin(\phi_2 - \phi_0),
\end{aligned} \tag{6.28}$$

$$\begin{aligned}
\frac{d\phi_0}{dt} = & -2U_{01}N_1 \cos 2(\phi_0 - \phi_1) - 2U_{02}N_2 \cos 2(\phi_0 - \phi_2) \\
& - 4U_{01}N_1 - 4U_{02}N_2 - 2U_0N_0 - E_0 \\
& - 2U_{0112}N_1\sqrt{N_2/N_0}[\cos(2\phi_1 - \phi_2 - \phi_0) + 2\cos(\phi_2 - \phi_0)] \\
& - 2U_{0222}N_2\sqrt{N_2/N_0} \cos(\phi_2 - \phi_0) \\
& - 2U_{0002}3N_0\sqrt{N_2/N_0} \cos(\phi_2 - \phi_0),
\end{aligned} \tag{6.29}$$

with similar equations for  $N_2$  and  $\phi_2$ , and

$$\begin{aligned}
\frac{dN_1}{dt} = & -4U_{01}N_0N_1 \sin 2(\phi_1 - \phi_0) - 4U_{12}N_1N_2 \sin 2(\phi_1 - \phi_2) \\
& - 8U_{0112}N_1\sqrt{N_0N_2} \sin(2\phi_1 - \phi_2 - \phi_0),
\end{aligned} \tag{6.30}$$

$$\begin{aligned}
\frac{d\phi_1}{dt} = & -2U_{01}N_0 \cos 2(\phi_1 - \phi_0) - 2U_{12}N_2 \cos 2(\phi_1 - \phi_2) \\
& - 4U_{01}N_0 - 4U_{12}N_2 - 2U_1N_1 - E_1 \\
& - 4U_{0112}\sqrt{N_0N_2}[\cos(2\phi_1 - \phi_2 - \phi_0) + 2\cos(\phi_0 - \phi_2)].
\end{aligned} \tag{6.31}$$

An example of evolution following these equations of motion is plotted in fig. 6.14 (right). The initial state is a system with  $(N_0, N_1, N_2) = (350, 349, 1)$  atoms and all relative phases equal to zero. Several observations can be made. First, although the third mode is initially weakly populated, its population reaches up to 5% of the total atom number. Second, the evolution presents two types of oscillations with different timescales. A fast oscillation with a period  $T_{\text{fast}} \approx 0.5$  ms and a slow oscillation with a longer period  $T_{\text{slow}} \approx 5$  ms. In this regard, they are similar to the evolution observed with GPE simulations. Third, these oscillations continue over time, without showing any sign of damping.

Next to it, fig. 6.14 (left) shows an evolution starting from a state  $N_0 = N_1 = 350$  atoms, but with only the two lowest modes accessible. Interestingly, the evolution gets much simpler as only the fast oscillation remains. This comparison between two modes and three modes supports the statement that three modes are necessary to apprehend the complexity of the dynamics. As can be — and was — checked in this mean-field model, involving more than three modes does not bring significant changes to this evolution. We recall that this last remark is only valid for the case where the degeneracy between the different energy levels is lifted, as it is the case in the anharmonic potential. Would it not be the case, many more energy levels would be populated.

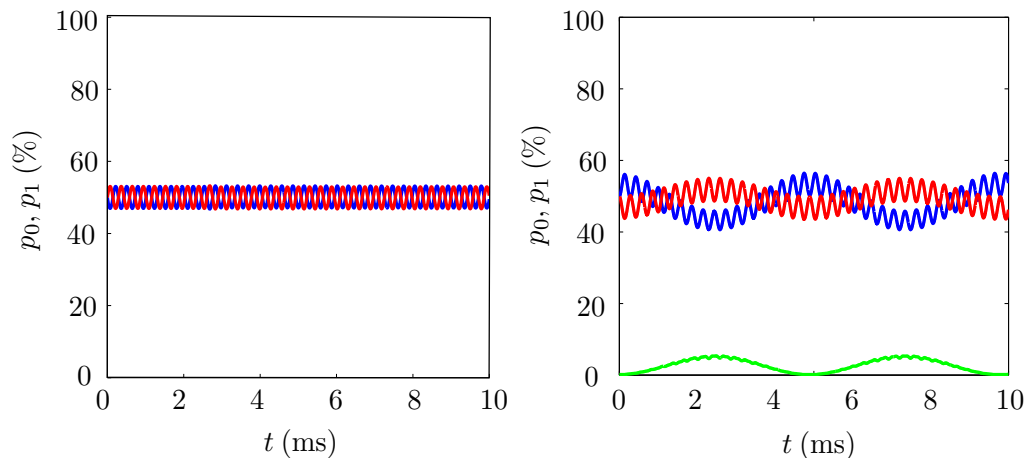


**Figure 6.14: Comparison between 2-mode and 3-mode evolution with classical field equations.** (Left) Two-mode evolution of ground state (blue) and first excited state (red) populations as a percentage of the total atom number. (Right) Three-mode evolution with ground state (blue), first excited state (red) and second excited state (green) populations.

### Roles of different interaction parameters

The model at hand can be used to gain more insight into the role of the different parameters, represented in fig. 6.13. In eq. (6.28) to (6.31), several parameters depending on overlap integrals appear to be playing a key role in the evolution of the amplitudes and phases. Although they are not physically independent in the system, the formulation used here makes it possible to explore the role of these parameters taken individually, and thus gain some insight on the impact of interactions on transfers between modes.

The parameters showing the strongest obvious effects are  $U_{01}$  and  $U_{0112}$ . The first parameter,  $U_{01} = \frac{g_y}{2} \int dx \phi_0^2 \phi_1^2$ , quantifies the interaction between ground and first excited state. Increasing this parameter in the simulations leads to a stronger amplitude of the fast oscillation. It acts on three different terms in eq. (6.24), which translate into exchanges of excitations between two states. The second parameter,  $U_{0112} = \frac{g_y}{2} \int dx \phi_0 \phi_1^2 \phi_2$ , involves all three states. It accounts for one term of eq. (6.24). This term accounts for two first excited state particles separating into one ground and one second excited state particles, and vice versa. It is the term defining the amplitude of the slow oscillation in fig. 6.14 (right). The role of the other terms is not as straightforward. The values of the different parameters for our typical experimental values are gathered in table 6.1.

### 6.4.3 Many-body simulations

The many-body simulations applied here rely on a numerical exact diagonalization of the many-body Hamiltonian presented above. This approach is very general and can be adapted to different models (e.g. Lipkin-Meshkov-Glick [152, 214] or Bose-

$U_0$	$U_1$	$U_2$	$U_{01}$	$U_{02}$	$U_{12}$	$U_{0112}$	$U_{0002}$	$U_{0222}$
0.303	0.248	0.218	0.17	0.14	0.15	-0.06	0.11	-0.007

**Table 6.1:** Values of the different parameters, given in Hz, of the Hamiltonian  $\hat{H}_{3m}$  for typical experimental parameters (potential  $V_y$ ,  $N=700$  atoms).

Hubbard Hamiltonian [215]). In the present case, the approach adopted is a semi-classical description of a system described in three fixed orbitals, which are the single-particle eigenstates of the anharmonic potential. The exact diagonalization approach has the advantage to be relatively simple, such that it is possible to make physical sense from the equations of simulated behaviors, as previously shown. By comparison, other methods to describe many-body systems, such as the MultiConfigurational Time-Dependent Hartree-Fock for Bosons (MCTDHB) can include more features, but the physical phenomena at the origin of the observed features can be difficult to identify.

It has however one serious limitation. Each additional mode or particle increases almost exponentially the problem's complexity. With two modes, it is possible to compute the evolution for our typical number of particles,  $N = 700$ . For three modes, however, the limit for computing the evolution in a reasonable time is reached for  $N = 140$  atoms. To get around this difficulty we consider, instead of the atom number  $N$  alone, the product of the atom number and the effective interaction constant,  $g_y N$ . This assumption comes from the observation that all terms in the Hamiltonian are dependent on this product rather than on the atom number alone. In this case, it would be possible to simulate the behavior of the experiment by taking a smaller atom number and increasing the interaction constant accordingly such that the product  $g_{\text{eq}} N_{\text{eq}}$  stays the same.

However, the situation is more complex. First, the interaction constant  $g_y$  depends weakly on the atom number (see chap. 2). To be accurate in the simulations at low atom numbers, one must account for this dependence. Second, in many-body problems, varying the interaction constant or the atom number is not equivalent in all cases [216]. For the same value of the equivalent product  $g_{\text{eq}} N_{\text{eq}}$ , a small interaction constant  $g_{\text{eq}}$  and a big value of  $N_{\text{eq}}$  ensures that the semi-classical description is valid. However, a small number of atoms  $N_{\text{eq}}$  and large interactions lead into the strongly correlated quantum regime. The limit between the two regimes can be estimated to  $\hbar\omega_y l_y \approx 3 \times 10^{-37}$  J m where  $l_y$  is the length of the harmonic oscillator. In our case,  $g_y \approx 3 \times 10^{-40}$  J m places us in the semi-classical limit for high atom numbers, although the limit between low and high atom number remains to be defined.

For low atom numbers, it is possible to be in the quantum regime. Phenomena leading to a loss of coherence, such as fragmentation, can occur. In the fragmentation process, the initially fully condensed state separates into two or more condensed parts. At fixed  $g_{\text{eq}} N_{\text{eq}}$ , to extend the results obtained for low atom numbers (and high  $g_{\text{eq}}$ ) to the case of high  $N_{\text{eq}}$  (and low  $g_{\text{eq}}$ ), a mapping to a known problem (e.g. a Bose-Hubbard model in a lattice) could provide some answers, but such a mapping is difficult. Here, we simulated the fragmentation for a range of low atom numbers, and obtained a rough estimation of

the expected fragmentation timescales at higher atom numbers by extrapolation.

We started from an initial state that is coherent, and where only the two lowest-lying single-particle states are occupied. We can write in general:

$$|\psi_{\text{ini}}\rangle = \frac{1}{N!}(\alpha\hat{a}_0^\dagger + \beta\hat{a}_1^\dagger)^N|\text{vac}\rangle \quad (6.32)$$

where  $|\alpha|^2 + |\beta|^2 = 1$ . The initial average population of the two first modes is  $N_0(0) = |\alpha|^2$  and  $N_1(0) = |\beta|^2$ , with  $N_i(t) = \langle\psi(t)|\hat{a}_i^\dagger\hat{a}_i|\psi(t)\rangle$ . For this state, the initial quantum fluctuations are given by:

$$\sigma_k = \sqrt{N}\alpha\sqrt{1-\alpha^2}. \quad (6.33)$$

The results of the simulations, presented below, are thus obtained for a three-mode, semi-classical representation of an equal superposition of ground and first excited state.

### Numerical findings

For our experimental parameters,  $g_y = 2.76 \times 10^{-40} \text{ J m} = 4.16 \times 10^{-4} \text{ kHz } \mu\text{m}$ . For the simulations, we use values of  $N_{\text{eq}}$  between 60 and 140, and we vary  $g_{\text{eq}}$ . The initial state for the simulations is the equal superposition of ground state and first excited state with fluctuations corresponding to a coherent state. The evolution is then computed for several tens of milliseconds.

First, the momentum distribution evolution for is simulated in order to have a comparison with the mean-field approximation. The simulation is done for  $N_{\text{eq}} = 120$  and the corresponding interaction constant  $g_{\text{eq}} = 4.2 \times 10^{-3} \text{ kHz } \mu\text{m}$ . The first observation we can make is that the evolution of the many-body momentum distribution show the same beating pattern as the GPE, with in addition a loss of contrast. The evolution of the populations in the different states also shows an evolution that differ from the GPE. Although the initial evolution is compatible with GPE, the oscillations are clearly damped.

Moreover, the one-body density matrix of the system has initially only one dominant eigenvalue, indicating that the system is fully condensed. However, after some time, the density matrix presents two eigenvalues of comparable magnitude. The eigenvalues of the density matrix correspond to different occupation numbers of the orbitals for the many-body Hamiltonian. This indicates a fragmentation of the condensate.

The effect of fragmentation can also be investigated and related to experimental observables by the calculation of the two-body correlation function. As explained in sec. 6.2, the  $G^{(2)}$  function is different for a state where the phase is randomized (dephasing) and for a state where coherence is lost (decoherence). The  $G^{(2)}$  calculated at long times from the many-body simulations is shown in fig. 6.16 (left). It exhibits a strong double-peak on the diagonal, as in fig. 6.2 (left), proving that the fragmentation effect is a dephasing. A comparison with fig. 6.2 shows that the pattern does not exactly match a pure dephasing nor a pure decoherence. There are two possible reasons for this. First, there could be some small dynamics remaining at the time at which this function was simulated. Another reason is that this  $G^{(2)}$  accounts for three modes, instead of two in

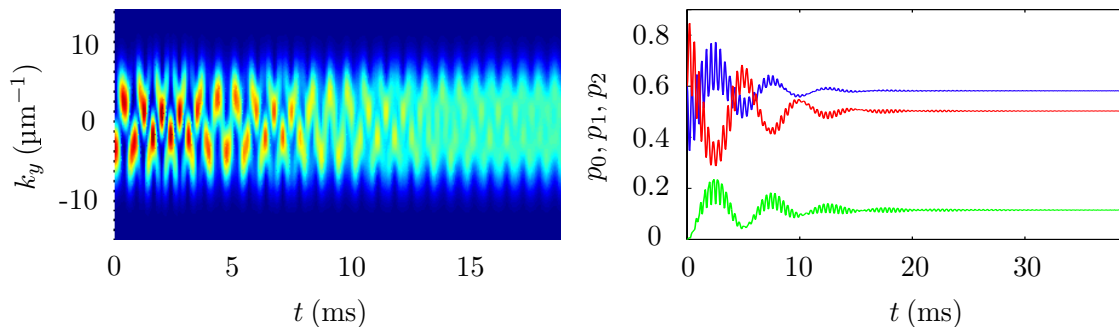


**Figure 6.15: Evolution of the equal superposition in the many-body three-mode model.** (Left) Momentum distribution simulated for  $N = 120$  and  $g = 4.2 \times 10^{-3} \text{ kHz } \mu\text{m}$ . (Right) Average populations of the three modes: ground state (blue), first excited state (red) and second excited state (green).

the simplistic models of fig. 6.2. In any case, the global aspect is qualitatively closer to the  $G^{(2)}$  function characteristic of dephasing than decoherence.

Finally, the loss of contrast as a function of  $g_{\text{eq}}N_{\text{eq}}$  is evaluated. Simulations are carried out for different values of  $g_{\text{eq}}N_{\text{eq}}$  and the results plotted as a function of the corresponding values of  $N$  for the experimental value of  $g_y$ . A decay time  $\tau$ , estimated from the fragmentation rate, is then extracted from the one-body density matrices. The simulated decay times are plotted as colored lines in fig. 6.16 (right), as a function of  $g_{\text{eq}}N_{\text{eq}}$ . The dependence of  $\tau$  on  $N_{\text{eq}}$  is close to a polynomial function of the form  $t_{\text{crit}} = aN_{\text{eq}}^b$ , where  $b \approx -\frac{3}{2}$ . Again, the simulations can only be carried out for low atom numbers. For higher atom numbers, the damping time is roughly estimated by an extrapolation from the dependence on  $N$  of the damping time for a given value of  $g_{\text{eq}}N_{\text{eq}}$ . The damping time as a function of  $g_{\text{eq}}N_{\text{eq}}$  appears to strongly increase for high atom numbers, in agreement with the previous statement that increasing the atom number leads to a classical behavior. For the different values of  $N$  that were experimentally probed,  $N = 450$  (leftmost black curve in fig. 6.16 (right)) to  $N = 2800$  (rightmost curve), the damping time remains high, in particular for the highest atom numbers, and only very strong interactions can lead to a fast fragmentation. The experimental interaction parameters are much weaker than this, as shown by the vertical lines in fig. 6.16 (right).

#### 6.4.4 Comparison to experimental data

From the simulations, we extracted three observables that can be compared to experimental data: the momentum distributions, the second-order correlation functions  $G^{(2)}$  and the decay time constant for different atom numbers.

For a low atom number, the momentum distributions in fig. 6.15 (left) present the same characteristic patterns as the GPE simulations and the experimental data: a fast beating of period  $\sim 0.6$  ms and a slower modulation of the whole density. The final state is reached after about 20 ms, as confirmed by the populations' evolution in fig. 6.15

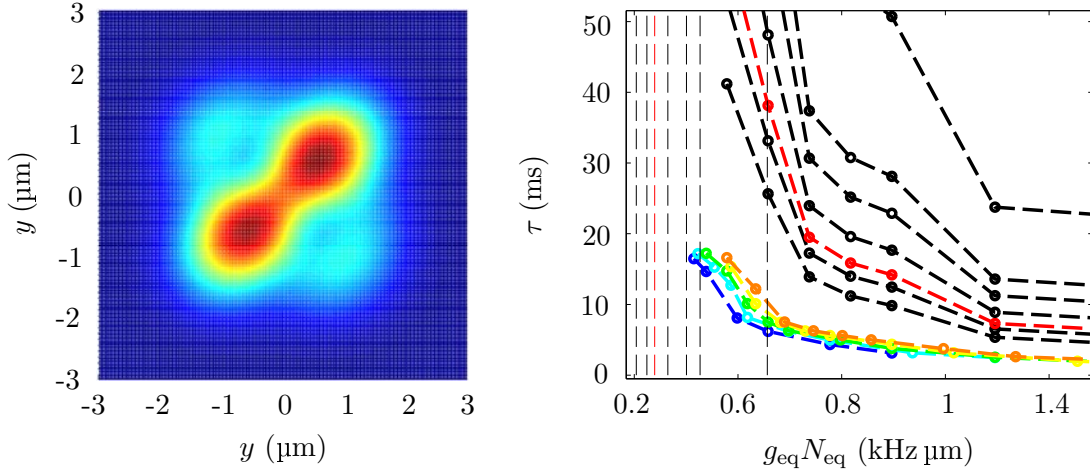


**Figure 6.16: Other simulation results for the many-body three-mode model** (Left) Second-order correlation function at long time for a fully fragmented condensate. (Right) Decay time  $\tau$  vs.  $g_{\text{eq}}N_{\text{eq}}$ . The thick lines correspond to different atom numbers. For the low atom numbers, from  $N = 60$  (blue) to  $N = 140$  (orange), the decay time is obtained from the many-body simulations. For higher atom numbers, the decay time is estimated from the results at lower atom numbers by interpolation. The red line shows the expected behavior for  $N = 700$ . The black lines stand for the same atom numbers as in sec. 6.2.3, from  $N = 450$  (leftmost curve) to  $N = 2800$  (rightmost curve). The vertical lines correspond to the actual value of  $gN$  in our experiment for these different atom numbers, again from  $N = 450$  (leftmost line) to  $N = 2800$  (rightmost line).

(right). The shape of this final state evokes a dephasing rather than a decoherence, with the width of the density staying globally constant over the whole evolution time, and the persisting presence of small structures. This seems to be confirmed by the  $G^{(2)}$  in fig. 6.16 (left), which is reminiscent of a dephasing pattern. It does not match, however, the experimental  $G^{(2)}$  at long times presented in fig. 6.4. On the latter, the patterns are much closer to what would be expected from decoherence.

Finally, the characteristic time for the fragmentation in fig. 6.16 (right), extracted from the many-body simulations, has a strong dependency on the atom number, going in the same direction as the experimental data shown in fig. 6.6. However, the damping times estimated by extrapolation do not match the timescale of the observed loss of contrast. From this result, it can be concluded that the three-mode many-body model, as we developed it, does not on its own explain the fast damping observed on the data.

## 6.5 Other considerations

Other ideas were raised when searching for the source of the contrast loss. One of them was a transfer of excitation between the two transverse directions. This could happen if the two directions are not completely decoupled. A direct observation of such an effect is not possible with our light sheet imaging system, because the signal is integrated

along the vertical direction (see chap. 3). However, we can use our absorption imaging system, able to record a vertical motion, to detect such excitations. Experimentally, we do not observe an increase of the amplitude of the center-of-mass motion, nor of the rms size, in the vertical dimension. Moreover, if a coherent transfer of excitation were to take place, one would expect to see a revival of the interference pattern after a time corresponding roughly to the time the pattern takes to disappear. We did not observe this effect either. As a numerical test, we carried out some simulations with a 3d GPE, which did not show any transfer of excitations between the different directions.

Another possible explanation, inherent to any practical experiment, is a deleterious effect of technical noise. This option is nearly impossible to rule out, as a complex experimental setup like ours has numerous potential sources of noise. We know, however, that the initial condensate is stable in the ground state of the transverse potential with a lifetime of several hundreds of milliseconds. When producing superpositions using the two different setups described in chap. 3, different devices and physical connections were made. The timescale of the contrast loss was affected, with a faster decay time (1.6 ms) when using the radio-frequency wire to produce the transfer pulse. This is likely to be due to additional noise, although no significant noise in a relevant frequency range was measured when characterizing the device. Moreover, GPE simulations of the dynamics with a noisy transfer pulse or in an unstable trap were carried out. They could not reproduce the observed results. This, in addition to the clear dependence on atom number, encourages a continuation of the search for more interesting, physical explanations.

## 6.6 Conclusions

In the different models investigated, two showed interesting features compatible with experimental observations of the loss of contrast: the longitudinal dephasing for a homogeneous condensate, and the production of twin-atom beams. Both take place on the expected timescale, and show a dependence on the atom number in line with the experimental results. However, in the longitudinal dephasing model, the final contrast remains rather high, which is not the case experimentally. It also shows a dependence on the temperature that was not observed on the data. Finally, as no dissipation mechanism is included, the final state in this model can only correspond to a dephasing. In contrast, the experimental second-order correlation functions at long times give hints of a decoherence rather than a dephasing phenomenon. One dissipation mechanism that is without a doubt taking place is the emission of twin-beams. A dephased state, if combined with a depletion due to twin-beam emission, is compatible with the transverse profiles observed at long times. The sole production of twin-beam does not explain, however, the loss of contrast. If secondary collisions with atoms in the condensate occur, no clear experimental signature for them have been identified yet.

Further investigations, both theoretical and experimental, are necessary to identify the damping mechanism(s). On the experimental side, a clean method to stretch the atomic cloud in the longitudinal direction would be useful. In the current setup, longitudinal effects are difficult to analyze, due to the very limited expansion in the longitudinal

direction in time-of-flight and the resolution of the imaging system. On the theoretical side, a more complete model including different effects studied in this chapter would help understanding the interplay between them.

Additionally, these models could be further tested experimentally. One could probe the many-body three-mode model with low atom numbers, and/or larger interaction constants. Obtaining a stable output for 100 atoms or less in our experimental setup is challenging, but increasing the effective interaction constant can be done by changing the trap geometry, such that the combination of both could allow to explore the regime where fast fragmentation occurs.

# 7

## Summary and perspectives

The experiments presented in this thesis showed the feasibility of manipulating motional states of a BEC in a fast and controlled way while maintaining the coherence of the system. They also gave a taste for potential applications to interferometry, and brought to light complex beyond-mean-field decay mechanisms.

The transfer scheme, initially demonstrated in ref. [115] for the efficient production of twin-atom beams, was improved and extended to the creation of different superposition states. The CRAB algorithm applied to the optimization of the transfer pulses yielded pulses that are not only faster and more efficient than previously possible, but also more robust. These optimizations rely on a one-dimensional GPE, which is a mean-field approximation of the experimental system. Images of the condensate taken after a long time-of-flight allow us to reconstruct the evolution of the momentum distribution in the trap, which shows an excellent agreement with the GPE simulations during and shortly after the transfer pulse. We also developed a method to read out the populations in each motional state for a coherent superposition of up to three motional states, based on the analysis of the momentum distribution's evolution.

Pushing further in complexity, the transfer scheme was extended to combine two different pulses and a varying time in between, forming all together a new type of interferometer based on motional states. We showed that the phase accumulated during the varying time can be read out after the second pulse from the populations of the two motional states.

The created superpositions exhibit at longer times effects beyond the 1d mean-field approximation, which are witnessed by a rapid loss of contrast for the momentum distributions. Several models are proposed, which unveil the high complexity arising from the elongation of the atomic cloud and its many particles. In the longitudinal direction, the finite temperature gives rise to Bogoliubov excitations, in addition to the inhomogeneous density profiles due to harmonic trapping, make the relative phase between the motional states space-dependent, leading to a loss of contrast upon longitudinal integration. In

addition, the formation of twin-beams induces a depletion of the first excited state. By adopting a many-body description of the system, it also appears that dephasing effects between modes and fragmentation could take place. The different models were examined to determine whether they could cause a loss of contrast, and on which timescale, to identify dependencies on parameters such as atom numbers and temperature and to characterize the final state in each case. A comparison with experimental data reveals that none of the models taken individually lead to a perfect agreement. Further studies are required to clarify some of the assumptions behind the models and if possible to investigate a meta-model including several of these effects.

The results presented here open new perspectives for the the study and potential applications of motional state superpositions. With our increased capabilities for motional states manipulation, many promising directions can be envisaged.

### Motional states in double-well potential

One application that is already under investigation is the creation of pulses targeting higher excited levels. In particular, this idea finds a direct use in the study of correlations and entanglement between twin-atom beams in a double-well geometry, as illustrated in fig. 7.1. For such a trapping potential, a condensate in the second motional excited state is expected to produce pairs of twin-beams in each of the well, forming a total of four beams which could be applied to test Bell's inequalities, in the spirit to the proposal of ref. [217]. This would be the first test of Bell inequalities with external degrees of freedom of massive particles.

The optimization of the required transfer pulse is complexified compared to the optimization of chap. 4 by the presence of an energy level between the initial and the target state. A series of optimizations was already carried out, which showed that the fidelities attainable with a displacement of the trap was limited. However, by complementing the displacement with a modulation of the trapping potential, high transfer efficiencies between ground state and second excited state are achieved. This type of manipulation is perfectly realistic and will be implemented soon on our experimental setup.

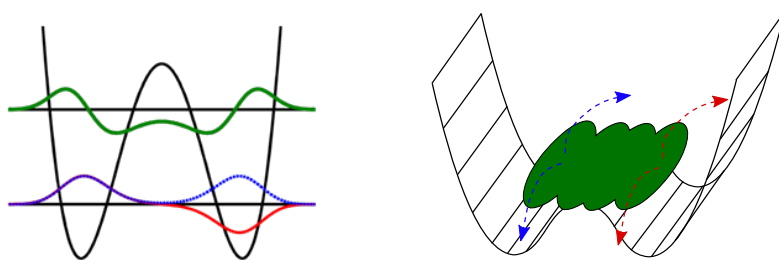


**Figure 7.1: Excitation and decay of motional states in a double-well potential.**

(Left) Ground state (blue), first excited state (red), and second-excited state (green) of the transverse double-well potential.

(Right) Twin-beam emission in the two wells.

## Gate operations

In chap. 4, we showed that an optimized half transfer pulse that can be viewed as a  $\pi/2$  pulse for a limited number of states on the equator of the Bloch sphere. In the perspective of quantum information, a relevant question is whether the pulse can also perform a  $\pi/2$  pulse for other states within the two-mode subspace. The problem is not straightforward, as the “qubit” at hand is weakly interacting and placed in a space where other modes are accessible. It is in that sense more complex than the usual systems used as qubits. It is however still simple enough to be treated in a mean-field picture at short times, making it an interesting object to study the feasibility of quantum operations on complex system, in anticipation of further schemes for quantum information with many-body systems [218].

We have started investigating this question numerically. We found that the second  $\pi/2$  pulse indeed performs a close-to-unitary operation, similar to a Hadamard gate, with limited leakage to higher excited states. But as the pulse is not optimized for this task, it does not yield the best achievable fidelity for a  $\pi/2$  pulse on the whole Bloch sphere. Currently, the best result was given by a simple transverse displacement, by performing an optimization on six different initial states distributed on the Bloch sphere (the two basis states and four states on the equator). This pulse allows us to reach a minimum overlap of 95 % with the target states when computed over the whole Bloch sphere, as can be seen in fig. 7.2 (top). A significant part of the 5 % error can be attributed to leakage to higher excited states, shown in fig. 7.2 (bottom right), in addition to a small contribution from the error on the phase (fig. 7.2 (bottom left)).

## Motional states control in other dimensions

Up to now, the scheme for motional state manipulation was confined to the horizontal transfer direction of the trapping potential. By extending the scheme to other dimensions, more exotic motional states could be engineered. For example, by exciting atoms to the first excited state in both transverse directions, a two-dimensional excited state carrying angular momentum could be obtained, analogous to a Laguerre mode for optical beams. Exciting a motion in the vertical direction is feasible by doubling up the device driving the trap displacement from the two symmetric radio-frequency carrying wires (DP400) to control each wire independently.

In the longitudinal direction, controlling the motional states independently is not possible, as the energy splitting in that direction is much smaller and the condensate occupies many modes. However, one could imagine applying displacement or modulation pulses for other purposes. One example would be to use optimal control methods to trigger or hinder additional dynamical effects in that direction.

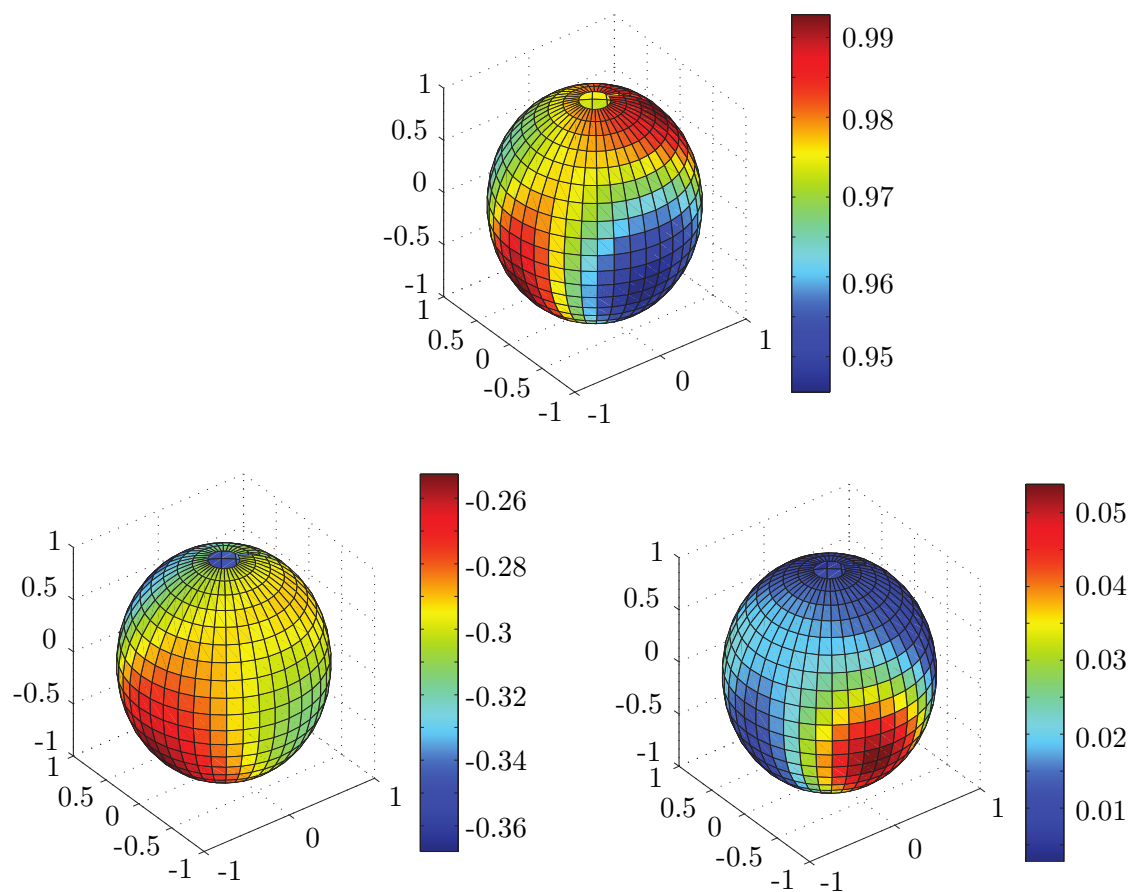


**Figure 7.2: Results of the Hadamard gate optimization.** (Top) Overlap fidelity distribution with respect to the initial states.  
(Bottom left) Global phase distribution (in units of  $\pi$ ).  
(Bottom right) Higher excitations distribution.

## Appendix A: Bogoliubov model

We describe here in more details the Bogoliubov model of excitations chosen to study the longitudinal dephasing in a motional state superposition. The starting point of the Bogoliubov model for the 2 transverse states is the system of coupled GPE:

$$\begin{cases} i\hbar\partial_t\Psi_i = -\frac{\hbar^2}{2m}\partial_z^2\Psi_i + g_i|\Psi_i|^2\Psi_i + g_{01}|\Psi_{1-i}|^2\Psi_i - \mu\Psi_i \\ (i = 0, 1). \end{cases} \quad (\text{A.1})$$

The field operator can be expanded in a field-density representation  $\Psi_i = \sqrt{n_i}e^{i\theta_i}$ , where  $n_i$  and  $\theta_i$  are two Hermitian operators for the density and the phase. For a quasi-condensate, the fluctuations in density are small and the field can be written to first order in  $\theta_i$  and  $\delta n_i$  as:

$$\Psi_i = \sqrt{n_{i,0} + \delta n_i}e^{i\theta_i}. \quad (\text{A.2})$$

In the case of a balanced superposition,  $n_{0,0} = n_{1,0} = n_0$ . The chemical potential is then  $\mu = (\frac{g_0+g_1}{2} + g_{01})n_0$ . Replacing  $\Psi_i \rightarrow \tilde{\Psi}_i e^{-in_0\frac{g_0-g_1}{2}t}$  in the above system, we get:

$$\begin{cases} i\hbar\partial_t\tilde{\Psi}_i = -\frac{\hbar^2}{2m}\partial_z^2\tilde{\Psi}_i + g_i|\tilde{\Psi}_i|^2\tilde{\Psi}_i + g_{01}|\tilde{\Psi}_{1-i}|^2\tilde{\Psi}_i - n_0(g_i - g_{01})\tilde{\Psi}_i \\ (i = 0, 1). \end{cases} \quad (\text{A.3})$$

After linearization, the system becomes a system of 4 coupled equations in  $\delta n_i$  and  $\theta_i$ :

$$\begin{cases} \frac{\hbar}{2\sqrt{n_0}} \cdot \partial_t\delta n_i & = -\frac{\hbar^2}{2m}\sqrt{n_0} \cdot \partial_z^2\theta_i \\ -\hbar \cdot \partial_t\theta_i & = -\frac{\hbar^2}{2m}\frac{1}{2n_0}\partial_z^2\delta n_i + g_i\delta n_i + g_{01}\delta n_{1-i}. \end{cases} \quad (\text{A.4})$$

These equations have a plane wave solution in  $e^{ikz}$  ( $\theta(z) = \sum_k \theta_k e^{ikz}$  resp.  $\delta n(z) = \sum_k \delta n_k e^{ikz}$ ) and can be re-written as:

$$\begin{cases} \frac{\hbar}{2\sqrt{n_0}} \cdot \partial_t\delta n_{i,k} & = \frac{\hbar^2}{2m}\sqrt{n_0}k^2\theta_{i,k} \\ -\hbar \cdot \partial_t\theta_{i,k} & = \frac{\hbar^2}{2m}\frac{1}{2n_0}k^2\delta n_{i,k} + g_i\delta n_{i,k} + g_{01}\delta n_{1-i,k} \end{cases} \quad (\text{A.5})$$

which can be divided into 2 equations for each variable, in particular for the phase variables we are interested in:

$$\begin{cases} \hbar^2 \cdot \partial_t^2 \theta_{i,k} = -\frac{\hbar^2}{4m^2} k^4 \theta_{i,k} - \frac{\hbar^2}{m} g_i n_0 k^2 \theta_{i,k} - \frac{\hbar^2}{m} g_{01} n_0 k^2 \theta_{1-i,k} \\ (i = 0, 1). \end{cases} \quad (\text{A.6})$$

The eigenmodes evolve in time as  $\theta_{i,k} = \hat{\theta}_{i,k} e^{-i\omega_k t}$ , which integrated in eq. (A.6) yields

$$(\hbar\omega_k)^2 \hat{\theta}_{i,k} = \frac{\hbar^2 k^2}{2m} \left( \frac{\hbar^2 k^2}{2m} + 2g_i n_0 \right) \hat{\theta}_{i,k} + \frac{\hbar^2}{m} g_{01} n_0 k^2 \hat{\theta}_{1-i,k} \quad (\text{A.7})$$

which then, expressed in matrix form, is:

$$(\hbar\omega_k)^2 \begin{bmatrix} \theta_0 \\ \theta_1 \end{bmatrix} = \begin{bmatrix} \frac{\hbar^2 k^2}{2m} \left( \frac{\hbar^2 k^2}{2m} + 2g_0 n_0 \right) & \frac{\hbar^2}{m} g_{01} n_0 k^2 \\ \frac{\hbar^2}{m} g_{01} n_0 k^2 & \frac{\hbar^2 k^2}{2m} \left( \frac{\hbar^2 k^2}{2m} + 2g_1 n_0 \right) \end{bmatrix} \begin{bmatrix} \theta_0 \\ \theta_1 \end{bmatrix} \quad (\text{A.8})$$

$$= \begin{bmatrix} \varepsilon_{k_0}^2 & \frac{\hbar^2}{m} g_{01} n_0 k^2 \\ \frac{\hbar^2}{m} g_{01} n_0 k^2 & \varepsilon_{k_1}^2 \end{bmatrix} \begin{bmatrix} \theta_0 \\ \theta_1 \end{bmatrix}. \quad (\text{A.9})$$

The eigenvalues of the eq. A.6 are:

$$(\hbar\omega_k^\pm)^2 = \frac{1}{2} \left\{ \varepsilon_{k_0}^2 + \varepsilon_{k_1}^2 \pm \sqrt{(\varepsilon_{k_0}^2 - \varepsilon_{k_1}^2)^2 + \left( \frac{\hbar^2}{m} g_{01} n_0 k^2 \right)^2} \right\}. \quad (\text{A.10})$$

In the end, we obtain 4 different solutions and hence 4 branches in the Bogoliubov spectrum.

In order to gain more insight into the spectrum, we re-express eq. (A.6) as:

$$(\hbar\omega_k)^2 \hat{\theta}_{i,k} = \varepsilon_{k_i}^2 \hat{\theta}_{i,k} + \frac{\hbar^2}{m} g_{01} n_0 k^2 \hat{\theta}_{1-i,k} = \frac{1}{2} \left\{ \varepsilon_{k_0}^2 + \varepsilon_{k_1}^2 \pm \sqrt{\nu} \right\} \hat{\theta}_{i,k} \quad (\text{A.11})$$

$$\Leftrightarrow \hat{\theta}_{i,k} = \frac{2}{\pm\sqrt{\nu}} \left\{ \frac{\varepsilon_{k_0}^2 - \varepsilon_{k_1}^2}{2} \hat{\theta}_{i,k} + \frac{\hbar^2}{m} g_{01} n_0 k^2 \hat{\theta}_{1-i,k} \right\} \quad (\text{A.12})$$

where  $\nu = (\varepsilon_{k_0}^2 - \varepsilon_{k_1}^2)^2 + \left( 2 \frac{\hbar^2}{m} g_{01} n_0 k^2 \right)^2$ . This leads to the following expression for the 2 different eigenmodes in matrix form:

$$\begin{bmatrix} \theta_0^\pm \\ \theta_1^\pm \end{bmatrix} = \pm \frac{2}{\sqrt{\nu}} \begin{bmatrix} \frac{\varepsilon_{k_0}^2 - \varepsilon_{k_1}^2}{2} & \frac{\hbar^2}{m} g_{01} n_0 k^2 \\ \frac{\hbar^2}{m} g_{01} n_0 k^2 & \frac{\varepsilon_{k_1}^2 - \varepsilon_{k_0}^2}{2} \end{bmatrix} \begin{bmatrix} \theta_0^\pm \\ \theta_1^\pm \end{bmatrix}. \quad (\text{A.13})$$

From there, we find an expression for both vectors (normalized to 1):

$$\begin{bmatrix} \theta_0^+ \\ \theta_1^+ \end{bmatrix} = c^+ \begin{bmatrix} 1 \\ \frac{2g_{01}n_0k^2}{\sqrt{\nu} - (\varepsilon_{k_0}^2 - \varepsilon_{k_1}^2)} \end{bmatrix} \quad (\text{A.14})$$

$$\begin{bmatrix} \theta_0^- \\ \theta_1^- \end{bmatrix} = c^- \begin{bmatrix} 1 \\ \frac{2g_{01}n_0k^2}{\sqrt{\nu} + (\varepsilon_{k_0}^2 - \varepsilon_{k_1}^2)} \end{bmatrix}. \quad (\text{A.15})$$

They are used to define a new basis for each set of frequencies, corresponding to the 2 branches of the Bogoliubov spectrum:

$$\begin{bmatrix} \theta^+ \\ \theta^- \end{bmatrix} = \begin{bmatrix} \theta_0^+ & \theta_1^+ \\ \theta_0^- & \theta_1^- \end{bmatrix} \begin{bmatrix} \theta_0 \\ \theta_1 \end{bmatrix}. \quad (\text{A.16})$$

This basis is used in the simulations of the quasi-condensates' evolution.

### Case of uncoupled quasi-condensates

In the case where the two quasi-condensates are uncoupled, the basis of Bogoliubov excitations is simply:

$$\begin{cases} \theta^+ = \theta_0 \\ \theta^- = \theta_1. \end{cases} \quad (\text{A.17})$$

We assume that the initial state is a state with no relative phase difference, and that the fluctuations are due to thermal fluctuations on the collective modes. Given that the modes are orthogonal and that the interaction energy dominates, we obtain a useful expression for the dephasing between the condensates as follows:

$$\begin{aligned} \langle |\theta_0(z, t) - \theta_1(z, t)|^2 \rangle &= \langle |\theta^+(z, t) - \theta^-(z, t)|^2 \rangle \\ &= \langle \left| \sum_k \theta_{+k}^{(0)} e^{i\omega_k^+ t} - \sum_k \theta_{-k}^{(0)} e^{i\omega_k^- t} \right|^2 \rangle \\ &= \sum_k \langle |\theta_k^{(0)}|^2 (e^{-i\omega_k^+ t} - e^{-i\omega_k^- t})(e^{i\omega_k^+ t} - e^{i\omega_k^- t}) \rangle \\ &= \sum_k \langle |\theta_k^{(0)}|^2 (2 - 2 \cos[(\omega_k^+ - \omega_k^-)t]) \rangle \\ &= \sum_k 2 \langle |\theta_k^{(0)}|^2 (1 - \cos \left[ \frac{k}{\sqrt{2m}} \left( \sqrt{\frac{k}{\sqrt{2m}} + 2g_0 n_0} - \sqrt{\frac{k}{\sqrt{2m}} + 2g_1 n_0} \right) t \right]) \rangle \\ &= \sum_k 2 \langle |\theta_k^{(0)}|^2 (1 - \cos \left[ \frac{k}{\sqrt{2m}} \sqrt{n_0} (\sqrt{2g_0} - \sqrt{2g_1}) t \right]) \rangle. \end{aligned} \quad (\text{A.18})$$

Using the approximation:

$$\frac{2\pi}{L} \sum_k \frac{1 - \cos(kz)}{k^2} \approx \int_0^\infty dk \frac{1 - \cos(kz)}{k^2}. \quad (\text{A.19})$$

and the equality  $1 - \cos(kz) = 2 \sin^2(kz/2)$ , we transform the integral using a integration per part:

$$\int_0^\infty dk \frac{1 - \cos(kz)}{k^2} = \int_0^\infty dk \cdot 2 \frac{\sin^2(kz/2)}{k^2} = \left[ -2 \frac{\sin^2(kz/2)}{k} \right]_0^\infty + \int_0^\infty dk \cdot z \frac{\sin(kz)}{k} = \frac{\pi}{2} z, \quad (\text{A.20})$$

which, combined with the expression of  $\langle (\theta_k^{(0)})^2 \rangle$ , yields:

$$\sum_k \langle (\theta_k^{(0)})^2 \rangle (1 - \cos(k \sqrt{\frac{n_0}{m}} (\sqrt{g_0} - \sqrt{g_1}) t)) = \frac{1}{L} \frac{mk_B T}{n_0 \hbar^2} \cdot \frac{L}{4} \sqrt{\frac{n_0}{m}} (\sqrt{g_0} - \sqrt{g_1}) t. \quad (\text{A.21})$$

The dephasing between the condensates is then estimated from:

$$\langle |\theta_0(z, t) - \theta_1(z, t)|^2 \rangle = \sum_k \langle |\theta_k^{(0)}|^2 \rangle (1 - \cos(k \sqrt{\frac{n_0}{m}} (\sqrt{g_0} - \sqrt{g_1}) t)). \quad (\text{A.22})$$

The first term  $\langle |\theta_k^{(0)}|^2 \rangle$  can be deduced from the equipartition theorem. For the initial condensate, using the fact that phonons are uncorrelated, the mean value of the Hamiltonian describing phonon modes in each mode can be expressed as  $H_{i,k} = L \frac{\hbar^2 k^2 n}{2m} \langle |\theta_{i,k}|^2 \rangle + L \frac{g}{2} \langle |\delta n_{i,k}|^2 \rangle$  [219]. The equipartition theorem states the mean energy per quadratic degree of freedom is  $k_B T/2$ , from which it follows that

$$\langle |\theta_k^{(0)}|^2 \rangle = \frac{1}{L} \frac{mk_B T}{n_i \hbar^2 k^2}. \quad (\text{A.23})$$

where  $n_i$  designates from now on the linear density of the initial condensate. The term  $\frac{2\pi}{L} \sum_{k>0}^{k_{\text{lim}}} \frac{1 - \cos(kz)}{k^2}$  can be to a good extent (i.e for large enough  $k_{\text{lim}}$ ) approximated by an integral of the form  $\int_0^\infty \frac{dk}{\pi} \frac{a}{k^2} [1 - \cos(kz)] = \frac{1}{2} a |z|$ . This leads to the final result for relative phase fluctuations:

$$\langle |\theta_0(z, t) - \theta_1(z, t)|^2 \rangle = \frac{mk_B T}{n_i \hbar^2} \cdot 2 \left| \sqrt{\frac{g_0 n_0}{m}} - \sqrt{\frac{g_1 n_0}{m}} \right| t. \quad (\text{A.24})$$

With similar calculation, the contrast of the interference pattern can be expressed analytically, as presented in sec. 6.3.2.

## Appendix B: Data sets

The main data sets presented in this thesis are referenced in the table below.

Date(s) & scan(s)	Purpose	Parameter(s)	Used in
22.11.2012 - scan 18	Half transfer	$t = 0:0.05:6$ ms $N = 700$	sec. 4.6
28.04.2015 - scan 16 29.04.2015 - scan 15	Full transfer	$t = 0:0.05:6$ ms $N = 700$	sec. 4.7
23.11.2015 - scan 7,9	Interferometer	$t_{\text{hold}} = 0...2.5$ ms	sec. 5.4
11.05.2015 - scan 1,3,5,15,16 15.05.2015 - scan 14 20.05.2015 - scan 1 21.05.2015 - scan 2	Half transfer Vary $N$	$t = 1:0.05:13$ ms rf knife = 0.9577... 0.9589 MHz	sec. 6.2
15.05.2015 - scan 1 14.08.2015 - scan 20	Half transfer Vary $T$	$t = 1:0.05:12$ ms $t_{\text{prep}} = 15:150:615$ ms	sec. 6.2
15.05.2015 - scan 3	Half transfer Twin-beams	rf knife = 0.9577... 0.9589 MHz	sec. 6.3
14.08.2015 - scan 7 14.08.2015 - scan 11	Half transfer Correlations	$t = 12...12.7$ ms $t = 0...0.7$ ms 50 repeats	sec. 6.2 sec. 6.2

## Appendix C: List of publications

The main results of this thesis are published in:

S. van Frank, A. Negretti, T. Berrada, R. Bücker, S. Montangero, J.-F. Schaff, T. Schumm, T. Calarco, J. Schmiedmayer. Interferometry with non-classical motional states of a Bose-Einstein condensate. *Nature Communications* **5**, 4009 (2014).

Other publications to which the author has contributed:

S. van Frank, M. Bonneau, J. Schmiedmayer, S. Hild, C. Gross, M. Cheneau, I. Bloch, T. Pichler, A. Negretti, T. Calarco, S. Montangero. Optimal control of complex atomic quantum systems. *In preparation*.

T. Berrada, S. van Frank, R. Bücker, T. Schumm, J.-F. Schaff, J. Schmiedmayer. Integrated Mach-Zehnder interferometer for Bose-Einstein condensates. *Nature Communications* **4**, 2077 (2013).

R. Bücker, T. Berrada, S. van Frank, J.-F. Schaff, T. Schumm, J. Schmiedmayer, G. Jäger, J. Grond, U. Hohenester. Vibrational state inversion of a Bose-Einstein condensate: optimal control and state tomography. *Journal of Physics B* **46**, 104012 (2013).

R. Bücker, U. Hohenester, T. Berrada, S. van Frank, A. Perrin, S. Manz, T. Betz, J. Grond, T. Schumm, and J. Schmiedmayer. Dynamics of parametric matter-wave amplification. *Physical Review A* **86**, 013638 (2012).

# List of Symbols

Symbol	Description
$ 0\rangle$	Transversal ground state
$ 1_y\rangle$	Transversal first excited state in the $y$ -direction
$\hat{a}_i, \hat{a}_i^\dagger$	Annihilation and creation operators for transversal field modes
$\alpha$	Absorption imaging factor
$\alpha_i$	Simulated potential's parameters
$\beta$	Inverse temperature in units of $k_B$
$\beta_k$	Complex amplitude of the Bogoliubov elementary excitations
$a_s$	3d s-wave scattering length in $ 1, -1\rangle$ (5.3 nm)
$C$	Contrast
$d_0$	Distance from the chip surface to the center of the trap
$E_{01}^{\text{eff}}$	Effective energy level splitting between $ 0\rangle$ and $ 1_y\rangle$
$E_{01}^{\text{s.p.}}$	Single-particle energy difference between $ 0\rangle$ and $ 1_y\rangle$
$\mathcal{F}$	Transfer pulse fidelity
$\mathcal{F}_{\text{half}}$	Half transfer pulse fidelity
$\mathcal{F}_{\text{full}}$	Full transfer pulse fidelity
$G^{(n)}(x_1, x_2, \dots, x_{2n})$	$n$ -th order correlation function
$\hat{G}^{(2)}$	Second-order autocorrelation of individual images
$\overline{G^{(2)}}$	Average of $\hat{G}^{(2)}$
$C^{(2)}$	Normalization function of $\hat{G}^{(2)}$
$g$	3d interaction constant
$g_{\text{eq}}$	Equivalent interaction constant for many-body simulations
$g_F$	Landé g-factor
$g_l$	1d effective interaction constant in direction $l$
$g_0^y$	Effective 1d interaction constant for $ 0\rangle$

---

$g_1^y$	Effective 1d interaction constant for $ 1_y\rangle$
$g_{01}^y$	Effective 1d interaction constant between $ 0\rangle$ and $ 1_y\rangle$
$\gamma$	Lieb-Liniger degeneracy parameter
$\hat{H}$	Many-body Hamiltonian
$\hbar$	Reduced Planck constant ( $1.06 \times 10^{-26}$ J s)
$I_0^{\text{sat}}$	Saturation intensity for absorption imaging
$I_{in/out}$	Absorption imaging intensity before/after atomic cloud
$\mathcal{J}$	Transfer pulse infidelity, i.e. $1 - \mathcal{F}$
$\mathcal{J}_{half}$	Half transfer pulse infidelity
$\mathcal{J}_{full}$	Full transfer pulse infidelity
$\mathcal{J}^{(2)}$	Visibility of the motional state interferometer
$k_B$	Boltzmann constant ( $1.38 \times 10^{-23}$ J K <sup>-1</sup> )
$k_y$	Momentum in the horizontal transverse direction
$L$	Length of the condensate in the homogeneous trap
$l_l$	Harmonic oscillator length in direction $l$
$\lambda(t)$	Transfer pulse trajectory
$\lambda_{dB}$	Thermal de Broeglie wavelength
$\lambda_T^{(s)}$	Thermal coherence length of a single condensate
$\lambda_T$	Thermal coherence length of a pair of condensates
$m$	Mass of Rubidium 87 ( $1.443 \times 10^{-25}$ kg)
$\mu$	Chemical potential
$\mu_B$	Bohr magneton ( $9.27 \times 10^{-28}$ J T <sup>-1</sup> )
$\mu_F$	Zeeman state
$N$	Total number of atoms in the condensate
$N_0$	Number of atoms in $ 0\rangle$
$N_1$	Number of atoms in $ 1_y\rangle$
$N_{\text{eq}}$	Equivalent atom number for many-body simulations
$n$	3d gas density
$n_0$	1d density of $ 0\rangle$ in the longitudinal direction
$n_1$	1d density of $ 1_y\rangle$ in the longitudinal direction
$n_{1d}$	1d gas density
$n_c$	Critical gas density
$n_{\text{dephasing}}$	Gas density after dephasing

---

$n_{\text{decoherence}}$	Gas density after decoherence
$\delta\hat{n}_k$	Bogoliubov elementary density fluctuations
$\nu_L$	Larmor frequency
$\nu_{s.p.}$	First level splitting of the trap in the $y$ -direction
$\xi$	Healing length
$OD$	Optical density
$p$	Photon-per-atom detected in light sheet
$p_0$	Population in the transverse ground state, normalized to $N$
$p_1$	Population in the transverse first excited state, normalized to $N$
$p_2$	Population in the transverse second excited state, normalized to $N$
$p_{\text{res}}$	Population in higher excited states, normalized to $N$
$\varphi_i(r)$	Single-particle wavefunction at position $r$
$\phi_0$	Phase of the transversal ground state
$\phi_1$	Phase of the transversal first excited state
$\Delta\phi$	Phase difference between transversal ground and first excited state
$\hat{\Psi}(\mathbf{r}, t), \hat{\Psi}^\dagger(\mathbf{r}, t)$	Field annihilation and creation operators
$\psi$	Transverse wavefunction
$\psi_0$	Ground state transverse wavefunction
$\psi_1$	First excited state transverse wavefunction
$\psi_{\text{target}}$	Target wavefunction for the optimization
$\psi_y(T_{\text{pulse}})$	Wavefunction obtained at the final time of the transfer pulse
$R$	Condensate radius
$R_{TF}$	Thomas-Fermi radius
$r$	Number of degrees of freedom in the GP fits
$S$	Signal detected and corrected in light sheet
$\sigma_s$	Scattering cross-section
$t$	Time
$t_{\text{hold}}$	Time between the two pulses of the motional state interferometer
$T$	Temperature
$T_c$	Critical temperature
$T_{\text{pulse}}$	Transfer pulse duration
$T_{\text{QSL}}$	Quantum speed limit timescale
$T_{\text{fast}}$	Period of the beating pattern

---

$T_{\text{slow}}$	Period of the modulation pattern
$\tau$	Reduced temperature parameter
$\hat{\theta}_k$	Bogoliubov elementary phase fluctuations
$\theta_{01}$	Relative phase between ground and first excited states
$U(r_{ij})$	Interaction potential between particles $i$ and $j$
$U_{ijkl}$	Interaction parameter in the many-body Hamiltonian
$V(\mathbf{r}, t)$	Trapping potential at position $\mathbf{r}$ and time $t$
$V_d$	Dressed potential
$w_i$	Error bars on the experimental points
$\Omega_{RF}$	Rabi frequency associated with the dressing fields
$\Omega_s$	Rabi frequency associated with the static fields
$\omega_l$	Trap frequency in direction $l$
$\omega_{\perp}$	Transverse trap frequency
$\omega_{01}$	Effective frequency splitting between $ 0\rangle$ and $ 1_y\rangle$
$\chi^2$	Goodness-of-fit parameter
$\chi_r^2$	Reduced goodness-of-fit parameter
$y$	Position in the horizontal transverse direction
$y_i$	Experimental data points
$y(x_i)$	Fit values corresponding to the experimental data points $y_i$

# Bibliography

- [1] K. B. Davis *et al.* Bose-Einstein condensation in a gas of sodium atoms. *Physical Review Letters* **75**, 3969–3973 (1995).
- [2] M. H. Anderson, J. R. Ensher, M. R. Matthews, C. E. Wieman & E. A. Cornell. Observation of bose-einstein condensation in a dilute atomic vapor. *Science* **269**, 198–201 (1995).
- [3] C. C. Bradley, C. A. Sackett, J. J. Tollett & R. G. Hulet. Evidence of Bose-Einstein condensation in an atomic gas with attractive interactions. *Physical Review Letters* **75**, 1687–1690 (1995).
- [4] S. Bose. Planck’s law and the light quantum hypothesis. *Zeitschrift für Physik* **26**, 178–181 (1924).
- [5] M. Greiner, O. Mandel, T. Esslinger, T. W. Hänsch & I. Bloch. Quantum phase transition from a superfluid to a Mott insulator in a gas of ultracold atoms. *Nature* **415**, 39–44 (2002).
- [6] W. S. Bakr *et al.* Probing the superfluid-to-Mott insulator transition at the single-atom level. *Science* **329**, 547–550 (2010).
- [7] J. R. Anglin & W. H. Zurek. Winding up by a quench: vortices in the wake of rapid Bose-Einstein condensation. *Physical Review Letters* **83**, 1707–1710 (1998).
- [8] B. Nowak, D. Sexty & T. Gasenzer. Superfluid turbulence: Nonthermal fixed point in an ultracold Bose gas. *Physical Review B* **84**, 020506 (2011).
- [9] M. Anderlini *et al.* Controlled exchange interaction between pairs of neutral atoms in an optical lattice. *Nature* **448**, 452–456 (2007).
- [10] T. M. Hoang *et al.* Dynamic Stabilization of a Quantum Many-Body Spin System. *Physical Review Letters* **111**, 090403 (2013).
- [11] S. Trotzky *et al.* Time-resolved observation and control of superexchange interactions with ultracold atoms in optical lattices. *Science* **319**, 295–299 (2008).
- [12] J. Simon *et al.* Quantum simulation of antiferromagnetic spin chains in an optical lattice. *Nature* **472**, 307–312 (2011).
- [13] D. Jaksch, C. Bruder, J. I. Cirac, C. W. Gardiner & P. Zoller. Cold bosonic atoms in optical lattices. *Physical Review Letters* **81**, 3108–3111 (1998).

- [14] D. J. Wineland & H. Dehmelt. Proposed  $10^{14}\Delta\nu < \nu$  laser fluorescence spectroscopy on Tl<sup>+</sup> mono-ion oscillator. *Bulletin of the American Physical Society* **20**, 637 (1975).
- [15] T. W. Hänsch & A. L. Schawlow. Cooling of gases by laser radiation. *Optics Communications* **13**, 68 (1975).
- [16] E. L. Raab, M. Prentiss, A. Cable, S. Chu & D. E. Pritchard. Trapping of Neutral Sodium Atoms with Radiation Pressure. *Physical Review Letters* **59**, 2631–2634 (1987).
- [17] P. Verkerk *et al.* Search for superheavy hydrogen in sea water. *Physical Review Letters* **68**, 1116–1119 (1992).
- [18] J. Reichel & V. Vuletic. *Atom Chips* (Wiley, 2010).
- [19] T. Gasenzer. Ultracold gases far from equilibrium. *European Physical Journal: Special Topics* **168**, 89–148 (2009).
- [20] C. Gross, T. Zibold, E. Nicklas, J. Estève & M. K. Oberthaler. Nonlinear atom interferometer surpasses classical precision limit. *Nature* **464**, 1165–1174 (2010).
- [21] T. Berrada. *Mach-Zehnder interferometry with interacting Bose-Einstein condensates in a double-well potential* PhD Thesis (TU Wien, 2014).
- [22] U. Schollwöck. The density-matrix renormalization group. *Reviews of Modern Physics* **77**, 259–315 (2005).
- [23] T. Kinoshita, T. Wenger & D. S. Weiss. A quantum Newton’s cradle. *Nature* **440**, 900–903 (2006).
- [24] L. E. Sadler, J. M. Higbie, S. R. Leslie, M. Vengalattore & D. M. Stamper-Kurn. Spontaneous symmetry breaking in a quenched ferromagnetic spinor Bose-Einstein condensate. *Nature* **443**, 312–315 (2006).
- [25] S. Diehl *et al.* Quantum States and Phases in Driven Open Quantum Systems with Cold Atoms. *Nature Physics* **4**, 878–883 (2008).
- [26] E. G. Dalla Torre, E. Demler, T. Giamarchi & E. Altman. Quantum critical states and phase transitions in the presence of non equilibrium noise. *Nature Physics* **6**, 806–810 (2009).
- [27] A. Polkovnikov, K. Sengupta, A. Silva & M. Vengalattore. *Colloquium* : Nonequilibrium dynamics of closed interacting quantum systems. *Reviews of Modern Physics* **83**, 863–883 (2011).
- [28] M. Rigol, V. Dunjko & M. Olshanii. Thermalization and its mechanism for generic isolated quantum systems. *Nature* **452**, 854–858 (2008).
- [29] T. Langen, R. Geiger, M. Kuhnert, B. Rauer & J. Schmiedmayer. Local emergence of thermal correlations in an isolated quantum many-body system. *Nature Physics* **9**, 640–643 (2013).

- [30] L. J. Garay, J. R. Anglin, J. I. Cirac & P. Zoller. Sonic analog of gravitational black holes in Bose-Einstein condensates. *Physical Review Letters* **85**, 4643–4647 (2000).
- [31] C. Barceló, S. Liberato & M. Visser. Analogue models for FRW cosmologies. *International Journal of Modern Physics D* **12**, 1641–1649 (2003).
- [32] E. A. Calzetta & B. L. Hu. Early universe quantum processes in BEC collapse experiments. *International Journal of Theoretical Physics* **44**, 1691–1704 (2005).
- [33] J. Cirac & P. Zoller. Quantum Computations with Cold Trapped Ions. *Physical Review Letters* **74**, 4091–4094 (1995).
- [34] C. Monroe, D. Meekhof, B. King, W. Itano & D. Wineland. Demonstration of a Fundamental Quantum Logic Gate. *Physical Review Letters* **75**, 4714–4717 (1995).
- [35] A. H. Myerson *et al.* High-fidelity readout of trapped-ion qubits. *Physical Review Letters* **100**, 200502 (2008).
- [36] K. R. Brown *et al.* Single-qubit-gate error below  $10^{-4}$  in a trapped ion. *Physical Review A* **84**, 063424 (2011).
- [37] K.-A. Brickman Soderberg, N. Gemelke & C. Chin. Ultracold molecules: Vehicles to scalable quantum information processing. *New Journal of Physics* **11**, 055022 (2009).
- [38] A. Einstein. Quantentheorie des einatomigen idealen Gases, 2. Abhandlung. *Sitzber. Preuss. Akad. Wiss.* 3–14 (1925).
- [39] P. L. Kapitza. Viscosity of liquid Helium below the lambda-point. *Nature* **141**, 74–75 (1938).
- [40] J. F. Allen & A. D. Misener. Flow Phenomena in Liquid Helium II. *Nature* **142**, 643–644 (1938).
- [41] F. London. The lambda-phenomenon of liquid helium and the Bose-Einstein degeneracy. *Nature* **141**, 643–644 & 913 (1938).
- [42] N. N. Bogoliubov. On the Theory of Superfluidity. *Izvestia Akademii Nauk (USSR)* **11**, 77 (1938).
- [43] L. P. Pitaevskii & S. Stringari. *Bose-Einstein Condensation* (Clarendon Press, 2003).
- [44] L. Landau & E. Lifshitz. *Statistical Physics, 3rd Edition, Vol. 5* (Elsevier Science, 2013).
- [45] C. Pethick & H. Smith. *Bose-Einstein Condensation in Dilute Gases* (Cambridge University Press, 2002).
- [46] W Ketterle & van Druten NJ. Bose-Einstein condensation of a finite number of particles trapped in one or three dimensions. *Physical review A* **54**, 656–660 (1996).

- [47] N. van Druten & W. Ketterle. Two-Step Condensation of the Ideal Bose Gas in Highly Anisotropic Traps. *Physical Review Letters* **79**, 549–552 (1997).
- [48] R. P. Smith, R. L. D. Campbell, N. Tammuz & Z. Hadzibabic. Effects of interactions on the critical temperature of a trapped bose gas. *Physical Review Letters* **106**, 250403 (2011).
- [49] E. P. Gross. Structure of a quantized vortex in boson systems. English. *Il Nuovo Cimento Series 10* **20**, 454–477 (1961).
- [50] L. P. Pitaevskii. Vortex lines in an imperfect Bose gas. *Soviet Physics JETP* **13**, 451–454 (1961).
- [51] S. T. Beliaev. Energy spectrum of a non-ideal Bose gas. *Sov. Phys. JETP* **7** (1958).
- [52] S. Stringari, C. Wieman & S. italiana di fisica. *Bose-Einstein Condensation in Atomic Gases: Proceedings of the International School of Physics "Enrico Fermi", Varenna on Lake Como, Villa Monastero, 7-17 July 1998* (IOS Press, 1999).
- [53] K. Huang & C. N. Yang. Quantum-mechanical many-body problem with hard-sphere interaction. *Physical Review* **105**, 767–775 (1957).
- [54] Y. Castin. English. in *Coherent atomic matter waves* (eds R. Kaiser, C. Westbrook & F. David) 1–136 (Springer Berlin Heidelberg, 2001).
- [55] C. Mora & Y. Castin. Extension of Bogoliubov theory to quasi-condensates. *Physical Review Letters* **67**, 053615 (2002).
- [56] R. Bücke. *Twin-atom beam generation in a one-dimensional Bose gas*. PhD Thesis (TU Wien, 2013).
- [57] M. Olshanii. Atomic Scattering in Presence of an External Confinement and a Gas of Impenetrable Bosons. *Physical Review Letters* **81**, 938–941 (1998).
- [58] G. E. Astrakharchik, J. Boronat, J. Casulleras & S. Giorgini. Beyond the Tonks-Girardeau gas: Strongly correlated regime in quasi-one-dimensional Bose gases. *Physical Review Letters* **95**, 190407 (2005).
- [59] E. Haller *et al.* Realization of an excited, strongly correlated quantum gas phase. *Science* **325**, 1224–1227 (2009).
- [60] M. Girardeau. Relationship between Systems of Impenetrable Bosons and Fermions in One Dimension. *Journal of Mathematical Physics* **1**, 516–523 (1960).
- [61] E. H. Lieb & W. Liniger. Exact analysis of an interacting Bose gas. 1. The General solution and the ground state. *Physical Review* **130**, 1605–1616 (1963).
- [62] E. H. Lieb. Exact analysis of an interacting bose gas. II. the excitation spectrum. *Physical Review* **130**, 1616–1624 (1963).
- [63] K. V. Kheruntsyan, D. M. Gangardt, P. D. Drummond & G. V. Shlyapnikov. Pair correlations in a finite-temperature 1D Bose gas. *Physical review letters* **91**, 040403 (2003).

- [64] D. S. Petrov, D. M. Gangardt & G. V. Shlyapnikov. Low-dimensional trapped gases. *Journal de Physique IV* **116**, 5–44 (2004).
- [65] K. V. Kheruntsyan, D. M. Gangardt, P. D. Drummond & G. V. Shlyapnikov. Finite-temperature correlations and density profiles of an inhomogeneous interacting one-dimensional Bose gas. *Physical Review A* **71**, 053615 (2005).
- [66] H. P. Stimming, N. J. Mauser, J. Schmiedmayer & I. E. Mazets. Fluctuations and stochastic processes in one-dimensional many-body quantum systems. *Physical Review Letters* **105**, 015301 (2010).
- [67] A. Imambekov *et al.* Density ripples in expanding low-dimensional gases as a probe of correlations. *Physical Review A* **80**, 033604 (2009).
- [68] S. Manz *et al.* Two-point density correlations of quasicondensates in free expansion. *Physical Review A* **81**, 031610 (2010).
- [69] C. Menotti & S. Stringari. Collective oscillations of a 1D trapped Bose gas. *Physical Review A* **66**, 043610 (2002).
- [70] F. Gerbier. Quasi-1D Bose-Einstein condensates in the dimensional crossover regime. *Europhysics Letters* **66**, 771–777 (2004).
- [71] H. Gimpel. *Magnetische Oberflächenfallen für Atom-Interferometer*. Diploma Thesis (University of Heidelberg, 2002).
- [72] C. Becker. *Eine neuartige magneto-optische Falle für Atomchip-Experimente*. Diploma Thesis (University of Heidelberg, 2002).
- [73] S. Haupt. *Setup of a new Experiment with ultracold  $87\text{Rb}$  Atoms: Towards Quantum Information Processing on an Atom Chip*. PhD Thesis (University of Heidelberg, 2003).
- [74] P. Krüger. *Coherent matter waves near surfaces*. PhD Thesis (University of Heidelberg, 2004).
- [75] S. Hofferberth. *Experiments with ultracold atoms and Bose-Einstein condensates in microtraps near surfaces*. Diploma Thesis (University of Heidelberg, 2004).
- [76] S. Wildermuth. *One-dimensional Bose-Einstein condensates in micro-traps*. PhD Thesis (University of Heidelberg, 2005).
- [77] S. Manz. *Density correlations of expanding one-dimensional Bose gases*. PhD Thesis (TU Wien, 2010).
- [78] T. Betz. *Phase correlations of coupled one-dimensional Bose gases* PhD Thesis (TU Wien, 2011).
- [79] R. Bücker. *Fluorescence imaging of ultracold atoms*. Diploma Thesis (University of Heidelberg, 2007).
- [80] S. Groth. *Development, fabrication, and characterisation of atom chips*. PhD Thesis (University of Heidelberg, 2006).

- [81] T. Schumm. *Bose-Einstein condensates in magnetic double well potentials*. PhD Thesis (Université Paris 11, 2005).
- [82] S. Hofferberth. *Coherent manipulation of Bose-Einstein condensates with rf adiabatic potentials*. PhD Thesis (University of Heidelberg, 2007).
- [83] T. Plisson. *Coherent Manipulation of Bose-Einstein Condensates with Microwave and Radio Frequency Fields*. Diploma Thesis (Télécom Paristech, 2009).
- [84] B. Engeser. *Optische Abbildung einer atomaren Dichteverteilung*. Diploma Thesis (University of Heidelberg, 2002).
- [85] M. Brajdic. *Entwicklung einer Computersteuerung und ihre Anwendung in einem Experiment zur vereinfachten Bose-Einstein Kondensation in einer Oberflächenfalle*. Diploma Thesis (University of Heidelberg, 2003).
- [86] W. Rohringer. *Stochastic Optimization in an Ultracold Atom Experiment*. Diploma Thesis (TU Wien, 2008).
- [87] S. Schneider. *Bose-Einstein Kondensation in einer magnetischen Z-Falle* PhD Thesis (University of Heidelberg, 2003).
- [88] R. Bücker *et al.* Single-particle-sensitive imaging of freely propagating ultracold atoms. *New Journal of Physics* **11**, 103039 (2009).
- [89] C. Koller. *Towards the experimental realization of Hybrid Quantum Systems*. PhD Thesis (TU Wien, 2012).
- [90] M. Maiwöger. *Towards multiple measurements of a single Bose-Einstein condensate by coherent outcoupling*. Diploma Thesis (TU Wien, 2015).
- [91] W. H. Wing. On neutral particle trapping in quasistatic electromagnetic fields. *Progress in Quantum Electronics* **8**, 181–199 (1984).
- [92] J. Schmiedmayer. Guiding and trapping a neutral atom on a wire. *Physical Review A* **52**, R13–R16 (1995).
- [93] J. D. Weinstein & K. G. Libbrecht. Microscopic magnetic traps for neutral atoms. *Physical Review A* **52**, 4004–4009 (1995).
- [94] J. Reichel, W. Hänsel & T. Hänsch. Atomic Micromanipulation with Magnetic Surface Traps. *Physical Review Letters* **83**, 3398–3401 (1999).
- [95] R. Folman *et al.* Controlling Cold Atoms using Nanofabricated Surfaces: Atom Chips. *Physical Review Letters* **84**, 4749–4752 (2000).
- [96] R. Folman, P. Krüger, J. Schmiedmayer, J. Denschlag & C. Henkel. Microscopic atom optics: from wires to an atom chip. *Advances in Atomic, Molecular, and Optical Physics* **48**, 263–356 (2002).
- [97] E. Majorana. Atomi Orientati Incampo Magnetico Variabile. *Nuovo Cimento* **9** (1932).
- [98] K. Henderson, C. Ryu, C. MacCormick & M. G. Boshier. Experimental demonstration of painting arbitrary and dynamic potentials for Bose-Einstein condensates. *New Journal of Physics* **11**, 043030 (2009).

- [99] O. Zobay & B. M. Garraway. Two-dimensional atom trapping in field-induced adiabatic potentials. *Physical Review Letters* **86**, 1195–1198 (2001).
- [100] Y. Colombe *et al.* Ultracold atoms confined in rf-induced two-dimensional trapping potentials. *European Journal of Physics* **67**, 593–599 (2004).
- [101] I. Lesanovsky *et al.* Adiabatic radio-frequency potentials for the coherent manipulation of matter waves. *Physical Review A* **73**, 033619 (2006).
- [102] O. Morizot, Y. Colombe, V. Lorent, H. Perrin & B. M. Garraway. Ring trap for ultracold atoms. *Physical Review A* **74**, 023617 (2006).
- [103] T. Schumm *et al.* Matter-wave interferometry in a double well on an atom chip. *Nature Physics* **1**, 57–62 (2005).
- [104] S. Hofferberth, B. Fischer, T. Schumm, J. Schmiedmayer & I. Lesanovsky. Ultracold atoms in radio-frequency dressed potentials beyond the rotating-wave approximation. *Physical Review A* **76**, 013401 (2007).
- [105] T. Betz *et al.* Two-point phase correlations of a one-dimensional bosonic Josephson junction. *Physical Review Letters* **106**, 20407 (2011).
- [106] F. Baumgärtner *et al.* Measuring energy differences by BEC interferometry on a chip. *Physical Review Letters* **105**, 243003 (2010).
- [107] G. B. Jo *et al.* Matter-wave interferometry with phase fluctuating Bose-Einstein condensates. *Physical Review Letters* **99**, 240406 (2007).
- [108] T. Berrada *et al.* Integrated Mach-Zehnder interferometer for Bose-Einstein condensates. *Nature communications* **4**, 2077 (2013).
- [109] P. Böhi *et al.* Coherent manipulation of Bose-Einstein condensates with state-dependent microwave potentials on an atom chip. *Nature Physics* **5**, 592–597 (2009).
- [110] M. F. Ridel *et al.* Atom-chip-based generation of entanglement for quantum metrology. *Nature* **464**, 1170–1173 (2010).
- [111] T. Berrada. *to be published.* (2015).
- [112] J. H. Shirley. Solution of the schrödinger equation with a hamiltonian periodic in time. *Physical Review* **138**, 979–987 (1965).
- [113] H. Metcalf & P. van der Straten. *Laser Cooling and Trapping* (Springer New York, 1999).
- [114] S. Wildermuth *et al.* Optimized magneto-optical trap for experiments with ultracold atoms near surfaces. *Physical Review A* **69**, 030901 (2004).
- [115] R. Bücker *et al.* Twin-atom beams. *Nature Physics* **7**, 608–611 (2011).
- [116] S. van Frank *et al.* Interferometry with non-classical motional states of a Bose-Einstein condensate. *Nature communications* **5**, 4009 (2014).
- [117] A. Perrin *et al.* Hanbury Brown and Twiss correlations across the Bose-Einstein condensation threshold. *Nature Physics* **8**, 195–198 (2012).

- [118] A. Robert *et al.* A Bose-Einstein condensate of metastable atoms. *Science* **292**, 461–464 (2001).
- [119] T. Gericke, P. Würtz, D. Reitz, T. Langen & H. Ott. High-resolution scanning electron microscopy of an ultracold quantum gas. *Nature Physics* **4**, 949–953 (2008).
- [120] E. Streed, A. Jechow, B. Norton & D. Kielpinski. Absorption imaging of a single atom. *Nature communications* **3**, 933 (2012).
- [121] R. Hanbury Brown & R. Q. Twiss. Correlation between photons in two coherent beams of light. *Nature* **177**, 27–29 (1956).
- [122] G. A. Rebka & R. V. Pound. Time-Correlated Photons. *Nature* **180**, 1035–1036 (1957).
- [123] R. J. Glauber. The quantum theory of optical coherence. *Physical Review* **130**, 2529–2539 (1963).
- [124] G. Reinaudi, T. Lahaye, Z. Wang & D. Guéry-Odelin. Strong saturation absorption imaging of dense clouds of ultracold atoms. *Optics letters* **32**, 3143–3145 (2007).
- [125] M. Pigneur. *To be published*. PhD Thesis (2017).
- [126] S. van Frank *et al.* in preparation.
- [127] L. Cederbaum & A. Streltsov. Best mean-field for condensates. *Physics Letters A* **318**, 564–569 (2003).
- [128] L. Cederbaum & A. Streltsov. Self-consistent fragmented excited states of trapped condensates. *Physical Review A* **70**, 023610 (2004).
- [129] I. I. Rabi, J. R. Zacharias, S. Millman & P. Kusch. A New Method of Measuring Nuclear Magnetic Moment. *Physical Review* **53**, 318 (1937).
- [130] R. Bücker *et al.* Vibrational state inversion of a Bose-Einstein condensate : optimal control and state tomography. *Journal of Physics B* **46**, 104012 (2013).
- [131] H. Sussmann & J. Willems. 300 years of optimal control: from the brachystochrone to the maximum principle. *IEEE Control Systems Magazine* **17**, 32–44 (1997).
- [132] P. Peirce, M. Dahleh & H. Rabitz. Optimal control of quantum-mechanical systems: Existence, numerical approximation, and applications. *Physical Review A* **37**, 4950–4964 (1988).
- [133] R. Kosloff, S. Rice, P. Gaspard, S. Tersigni & D. Tannor. Wavepacket dancing: Achieving chemical selectivity by shaping light pulses. *Chemical Physics* **139**, 201–220 (1989).
- [134] R. Bianchetti *et al.* Control and Tomography of a Three Level Superconducting Artificial Atom. *Physical Review Letters* **105**, 223601 (2010).
- [135] M. Lapert, Y. Zhang, S. J. Glaser & D. Sugny. Towards the time-optimal control of dissipative spin-1/2 particles in nuclear magnetic resonance. *Journal of Physics B* **44**, 154014 (2011).

- [136] V. Nebendahl, H. Häffner & C. Roos. Optimal control of entangling operations for trapped-ion quantum computing. *Physical Review A* **79**, 012312 (2009).
- [137] N. Timoney *et al.* Error-resistant single-qubit gates with trapped ions. *Physical Review A* **77**, 052334 (2008).
- [138] S. Sklarz & D. Tannor. Loading a Bose-Einstein condensate onto an optical lattice: An application of optimal control theory to the nonlinear Schrödinger equation. *Physical Review A* **66**, 053619 (2002).
- [139] A. Rahmani, T. Kitagawa, E. Demler & C. Chamon. Cooling through optimal control of quantum evolution. *Physical Review A* **87**, 043607 (2013).
- [140] Optimal Quantum Control Using Randomized Benchmarking. *Physical Review Letters* **112**, 240504 (2014).
- [141] P. Doria, T. Calarco & S. Montangero. Optimal Control Technique for Many-Body Quantum Dynamics. *Physical Review Letters* **106**, 190501 (2011).
- [142] L. Salasnich, A. Parola & L. Reatto. Effective wave equations for the dynamics of cigar-shaped and disk-shaped Bose condensates. *Physical Review A* **65**, 043614 (2002).
- [143] G. Agrawal. *Nonlinear Fiber Optics* 195–211 (Academic Press, San Diego, 2001).
- [144] J. Auer, E. Krotscheck & S. A. Chin. A fourth-order real-space algorithm for solving local Schrödinger equations. *The Journal of Chemical Physics* **115**, 6841 (2001).
- [145] I. Spielman *et al.* Collisional deexcitation in a quasi-two-dimensional degenerate bosonic gas. *Physical Review A* **73**, 020702 (2006).
- [146] K. Bhattacharyya. Quantum decay and the Mandelstam-Tamm time-energy inequality. *Journal of Physics A* **16**, 2993 (1983).
- [147] T. Caneva *et al.* Optimal Control at the Quantum Speed Limit. *Physical Review Letters* **103**, 240501 (2009).
- [148] M. G. Bason *et al.* High-fidelity quantum driving. *Nature Physics* **8**, 147–152 (2011).
- [149] T. Caneva, T. Calarco & S. Montangero. Chopped random-basis quantum optimization. *Physical Review A* **84**, 022326 (2011).
- [150] J. A. Nelder & R. Mead. A Simplex Method for Function Minimization. *The Computer Journal* **7**, 308–313 (1965).
- [151] A. van Amerongen, J. van Es, P. Wicke, K. Kheruntsyan & N. van Druten. Yang-Yang Thermodynamics on an Atom Chip. *Physical Review Letters* **100**, 090402 (2008).
- [152] M. A. Garcia-March, D. R. Dounas-Frazer & L. D. Carr. Macroscopic superposition states of ultracold bosons in a double-well potential. *Frontiers of Physics* **1**, 131–145 (2012).

- [153] J. C. Lagarias, J. A. Reeds, M. H. Wright & P. E. Wright. Convergence Properties of the Nelder–Mead Simplex Method in Low Dimensions. *SIAM Journal on Optimization* **9**, 112–147 (1998).
- [154] L. deBroglie. *Recherche sur la théorie des quanta*. PhD Thesis (Paris, 1924).
- [155] M. O. Scully & J. P. Dowling. Quantum-noise limits to matter-wave interferometry. *Physical Review A* **48**, 3186–3190 (1993).
- [156] P. Hannaford, R. McLean, G. Opat, W. Rowlands & A. Sidorov. *Towards a Cold-Atom Matter-Wave Interferometer* (eds D. Walls & J. Harvey) 18–26 (Springer Berlin Heidelberg, 1994).
- [157] H. Rauch & M. Suda. Intensitätsberechnung für ein Neutronen-Interferometer. *Physica Status Solidi (a)* **25**, 495–505 (1974).
- [158] L. Marton. Electron Interferometer. *Physical Review* **85**, 1057–1058 (1952).
- [159] D. W. Keith, C. R. Ekstrom, Q. A. Turchette & D. E. Pritchard. An Interferometer for Atoms. *Phys. Rev. Lett.* **66**, 2693–2697 (1991).
- [160] J. D. Perreault & A. D. Cronin. Observation of atom wave phase shifts induced by van der Waals atom-surface interactions. *Physical Review Letters* **95**, 133201 (2005).
- [161] D. J. Wineland, R. E. Drullinger & F. L. Walls. Radiation-pressure cooling of bound resonant absorbers. *Physical Review Letters* **40**, 1639–1642 (1978).
- [162] W. Neuhauser, M. Hohenstatt, P. Toschek & H. Dehmelt. Optical-sideband cooling of visible atom cloud confined in parabolic well. *Physical Review Letters* **41**, 233–236 (1978).
- [163] W. Paul *pat.* 773,689 (Germany) (1953).
- [164] W. Paul. Electromagnetic Traps for Charged and Neutral Particles. *Reviews of Modern Physics* **62**, 531–540 (1990).
- [165] H. Dehmelt. Less is more: Experiments with an individual atomic particle at rest in free space. *American Journal of Physics* **58**, 17–27 (1990).
- [166] E. M. Rasel, M. K. Oberthaler, H. Batelaan, J. Schmiedmayer & A. Zeilinger. Atom Wave Interferometry with Diffraction Gratings of Light. *Physical Review Letters*, 2633–2637 (1995).
- [167] D. M. Giltner & R. W. McGowan. Atom interferometer based on Bragg scattering from standing light waves. *Physical Review Letters* **75**, 2638–2641 (1995).
- [168] I. I. Rabi, S Millman, P Kusch & J. R. Zacharias. The molecular beam resonance method for measuring nuclear magnetic - Moments the magnetic moments of Li-3(6) Li-3(7) and F-9(19). *Physical Review* **55**, 526–535 (1939).
- [169] N. F. Ramsey. A Molecular Beam Resonance Method with Separated Oscillating Fields. *Physical Review* **78**, 695–699 (1950).

- [170] M. A. Lombardi, T. P. Heavner & S. R. Jefferts. NIST Primary Frequency Standards and the Realization of the SI Second. *Journal of Measurement Science* **2**, 74–89 (2007).
- [171] S. Altshuler & L. Frantz *pat.* US 3,761,721 (1973).
- [172] V. P. Chebotayev, B. Y. Dubetsky, A. P. Kasantsev & V. P. Yakovlev. Interference of atoms in separated optical fields. *Journal of the Optical Society of America B* **2**, 1791 (1985).
- [173] J. F. Clauser. Ultra-high sensitivity accelerometers and gyroscopes using neutral atom matter-wave interferometry. *Physica B+C* **151**, 262–272 (1988).
- [174] C. J. Bordé. Atomic interferometry with internal state labelling. *Physics Letters A* **140**, 10–12 (1989).
- [175] D. E. Pritchard & D. W. Keith *pat.* US 4,886,964 (1989).
- [176] M. Kasevich & S. Chu. Atomic interferometry using stimulated Raman transitions. *Physical Review Letters* **67**, 181–184 (1991).
- [177] D. S. Weiss, B. C. Young & S. Chu. Precision Measurement of the Photon Recoil of an Atom Using Atomic Interferometry. *Physical Review Letters* **70**, 2706–2709 (1993).
- [178] A. D. Cronin & D. E. Pritchard. Optics and interferometry with atoms and molecules. *Reviews of Modern Physics* **81**, 1051–1129 (2009).
- [179] Y.-J. Wang *et al.* Atom Michelson interferometer on a chip using a Bose-Einstein condensate. *Physical Review Letters* **94**, 090405 (2005).
- [180] H. T. C. Stoof. *Condensate Formation in a Bose Gas* (eds A. Griffin, D. W. Snoke & S. Stringari) Cambridge Books Online, 226–245 (Cambridge University Press, 1995).
- [181] Y. Castin & J. Dalibard. Relative phase of two Bose-Einstein condensates. *Physical Review A* **55**, 4330–4337 (1997).
- [182] M. R. Andrews *et al.* Observation of Interference Between Two Bose Condensates. *Science* **275**, 637–641 (1997).
- [183] M. Köhl, T. Hänsch & T. Esslinger. Measuring the Temporal Coherence of an Atom Laser Beam. *Physical Review Letters* **87**, 160404 (2001).
- [184] G.-B. Jo *et al.* Long Phase Coherence Time and Number Squeezing of Two Bose-Einstein Condensates on an Atom Chip. *Physical Review Letters* **98**, 030407 (2007).
- [185] C. Deutsch *et al.* Spin Self-Rephasing and Very Long Coherence Times in a Trapped Atomic Ensemble. *Physical Review Letters* **105**, 020401 (2010).
- [186] R. P. Anderson, C. Ticknor, A. I. Sidorov & B. V. Hall. Spatially inhomogeneous phase evolution of a two-component Bose-Einstein condensate. *Physical Review A* **80**, 023603 (2009).

- [187] M. Horikoshi & K. Nakagawa. Dephasing due to atom-atom interaction in a waveguide interferometer using a Bose-Einstein condensate. *Physical Review A* **74**, 031602 (2006).
- [188] J. Close & N. Robins. Precision Measurement with Cold Atoms. *Physics* **5**, 5–7 (2012).
- [189] W. Muessel, H. Strobel, D. Linnemann, D. B. Hume & M. K. Oberthaler. Scalable Spin Squeezing for Quantum-Enhanced Magnetometry with Bose-Einstein Condensates. *Physical Review Letters* **113**, 103004 (2014).
- [190] J. M. B. Kellogg, I. I. Rabi, N. F. Ramsey & J. R. Zacharias. The Magnetic Moments of the Proton and the Deuteron. *Physical Review* **56**, 728–743 (1939).
- [191] J. M. B. Kellogg, I. I. Rabi, N. F. Ramsey & J. R. Zacharias. An electrical quadrupole moment of the deuteron the radiofrequency spectra of HD and D2 molecules in a magnetic field. *Physical Review* **57**, 677–695 (1940).
- [192] N. Ramsey. A New Molecular Beam Resonance Method. *Physical Review* **76**, 996–996 (1949).
- [193] N. F. Ramsey. Experiments with separated oscillatory fields and hydrogen masers. *Science* **248**, 1612–1619 (1990).
- [194] M. Brune, S. Haroche, V. Lefevre, J. M. Raimond & N. Zagury. Quantum nondestruction measurement of small photon numbers by Rydberg-atom phase-sensitive detection. *Physical Review Letters* **65**, 976–979 (1990).
- [195] S. Haroche, M. Brune & J. M. Raimond. Atomic clocks for controlling light fields. *Physics Today* **66**, 27–32 (2013).
- [196] C. N. Yang. Concept of Off-Diagonal Long-Range Order and the Quantum Phases of Liquid He and of Superconductors. *Reviews of Modern Physics* **34**, 694 (1962).
- [197] B. Rauer *et al.* Cooling of a one-dimensional Bose gas. arXiv: 1505.04747 (2015).
- [198] R. Bücker *et al.* Dynamics of parametric matter-wave amplification. *Physical Review A* **86**, 013638 (2012).
- [199] R. Bistritzer & E. Altman. Intrinsic dephasing in one-dimensional ultracold atom interferometers. *Proceedings of the National Academy of Sciences of the United States of America* **104**, 9955–9959 (2007).
- [200] R. Geiger, T. Langen, I. E. Mazets & J. Schmiedmayer. Local relaxation and light-cone-like propagation of correlations in a trapped one-dimensional Bose gas. *New Journal of Physics* **16**, 053034 (2014).
- [201] D. S. Petrov, G. V. Shlyapnikov & J. T. Walraven. Phase-fluctuating 3D Bose-Einstein condensates in elongated traps. *Physical Review Letters* **87**, 050404 (2001).
- [202] S. Dettmer *et al.* Observation of phase fluctuations in elongated Bose-Einstein condensates. *Physical Review Letters* **87**, 160406 (2001).

- [203] E. V. Goldstein & P. Meystre. Quasiparticle instabilities in multicomponent atomic condensates. *Physical Review A* **55**, 2935–2940 (1997).
- [204] T. Langen. *Non-equilibrium dynamics of one-dimensional Bose gases*. PhD Thesis (TU Wien, 2013).
- [205] N. K. Whitlock & I. Bouchoule. Relative phase fluctuations of two coupled one-dimensional condensates. *Physical Review A* **68**, 053609 (2003).
- [206] M. Kuhnert *et al.* Multimode dynamics and emergence of a characteristic length scale in a one-dimensional quantum system. *Physical Review Letters* **110**, 090405 (2013).
- [207] T. Kitagawa, A. Imambekov, J. Schmiedmayer & E. Demler. The dynamics and prethermalization of one-dimensional quantum systems probed through the full distributions of quantum noise. *New Journal of Physics* **13**, 073018 (2011).
- [208] M. Lewenstein & L. You. Quantum Phase Diffusion of a Bose-Einstein Condensate. *Physical Review Letters* **77**, 3489–3493 (1996).
- [209] J. Javanainen & M. Wilkens. Phase and Phase Diffusion of a Split Bose-Einstein Condensate. *Physical Review Letters* **78**, 4675–4678 (1997).
- [210] Y. Shin *et al.* Atom interferometry with Bose-Einstein condensates in a double-well potential. *Physical Review Letters* **92**, 050405 (2004).
- [211] M. Kitagawa & M. Ueda. Squeezed spin states. *Physical review A* **47**, 5138–5143 (1993).
- [212] F. Piazza, L. Pezzé & A. Smerzi. Macroscopic superpositions of phase states with Bose-Einstein condensates. *Physical Review A* **78**, 051601 (2008).
- [213] M. Steel & M. Collett. Quantum state of two trapped Bose-Einstein condensates with a Josephson coupling. *Physical Review A* **57**, 2920–2930 (1998).
- [214] M. A. García-March, D. R. Dounas-Frazer & L. D. Carr. Macroscopic superposition of ultracold atoms with orbital degrees of freedom. *Physical Review A* **83**, 043612 (2011).
- [215] J. M. Zhang & R. X. Dong. Exact diagonalization: the Bose-Hubbard model as an example. *European Journal of Physics* **31**, 592–602 (2010).
- [216] K. Sakmann, A. I. Streltsov, O. E. Alon & L. S. Cederbaum. Universality of fragmentation in the Schrödinger dynamics of bosonic Josephson junctions. *Physical Review A* **89**, 023602 (2014).
- [217] R. J. Lewis-Swan & K. V. Kheruntsyan. Proposal for a motional-state Bell inequality test with ultracold atoms. *Physical Review A* **91**, 052114 (2015).
- [218] J. Eisert & M. B. Plenio. Focus on Quantum Information and Many-Body Theory. *New Journal of Physics* **12**, 025001 (2010).
- [219] T. Jacqmin. *Mesures de corrélations dans un gaz de bosons unidimensionnel sur puce*. PhD Thesis (Université Paris 11, 2012).

# Curriculum Vitae

## Personal details

Name: Ing.-Dipl. Sandrine van Frank  
Born on: July 13<sup>th</sup>, 1987 in Uccle, Brussels, Belgium  
Citizenship: Belgian  
Contact: Mollardgasse 70A/4  
1060 Wien, Austria  
sfrank@ati.ac.at

## Education

Apr. 2011 - Oct. 2015 PhD in Physics, Atominstitut, TU Wien.  
Experimental thesis in quantum optics under the supervision of Prof. Jörg Schmiedmayer. Control and study of matter-wave interference on an atomchip.

2009 - 2011 Master of Engineering, Kungliga Techniska Hogskolan (KTH), Stockholm. *Double degree with ECL*.  
Specialization in optics.

2007 - 2011 Master of Engineering, Centrale Lyon (ECL), Lyon.  
General engineering.

2005 - 2007 Preparation for the french competitive exams to the engineering schools, Lycé Hoche, Versailles.

2005 French high school diploma (*baccalauréat*) in Science, Lycée Richelieu, Rueil Malmaison, France.  
Graduated with honors.